QUANTUM COHERENCE, CORRELATION AND CONTROL IN FINITE QUANTUM SYSTEMS

EDITED BY: Hui Yan, Aixi Chen, Weibin Li and Guangling Cheng

PUBLISHED IN: Frontiers in Physics

frontiers Research Topics

frontiers

ISSN 1664-8714
ISBN 978-2-83250-316-4
DOI 10.3389/978-2-83250-316-4

About Frontiers

Frontiers is more than just an open-access publisher of scholarly articles: it is a pioneering approach to the world of academia, radically improving the way scholarly research is managed. The grand vision of Frontiers is a world where all people have an equal opportunity to seek, share and generate knowledge. Frontiers provides immediate and permanent online open access to all its publications, but this alone is not enough to realize our grand goals.

Frontiers Journal Series

The Frontiers Journal Series is a multi-tier and interdisciplinary set of open-access, online journals, promising a paradigm shift from the current review, selection and dissemination processes in academic publishing. All Frontiers journals are driven by researchers for researchers; therefore, they constitute a service to the scholarly community. At the same time, the Frontiers Journal Series operates on a revolutionary invention, the tiered publishing system, initially addressing specific communities of scholars, and gradually climbing up to broader public understanding, thus serving the interests of the lay society, too.

Dedication to Quality

Each Frontiers article is a landmark of the highest quality, thanks to genuinely collaborative interactions between authors and review editors, who include some of the world's best academicians. Research must be certified by peers before entering a stream of knowledge that may eventually reach the public - and shape society; therefore, Frontiers only applies the most rigorous and unbiased reviews.
Frontiers revolutionizes research publishing by freely delivering the most outstanding research, evaluated with no bias from both the academic and social point of view. By applying the most advanced information technologies, Frontiers is catapulting scholarly publishing into a new generation.

What are Frontiers Research Topics?

Frontiers Research Topics are very popular trademarks of the Frontiers Journals Series: they are collections of at least ten articles, all centered on a particular subject. With their unique mix of varied contributions from Original Research to Review Articles, Frontiers Research Topics unify the most influential researchers, the latest key findings and historical advances in a hot research area! Find out more on how to host your own Frontiers Research Topic or contribute to one as an author by contacting the Frontiers Editorial Office: frontiersin.org/about/contact

QUANTUM COHERENCE, CORRELATION AND CONTROL IN FINITE QUANTUM SYSTEMS

Topic Editors:
Hui Yan, South China Normal University, China
Aixi Chen, Zhejiang Sci-Tech University, China
Weibin Li, University of Nottingham, United Kingdom
Guangling Cheng, East China Jiaotong University, China

Citation: Yan, H., Chen, A., Li, W., Cheng, G., eds. (2022). Quantum Coherence, Correlation and Control in Finite Quantum Systems. Lausanne: Frontiers Media SA. doi: 10.3389/978-2-83250-316-4

Table of Contents

frontiers in Physics

ORIGINAL RESEARCH
published: 25 January 2022
doi: 10.3389/fphy.2021.822694

Controlled Bistable Transmission Non-Reciprocity in a Four-Mode Optomechanical System

Bo Jiang[1], *Dong Yan*[2], *Jing Wang*[3]*, *Dezhan Qu*[4] *and Jin-Hui Wu*[1]*

[1]Center for Quantum Sciences and School of Physics, Northeast Normal University, Changchun, China, [2]School of Science, Changchun University, Changchun, China, [3]College of Physics, Tonghua Normal University, Tonghua, China, [4]School of Information Science and Technology, Northeast Normal University, Changchun, China

We examine the bistable transmission non-reciprocity in a four-mode optomechanical system, where a mechanical oscillator interacts with one of three coupled optical cavities so as to generate an asymmetric optomechanical non-linearity. Two transmission coefficients in opposite directions are found to exhibit non-reciprocal bistable behaviors due to this asymmetric optomechanical non-linearity as the impedance-matching condition is broken for a not too weak input field. Such a bistable transmission non-reciprocity can be well manipulated to exhibit reversible higher isolation ratios in tunable wider ranges of the input field power or one cavity mode detuning by modulating relevant parameters like optical coupling strengths, optomechanical coupling strengths, and mechanical frequencies. This optomechanical system provides a flexible platform for realizing transmission non-reciprocity of weal light signals and may be extended to optical networks with more coupled cavities.

Keywords: transmission non-reciprocity, bistable non-linearity, cavity optomechanics, impedance-matching breaking, optical isolation

OPEN ACCESS

Edited by:
Hui Yan,
South China Normal University, China

Reviewed by:
Keyu Xia,
Nanjing University, China
Jianming Wen,
Kennesaw State University, United States

***Correspondence:**
Jing Wang
pwl1207wj@163.com
Jin-Hui Wu
jhwu@nenu.edu.cn

Specialty section:
This article was submitted to Quantum Engineering and Technology, a section of the journal Frontiers in Physics

Received: *26 November 2021*
Accepted: *20 December 2021*
Published: *25 January 2022*

Citation:
Jiang B, Yan D, Wang J, Qu D and Wu J-H (2022) Controlled Bistable Transmission Non-Reciprocity in a Four-Mode Optomechanical System. Front. Phys. 9:822694. doi: 10.3389/fphy.2021.822694

1 INTRODUCTION

Cavity optomechanics, focusing on enhanced radiation pressure interactions between light fields and mechanical motions, has attracted extensive experimental and theoretical interests owing to its wide applications in processing quantum information, measuring weak signals, and developing new devices [1–9]. Various optomechanical systems have been proposed and fabricated to realize non-trivial tasks and interesting phenomena, such as entanglement generation between cavity and mechanical modes [10–15], ground-state cooling of mechanical resonators [16–20], optomechanically induced transparency (OMIT) and absorption (OMIA) [21–26], Bell non-locality verification [27], parity-time (PT) symmetry-breaking chaos [28], and tumor structural imaging [29]. We note in particular that optomechanical systems can provide an effective avenue for implementing non-reciprocal devices, like isolators and circulators, required in constructing all-optical communication networks [30–34].

Non-reciprocal devices promise the transmission of signals in one direction while blocking those propagating in the opposite direction and can be utilized to avoid unwanted interference of signals and protect optical sources and systems from noises [35–42]. Breaking reciprocity or time reversal symmetry is typically accomplished with magneto-optical effects [43–45] and has resulted in the emergence of new physics such as topologically protected one-way photonic edge modes [46] and non-reciprocal behaviors in giant atom systems [47, 48]. Unfortunately, magneto-optical effects are not present in standard optoelectronic materials including most metals and semiconductors and may

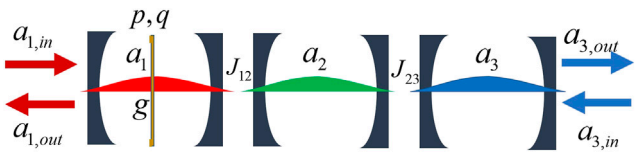

FIGURE 1 | (Color online) Schematic of an optomechanical system consisting of three cavities described by optical modes a_1, a_2, and a_3 as well as a membrane described by position q and momentum p. This system could be driven by an input field $a_{1,in}$ and exhibit an output field $a_{3,out}$, or driven by an input field $a_{3,in}$ and exhibit an output field $a_{1,out}$. Here, g denotes the optomechanical coupling strength, while J_{lk} represents the coupling strength between optical modes a_l and a_k.

result in crosstalk and other problems hampering on-chip implementations. This is why non-magnetic approaches for achieving optical non-reciprocity have been extensively studied with significant advances, for example, in chiral atomic systems [49–51] and optomechanical systems [30–34]. The latter includes, for instance, a three-mode optomechanical system with additional gain in one cavity [31] and a two-cavity optomechanical system with a blue-detuned driving [32].

Coupled micro-cavities are essential elements for constructing quantum information networks in that they are scalable via mode swapping or fiber coupling, compatible with mechanical oscillators and other elements, and easy to be controlled by driving fields. With this consideration, here we extend previous works [30–34] to seek more flexible manipulations on optical non-reciprocity by investigating a four-mode optomechanical system with three optical cavities and one mechanical oscillator. This system is found to exhibit an asymmetric optomechanical non-linearity, which then result in staggered bistable behaviors of two opposite-direction transmission coefficients, under the broken impedance-matching condition. Numerical results show in particular that quite a few parameters can be modulated on demand to manipulate, in different ways, the upper and lower stable branches of both transmission coefficients. This allows us to tune and widen non-reciprocal ranges in terms of the input power or a cavity detuning on the one hand, while improve isolation ratio and reverse isolation direction with respect to transmission coefficients on the other hand.

2 MODEL AND EQUATIONS

We consider a cavity optomechanical system consisting of three optical modes described by annihilation operators a_1, a_2, and a_3 and a mechanical mode described by position operator q and momentum operator p, as shown in **Figure 1**. These optical and mechanical modes exhibit frequencies ω_1, ω_2, ω_3, and ω_m, respectively. The 2*nd* optical mode is coupled to the 1*st* optical mode with strength J_{12}, while to the 3*rd* optical mode with strength J_{23}, in a linear way controlled via the in-between waveguide or fiber. The mechanical mode is coupled only to the 1*st* optical mode with single-photon optomechanical coupling strength g. A driving field of frequency ω_d is applied to excite the 1*st* optical mode with annihilation operator $a_{1,in}$ or the 3*rd* optical mode with annihilation operator $a_{3,in}$. With these considerations, we can write down the following Hamiltonian ($\hbar = 1$):

$$\begin{aligned} H &= \omega_1 a_1^\dagger a_1 + \omega_2 a_2^\dagger a_2 + \omega_3 a_3^\dagger a_3 + \frac{1}{2}\omega_m\left(p^2+q^2\right) \\ &+ g a_1^\dagger a_1 q + J_{12}\left(a_1^\dagger a_2 + a_2^\dagger a_1\right) + J_{23}\left(a_2^\dagger a_3 + a_3^\dagger a_2\right) \\ &+ i\sqrt{\gamma_{1,e}}\left(a_1^\dagger a_{1,in} e^{-i\omega_d t} - a_1 a_{1,in}^\dagger e^{i\omega_d t}\right) \\ &+ i\sqrt{\gamma_{3,e}}\left(a_3^\dagger a_{3,in} e^{-i\omega_d t} - a_3 a_{3,in}^\dagger e^{i\omega_d t}\right), \end{aligned} \tag{1}$$

where $\gamma_{j,e}$ has been taken as the coupling constant to the driving field, that is, the external decay rate, of the jth optical mode. It is worth noting that the jth optical mode also exhibits an intrinsic decay rate $\gamma_{j,i}$ so that its total decay rate turns out to be $\gamma_j = \gamma_{j,i} + \gamma_{j,e}$. Then we can define $\eta_j = \gamma_{j,e}/\gamma_j$ as an effective coupling ratio with $\eta_j = 0$ denoting a vanishing coupling, while $\eta_j = 1$ denoting the maximal coupling. To be more specific, our optomechanical system may be implemented either with a vibrational membrane coupled to one of three Fabry-Pérot cavities, or with an optomechanical crystal coupled to one of three photonic crystal cavities [52].

In the rotating frame of the driving frequency ω_d, it is viable to attain from the Hamiltonian in **Eq. 1** the following quantum Langevin equations (QLEs):

$$\begin{aligned} \partial_t a_1 &= -\left(\gamma_1/2 + i\Delta_1\right)a_1 - igqa_1 - iJ_{12}a_2 \\ &\quad + \sqrt{\gamma_{1,e}}a_{1,in} + \sqrt{\gamma_{1,i}}a_{1,vac}, \\ \partial_t a_2 &= -\left(\gamma_2/2 + i\Delta_2\right)a_2 - iJ_{12}a_1 - iJ_{23}a_3 \\ &\quad + \sqrt{\gamma_{2,i}}a_{2,vac}, \\ \partial_t a_3 &= -\left(\gamma_3/2 + i\Delta_3\right)a_3 - iJ_{23}a_2 \\ &\quad + \sqrt{\gamma_{3,e}}a_{3,in} + \sqrt{\gamma_{3,i}}a_{3,vac}, \\ \partial_t q &= \omega_m p, \\ \partial_t p &= -\omega_m q - g a_1^\dagger a_1 - \gamma_m p + \xi, \end{aligned} \tag{2}$$

where $\Delta_j = \omega_j - \omega_d$ is defined as the detuning of the jth optical mode to the driving field, while γ_m refers to the decay rate of the mechanical mode. In addition, we have used $a_{1,vac}$, $a_{2,vac}$, $a_{3,vac}$, and ξ to denote the input quantum noise operators with zero mean values $\langle a_{1,vac}\rangle = 0$, $\langle a_{2,vac}\rangle = 0$, $\langle a_{3,vac}\rangle = 0$, and $\langle\xi\rangle = 0$ [54].

Each operator of the optical and mechanical modes can be split into a classical mean value and a quantum fluctuation as usual. That means, we can set $a_j = \alpha_j + \delta a_j$, $a_{j,in} = \alpha_{j,in} + \delta a_{j,in}$, $q = \bar{q} + \delta q$, and $p = \bar{p} + \delta p$ with the ansatz $\alpha_j = \langle a_j\rangle$, $\alpha_{j,in} = \langle a_{j,in}\rangle$, $\bar{q} = \langle q\rangle$, and $\bar{p} = \langle p\rangle$. In the limit of a much stronger optical driving than the optomechanical coupling, that is, $\sqrt{\gamma_{j,e}}|\alpha_{j,in}| \gg \gamma_j \gg g$, the classical mean values and the fluctuation operators can be treated separately. Then we can determine the classical mean values, in the steady state ($\partial_t\alpha_i = \partial_t\bar{p} = \partial_t\bar{q} = 0$), via the following equations:

$$\begin{aligned} 0 &= -\left(\gamma_1/2 + i\Delta_1\right)\alpha_1 - ig\bar{q}\alpha_1 - iJ_{12}\alpha_2 + \sqrt{\gamma_{1,e}}\alpha_{1,in}, \\ 0 &= -\left(\gamma_2/2 + i\Delta_2\right)\alpha_2 - iJ_{12}\alpha_1 - iJ_{23}\alpha_3, \\ 0 &= -\left(\gamma_3/2 + i\Delta_3\right)\alpha_3 - iJ_{23}\alpha_2 + \sqrt{\gamma_{3,e}}\alpha_{3,in}, \\ 0 &= \bar{p}, \\ 0 &= -\omega_m\bar{q} - g|\alpha_1|^2, \end{aligned} \tag{3}$$

where the mean field approximation $\langle q\alpha_1\rangle \approx \langle q\rangle\langle\alpha_1\rangle$ has been taken into account. It is not difficult to see that the first (α_1) and

third (α_3) optical modes are not reciprocal because the mean position $\bar{q}$ of the mechanical mode is just coupled to the mean amplitude α_1 of the first optical mode via $-ig\bar{q}\alpha_1$ with $\bar{q} = -g|\alpha_1|^2/\omega_m$. That means, the aforementioned equations do not remain unchanged if we exchange subscripts "1" and "3." Therefore, a transmission non-reciprocity is expected to occur no matter the driving field comes from either one direction ($\alpha_{1,in} \neq 0$ or $\alpha_{3,in} \neq 0$) or both directions ($\alpha_{1,in} \neq 0$ and $\alpha_{3,in} \neq 0$). With these classical mean values in hand, we can attain a set of linearized QLEs for the fluctuation operators in the matrix form

$$\frac{\partial f}{\partial t} = Af + \zeta, \tag{4}$$

by introducing two column vectors

$$\begin{aligned} f &= \left(\delta a_1, \delta a_1^\dagger, \delta a_2, \delta a_2^\dagger, \delta a_3, \delta a_3^\dagger, \delta q, \delta p\right)^T, \\ \zeta &= \left(\delta A_{1,in}, \delta A_{1,in}^\dagger, \delta A_{2,in}, \delta A_{2,in}^\dagger, \delta A_{3,in}, \delta A_{3,in}^\dagger, 0, \xi\right)^T \end{aligned} \tag{5}$$

and a coefficient matrix

$$A = \begin{bmatrix} -\left(\frac{\gamma_1}{2} + i\Delta_1'\right) & 0 & -iJ_{12} & 0 & 0 & 0 & -ig\alpha_1 & 0 \\ 0 & -\left(\frac{\gamma_1}{2} - i\Delta_1'\right) & 0 & iJ_{12} & 0 & 0 & ig\alpha_1^* & 0 \\ -iJ_{12} & 0 & -\left(\frac{\gamma_2}{2} + i\Delta_2\right) & 0 & -iJ_{23} & 0 & 0 & 0 \\ 0 & iJ_{12} & 0 & -\left(\frac{\gamma_2}{2} - i\Delta_2\right) & 0 & iJ_{23} & 0 & 0 \\ 0 & 0 & -iJ_{23} & 0 & -\left(\frac{\gamma_3}{2} + i\Delta_3\right) & 0 & 0 & 0 \\ 0 & 0 & 0 & iJ_{23} & 0 & -\left(\frac{\gamma_3}{2} - i\Delta_3\right) & 0 & 0 \\ 0 & 0 & 0 & 0 & 0 & 0 & 0 & \omega_m \\ -g\alpha_1^* & -g\alpha_1 & 0 & 0 & 0 & 0 & -\omega_m & -\gamma_m \end{bmatrix}, \tag{6}$$

where we have further defined $\delta A_{1,in} = \sqrt{\gamma_{1,e}}\delta a_{1,in} + \sqrt{\gamma_{1,i}}a_{1,vac}$, $\delta A_{2,in} = \sqrt{\gamma_{2,i}}a_{2,vac}$, $\delta A_{3,in} = \sqrt{\gamma_{3,e}}\delta a_{3,in} + \sqrt{\gamma_{3,i}}a_{3,vac}$, and $\Delta_1' = \Delta_1 + g\bar{q}$. Our optomechanical system can work in the stable regime only if all the eigenvalues of matrix A are negative in their real parts. This problem is difficult or impossible to be solved analytically but can be by numerically examined via the Routh–Hurwitz criterion [53] as adopted later.

In the following, we consider two specific cases where the driving field of amplitude $s_{in} = \sqrt{p_{in}/(\hbar\omega_d)}$ and power p_{in} is input just from the 1*st* optical mode with $\alpha_{1,in} = s_{in}$ and $\alpha_{3,in} = 0$ (*I*), or just from the 3*rd* optical mode with $\alpha_{1,in} = 0$ and $\alpha_{3,in} = s_{in}$ (*II*). In case (*I*), it is easy to attain from **Eq. 3** that

$$\begin{aligned} \alpha_3 &= \frac{-J_{12}J_{23}\alpha_1}{\left(\gamma_2/2 + i\Delta_2\right)\left(\gamma_3/2 + i\Delta_3\right) + J_{23}^2}, \\ \alpha_1 &= \frac{-J_{12}J_{23}\alpha_3 + \left(\gamma_2/2 + i\Delta_2\right)\sqrt{\gamma_{1,e}}s_{in}}{\left(\gamma_2/2 + i\Delta_2\right)\left(\gamma_1/2 + i\Delta_1 - iU|\alpha_1|^2\right) + J_{12}^2}, \end{aligned} \tag{7}$$

with $U = g^2/\omega_m$ characterizing the non-linear optomechanical interaction. Considering the input–output relation $\alpha_{3,out} = \sqrt{\gamma_{3,e}}\alpha_3$ [55, 56], we finally attain

$$\left(\Gamma/2 + i\bar{\Delta}\right)\alpha_{3,out} + iU_{31}|\alpha_{3,out}|^2\alpha_{3,out} = \varepsilon_{eff}. \tag{8}$$

In this equation, we have introduced the effective damping rate Γ, detuning $\bar{\Delta}$, non-linear interaction strength U_{31}, and driving amplitude ε_{eff} by setting

$$\begin{aligned} \Gamma &= \frac{A\left(\gamma_2\gamma_3/4 - \Delta_2\Delta_3 + J_{23}^2\right) + B\left(\gamma_2\Delta_3 + \gamma_3\Delta_2\right)}{\left|\left(\gamma_2/2 + i\Delta_2\right)\left(\gamma_3/2 + i\Delta_3\right) + J_{23}^2\right|^2}, \\ \bar{\Delta} &= \frac{B\left(\gamma_2\gamma_3/4 - \Delta_2\Delta_3 + J_{23}^2\right) - A\left(\gamma_2\Delta_3 + \gamma_3\Delta_2\right)/4}{\left|\left(\gamma_2/2 + i\Delta_2\right)\left(\gamma_3/2 + i\Delta_3\right) + J_{23}^2\right|^2}, \\ \varepsilon_{eff} &= \frac{-J_{12}J_{23}\sqrt{\gamma_{1,e}\gamma_{3,e}}s_{in}}{\left(\gamma_2/2 + i\Delta_2\right)\left(\gamma_3/2 + i\Delta_3\right) + J_{23}^2}, \\ U_{31} &= \frac{-U\left|\left(\gamma_2/2 + i\Delta_2\right)\left(\gamma_3/2 + i\Delta_3\right) + J_{23}^2\right|^2}{J_{12}^2J_{23}^2\gamma_{3,e}}, \end{aligned} \tag{9}$$

with newly defined coefficients

$$\begin{aligned} A &= \gamma_3\left(\gamma_1\gamma_2/4 - \Delta_1\Delta_2\right) - \Delta_3\left(\Delta_1\gamma_2 + \Delta_2\gamma_1\right) \\ &\quad + J_{23}^2\gamma_1 + J_{12}^2\gamma_3, \\ B &= \gamma_3\left(\Delta_1\gamma_2 + \Delta_2\gamma_1\right)/4 + \Delta_3\left(\gamma_1\gamma_2/4 - \Delta_1\Delta_2\right) \\ &\quad + J_{23}^2\Delta_1 + J_{12}^2\Delta_3. \end{aligned} \tag{10}$$

In case (*II*), we attain via a similar procedure.

$$\begin{aligned} \alpha_1 &= \frac{-J_{12}J_{23}\alpha_3}{\left(\gamma_1/2 + i\Delta_1 - iU|\alpha_1|^2\right)\left(\gamma_2/2 + i\Delta_2\right) + J_{12}^2}, \\ \alpha_3 &= \frac{-J_{12}J_{23}\alpha_1 + \left(\gamma_2/2 + i\Delta_2\right)\sqrt{\gamma_{3,e}}s_{in}}{\left(\gamma_2/2 + i\Delta_2\right)\left(\gamma_3/2 + i\Delta_3\right) + J_{23}^2}, \end{aligned} \tag{11}$$

which, when substituting into the input–output relation $\alpha_{1,out} = \sqrt{\gamma_{1,e}}\alpha_1$, finally yields

$$\left(\Gamma/2 + i\bar{\Delta}\right)\alpha_{1,out} + iU_{13}|\alpha_{1,out}|^2\alpha_{1,out} = \varepsilon_{eff}, \tag{12}$$

with a new effective non-linear interaction strength $U_{13} = -U/\gamma_{1,e}$, clearly different from U_{31}.

For convenience, we now translate **Eqs 8**, **12** into a unified form in terms of $X_i = |\alpha_{i,out}|^2$

$$\left(\Gamma^2/4 + \bar{\Delta}^2\right)X_i + 2\bar{\Delta}U_{eff}X_i^2 + U_{eff}^2X_i^3 = |\varepsilon_{eff}|^2, \tag{13}$$

with $U_{eff} = U_{13}$ for $X_1 = |\alpha_{1,out}|^2$, while $U_{eff} = U_{31}$ for $X_3 = |\alpha_{3,out}|^2$. This non-linear equation indicates that X_i can take three real values, corresponding to the bistability of output against input, under appropriate conditions. One way for determining the bistable region is to take a derivative of **Eq. 13** with respect to X_i, yielding

$$\left(\Gamma^2/4 + \bar{\Delta}^2\right) + 4\bar{\Delta}U_{eff}X_i + 3U_{eff}^2X_i^2 = 0, \tag{14}$$

whose two positive roots

$$X_i^{\pm} = \frac{-4\bar{\Delta} \mp \sqrt{4\bar{\Delta}^2 - 3\Gamma^2}}{6U_{eff}} > 0, \tag{15}$$

restricted by $\bar{\Delta} < -\sqrt{3}\Gamma/2$ referring to two turning points of the bistable region. That means, the solution of **Eq. 15** takes three branches in the bistable region of $X_i^- \leq X_i \leq X_i^+$. The intermediate branch is known to be definitely unstable because it corresponds to the maximum (not minimum) point in an effective potential, while the upper and lower branches are usually stable, for example, in a non-linear Kerr medium [57, 58]. In our optomechanical system, the upper branch may also be unstable as the mechanical mode exhibits a negative effective

damping rate owing to a heating effect in the blue-detuned or strong-driving regime, which will be numerically examined via the Routh–Hurwitz criterion [53].

The expected non-linear bistability is straightforward to be examined by two transmission coefficients:

$$T_{31} = |\alpha_{3,out}/\alpha_{1,in}|^2, \quad T_{13} = |\alpha_{1,out}/\alpha_{3,in}|^2, \tag{16}$$

referring, respectively, to a transport from the 1*st* optical mode to the 3*rd* optical mode and that from the 3*rd* optical mode to the 1*st* optical mode. Considering that U_{31} and U_{13} have different expressions, we know from **Eqs 8**, **12** that $a_{3,out} \neq a_{1,out}$ in general and therefore $T_{31} \neq T_{13}$ for light signals of amplitudes $a_{1,in} = a_{2,in} = s_{in}$ input from the opposite sides of our optomechanical system. The efficiency of such a non-reciprocal transport can be quantified by defining

$$I_{tr} = 10\log(T_{31}/T_{13}), \tag{17}$$

as the isolation ratio. We should note however that it is also possible to have $U_{31} = U_{13}$ in the case of

$$\gamma_{1,e} = \frac{J_{12}^2 J_{23}^2 \gamma_{3,e}}{|(\gamma_2/2 + i\Delta_2)(\gamma_3/2 + i\Delta_3) + J_{23}^2|^2}, \tag{18}$$

referred to as the impedance-matching condition, from which it is viable to get a critical coupling strength

$$J_{23}^c = \sqrt{\frac{\gamma_{3,e}J_{12}^2 - 2\gamma_{1,e}(\gamma_2\gamma_3/4 - \Delta_2\Delta_3) \pm \sqrt{C}}{2\gamma_{1,e}}}, \tag{19}$$

with $C = \gamma_{3,e}^2 J_{12}^4 - \gamma_{1,e}\gamma_{3,e}J_{12}^2(\gamma_2\gamma_3 - 4\Delta_2\Delta_3) - \gamma_{1,e}^2(\gamma_2\Delta_3 - \Delta_2\gamma_3)$ independent of input power p_{in}. It is clear that in the case of $J_{23} \neq J_{23}^c$, the impedance-matching condition will be broken, and we could have unequal (optomechanical) non-linear interaction strengths $U_{31} \neq U_{13}$. This would result in the optical transmission non-reciprocity characterized by $T_{31} \neq T_{13}$ and thus $I_{tran} \neq 0$.

3 RESULTS AND DISCUSSION

In this section, we examine the effects of relevant tunable parameters on the non-reciprocal bistable transmission of light signals input from the opposite sides of our optomechanical system via numerical calculations. Most parameters are chosen based on two recent works and accessible in up-to-date experiments [31, 44], among which $\gamma_1/2\pi = 1.0$ GHz, $\gamma_2/2\pi = 0.5$ GHz, $\gamma_3/2\pi = 4.5$ GHz, $\eta_1 = \eta_2 = \eta_3 = 0.9$, $\omega_d/2\pi = 300$ THz, and $\gamma_m/2\pi = 6.0$ MHz are fixed in the following discussions. Numerical results will be shown in two cases where transmission coefficients T_{31} and T_{13} are plotted against input power p_{in} and detuning Δ_1, respectively, as they are much easier to modulate in regard of real applications. The main difficulty relevant to an experimental realization of our proposal lies in that the accurate preparation and arrangement of three (micro)coupled cavities of identical optical modes while different decay rates. A (micro) mechanical oscillator of proper resonant frequency and optomechanical coupling strength may also be hard to be integrated with one (micro)optical cavity.

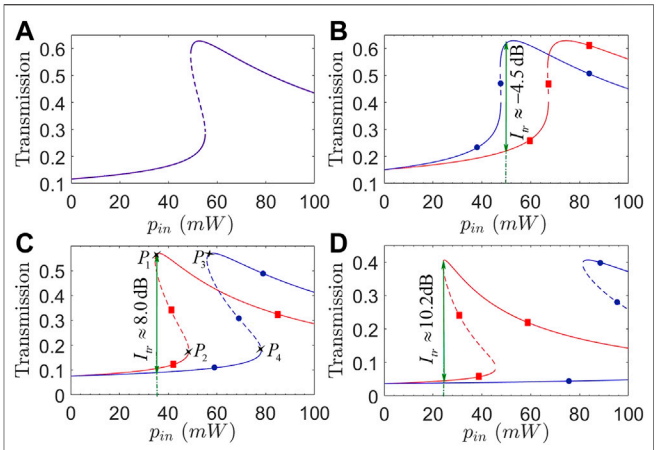

FIGURE 2 | (Color online) Transmission coefficients T_{31} (red squares) and T_{13} (blue circles) against input power p_{in} with **(A)** $J_{23}/2\pi = 1.725$ GHz; **(B)** $J_{23}/2\pi = 2.0$ GHz; **(C)** $J_{23}/2\pi = 1.4$ GHz; **(D)** $J_{23}/2\pi = 1.0$ GHz. Solid and dashed parts of each curve refer to stable and unstable regions, respectively. Other parameters are $\Delta_1/2\pi = \Delta_2/2\pi = 4.5$ GHz, $\Delta_3/2\pi = 1.5$ GHz, $g/2\pi = 0.9$ MHz, $\omega_m/2\pi = 10$ GHz, and $J_{12}/2\pi = 3.0$ GHz, except those at the beginning of **Section 3**.

3.1 Non-Reciprocal Transmission Against Input Power

In **Figure 2**, we plot transmission coefficients T_{31} and T_{13} as a function of input power p_{in} for different optical coupling strengths J_{23}. **Figure 2A** shows that transmission non-reciprocity (i.e., $T_{13} \neq T_{31}$ or $I_{tran} \neq 0$) cannot be attained as the impedance-matching condition is well satisfied with $J_{23}/2\pi = J_{23}^c/2\pi \simeq 1.725$ GHz, though our optomechanical system works in the bistable regime. Increasing or decreasing J_{23} to deviate from the critical value J_{23}^c, we can see from **Figures 2B–D** that transmission non-reciprocity occurs with different isolation ratios for different input powers. We have, in particular, that $I_{tr} \approx -4.5$ dB for $p_{in} = 50$ mW in the case of $J_{23}/2\pi = 2.0$ GHz, $I_{tr} \approx 8.0$ dB for $p_{in} = 36$ mW in the case of $J_{23}/2\pi = 1.4$ GHz, and $I_{tr} \approx 10.2$ dB for $p_{in} = 25$ mW in the case of $J_{23}/2\pi = 1.0$ GHz. These results indicate that it is viable to reverse the transmission non-reciprocity from $I_{tr} < 0$ to $I_{tr} > 0$ ($I_{tr} > 0$ to $I_{tr} < 0$) as J_{23} is decreased (increased) to cross the critical value J_{23}^c, and we can attain higher isolation ratios in wider bistable regions by modulating J_{23} to be more deviating from the critical value J_{23}^c. Taking **Figure 2C** as an example, it is also important to note that we should choose to work in the region between turning points P_2 and P_4 as p_{in} is increased from a small value, while between P_1 and P_3 as p_{in} is decreased from a large value. This promises for attaining a more efficient transmission non-reciprocity corresponding to a larger $|I_{tr}|$ because it can be evaluated with the upper branch of T_{31} and the lower branch of T_{13}. Otherwise, T_{31} and T_{13} will both work in the lower or

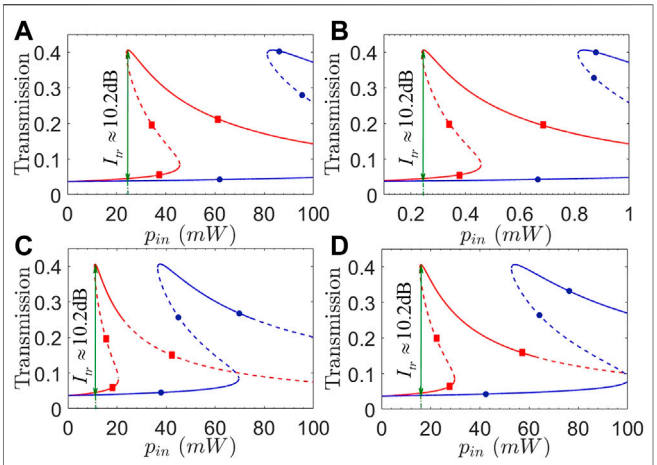

FIGURE 3 | (Color online) Transmission coefficients T_{31} (red squares) and T_{13} (blue circles) against input power p_{in} with **(A)** $g/2\pi = 0.9$ MHz; **(B)** $g/2\pi = 9.0$ MHz; **(C)** $\omega_m/2\pi = 4.5$ GHz; **(D)** $\omega_m/2\pi = 6.5$ GHz. Solid and dashed parts of each curve refer to stable and unstable regions, respectively. Other parameters are the same as in **Figure 2**, except $J_{23}/2\pi = 1.0$ GHz.

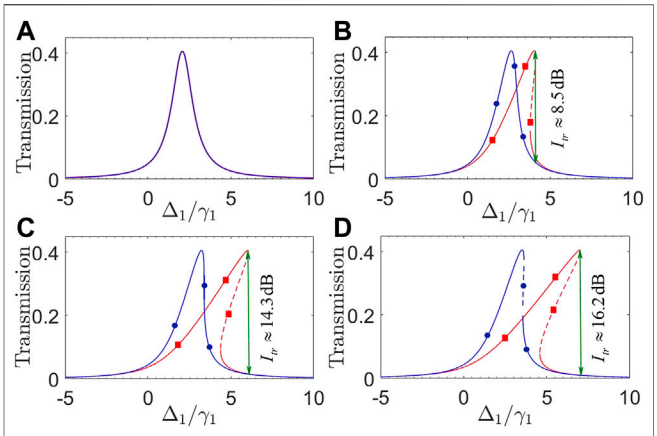

FIGURE 5 | (Color online) Transmission coefficients T_{31} (red squares) and T_{13} (blue circles) against detuning Δ_1 with **(A)** $p_{in} = 0.1$ mW; **(B)** $p_{in} = 20$ mW; **(C)** $p_{in} = 40$ mW; **(D)** $p_{in} = 50$ mW. Solid and dashed parts of each curve refer to stable and unstable regions, respectively. Other parameters are $\Delta_2/2\pi = 4.5$ GHz, $\Delta_3/2\pi = 1.5$ GHz, $g/2\pi = 0.9$ MHz, $\omega_m/2\pi = 10$ GHz, $J_{12}/2\pi = 3.0$ GHz, and $J_{23} = 1.0$ GHz, except those at the beginning of **Section 3**.

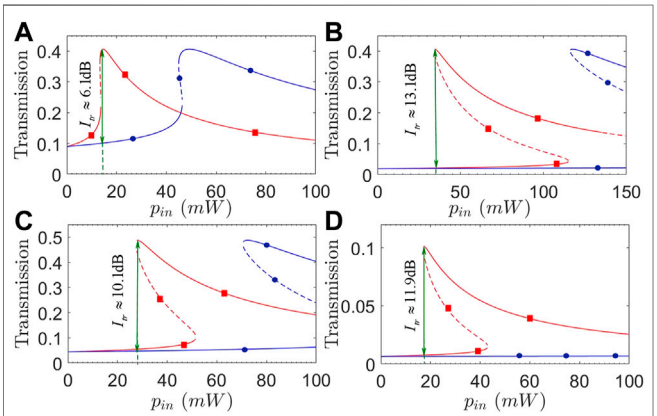

FIGURE 4 | (Color online) Transmission coefficients T_{31} (red squares) and T_{13} (blue circles) against input power p_{in} with **(A)** $\Delta_1/2\pi = 3.5$ GHz; **(B)** $\Delta_1/2\pi = 5.5$ GHz; **(C)** $\Delta_3/2\pi = 0.1$ GHz; **(D)** $\Delta_3/2\pi = 6.0$ GHz. Solid and dashed parts of each curve refer to stable and unstable regions, respectively. Other parameters are the same as in **Figure 2**, except $J_{23}/2\pi = 1.0$ GHz.

upper branch to result in well suppressed transmission non-reciprocity of smaller or vanishing $|I_{tr}|$.

Comparing **Eqs 8**, **12**, it is easy to see that the transmission non-reciprocity will be attained as long as we have $U_{13} \neq U_{31}$, which requires not only a broken impedance-matching condition but also $U = g^2/\omega_m \neq 0$. Thus, it is essential to examine in **Figure 3** different effects of optomechanical coupling strength g and mechanical frequency ω_m on transmission coefficients T_{31} and T_{13} plotted against input power p_{in}. **Figures 3A,B** show that as g is enhanced by one order, p_{in} required for observing the transmission non-reciprocity (in the bistable region where T_{13} and T_{31} work in the lower and upper branches, respectively) is reduced by two orders without changing the maximal isolation ratio $I_{tr} \approx 10.2$ dB. That means the observed transmission non-reciprocity exhibits an inverse dependence on input power p_{in} and optomechanical coupling strength g. **Figures 3C,D** further show that the non-reciprocal region in terms of p_{in} is not so sensitive to ω_m though this region can be enlarged in the case of a larger ω_m. It is more important to note that the upper branches of T_{31} and T_{13} may not be always stable and a larger ω_m is helpful to reduce the unstable regions. These findings tell us how to choose g and ω_m for attaining a wide enough non-reciprocal region corresponding to low enough input powers.

Considering that the driving field and relevant optical modes are easy to be modulated in frequency, we plot in **Figure 4** transmission coefficients T_{31} and T_{13} as a function of input power p_{in} for different detunings Δ_1 and Δ_3. We can see from **Figures 4A,B** that the isolation ratio may be evidently improved in a wider non-reciprocal region by choosing a slightly larger Δ_1 to well suppress the lower branches of T_{31} and T_{13}, while leaving the upper branches unchanged yet in magnitude. To be more specific, we have $I_{tr} \approx 6.1$ dB for $p_{in} = 14$ mW with $\Delta_1/2\pi = 3.5$ GHz, while $I_{tr} \approx 13.1$ dB for $p_{in} = 35$ mW with $\Delta_1/2\pi = 5.5$ GHz. **Figures 4C,D** show instead that a significant increase of Δ_3, though can result in a wider non-reciprocal region, will not change the isolation ratio too much as the upper and lower branches are suppressed to the roughly same extent. We also note from **Figure 4B** that the upper branch of T_{31} starts to become unstable at $p_{in} \gtrsim 140$ mW for $\Delta_1 = 5.5$ GHz. It is thus clear that detunings Δ_1 and Δ_3 play different roles in manipulating the transmission non-reciprocity and can be jointly modulated for observing an ideal transmission non-reciprocity with larger isolation ratios and well suppressed lower branches for moderate input powers.

3.2 Non-Reciprocal Transmission Against Detuning

We first plot in **Figure 5** transmission coefficients T_{31} and T_{13} as a function of detuning Δ_1 for different input powers p_{in}. As the

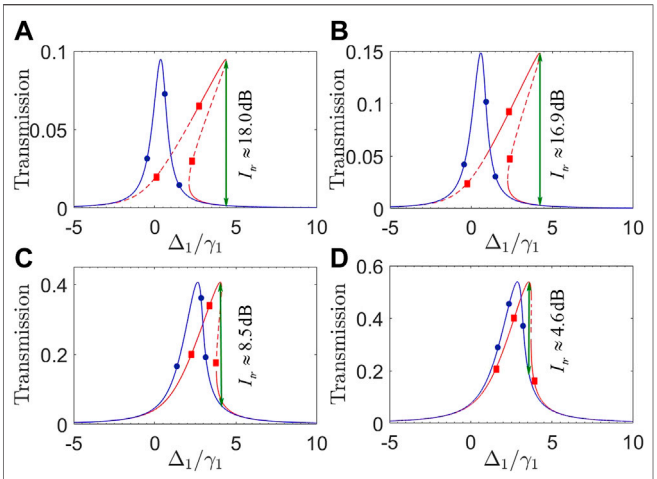

FIGURE 6 | (Color online) Transmission coefficients T_{31} (red squares) and T_{13} (blue circles) against detuning Δ_1 with **(A)** $J_{12}/2\pi = 1.0$ GHz; **(B)** $J_{12}/2\pi = 1.3$ GHz; **(C)** $J_{23}/2\pi = 1.0$ GHz; **(D)** $J_{23}/2\pi = 1.3$ GHz. Solid and dashed parts of each curve refer to stable and unstable regions, respectively. Other parameters are the same as in **Figure 5**, except $p_{in} = 20$ mW.

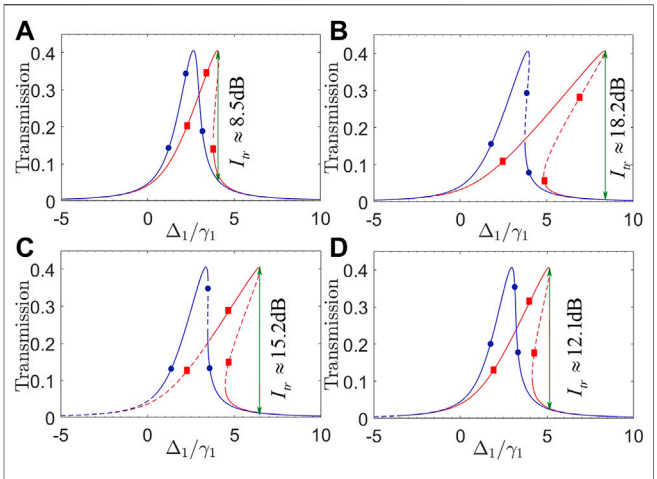

FIGURE 7 | (Color online) Transmission coefficients T_{31} (red squares) and T_{13} (blue circles) against detuning Δ_1 with **(A)** $g/2\pi = 0.9$ MHz; **(B)** $g/2\pi = 1.6$ MHz; **(C)** $\omega_m/2\pi = 4.5$ GHz; **(D)** $\omega_m/2\pi = 6.5$ GHz. Solid and dashed parts of each curve refer to stable and unstable regions, respectively. Other parameters are the same as in **Figure 5**, except $p_{in} = 20$ mW.

input power is very low (i.e., $p_{in} = 0.1$ mW), **Figure 5A** shows that T_{31} and T_{13} overlap well with a symmetric peak centered at $\Delta_1 \approx (J_{12} + J_{23})/2 = 2$ GHz, therefore leading to a vanishing transmission non-reciprocity. This can be attributed to the fact that both **Eqs 8**, **12** reduce to $(\Gamma/2 + i\bar{\Delta})\alpha_{j,out} \approx \varepsilon_{eff}$ when $U_{jj'}|\alpha_{j,out}|^2$ with $j + j' = 4$ is much smaller than $\bar{\Delta}$. As the input power increases to be large enough, we find from **Figures 5B–D** that T_{31} and T_{13} start to exhibit different bistable behaviors and thus become distinguishable on the side of $\Delta_1 > (J_{12} + J_{23})/2$ because U_{13} and U_{31} always take negative values. That means the deviation of a transmission peak from its original position may serve as a good estimation on the strength of non-linear optomechanical interaction. To be more specific, the input power p_{in} has less influence on T_{13} than T_{31} so that the transmission non-reciprocity occurs and becomes more and more evident as p_{in} increases. It is also noted that a larger input power always results in a wider bistable region with a higher isolation ratio at the right turning point of T_{31}: $I_{tr} \approx 8.5$ dB at $\Delta_1/\gamma_1 = 4.0$ for $p_{in} = 20$ mW; $I_{tr} \approx 14.3$ dB at $\Delta_1/\gamma_1 = 6.0$ for $p_{in} = 40$ mW; $I_{tr} \approx 16.2$ dB at $\Delta_1/\gamma_1 = 7.0$ for $p_{in} = 50$ mW.

Then we examine different effects of optical coupling strengths J_{12} and J_{23} by plotting in **Figure 6** transmission coefficients T_{31} and T_{13} against detuning Δ_1. **Figures 6A,B** show that a slight increase in J_{12} will result in an evidently identical rising of T_{31} and T_{13} but leaving their peaks roughly unchanged in position. The main difference lies in that the upper branch of T_{31} in **Figure 6A** exhibits a wider stable region than that in **Figure 6B**, indicating that a larger J_{12} helps to suppress quantum fluctuations arising from the non-linear optomechanical interaction. On the other hand, **Figures 6C,D** show that a slight increase in J_{23} can also result in an evidently identical rising of T_{31} and T_{13}, but their peaks become evidently closer to each other, leading to a narrowing of the non-reciprocal bistable region as well as a reduction in the isolation ratio. These findings tell that a moderate J_{23} and a larger J_{12} are appropriate for attaining non-reciprocal bistable regions of wide enough stable upper branches and large enough isolation ratios.

Finally, we examine different effects of mechanical frequency ω_m and optomechanical coupling strength g by plotting in **Figure 7** transmission coefficients T_{31} and T_{13} against detuning Δ_1. Comparing **Figures 7A,B**, we can see that both T_{31} and T_{13} remain unchanged in their peak values but clearly become more inclined toward $\Delta_1 > 0$ so as to yield wider bistable regions, with the increase in g. This then results in a wider non-reciprocal transmission region considering that T_{31} is much more sensitive to g and thus exhibits a much wider bistable region than T_{13}. **Figures 7C,D** show however that an increase in ω_m is helpful to reduce the unstable region of T_{31} in its upper branch but meanwhile also results in a reduction of the bistable regions for both T_{31} and T_{13}. These findings tell that one should choose a lower ω_m and a higher g to enhance the non-linear optomechanical interaction required for attaining wider non-reciprocal transmission regions of high isolation ratios.

In figures, the bistable transmission non-reciprocity occurs as the two curves for T_{31} and T_{13} do not overlap in each plot. It is thus appropriate to roughly determine a non-reciprocal bandwidth as the absolute difference of two values of p_{in} or Δ_1 corresponding, respectively, to the peak of T_{31} and that of T_{13}. This non-reciprocal bandwidth is a few or tens of mW in **Figures 2–4**, while several times of γ_1 in **Figures 5–7**, depending on relevant parameters like J_{12}, J_{23}, g, and ω_m. Note also that a dynamic reciprocity, referring to the fact that a (weak) backward noise, can also be transmitted with little loss in the presence of a (strong) forward signal of high transmission, typically exists in the non-reciprocal systems based on optical non-linearities [59].

Accordingly, one limitation of our optomechanical system may be that it cannot break the dynamic reciprocity because the transmission non-reciprocity arises from a bistable non-linearity. This is clear by looking at **Figures 2–4** where we have $T_{31} \neq T_{13}$ only when input power p_{in} is not too small.

4 CONCLUSION

In summary, we have studied a four-mode optomechanical system for attaining the transmission non-reciprocity, in the presence of an optomechanically induced non-linearity, with respect to a driving field input from the left or right side. As the impedance-matching condition is broken, we find that transmission coefficients T_{31} and T_{13}, plotted against input power p_{in} or cavity detuning Δ_1, may exhibit staggered bistable behaviors and therefore can work in the upper and lower branches, respectively. The isolation ratio of such a non-reciprocal transmission is viable to switch between $I_{tr} > 0$ and $I_{tr} < 0$ and can be improved in magnitude by modulating optical coupling strengths $J_{12,23}$ and detunings $\Delta_{1,3}$ to suppress the lower branches or enhance the upper branches. It is also viable to broaden the non-reciprocal bistable region in terms of p_{in} (Δ_1) by modulating optomechanical coupling strength g and mechanical frequency ω_m in addition to $J_{12,23}$ and $\Delta_{1,3}$ (p_{in}). But we should note that an increasing part of the upper branch may become unstable as the non-reciprocal region becomes wider, which restricts the tunable ranges of relevant parameters. Our results well extend the previous works on realizing non-reciprocal transmission in optomechanical systems and are instructive for designing non-reciprocal devices in optical networks based on coupled cavities.

DATA AVAILABILITY STATEMENT

The original contributions presented in the study are included in the article/supplementary material; further inquiries can be directed to the corresponding authors.

AUTHOR CONTRIBUTIONS

The idea was first conceived by J-HW. BJ was responsible for the physical modeling, the numerical calculations, and writing most of the manuscript. J-HW contributed to writing the manuscript, JW verified results of the theoretical calculation, and DY contributed to the discussion of the results. DQ provided technical support in computer simulation.

FUNDING

This work is supported by the National Natural Science Foundation of China (12074061, 11674049, and 11874004), Science Foundation of Education Department of Jilin Province (JJKH20200557KJ), and Nature Science Foundation of Science and Technology Department of Jilin Province (20210101411JC).

ACKNOWLEDGMENTS

BJ thanks Luning Song, Yan Zhang, and Zhihai Wang for helpful discussions.

REFERENCES

1. Teufel JD, Harlow JW, Regal CA, Lehnert KW. Dynamical Backaction of Microwave fields on a Nanomechanical Oscillator. *Phys Rev Lett* (2008) 101: 197203. doi:10.1103/PhysRevLett.101.197203
2. Aspelmeyer M, Kippenberg TJ, Marquardt F. Cavity Optomechanics. *Rev Mod Phys* (2014) 86:1391–452. doi:10.1103/RevModPhys.86.1391
3. Liu Y-C, Hu Y-W, Wong C-W, Xiao Y-F. Review of Cavity Optomechanical Cooling. *Chin Phys B* (2013) 22:114213. doi:10.1088/1674-1056/22/11/114213
4. He B. Quantum Optomechanics beyond Linearization. *Phys Rev A* (2012) 85: 063820. doi:10.1103/PhysRevA.85.063820
5. Cao C, Mi S-C, Gao Y-P, He L-Y, Yang D, Wang T-J, et al. Tunable High-Order Sideband Spectra Generation Using a Photonic Molecule Optomechanical System. *Sci Rep* (2016) 6:1–8. doi:10.1038/srep22920
6. Xiong X-R, Gao Y-P, Liu X-F, Cao C, Wang T-J, Wang C. The Analysis of High-Order Sideband Signals in Optomechanical System. *Sci China Phys Mech Astron* (2018) 61:1–4. doi:10.1007/s11433-017-9187-2
7. Shi H-Q, Xie Z-Q, Xu X-W, Liu N-H. Unconventional Phonon Blockade in Multimode Optomechanical System. *Acta Phys Sin* (2018) 67:044203. doi:10.7498/aps.67.20171599
8. Marinković I, Wallucks A, Riedinger R, Hong S, Aspelmeyer M, Gröblacher S. Optomechanical bell Test. *Phys Rev Lett* (2018) 121:220404. doi:10.1103/PhysRevLett.121.220404
9. Xu H, Lai D-G, Qian Y-B, Hou B-P, Miranowicz A, Nori F. Optomechanical Dynamics in the PT - and Broken- PT -symmetric regimes*mathcalPT*- and broken-*mathcalPT*-symmetric Regimes. *Phys Rev A* (2021) 104:053518. doi:10.1103/PhysRevA.104.053518
10. Vitali D, Gigan S, Ferreira A, Böhm HR, Tombesi P, Guerreiro A, et al. Optomechanical Entanglement between a Movable Mirror and a Cavity Field. *Phys Rev Lett* (2007) 98:030405. doi:10.1103/PhysRevLett.98.030405
11. Chen R-X, Shen L-T, Yang Z-B, Wu H-Z, Zheng S-B. Enhancement of Entanglement in Distant Mechanical Vibrations via Modulation in a Coupled Optomechanical System. *Phys Rev A* (2014) 89:023843. doi:10.1103/PhysRevA.89.023843
12. Liao J-Q, Wu Q-Q, Nori F. Entangling Two Macroscopic Mechanical Mirrors in a Two-Cavity Optomechanical System. *Phys Rev A* (2014) 89:014302. doi:10.1103/PhysRevA.89.014302
13. Yan X-B. Enhanced Output Entanglement with Reservoir Engineering. *Phys Rev A* (2017) 96:053831. doi:10.1103/PhysRevA.96.053831
14. He Q, Ficek Z. Einstein-podolsky-rosen Paradox and Quantum Steering in a Three-Mode Optomechanical System. *Phys Rev A* (2014) 89:022332. doi:10.1103/PhysRevA.89.022332
15. Zhang X-L, Bao Q-Q, Yang M-Z, Tian X-S. Entanglement Characteristics of Output Optical fields in Double-Cavity Optomechanics. *Acta Phys Sin* (2018) 67:104203. doi:10.7498/aps.67.20172467
16. Poot M, Herre SJ. Mechanical Systems in the Quantum Regime. *Phys Rep* (2012) 511:273–335. doi:10.1016/j.physrep.2011.12.004
17. He B, Yang L, Lin Q, Xiao M. Radiation Pressure Cooling as a Quantum Dynamical Process. *Phys Rev Lett* (2017) 118:233604. doi:10.1103/PhysRevLett.118.233604
18. Chen H-J, Mi X-W. Normal Mode Splitting and Cooling in strong Coupling Optomechanical Cavity. *Acta Phys Sin* (2011) 60:124206–244. doi:10.7498/aps.60.124206
19. Li Y, Wu L-A, Wang Z-D. Fast Ground-State Cooling of Mechanical Resonators with Time-dependent Optical Cavities. *Phys Rev A* (2011) 83: 043804. doi:10.1103/PhysRevA.83.043804

20. Liu Z-Q, Hu C-S, Jiang Y-K, Su W-J, Wu H, Li Y, et al. Engineering Optomechanical Entanglement via Dual-Mode Cooling with a Single Reservoir. *Phys Rev A* (2021) 103:023525. doi:10.1103/PhysRevA.103.023525
21. Bai C, Hou B-P, Lai D-G, Wu D. Tunable Optomechanically Induced Transparency in Double Quadratically Coupled Optomechanical Cavities within a Common Reservoir. *Phys Rev A* (2016) 93:043804. doi:10.1103/PhysRevA.93.043804
22. Yan X-B. Optomechanically Induced Transparency and Gain. *Phys Rev A* (2020) 101:043820. doi:10.1103/PhysRevA.101.043820
23. Lü H, Wang C, Yang L, Jing H. Optomechanically Induced Transparency at Exceptional Points. *Phys Rev Appl* (2018) 10:014006. doi:10.1103/PhysRevApplied.10.014006
24. Hou B-P, Wei L-F, Wang S-J. Optomechanically Induced Transparency and Absorption in Hybridized Optomechanical Systems. *Phys Rev A* (2015) 92: 033829. doi:10.1103/PhysRevA.92.033829
25. Qu K, Agarwal GS. Phonon-mediated Electromagnetically Induced Absorption in Hybrid Opto-Electromechanical Systems. *Phys Rev A* (2013) 87:031802. doi:10.1103/PhysRevA.87.031802
26. Zhang J-Q, Li Y, Feng M, Xu Y. Precision Measurement of Electrical Charge with Optomechanically Induced Transparency. *Phys Rev A* (2012) 86:053806. doi:10.1103/PhysRevA.86.053806
27. Brunner N, Cavalcanti D, Pironio S, Scarani V, Wehner S. Bell Nonlocality. *Rev Mod Phys* (2014) 86:419–78. doi:10.1103/RevModPhys.86.419
28. Lü X-Y, Jing H, Ma J-Y, Wu Y. PT-Symmetry-Breaking Chaos in Optomechanics. *Phys Rev Lett* (2015) 114:253601. doi:10.1103/PhysRevLett.114.253601
29. Margueritat J, Virgone-Carlotta A, Monnier S, Delanoë-Ayari H, Mertani HC, Berthelot A, et al. High-frequency Mechanical Properties of Tumors Measured by Brillouin Light Scattering. *Phys Rev Lett* (2019) 122:018101. doi:10.1103/PhysRevLett.122.018101
30. Song L-N, Zheng Q, Xu X-W, Jiang C, Li Y. Optimal Unidirectional Amplification Induced by Optical Gain in Optomechanical Systems. *Phys Rev A* (2019) 100:043835. doi:10.1103/PhysRevA.100.043835
31. Xu X-W, Song L-N, Zheng Q, Wang Z-H, Li Y. Optomechanically Induced Nonreciprocity in a Three-Mode Optomechanical System. *Acta Phys Sin* (2018) 98:063845. doi:10.1103/PhysRevA.98.063845
32. Zhang L-W, Li X-L, Yang L. Optical Nonreciprocity with Blue-Detuned Driving in Two-Cavity Optomechanics. *Acta Phys Sin* (2019) 68:170701–9. doi:10.7498/aps.68.20190205
33. Miri M-A, Ruesink F, Verhagen E, Alù A. Optical Nonreciprocity Based on Optomechanical Coupling. *Phys Rev Appl* (2017) 7:064014. doi:10.1103/PhysRevApplied.7.064014
34. Li E-Z, Ding D-S, Yu Y-C, Dong M-X, Zeng L, Zhang W-H, et al. Experimental Demonstration of Cavity-free Optical Isolators and Optical Circulators. *Phys Rev Res* (2020) 2:033517. doi:10.1103/PhysRevResearch.2.033517
35. Li B, Özdemir ŞK, Xu X-W, Zhang L, Kuang L-M, Jing H. Nonreciprocal Optical Solitons in a Spinning Kerr Resonator. *Phys Rev A* (2021) 103:053522. doi:10.1103/PhysRevA.103.053522
36. Verhagen E, Alù A. Optomechanical Nonreciprocity. *Nat Phys* (2017) 13: 922–4. doi:10.1038/nphys4283
37. Lira H, Yu Z, Fan S, Lipson M. Electrically Driven Nonreciprocity Induced by Interband Photonic Transition on a Silicon Chip. *Phys Rev Lett* (2012) 109: 033901. doi:10.1103/PhysRevLett.109.033901
38. Manipatruni S, Robinson JT, Lipson M. Optical Nonreciprocity in Optomechanical Structures. *Phys Rev Lett* (2009) 102:213903. doi:10.1103/PhysRevLett.102.213903
39. Gridnev VN. Nonreciprocal Reflection of Light from Antiferromagnets. *Jetp Lett* (1996) 64:110–3. doi:10.1134/1.567141
40. Lu X, Cao W, Yi W, Shen H, Xiao Y. Nonreciprocity and Quantum Correlations of Light Transport in Hot Atoms via Reservoir Engineering. *Phys Rev Lett* (2021) 126:223603. doi:10.1103/PhysRevLett.126.223603
41. Wang Y-P, Rao J-W, Yang Y, Xu P-C, Gui Y-S, Yao B-M, et al. Nonreciprocity and Unidirectional Invisibility in Cavity Magnonics. *Phys Rev Lett* (2019) 123: 127202. doi:10.1103/PhysRevLett.123.127202
42. Lai D-G, Huang J-F, Yin X-L, Hou B-P, Li W, Vitali D, et al. Nonreciprocal Ground-State Cooling of Multiple Mechanical Resonators. *Phys Rev A* (2020) 102:011502. doi:10.1103/PhysRevA.102.011502
43. Khanikaev AB, Mousavi SH, Shvets G, Kivshar YS. One-way Extraordinary Optical Transmission and Nonreciprocal Spoof Plasmons. *Phys Rev Lett* (2010) 105:126804. doi:10.1103/PhysRevLett.105.126804
44. Fang K, Luo J, Metelmann A, Matheny MH, Marquardt F, Clerk AA, et al. Generalized Non-reciprocity in an Optomechanical Circuit via Synthetic Magnetism and Reservoir Engineering. *Nat Phys* (2017) 13:465–71. doi:10.1038/nphys4009
45. Dzyaloshinskii I, Papamichail EV. Nonreciprocal Optical Rotation in Antiferromagnets. *Phys Rev Lett* (1995) 75:3004–7. doi:10.1103/PhysRevLett.75.3004
46. Ni X, He C, Sun X-C, Liu X-P, Lu M-H, Feng L, et al. Topologically Protected One-Way Edge Mode in Networks of Acoustic Resonators with Circulating Air Flow. *New J Phys* (2015) 17:053016. doi:10.1088/1367-2630/17/5/053016
47. Yu H, Wang Z, Wu J-H. Entanglement Preparation and Nonreciprocal Excitation Evolution in Giant Atoms by Controllable Dissipation and Coupling. *Phys Rev A* (2021) 104:013720. doi:10.1103/PhysRevA.104.013720
48. Du L, Cai M-R, Wu J-H, Wang Z, Li Y. Single-photon Nonreciprocal Excitation Transfer with Non-markovian Retarded Effects. *Phys Rev A* (2021) 103:053701. doi:10.1103/PhysRevA.103.053701
49. Zhang S, Hu Y, Lin G, Niu Y, Xia K, Gong J, et al. Thermal-motion-induced Non-reciprocal Quantum Optical System. *Nat Photon* (2018) 12:744–8. doi:10.1038/s41566-018-0269-2
50. Xia K, Nori F, Min X. Cavity-free Optical Isolators and Circulators Using a Chiral Cross-Kerr Nonlinearity. *Phys Rev Lett* (2018) 121:203602. doi:10.1103/PhysRevLett.121.203602
51. Hu Y, Zhang S, Qi Y, Lin G, Niu Y, Gong S. Multiwavelength Magnetic-free Optical Isolator by Optical Pumping in Warm Atoms. *Phys Rev Appl* (2019) 12: 054004. doi:10.1103/PhysRevApplied.12.054004
52. Paraïso TK, Kalaee M, Zang L, Pfeifer H, Marquardt F, Painter O. Position-squared Coupling in a Tunable Photonic crystal Optomechanical Cavity. *Phys Rev X* (2015) 5:041024. doi:10.1103/PhysRevX.5.041024
53. DeJesus EX, Kaufman C. Routh-hurwitz Criterion in the Examination of Eigenvalues of a System of Nonlinear Ordinary Differential Equations. *Phys Rev A* (1987) 35:5288–90. doi:10.1103/PhysRevA.35.5288
54. Paternostro M, Gigan S, Kim MS, Blaser F, Böhm HR, Aspelmeyer M. Reconstructing the Dynamics of a Movable Mirror in a Detuned Optical Cavity. *New J Phys* (2006) 8:107. doi:10.1088/1367-2630/8/6/107
55. Gardiner CW, Collett MJ. Input and Output in Damped Quantum Systems: Quantum Stochastic Differential Equations and the Master Equation. *Phys Rev A* (1985) 31:3761–74. doi:10.1103/PhysRevA.31.3761
56. Agarwal GS, Huang S. Optomechanical Systems as Single-Photon Routers. *Phys Rev A* (2012) 85:021801. doi:10.1103/PhysRevA.85.021801
57. Aldana S, Bruder C, Nunnenkamp A. Equivalence between an Optomechanical System and a Kerr Medium. *Phys Rev A* (2013) 88:043826. doi:10.1103/PhysRevA.88.043826
58. Fabre C, Pinard M, Bourzeix S, Heidmann A, Giacobino E, Reynaud S. Quantum-noise Reduction Using a Cavity with a Movable Mirror. *Phys Rev A* (1994) 49:1337–43. doi:10.1103/PhysRevA.49.1337
59. Shi Y, Yu Z, Fan S. Limitations of Nonlinear Optical Isolators Due to Dynamic Reciprocity. *Nat Photon* (2015) 9:388–92. doi:10.1038/nphoton.2015.79

Conflict of Interest: The authors declare that the research was conducted in the absence of any commercial or financial relationships that could be construed as a potential conflict of interest.

Publisher's Note: All claims expressed in this article are solely those of the authors and do not necessarily represent those of their affiliated organizations, or those of the publisher, the editors, and the reviewers. Any product that may be evaluated in this article, or claim that may be made by its manufacturer, is not guaranteed or endorsed by the publisher.

frontiers in Physics

ORIGINAL RESEARCH
published: 22 March 2022
doi: 10.3389/fphy.2022.880117

Realization of Tunable Highly-Efficient Quantum Routing in Chiral Waveguides

Guo-An Yan[1]* *and Hua Lu*[2]*

[1]School of Physics and Physical Engineering, Qufu Normal University, Qufu, China, [2]School of Science, Hubei University of Technology, Wuhan, China

The chiral interaction between single photons in waveguides and quantum emitters has gained considerable attention. Here, we proposed a tunable quantum routing scheme with a chiral quantum system by coupling an emitter to two chiral waveguides. Conventional quantum routers can only be achieved with each port output probability no larger than 25%. But our scheme can transfer quantum information arbitrarily from an input port to another, and each port's output probability is 100%. Besides, we investigated the influence of the Purcell factor in quantum routing properties. No matter how to change the size of the directionalities S_j or set a specific value to the dissipation of the emitter, we always found that the quantum routing has very high efficiency. Moreover, we also used a superconducting qubit coupled to two resonators to show the present scheme is pretty feasible for experimental implementation.

Keywords: photon-atom interactions, quantum router, chiral waveguides, quantum coherence, purcell factor

OPEN ACCESS

Edited by:
Guangling Cheng,
East China Jiaotong University, China

Reviewed by:
Minghao Wang,
Hubei University, China
Meng Shan Wu,
Hainan University, China

***Correspondence:**
Guo-An Yan
guoanyan@qfnu.edu.cn
Hua Lu
lvhuahg@163.com

Specialty section:
This article was submitted to Quantum Engineering and Technology, a section of the journal Frontiers in Physics

Received: *21 February 2022*
Accepted: *03 March 2022*
Published: *22 March 2022*

Citation:
Yan G-A and Lu H (2022) Realization of Tunable Highly-Efficient Quantum Routing in Chiral Waveguides. Front. Phys. 10:880117. doi: 10.3389/fphy.2022.880117

1 INTRODUCTION

To further improve the rapid-developing quantum information technology, the establishment of a global quantum network [1] is an inevitable trend in the future. The quantum network requires the realization of quantum entanglement [2–4] among multiple remote quantum memories [5], and enables multi-party quantum communication [6, 7]. Such a network can also be applied to quantum computing, distributing quantum precision measurement and fundamental tests of physics in large-scale space. Quantum internet is consisted of three basic elements, which are quantum nodes, quantum channels and quantum repeaters. Quantum nodes, which generate, process and store quantum information, are connected by long-distance quantum channels, while quantum repeaters establish and distribute entanglement. As one kind of node devices, quantum routers [8–22] are a key component of quantum network, which can transmit information continuously between remote quantum nodes. Photons play significant roles in the construction of quantum router because they are relatively free of the decoherence [23, 24]that plagues other quantum systems, and can be manipulated and detected easily. Thus, photon is an ideal candidate of the flying qubit. The waveguide is conveniently scalable so it can be easily integrated on the chip to expand the number of nodes in the quantum network. Based on these excellent characteristics, the coupled waveguide-emitter system has attracted extensive attention in the field in quantum information processing [25–33] and quantum network. In the last several years, numerous theoretical and experimental jobs have showed a variety of quantum router plans based on superconducting circuit [34], cavity-atom [35], coupled resonator [18, 39], optomechanical system [36], or quantum dot [37] for controlling the photonic transport in quantum networks. However, the expectable routing probabilities from the incident channel to the other quantum channels are limited to no more than 50% in all previous

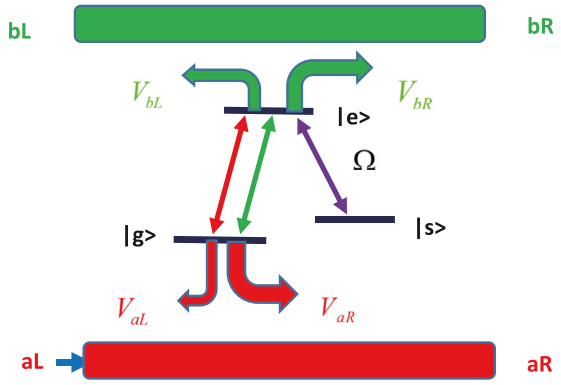

FIGURE 1 | Schematic diagram of the system. Two waveguides are chirally coupled to a Λ-type three-level system, the Λ-type three-level system is located at $x = 0$, and the similar model has been considered in Ref. [17].

schemes. But in the paper by Li et al [38], they investigate the input-output relations of the system and analyze the effect of the atomic states on the photon transmission. They scheme can route the input signal into different output ports guided by the quantum states of a two-level atom, and they also realized 100% output. In this paper we also present a physical scheme that also achieves the output of 100%. In fact, for a complex quantum network, quantum nodes can not only be used for the localized generation, processing, and storage of quantum information, but also generate and process a single qubit. Therefore, improving the routing capabilities of quantum routers is crucial.

Here, we put forward a plan to realize quantum router, our scheme is composed of two chiral waveguides and a Λ-type three-level system. Similar model has been considered in Ref. [17] to demonstrate nonreciprocal few-photon scatterings. The single-photon scattering amplitudes are given analytically. The result shows that the quantum information incident from one waveguide can be redirected into another with 100% probability when the coupling is chiral. Compared to the previous quantum routing plans [18, 39–43] that are based on single photons, our design quantum routing can transport the quantum information deterministically from an input port to arbitrary output port with high efficiency. Such a chiral quantum system could be a genuinely compact, versatile, and powerful improvement to the development of a complex quantum network.

2 MODEL SETUP

The physical system configuration considered in this article is shown in **Figure 1**. Similar model has been considered in Ref. [17] to demonstrate nonreciprocal few-photon scatterings. The hybrid system located at $x = 0$ is consists of two parallel waveguides and an emitter with ground states $|g\rangle$, intermediate state $|s\rangle$ and excited state $|e\rangle$. The waveguides are labeled a and b respectively. In theory, we allow these couplings to be chiral and marked as λ_{jL} and λ_{jR} $(j = a, b)$ respectively. When a single photon is incident from the left of waveguide a, it will propagate or be reflected by the atom along with the four ports of the two waveguide channels. Specifically, in this configuration, the perfect nonreciprocity of single-photon transport means when the single photon is incident from the left of a, it will be output from the right of b with a probability of 1. The Hamiltonian of the system is given by (setting $\hbar = 1$)

$$H = H_0 + H_w + H_I, \tag{1}$$

where H_0, H_w and H_I denote the free atomic Hamiltonian, the free-transport photon in the waveguide Hamiltonian and the interactions between the atom and the waveguides Hamiltonian respectively. The free atomic Hamiltonian H_0 is given by

$$H_0 = (\omega_s - i\gamma/2)|s\rangle\langle s| + (\omega_e - i\Gamma/2)|e\rangle\langle e| + \Omega(|e\rangle\langle s| + h.c)$$

where ω_s (ω_e) is the frequency of the intermediate (excited)state, γ and Γ account for the spontaneous emission of the state $|s\rangle$ and $|e\rangle$ into other modes different from the waveguide modes, e.g., free space. Ω is the Rabi frequency of the control field that is applied to couple the atomic states $|s\rangle$ and $|e\rangle$. The Hamiltonian of the photon mode in the two waveguides is given by

$$H_w = \sum_{j=a,b} \int dx \left[C_{jR}^{\dagger}(x)\left(\omega_{0j} - iv_g\frac{\partial}{\partial x}\right)C_{jR}(x) + C_{jL}^{\dagger}(x)\left(\omega_{0j} + iv_g\frac{\partial}{\partial x}\right)C_{jL}(x)\right]$$

where ω_{0j} space is the reference frequency. Here, we set $\omega_{0j} = \omega_{0a} = \omega_{0b}$. $C_{jR(L)}^{\dagger}(x)(j = a, b)$ is the creation operator for the right-moving (left-moving) photon along the waveguide j at position x. v_g is the group velocity of a photon in waveguide j which is considered as equal in this work. The interaction Hamiltonian is given by

$$H_I = \int dx\delta(x)\left(V_{aR}C_{aR}^{\dagger}(x)|g\rangle\langle e| + V_{aL}C_{aL}^{\dagger}(x)|g\rangle\langle e| + h.c\right) + \int dx\delta(x)\left(V_{bR}C_{bR}^{\dagger}(x)|g\rangle\langle e| + V_{bL}C_{bL}^{\dagger}(x)|g\rangle\langle e| + h.c\right)$$

where δ represents the Dirac δ function. In this expression, we choose the four coupling constants $[V_{aR}, V_{aL}, V_{bR}, V_{bL}]$ to be real numbers for simplicity. $V_{aR(bR)}$ $(V_{aL(bL)})$ is the photon-atom coupling strength for the photon propagating along the right (left) direction, and due to the chiral interactions, $V_{jR} \neq V_{jL}$ $(j = a, b)$. They are related to the final decay rates into the waveguides through $\lambda_{jR(L)} = V_{jR(L)}^2/v_g$. To measure the chiral coupling character, we bring in the parameter [17].

$$S_j = \left|\frac{\lambda_{jR} - \lambda_{jL}}{\lambda_{jR} + \lambda_{jL}}\right| (j = a, b). \tag{2}$$

Here, $S_j = 0$ when $\lambda_{jR} = \lambda_{jL}$, which occurs in nonchiral interaction, $0 < S_j < 1$ when $\lambda_{jR} \neq \lambda_{jL}$, existing chiral interaction, and whereas for maximally asymmetric coupling $S_j = 1$. The other relevant element is the Purcell factor [44–48], which accounts for the modification of the total decay rate of an emitter placed in the vicinity of a nanostructure, $P = \frac{\lambda_a + \lambda_b}{\gamma + \Gamma}$.

Finally, $\lambda_j = \lambda_{jR} + \lambda_{jL}$ ($j = a, b$), which accounts for the total decay rate of the excited state $|e\rangle$ and intermediate state $|s\rangle$ into each of the waveguides.

We concentrate on single-photon scattering in this system. Suppose the atom is in the ground state $|g\rangle$ at the initial time. The wave function of the system can be expressed as

$$|\psi\rangle = \sum_{j=a,b}\sum_{m=R,L}\int dx\varphi_{jm}(x)C^{\dagger}_{jm}(x)|0g\rangle + u_s|0s\rangle + u_e|0e\rangle \quad (3)$$

where $\varphi_{jm}(x)$ denotes the probability amplitude of the right or left propagating photon in waveguide a or b. u_s and u_e are the amplitudes of the states $|s\rangle$ and $|e\rangle$, respectively, and $|0g\rangle$ denotes the ground state, wherein there is no photon in the waveguides and the atom is at the ground state $|g\rangle$. Suppose that the single photon is injected from the left of waveguide a, the probability that the photon propagates can be expressed as

$$\begin{aligned}\varphi_{aR}(x) &= e^{-ikx}[\theta(-x) + t^a\theta(x)],\\ \varphi_{aL}(x) &= e^{-ikx}r^a\theta(-x),\\ \varphi_{bR}(x) &= e^{ikx}t^b\theta(x),\\ \varphi_{bL}(x) &= e^{-ikx}r^b\theta(-x).\end{aligned} \quad (4)$$

Here, t^a (t^b) denotes the single-photon transmission amplitude in waveguide $a(b)$ and r^a (r^b) denotes the single-photon reflection amplitude in waveguide $a(b)$. $\theta(x)$ is the Heaviside step function with $\theta(0) = 1/2$. Using the eigenequation $H|\psi\rangle = \omega|\psi\rangle$, we obtain

$$\begin{aligned}t^a &= \frac{(\lambda_{aL}-\lambda_{aR}+\lambda_{bL}+\lambda_{bR})(\omega-\omega_s+i\gamma/2)-2i(\omega-\omega_s+i\gamma/2)(\omega-\omega_e+i\Gamma/2)+2i\Omega^2}{(\lambda_{aL}+\lambda_{aR}+\lambda_{bL}+\lambda_{bR})(\omega-\omega_s+i\gamma/2)-2i(\omega-\omega_s+i\gamma/2)(\omega-\omega_e+i\Gamma/2)+2i\Omega^2}\\ r^a &= \frac{-2\sqrt{\lambda_{aL}\lambda_{bR}}(\omega-\omega_s+i\gamma/2)}{(\lambda_{aL}+\lambda_{aR}+\lambda_{bL}+\lambda_{bR})(\omega-\omega_s+i\gamma/2)-2i(\omega-\omega_s+i\gamma/2)(\omega-\omega_e+i\Gamma/2)+2i\Omega^2}\\ t^b &= \frac{-2\sqrt{\lambda_{aR}\lambda_{bR}}(\omega-\omega_s+i\gamma/2)}{(\lambda_{aL}+\lambda_{aR}+\lambda_{bL}+\lambda_{bR})(\omega-\omega_s+i\gamma/2)-2i(\omega-\omega_s+i\gamma/2)(\omega-\omega_e+i\Gamma/2)+2i\Omega^2}\\ r^b &= \frac{-2\sqrt{\lambda_{aR}\lambda_{bL}}(\omega-\omega_s+i\gamma/2)}{(\lambda_{aL}+\lambda_{aR}+\lambda_{bL}+\lambda_{bR})(\omega-\omega_s+i\gamma/2)-2i(\omega-\omega_s+i\gamma/2)(\omega-\omega_e+i\Gamma/2)+2i\Omega^2}\end{aligned} \quad (5)$$

The quantum routing properties of single photons in the four ports are characterized by the transmission coefficient $T^{a(b)} = |t^{a(b)}|^2$ and the reflection coefficient $R^{a(b)} = |r^{a(b)}|^2$. The analytic expressions above provide a complete description of the single-photon transport properties of the proposed network. Obviously, the desired quantum routing can be implemented by properly designing the relevant geometric parameter and the other physical parameters.

3 IMPLEMENTING TUNABLE QUANTUM ROUTING USING CHIRAL WAVEGUIDES

In order to compare with previous research works, we first discuss the routing capability when the coupling strengths between the atom and two waveguides are equal, so the relevant photon-atom interactions are not chiral but symmetric, $\lambda_{aR} = \lambda_{aL} = \lambda_1$, $\lambda_{bR} = \lambda_{bL} = \lambda_2$. For simplicity, we assume $\lambda_1 = \lambda_2$, thus $r^a = t^b = r^b$. When $\Omega = 0$, single photons incident from one waveguide a will be absorbed by the atom, which transits from its ground state to excited state. Since the excited state is coupled to a continuum of states, the excited two-level atom will emit a photon spontaneously into the propagating mode of either waveguide a or b. Consequently, mediated by the atom, single photons could be routed from one quantum channel to the other. In **Figure 2A**, we plot the image of the coefficients T^a, R^a and $T^b + R^b$, respectively. Here, T^b and R^b reach the maximum value of 0.25. In **Figure 2B**, we plot the figure of the coefficients T^a, R^a and $T^b + R^b$ when $\Omega \neq 0$. The quantum routing due to the resonant tunneling process via the two dressed states is shown by the two peaks of the transfer rate in **Figure 2B**. When $\omega/\lambda = 0$, $T^a = 1$. This is the conventional scheme for single-photon routing, which has an equal probability of routing the photon to either of the two waveguides, specifically, $T^b = R^b = 0.25$.

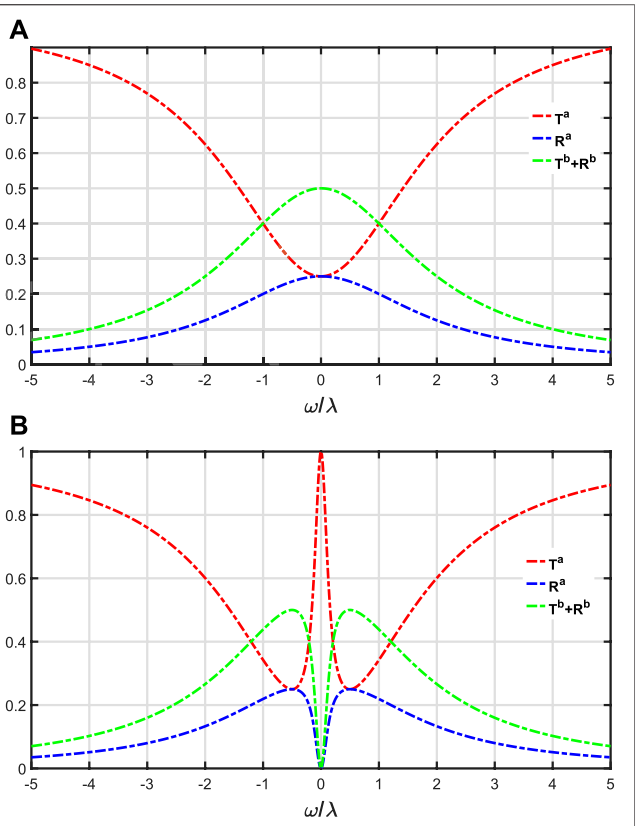

FIGURE 2 | (A,B) The coefficients T^a, R^a and $T^b + R^b$ as functions of the ω with $\Omega = 0$ ($\Omega \neq 0$). Other parameters are set as follows: $\omega_s = \omega_e = 0$, $\lambda_1 = \lambda_2 = \lambda$, $\gamma = \Gamma = 0$.

When the coupling is chiral, $\lambda_{aR} \neq \lambda_{aL}$, $\lambda_{bR} \neq \lambda_{bL}$, we assume the $\lambda_{aL} = \lambda_{bL} = 0$, $\lambda_{aR} = \lambda_{bR} = \lambda$. In this case, we find that $r^a = r^b = 0$, which means that the Λ-type three-level system only couples to the right-propagating mode in the two waveguides. **Figure 3** shows the probabilities of routing the incident photon to various output ports with respect to specific ω/λ. It indicates that the resonant photon incident from the left of waveguide a can output from the right of waveguide b with a probability of 100% whether $\Omega = 0$ or $\Omega \neq 0$. But when $\Omega \neq 0$, T^b has two peaks centered at $\omega = \pm\Omega$. If $\lambda_{aL} = \lambda_{bR} = 0$, $\lambda_{aR} = \lambda_{bL} = \lambda$, we can obtain $r^a = t^b = 0$, this means that the photon incident from the left of the waveguide a may output from the right of the waveguide a or the left of the waveguide b. When $\omega = \pm\Omega$, $R^b = 1$, this means that the single photon is transferred to waveguide b and output from the left of waveguide b with a

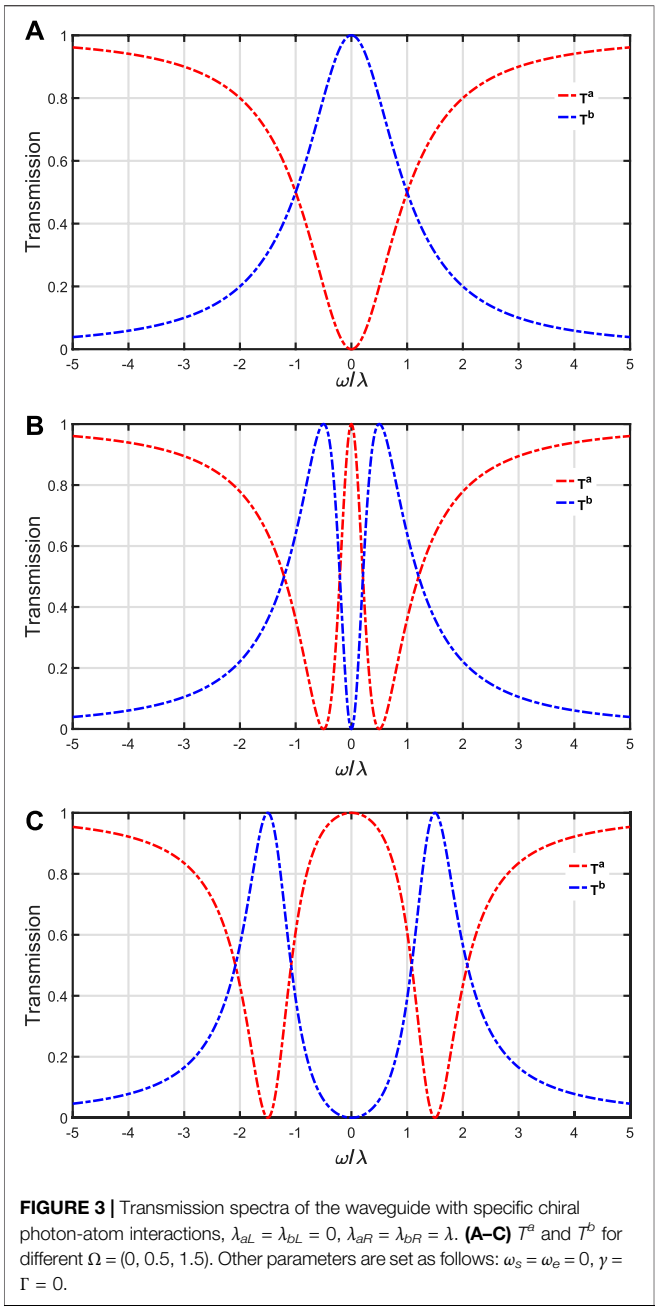

FIGURE 3 | Transmission spectra of the waveguide with specific chiral photon-atom interactions, $\lambda_{aL} = \lambda_{bL} = 0$, $\lambda_{aR} = \lambda_{bR} = \lambda$. **(A–C)** T^a and T^b for different $\Omega = (0, 0.5, 1.5)$. Other parameters are set as follows: $\omega_s = \omega_e = 0$, $\gamma = \Gamma = 0$.

probability of 100%. In **Figure 4**, we show the probabilities of routing the incident photon to various output ports with respect to specific values of ω/λ, and we find that **Figure 4**; **Figure 3** have the same physical phenomenon.

4 INFLUENCE OF DISSIPATION

In this part, we show how dissipation affects the photon routing probability. Here, we presume that $\lambda_{aL} \neq \lambda_{aR} \neq 0$ and $\lambda_{bR} \neq \lambda_{bL} \neq 0$. If $t^a = 0$ and an incoming photon in the resonance condition ($\omega = \omega_s = \omega_e$), we can get

$$\lambda_{aR} = \lambda_{aL} + \lambda_{bL} + \lambda_{bR} + \Gamma + 4\Omega/\gamma \tag{6}$$

Because $\lambda_j = \lambda_{jR} + \lambda_{jL}$ $(j = a, b)$ and $P = \frac{\lambda_a + \lambda_b}{\gamma + \Gamma}$

$$\lambda_b = \lambda_{aR} - \lambda_{aL} - \Gamma - 4\Omega\Big/\gamma = \lambda_a \frac{2S_a P - 1}{2P + 1} - 4\Omega\Big/\Gamma \tag{7}$$

Here, we assume that $\Gamma = \gamma$. Consequently, the corresponding transmission coefficient T^b can be expressed [17].

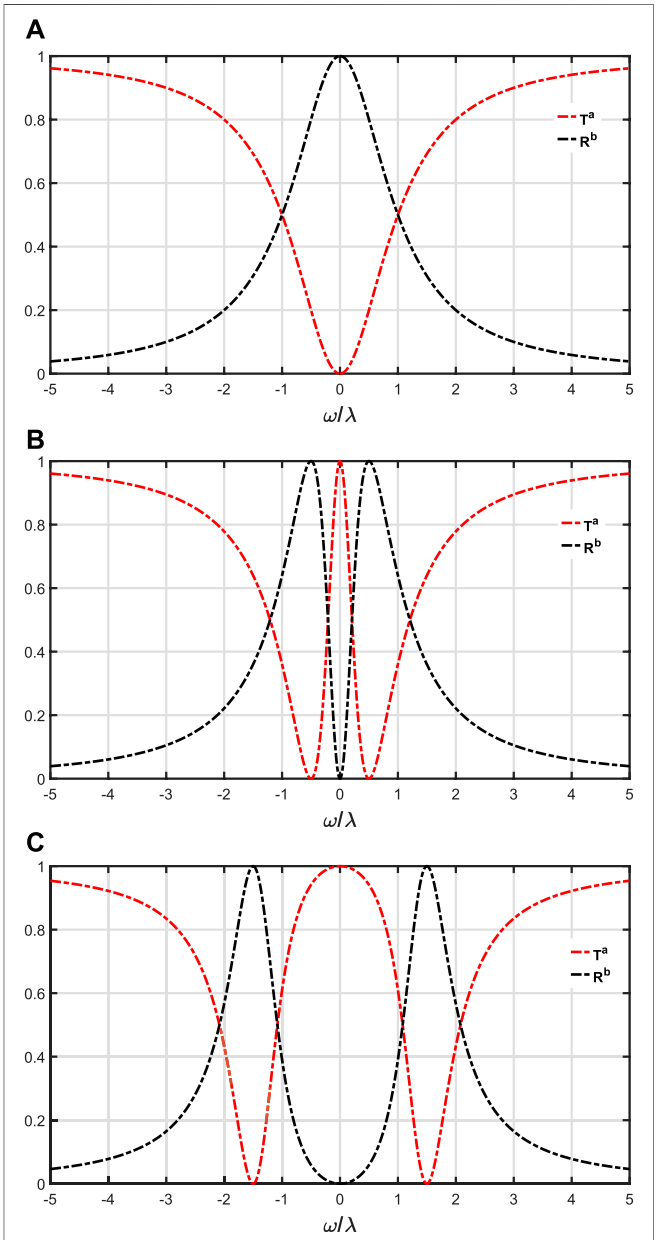

FIGURE 4 | Transmission spectra and reflection spectra of the waveguide with specific chiral photon-atom interactions, $\lambda_{aL} = \lambda_{bR} = 0$, $\lambda_{aR} = \lambda_{bL} = \lambda$. **(A–C)** T^a and R^b for different $\Omega = (0, 0.5, 1.5)$. Other parameters are set as follows: $\omega_s = \omega_e = 0$, $\gamma = \Gamma = 0$.

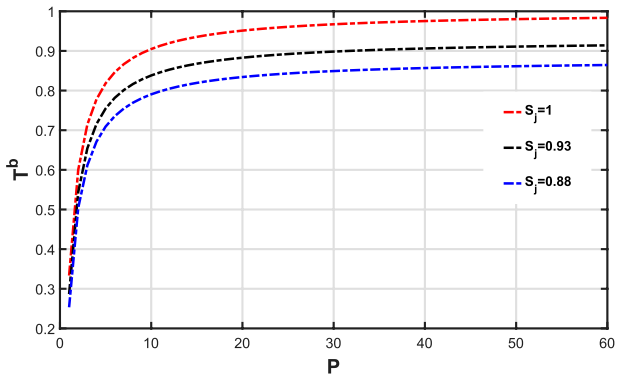

FIGURE 5 | The coefficients T^b as functions of Purcell factor P. Here, $S_a = S_b$.

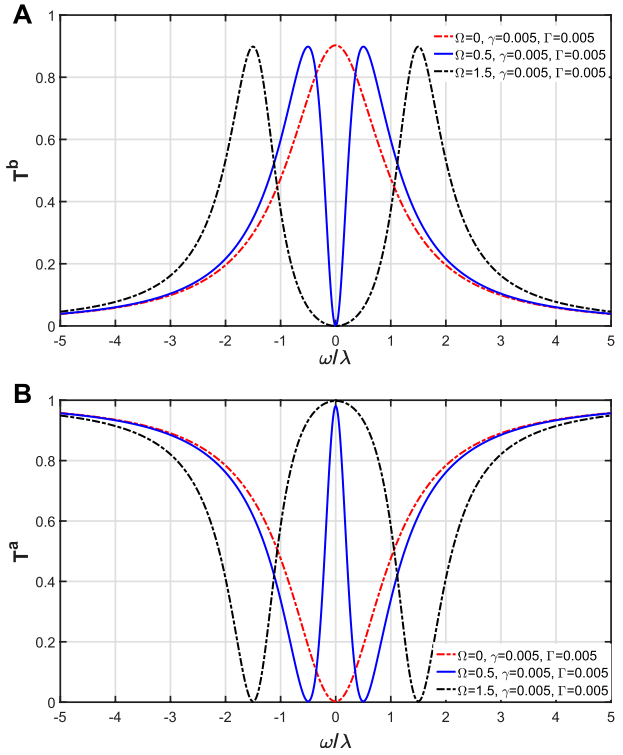

FIGURE 6 | (A) T^a as a function of ω/λ and **(B)** T^b as a function of ω/λ, here, $\omega = \omega_e = \omega_s$, $\gamma = \Gamma = 0.005$, $\lambda_{aR} = \lambda_{bR} = \lambda$ and $\lambda_{aL} = \lambda_{bL} = 0.05\lambda$.

$$T_b = |t^b|^2 = \frac{1+S_b}{1+S_a}\frac{2S_aP-1}{2P+1} \tag{8}$$

Note that in the ideal case the efficiency defined above is equal to 1, whereas in a realistic case the probability leakage into the undesired channels will reduce this value. In **Figure 5**, we plot the coefficients T^b with different S_j as functions of the Purcell factor P. We found that the lager Purcell factor P is, the lager coefficient T^b is, but the last T^b can reach a fixed value.

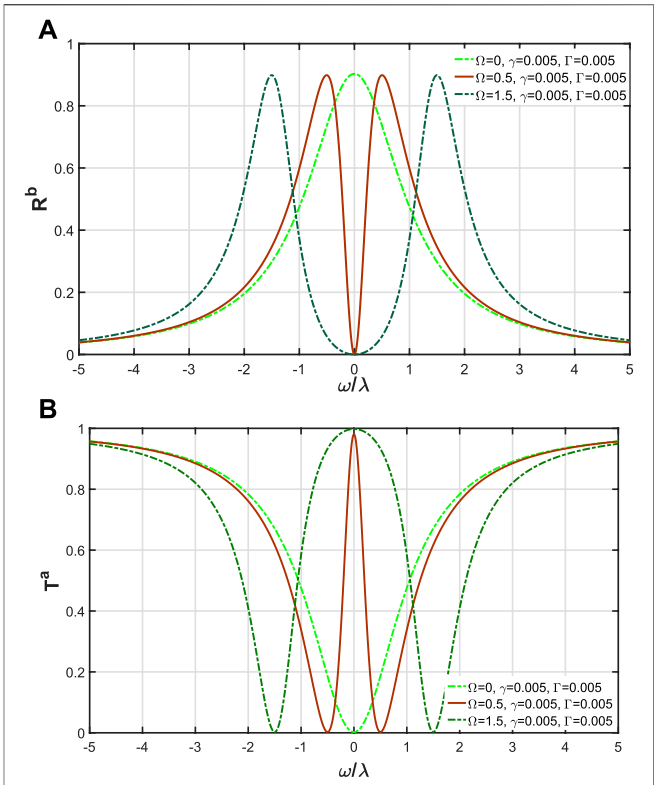

FIGURE 7 | (A) T^a as a function of ω/λ and **(B)** R^b as a function of ω/λ, here, $\omega = \omega_e = \omega_s$, $\gamma = \Gamma = 0.005$, $\lambda_{aR} = \lambda_{bL} = \lambda$ and $\lambda_{aL} = \lambda_{bR} = 0.05\lambda$.

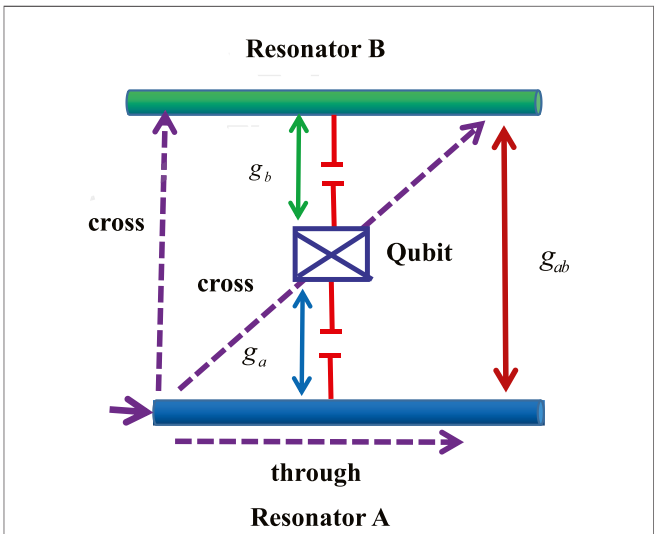

FIGURE 8 | chematic diagram of two transmission line resonators coupled to a superconducting qubit.

Under the resonance conditions ($\omega = \omega_s = \omega_e$), in order to observe the effect of the atomic dissipation on quantum routing more explicitly, we assume $\gamma = \Gamma = 0.005$. The first case is the real

system with $\lambda_{aR} = \lambda_{bR} = \lambda$ and $\lambda_{aL} = \lambda_{bL} = 0.05\lambda$, and we investigate the performance of the single-photon transport compared with the ideal case. However, the classical optical field can still determine the locations of the peaks of T^b. **Figure 6** shows T^a and T_b as a function of ω/λ. In **Figure 6A**, we find that when $\omega = \pm\Omega$, T_b reaches the maximum, but the maxima is less than 1, since the probabilities of the photon output from the left of waveguide a and b are not zero. The other case is when $\lambda_{aR} = \lambda_{bL} = \lambda$ and $\lambda_{aL} = \lambda_{bR} = 0.05\lambda$, and we plot the figure of T^a and R_b in **Figure 7**. At this point, we get the same physical phenomenon as **Figure 6**.

5 PHYSICAL IMPLEMENTATION

As schematically shown in **Figure 8**, we consider a system in which two resonators with the same fundamental mode frequencies $\omega_R/2\pi = 4.896\,GHz$ are coupled to a superconducting qubit. The coupling frequencies between the qubit and each resonator is $g/2\pi = 96.7\,MHz$. In addition to the geometric coupling $g_{ab}/2\pi = 8.4\,MHz$ there is the qubit mediated second-order dynamic coupling which depends on the magnetic flux applied to the qubit loop and on the qubit state, and the dynamical coupling on the qubit state can be used to realize switchable coupling between the two resonators [49–51]. The Hamiltonian of the whole system for the qubit coupled to the fundamental modes of the two resonators is (setting $\hbar = 1$) [49, 52].

$$H = \omega_{R_a} a^\dagger a + \omega_{R_b} b^\dagger b + \frac{1}{2}\omega_Q \sigma_z + g_a\left(a^\dagger \sigma_- + a\sigma_+\right) + g_b\left(b^\dagger \sigma_- + b\sigma_+\right) + g_{ab}\left(a^\dagger b + ab^\dagger\right)$$

where ω_Q is the qubit transition frequency, $\sigma_z = \sigma_+\sigma_- - \sigma_-\sigma_+$ and g_a and g_b are the qubit-resonator coupling, assumed to be real for simplicity. Furthermore, we denote the annihilation (creation) operators for the two resonators A and B as a and b ($a^\dagger$ and $b^\dagger$), respectively. Under the rotating-wave approximation, the effective Hamiltonian is [52].

$$H_{eff} = \omega_{R_a} a^\dagger a + \omega_{R_b} b^\dagger b + \frac{1}{2}\left(\omega_{R_a} + \omega_{R_b}\right)\sigma_z + \frac{1}{2}\sigma_z\left(\Delta_a + \Delta_b\right) + g_a\left(a^\dagger \sigma_- + a\sigma_+\right) + g_b\left(b^\dagger \sigma_- + b\sigma_+\right) + g_{ab}\left(a^\dagger b + ab^\dagger\right)$$

where $\Delta_a = \omega_Q - \omega_{R_a}$ and $\Delta_b = \omega_Q - \omega_{R_b}$. For the measurement, the qubit is kept in the ground state and the input power is chosen such that the mean resonator population is approximately one photon on average [50]. For coupled microwave resonators, we expect to observe two resonant modes corresponding to out-of-phase and in-phase oscillating currents in the two resonators. In this way, we can measure the transmission through the individual resonators and the transmission from the input of one resonator to the output of the second resonator [50, 51].

6 CONCLUSION

In summary, we implemented a targeted single-photon router by using an effective atom-photon interface with two chiral waveguides, and no matter a classical field is turned off or turned on, it can always achieve quantum routing. Using a full quantum theory, the single-photon transmission and reflection amplitudes were analytically obtained. By the numerical method, we analyzed the relevant transport properties in detail. When the coupling between the Λ-type atom system and the waveguides is non-chiral, the maximum probability for single-photon transfer from waveguide a to waveguide b is 0.5, but at this time $T^b = R^b = 0.25$. In other words, we cannot directionally select quantum channels for quantum information transport in this case. When the coupling is chiral, the maximum transfer probability can achieve 100% in the ideal system. What is more, we can control single photon output from the chosen port of the waveguide b. After that, we analyzed the performance of the quantum routing. Whether we change the size of the directionalities S_j or give a certain value to the dissipation of Λ-type atom, we always found that the quantum routing has very high efficiency. Moreover, we also use the quantum circuit of the superconducting qubit coupled to two resonators verification the present scheme pretty feasible for experimental implementation. Therefore, the targeted single-photon routers we proposed here provides an effective approach to build a promising optical quantum network.

DATA AVAILABILITY STATEMENT

The original contributions presented in the study are included in the article/Supplementary Material, further inquiries can be directed to the corresponding authors.

AUTHOR CONTRIBUTIONS

The idea was first conceived by G-AY. G-AY was responsible for the physical modeling, the numerical calculations, and writing most of the manuscript. HL contributed to writing the manuscript.

FUNDING

This work are supported by the National Natural Science Foundation of China (12147146 and 12175057), and the Natural Science Foundation of Shandong Provincial (ZR2021QA046) and Shaanxi Youth Outstanding Talent Support Plan and Shaanxi Natural Science Foundation (Grant No. 2019JQ-900).

REFERENCES

1. Kimble HJ. The Quantum Internet. *Nature* (2008) 453:1023–30. doi:10.1038/nature07127
2. Pittman TB, Shih YH, Strekalov DV, Sergienko AV. Optical Imaging by Means of Two-Photon Quantum Entanglement. *Phys Rev A* (1995) 52:R3429. doi:10.1103/physreva.52.r3429
3. Deng DL, Li XP, Das Sarma S. Quantum Entanglement in Neural Network States. *Phys Rev X* (2017) 7:021021. doi:10.1103/physrevx.7.021021
4. Su X, Tian C, Deng X, Li Q, Xie C, Peng K. Quantum Entanglement Swapping between Two Multipartite Entangled States. *Phys Rev Lett* (2016) 117:240503. doi:10.1103/physrevlett.117.240503
5. Nunn J, Munns JHD, Thomas S, Kaczmarek KT, Qiu C, Feizpour A, et al. Theory of Noise Suppression in Λ-type Quantum Memories by Means of a Cavity. *Phys Rev A* (2017) 96:012338. doi:10.1103/physreva.96.012338
6. Lodahl P, Mahmoodian S, Stobbe S. Interfacing Single Photons and Single Quantum Dots with Photonic Nanostructures. *Rev Mod Phys* (2015) 87:347–400. doi:10.1103/revmodphys.87.347
7. Chang DE, Vuletić V, Lukin MD. Quantum Nonlinear Optics - Photon by Photon. *Nat Photon* (2014) 8:685–94. doi:10.1038/nphoton.2014.192
8. Liu K, Yang J, Li XL, Li JY, Yan GA. Realization of Single-Photon Transport in One-Dimensional Coupled-Resonator Waveguides via Phase Control. *Chin J Phys* (2021) 72:207–13. doi:10.1016/j.cjph.2021.02.016
9. Yan GA, Lu H. Nonreciprocal Single-Photon Router in Quantum Networks. *Phys Scr* (2021) 96:105102. doi:10.1088/1402-4896/ac0c5a
10. Li JY, Li XL, Yan GA. Single-photon Quantum Router Based on Asymmetric Intercavity Couplings. *Commun Theor Phys* (2020) 72(5):055101. doi:10.1088/1572-9494/ab7ed5
11. Huang JS, Zhang JH, Wei LF. Single-photon Routing with Whispering-Gallery Resonators. *J Phys B: Mol Opt Phys* (2018) 51:085501. doi:10.1088/1361-6455/aab5a9
12. Yan CH, Li Y, Yuan HD, Wei LF. Targeted Photonic Routers with Chiral Photon-Atom Interactions. *Phys Rev A* (2018) 97:023821. doi:10.1103/physreva.97.023821
13. Li T, Miranowicz A, Hu XD, Xia KY, Nori F. Quantum Memory and gates Using a Λ-type Quantum Emitter Coupled to a Chiral Waveguide. *Phys Rev A* (2018) 97:062318. doi:10.1103/physreva.97.062318
14. Yang DC, Cheng MT, Ma XS, Xu JP, Zhu CJ, Huang XS. Phase-modulated Single-Photon Router. *Phys Rev A* (2018) 98:063809. doi:10.1103/physreva.98.063809
15. Cheng MT, Ma X, Fan JW, Xu J, Zhu C. Controllable Single-Photon Nonreciprocal Propagation between Two Waveguides Chirally Coupled to a Quantum Emitter. *Opt Lett* (2017) 42:2914–7. doi:10.1364/OL.42.002914
16. Cheng MT, Ma XS, Zhang JY, Wang B. Single Photon Transport in Two Waveguides Chirally Coupled by a Quantum Emitter. *Opt Express* (2016) 24:19988–93. doi:10.1364/OE.24.019988
17. Gonzalez-Ballestero C, Moreno E, Garcia-Vidal FJ, Gonzalez-Tudela A. Nonreciprocal Few-Photon Routing Schemes Based on Chiral Waveguide-Emitter Couplings. *Phys Rev A* (2016) 94:063817. doi:10.1103/physreva.94.063817
18. Zhou L, Yang LP, Li Y, Sun CP. Quantum Routing of Single Photons with a Cyclic Three-Level System. *Phys Rev Lett* (2013) 111:103604. doi:10.1103/physrevlett.111.103604
19. Zhu YT, Jia WZ. Single-photon Quantum Router in the Microwave Regime Utilizing Double Superconducting Resonators with Tunable Coupling. *Phys Rev A* (2019) 99:063815. doi:10.1103/physreva.99.063815
20. Witthaut D, Sørensen AS. Photon Scattering by a Three-Level Emitter in a One-Dimensional Waveguide. *New J Phys* (2010) 12:043052. doi:10.1088/1367-2630/12/4/043052
21. Hoi IC, Wilson CM, Johansson G, Palomaki T, Peropadre B, Delsing P. Demonstration of a Single-Photon Router in the Microwave Regime. *Phys Rev Lett* (2011) 107:073601. doi:10.1103/PhysRevLett.107.073601
22. Yan GA, Qiao HX, Lu H, Chen AX. Quantum Information-Holding Single-Photon Router Based on Spontaneous Emission. *SCIENCE CHINA Phys Mech Astron* (2017) 60:9. doi:10.1007/s11433-017-9059-3
23. Reiserer A, Kalb N, Blok MS, van Bemmelen KJM, Taminiau TH, Hanson R, et al. Robust Quantum-Network Memory Using Decoherence-Protected Subspaces of Nuclear Spins. *Phys Rev X* (2016) 6:021040. doi:10.1103/physrevx.6.021040
24. Kockum AF, Johansson G, Nori F. Decoherence-free Interaction between Giant Atoms in Waveguide Quantum Electrodynamics. *Phys Rev Lett* (2018) 120:140404. doi:10.1103/physrevlett.120.140404
25. Chen GY, Lambert N, Chou CH, Chen YN, Nor F. Surface Plasmons in a Metal Nanowire Coupled to Colloidal Quantum Dots: Scattering Properties and Quantum Entanglement. *Phys Rev B* (2011) 84:045310. doi:10.1103/physrevb.84.045310
26. Zheng H, Baranger HU. Persistent Quantum Beats and Long-Distance Entanglement from Waveguide-Mediated Interactions. *Phys Rev Lett* (2013) 110:113601. doi:10.1103/physrevlett.110.113601
27. Zheng H, Gauthier DJ, Baranger HU. Waveguide-QED-based Photonic Quantum Computation. *Phys Rev Lett* (2013) 111:090502. doi:10.1103/PhysRevLett.111.090502
28. Gonzalez-Ballestero C, Moreno E, Garcia-Vidal FJ. Generation, Manipulation, and Detection of Two-Qubit Entanglement in Waveguide QED. *Phys Rev A* (2014) 89:042328. doi:10.1103/physreva.89.042328
29. Facchi P, Kim MS, Pascazio S, Pepe FV, Pomarico D, Tufarelli T. Bound States and Entanglement Generation in Waveguide Quantum Electrodynamics. *Phys Rev A* (2016) 94:043839. doi:10.1103/physreva.94.043839
30. Vermersch B, Guimond PO, Pichler H, Zoller P. Quantum State Transfer via Noisy Photonic and Phononic Waveguides. *Phys Rev Lett* (2017) 118:133601. doi:10.1103/physrevlett.118.133601
31. Mahmoodian S, Lodahl P, Sørensen AS. Quantum Networks with Chiral-Light-Matter Interaction in Waveguides. *Phys Rev Lett* (2016) 117:240501. doi:10.1103/physrevlett.117.240501
32. Shen JT, Fan S. Coherent Single Photon Transport in a One-Dimensional Waveguide Coupled with Superconducting Quantum Bits. *Phys Rev Lett* (2005) 95:213001. doi:10.1103/physrevlett.95.213001
33. Roy D, Wilson CM, Firstenberg O Colloquium: Strongly Interacting Photons in One-Dimensional Continuum. *Rev Mod Phys* (2017) 89:021001. doi:10.1103/revmodphys.89.021001
34. Kemp A, Saito S, Munro WJ, Nemoto K, Semba K. Superconducting Qubit as a Quantum Transformer Routing Entanglement between a Microscopic Quantum Memory and a Macroscopic Resonator. *Phys Rev B* (2011) 84:104505. doi:10.1103/physrevb.84.104505
35. Xia K, Twamley J. All-optical Switching and Router via the Direct Quantum Control of Coupling between Cavity Modes. *Phys Rev X* (2013) 3:031013. doi:10.1103/physrevx.3.031013
36. Agarwal GS, Huang S. Optomechanical Systems as Singlephoton Routers. *Phys Rev A* (2012) 85:021801. doi:10.1103/physreva.85.021801
37. Bentham C, Itskevich IE, Coles RJ, Royall B, Clarke E, O'Hara J, et al. On-chip Electrically Controlled Routing of Photons from a Single Quantum Dot. *Appl Phys Lett* (2015) 106:221101. doi:10.1063/1.4922041
38. Li H, Cai H, Xu J, Yakovlev VV, Yang Y, Wang DW. Quantum Photonic Transistor Controlled by an Atom in a Floquet Cavity-QED System. *Opt Express* (2019) 27(5):6946–57. doi:10.1364/oe.27.006946
39. Lu J, Zhou L, M Kuang L, Nori F. Single-photon Router: Coherent Control of Multichannel Scattering for Single Photons with Quantum Interferences. *Phys Rev A* (2014) 89:013805. doi:10.1103/physreva.89.013805
40. Gorniaczyk H, Tresp C, Schmidt J, Fedder H, Hofferberth S. Single-photon Transistor Mediated by Interstate Rydberg Interactions. *Phys Rev Lett* (2014) 113:053601. doi:10.1103/PhysRevLett.113.053601
41. Tiarks D, Baur S, Schneider K, Dürr S, Rempe G. Single-photon Transistor Using a Förster Resonance. *Phys Rev Lett* (2014) 113:053602. doi:10.1103/PhysRevLett.113.053602
42. Hong FY, Xiong SJ. Single-photon Transistor Using Microtoroidal Resonators. *Phys Rev A* (2008) 78:013812. doi:10.1103/physreva.78.013812
43. Neumeier L, Leib M, Hartmann MJ. Single-photon Transistor in Circuit Quantum Electrodynamics. *Phys Rev Lett* (2013) 111:063601. doi:10.1103/PhysRevLett.111.063601
44. Muljarov EA, Langbein W. Exact Mode Volume and Purcell Factor of Open Optical Systems. *Phys Rev B* (2016) 94:235438. doi:10.1103/physrevb.94.235438
45. Chebykin AV, Babicheva VE, Iorsh IV, Orlov AA, Belov PA, Zhukovsky SV. Enhancement of the Purcell Factor in Multiperiodic Hyperboliclike Metamaterials. *Phys Rev A* (2016) 93:033855. doi:10.1103/physreva.93.033855

46. Rustomji K, Abdeddaim R, Martijn de Sterke C, Kuhlmey B, Enoch S. Measurement and Simulation of the Polarization-dependent Purcell Factor in a Microwave Fishnet Metamaterial. *Phys Rev B* (2017) 95:035156. doi:10.1103/physrevb.95.035156
47. Pick A, Lin Z, Jin W, Rodriguez AW. Enhanced Nonlinear Frequency Conversion and Purcell Enhancement at Exceptional Points. *Phys Rev B* (2017) 96:224303. doi:10.1103/physrevb.96.224303
48. Plankensteiner D, Sommer C, Reitz M, Ritsch H, Genes C. Enhanced Collective Purcell Effect of Coupled Quantum Emitter Systems. *Phys Rev A* (2019) 99:043843. doi:10.1103/physreva.99.043843
49. Mariantoni M, Deppe F, Marx A, Gross R, Wilhelm FK, Solano E. Two-resonator Circuit Quantum Electrodynamics: A Superconducting Quantum Switch. *Phys Rev B* (2008) 78:104508. doi:10.1103/physrevb.78.104508
50. Baust A, Hoffmann E, Haeberlein M, Schwarz MJ, Eder P, Goetz J, et al. Tunable and Switchable Coupling between Two Superconducting Resonators. *Phys Rev B* (2015) 91:014515. doi:10.1103/physrevb.91.014515
51. Baust A, Hoffmann E, Haeberlein M, Schwarz MJ, Eder P, Goetz J, et al. Ultrastrong Coupling in Two-Resonator Circuit QED. *Phys Rev B* (2016) 93:214501. doi:10.1103/physrevb.93.214501
52. Sete EA, Gambetta JM, Korotkov AN. Purcell Effect with Microwave Drive: Suppression of Qubit Relaxation Rate. *Phys Rev B* (2014) 89:104516. doi:10.1103/physrevb.89.104516

Conflict of Interest: The authors declare that the research was conducted in the absence of any commercial or financial relationships that could be construed as a potential conflict of interest.

Publisher's Note: All claims expressed in this article are solely those of the authors and do not necessarily represent those of their affiliated organizations, or those of the publisher, the editors and the reviewers. Any product that may be evaluated in this article, or claim that may be made by its manufacturer, is not guaranteed or endorsed by the publisher.

frontiers in Physics

ORIGINAL RESEARCH
published: 22 March 2022
doi: 10.3389/fphy.2022.838124

Spatial Manipulation *via* Four-Wave Mixing in Five-Level Cold Atoms

Shoufei Gan *

School of Information Engineering, Suzhou University, Suzhou, China

In a recent publication [S. Gan, Laser Phys. 31, 055401 (2021)], a scheme for controlling the vortex four-wave mixing (FWM) in a five-level atomic system has been put forward. Based on this work, we propose a new scheme for the spatial manipulation via four-wave mixing in a five-level atomic system when the radial index is considered. It is found that the phase and intensity of the FWM field can be spatially manipulated. More importantly, we show the superposition modes created by the interference between the FWM field and a same-frequency Gaussian beam, which can also be controlled *via* the corresponding parameters. Our research is helpful to understand and manipulate optical vortices and can be widely used in quantum computation and communication.

Keywords: four-wave mixing, cold atoms, optical vortices, orbital angular momentum, Laguerre-Gaussian beam

OPEN ACCESS

Edited by:
Weibin Li,
University of Nottingham,
United Kingdom

Reviewed by:
Zhiping Wang,
Anhui University, China
Liping Li,
Zhongyuan University of Technology,
China

***Correspondence:**
Shoufei Gan
ganshfei@163.com

Specialty section:
This article was submitted to Quantum Engineering and Technology, a section of the journal Frontiers in Physics

Received: *17 December 2021*
Accepted: *21 February 2022*
Published: *22 March 2022*

Citation:
Gan S (2022) Spatial Manipulation via Four-Wave Mixing in Five-Level Cold Atoms. Front. Phys. 10:838124. doi: 10.3389/fphy.2022.838124

1 INTRODUCTION

The Laguerre–Gaussian (LG) light carrying orbital angular momentum (OAM) [1] has attracted a lot of interest due to its unique amplitude and phase structures. In particular, the four-wave mixing (FWM) based on OAM light has emerged as a hot topic in recent years. For instance, Qiu et al. proposed a scheme to demonstrate the manipulation of space-dependent four-wave mixing (FWM) in a four-level atomic system [2]. By adjusting the detuning of the control field, one can effectively control the FWM output field. Yu et al. described a theoretical investigation of a FWM scheme in a six-level atomic system driven by a field with OAM and making use of two electromagnetically induced transparency (EIT) control fields [3]. The obtained results allow one to control the helical phase of the output FWM field by varying the intensities of the two EIT control fields as well as the detuning of the probe field. Quite recently, Wang et al. have also proposed some schemes to control vortex FWM carrying OAM in different nanostructures [4–6].

In this paper, we investigated the spatial manipulation *via* four-wave mixing in a five-level atomic system. Quite recently, we have proposed a scheme for modulating the spatial vortex FWM in a five-level atomic system [7]. However, different from this previous study, the major features of applying our considered scheme are as follows. First, the main difference between our scheme and the one in [7] is that we have shaped the LG field as a double-ring LG mode with the radial index $p = 1$ while in [7] the radial index is 0. This scheme has many advantages for controlling the FWM in comparison with the publication [7]. For example, the double-ring LG mode provides two FWM channels, and in different channels the spatial variation of the FWM are different. Second, in this scheme more physical parameters (e.g., the radial index $p = 1$) can be manipulated and hence one can select suitable radial index p to explore singularity characteristics of helical phase wavefront in nonlinear processes. Third, we display the superposition modes created by the interference between the FWM field and a same-frequency Gaussian beam, which show a more flexible intensity control or phase control for the superposition modes.

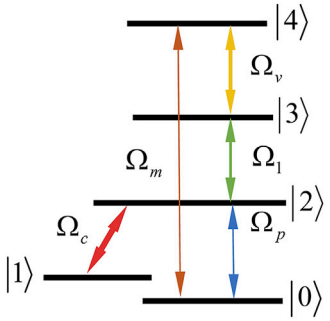

FIGURE 1 | Schematic of a five-level atomic system.

2 THEORETICAL MODEL AND EQUATIONS

We consider an atomic system as shown in **Figure 1**. A probe field with Rabi frequency $\Omega_p = \Omega_{p0}e^{-(r/R_p)^2}\sqrt{\pi/(2\ln 2)}\exp[-t^2/(2\ln 2/\pi^2)]$ (Ω_{p0} and R_p are the amplitude and transverse radius with t being the time) is applied to the transition $|2\rangle \leftrightarrow|0\rangle$. A control field with Rabi frequency Ω_c drives the transition $|2\rangle \leftrightarrow|1\rangle$. A pump field with Rabi frequency Ω_1 drives the transition $|3\rangle \leftrightarrow|2\rangle$, while a LG field with Rabi frequency Ω_v drives the transition $|4\rangle \leftrightarrow|3\rangle$. Here Ω_v is defined as

$$\Omega_v = \Omega_{v0}\Omega(r)e^{-il\phi}, \tag{1}$$

where $\Omega(r) = \frac{\sqrt{2p!/\pi(p+|l|)!}}{\omega_0}(\frac{\sqrt{2}r}{\omega_0})^{|l|}L_p^{|l|}(\frac{2r^2}{\omega_0^2})e^{-r^2/\omega_0^2}$, Ω_{v0} is the initial Rabi frequency, r is the radius and the beam waist is ω_0. ϕ is the azimuthal angle and $L_p^{|l|}$ is the Laguerre polynomial. The radial index and azimuthal index are defined by p and l, respectively.

Making use of the Schrödinger equation, the dynamical equations for the atomic probability amplitudes $A_j(j = 1–4)$ in the interaction picture are given by [8].

$$\dot{A}_1 = \left[i\left(\Delta_p - \Delta_c\right) - \gamma_1\right]A_1 + i\Omega_c^* A_2, \tag{2a}$$

$$\dot{A}_2 = i\Omega_p A_0 + \left(i\Delta_p - \gamma_2\right)A_2 + i\Omega_c A_1 + i\Omega_1^* A_3, \tag{2b}$$

$$\dot{A}_3 = i\Omega_1 A_2 + i\Omega_v^* e^{i\delta\vec{k}\cdot\vec{r}}A_4 + \left[i\left(\Delta_p + \Delta_3\right) - \gamma_3\right]A_3, \tag{2c}$$

$$\dot{A}_4 = i\Omega_m A_0 + i\Omega_v e^{-i\delta\vec{k}\cdot\vec{r}}A_3 + \left[i\left(\Delta_p + \Delta_3 + \Delta_4\right) - \gamma_4\right]A_4, \tag{2d}$$

where Δ_p, Δ_c, Δ_3 and Δ_4 are the detunings of the fields. The $\delta\vec{k} = \vec{k}_m - (\vec{k}_p + \vec{k}_1 + \vec{k}_v)$ is phase mis-matching condition, and $\vec{k}_i\,(i = p, 1, v, m)$ are the wave vectors of the corresponding fields. The γ_n $(n = 1–4)$ are decay rates.

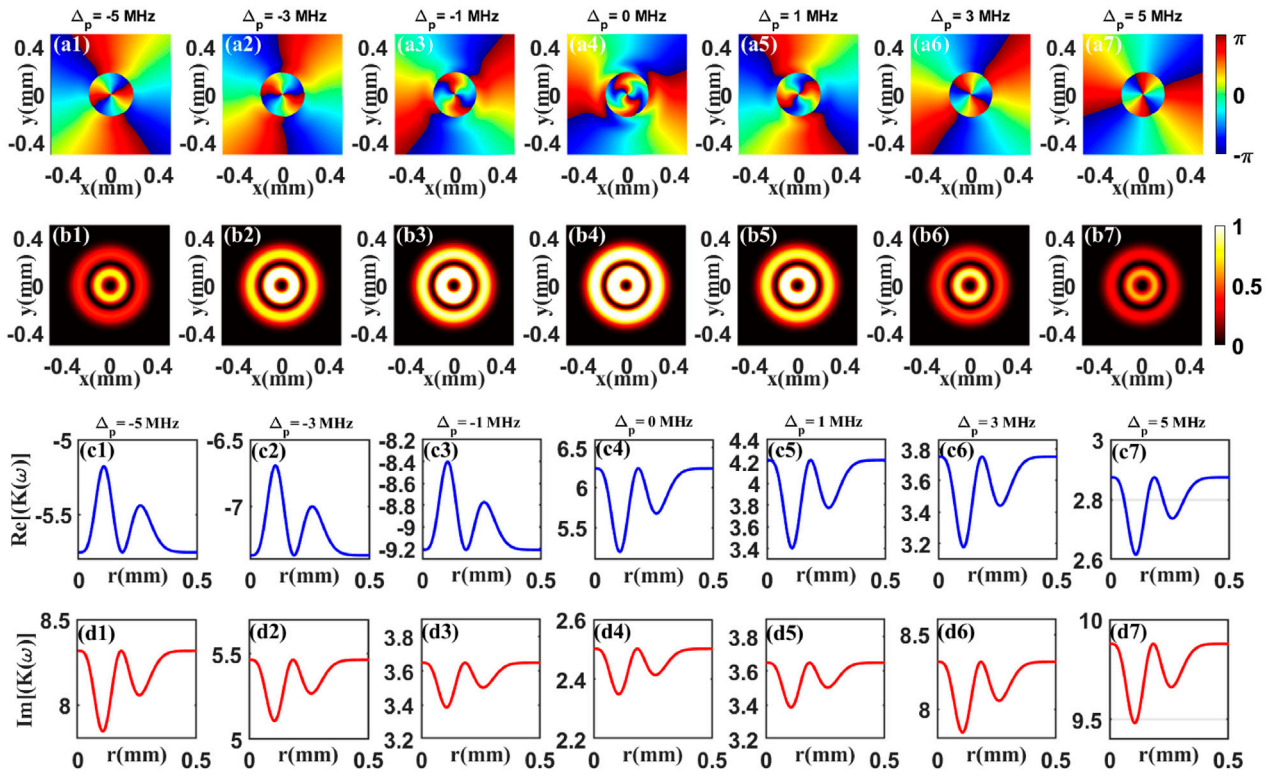

FIGURE 2 | Phase **(A1–A7)** and normalized intensity **(B1–B7)** patterns of the FWM field for different probe detuning Δ_p. The real **(C1–C7)** and imaginary **(D1–D7)** parts of dispersion relation $K(\omega)$ versus radius r for different probe detuning Δ_p. The other parameters are $\omega_0 = 0.18$ mm, $R_p = 3\omega_0$, $\omega = 3$ MHz, $z = 15$ mm, $p = 1$, $l = 2$, $\gamma_1 = 1 \times 10^{-4}$ MHz, $\gamma_2 = 6$ MHz, $\gamma_3 = 0.66$ MHz, $\gamma_4 = 0.08$ MHz, $\Omega_1 = 12$ MHz, $\Omega_{v0} = 2.5$ MHz, $\Omega_c = 5.5$ MHz, $\Omega_{p0} = 0.55$ MHz, $\Delta_c = \Delta_3 = \Delta_4 = 0$, $\kappa_{02} = 200$ MHz/mm, $\kappa_{04} = 0.01\kappa_{02}$.

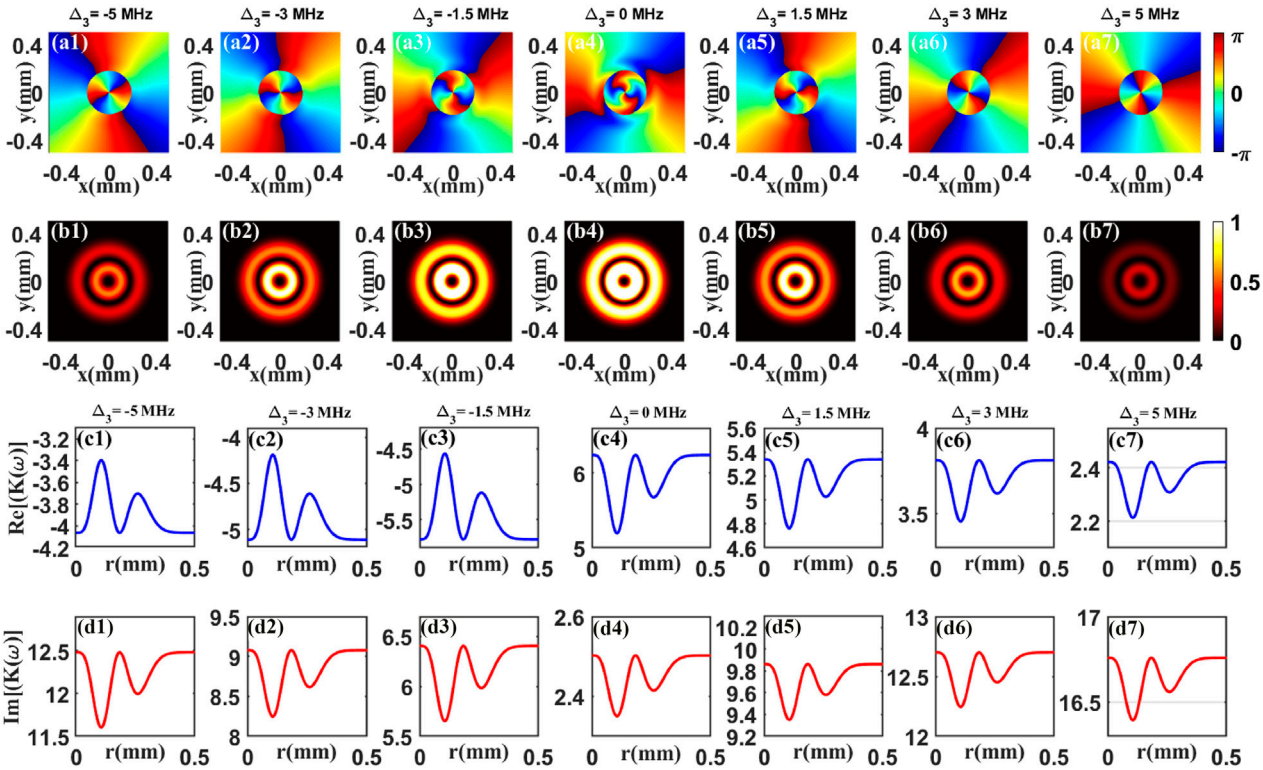

FIGURE 3 | Phase **(A1–A7)** and normalized intensity **(B1–B7)** patterns of the FWM field for different detuning Δ_3. The real **(C1–C7)** and imaginary **(D1–D7)** parts of dispersion relation $K(\omega)$ versus radius r for different detuning Δ_3. The other parameters are the same as in **Figure 2**.

Under the slowly varying envelope approximation, the propagation equations of the probe and FWM fields are governed by the Maxwell equations

$$\frac{\partial \Omega_{p(m)}}{\partial z} + \frac{\partial \Omega_{p(m)}}{c\partial t} = \frac{i}{2k_{p(m)}}\nabla_{\perp}^{2}\Omega_{p(m)} + i\kappa_{02(04)}aA_{2(4)}A_{0}^{*}, \tag{3}$$

where $k_{p(m)}$ is the wave number of the probe field (FWM field). $\kappa_{02(04)} = 2N\omega_{p(m)}|D_{02(04)}|^2/(c\hbar)$ is the propagation constant, which is related to the frequently used oscillator strengths of the transition $|0\rangle \leftrightarrow |2\rangle$ ($|4\rangle$). N and $D_{02(04)}$ are the atomic density and dipole moment between states $|0\rangle$ and $|2\rangle$ ($|4\rangle$), respectively.

We assume all the atoms are in the ground state $|0\rangle$ i.e. $|A_0|^2 \approx 1$ and use the condition of phase matching $\delta\vec{k} = 0$. By applying Fourier transformations $A_j(t) = \int \tilde{A}_j(\omega)e^{-i\omega t}d\omega$ ($j = 1-4$) to Eqs 2a, 3 and obtain [9].

$$f_1\tilde{A}_1 + \Omega_c^{*}\tilde{A}_2 = 0, \tag{4a}$$

$$\Omega_c\tilde{A}_1 + f_2\tilde{A}_2 + \Omega_1^{*}\tilde{A}_3 = -\tilde{\Omega}_p, \tag{4b}$$

$$\Omega_1\tilde{A}_2 + f_3\tilde{A}_3 + \Omega_v^{*}\tilde{A}_4 = 0, \tag{4c}$$

$$\Omega_v\tilde{A}_3 + f_4\tilde{A}_4 = -\tilde{\Omega}_m, \tag{4d}$$

and the Maxwell's equations $\Omega_{p(m)}$ obeyed as follows

$$\frac{\partial \tilde{\Omega}_{p(m)}}{\partial z} - \frac{i\omega}{c}\tilde{\Omega}_{p(m)} = \frac{i}{2k_{p(m)}}\nabla_{\perp}^{2}\tilde{\Omega}_{p(m)} + i\kappa_{02(04)}\tilde{A}_{2(4)}, \tag{5}$$

where ω is the Fourier frequency. $f_1 = \omega + \Delta_p - \Delta_c + i\gamma_1, f_2 = \omega + \Delta_p + i\gamma_2, f_3 = \omega + \Delta_p + \Delta_3 + i\gamma_3, f_4 = \omega + \Delta_p + \Delta_3 + \Delta_4 + i\gamma_4$, and $\tilde{\Omega}_{p(m)}$ are the Fourier transformations of $\Omega_{p(m)}$. The first terms on the right-hand sides of the **Eq. 5** accounts for light diffraction. Light diffraction can be neglected if the propagation distance is much smaller than the Rayleigh ranges of the probe pulse or the generated FWM field [10, 11], i.e. $\pi\omega_0^2/\lambda \gg L$. We take the propagation distance z = 15 mm, the transverse characteristic dimension $w_T = \omega_0$ = 0.18 mm and the wavelength of the FWM field $\lambda \approx$ 300 nm, obtaining $\pi\omega_0^2/\lambda \approx$ 339.12 mm $\gg$ 15 mm. So it is safe to ignore diffraction in this work.

Using the initial condition $\tilde{\Omega}_m(z = 0, \omega) = 0$, the generated FWM field is given by

$$\tilde{\Omega}_m(z,\omega) = \frac{\tilde{\Omega}_p(z = 0,\omega)\kappa_{04}\beta_1\Omega_1\Omega_v}{M[K_+(\omega) - K_-(\omega)]}\left(e^{iK_-(\omega)z} - e^{iK_+(\omega)z}\right), \tag{6}$$

where $K_{\pm}(\omega) = \frac{\omega}{c} + \frac{F_p+F_m}{2} \pm \sqrt{[\frac{F_p-F_m}{2}]^2 + G}$, $F_p = -(f_3f_4 - |\Omega_v|^2)f_1\kappa_{02}/M$, $F_m = -[M + (f_1f_2 - |\Omega_c|^2)|\Omega_v|^2]\kappa_{04}/Mf_4$, $G = f_1^2|\Omega_1|^2|\Omega_v|^2\kappa_{02}\kappa_{04}/M^2$, $M = (f_1f_2 - |\Omega_c|^2)(f_3f_4 - |\Omega_v|^2) - |\Omega_1|^2f_1f_4$, with $\tilde{\Omega}_p(z = 0, \omega) = \Omega_{p0}e^{-(r/\omega_{p0})^2}\exp[-\omega^2/(2\pi^2/\ln 2)]$. We can see that there exist two modes $K_+(\omega)$ and $K_-(\omega)$ described by the dispersion relation $K(\omega) = K_+(\omega) + K_-(\omega)$ in **Eq. 6**, the real part Re$[K(\omega)]$ reflects the phase while the imaginary part Im $[K(\omega)]$ represents the absorption [12].

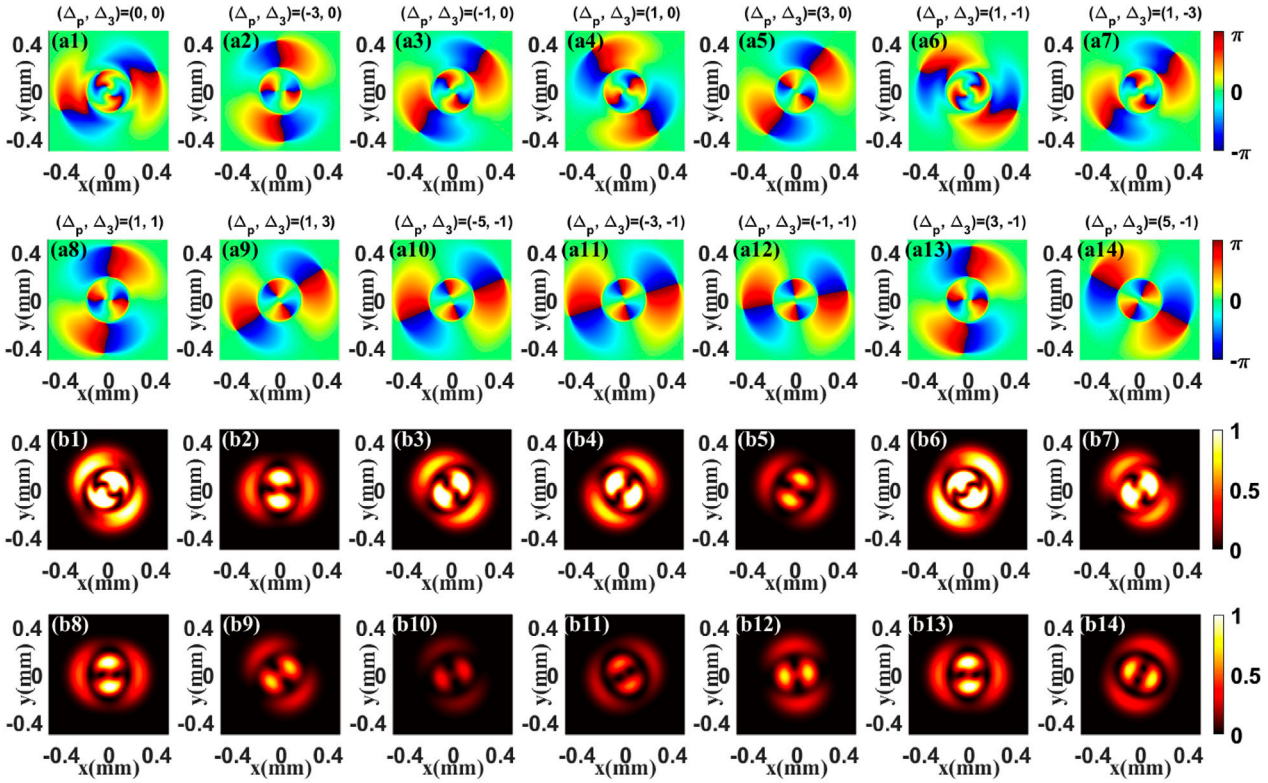

FIGURE 4 | Superposition phase **(A1–A14)** and intensity **(B1–B14)** patterns of FWM field and the same-frequency Gaussian beam $\Omega_G = e^{-(r/2\omega_0)^2}$ for different Δ_p and Δ_3. The other parameters are the same as in **Figure 2**.

3 RESULTS AND DISCUSSION

In this section, we aim to study the effects of the different parameters on phase and intensity of the FWM field $\tilde{\Omega}_m(z,\omega)$. In order to clearly show the spatial-dependent mechanism, the superposition modes created by the interference between the FWM field and a same-frequency Gaussian beam are also provided.

In **Figure 2**, we plot the phase and the normalized intensity patterns of the FWM field versus the (x, y) for different probe detuning Δ_p. As we expected, both the phase (**Figures 2A1–A7**) and intensity (**Figures 2B1–B7**) patterns are divided into two parts. From this figure, one can find that, upon increasing Δ_p from 1 MHz to ±5 MHz, the value of intensity decrease progressively while the phase twist is suppressed. The key factor is that the azimuthal dependent absorption and dispersion properties of the FWM field are modulated, which lead to the corresponding results. Moreover, the real (**Figures 2C1–C7**) part and imaginary (**Figures 2D1–D7**) part of dispersion relation $K(\omega)$ are shown in **Figure 2**, which have given the physical reason for the phase and the intensity patterns of the FWM field being changed in **Figure 2**.

In **Figure 3**, we present the phase and the normalized intensity patterns of the FWM field for different detuning Δ_3. By direct comparison in **Figures 2**, **3**, we obtain that the situation in **Figure 3** is nearly the same as the **Figure 2**. Such results indicate that the OAM phase is transferred to the FWM field and is modulated *via* detuning Δ_3. Here, we also provide the real part and imaginary part of dispersion relation in **Figures 3C1–C7** and **Figures 3D1–D7**. By increasing the detuning Δ_3, both the imaginary part and real part are changing. So we can see the varying phase and intensity of the FWM field.

Next, to obtain a better understanding of the vortex modulation, we show the superposition patterns of the FWM field and a same-frequency Gaussian beam in **Figure 4**. As illustrated in **Figure 4**, the superposition patterns are extremely rotated for different detunings Δ_p and Δ_3. The reason for this is that, due to the equiphase surface of Gaussian beam is a plane, azimuthally phase difference between the FWM field and Gaussian beam is very sensitive to detunings (Δ_p, Δ_3), which reflects the different superposition patterns. The findings in **Figure 4** imply that the OAM phase is indeed transferred to the FWM field and has a spatial dependency, which is originated from the spatial-sensitive absorption and dispersion properties induced by the three fields in the present system.

We note that, very recently, some theoretical schemes for controlling the space-dependent FWM in atoms [2, 3] or in semiconductor quantum wells [4–6] have been proposed. Comparing with those schemes, the major features of our proposal are the following. First, we have utilized the EIT induced by a additional control beam Ω_c. The EIT scheme has

many advantages for controlling the FWM in comparison with the one in [2]. For example, the coherent optical FWM with the EIT condition mediated by detunings Δ_p or Δ_3 will lead to many orders of magnitude enhancement in the amplitude of the generated wave (e.g., see **Figures 2**, **3**). Second, Different from the results obtained in [3], we display the superposition modes created by the interference between the FWM field and a same-frequency Gaussian beam. It is found that the superposition modes can be spatially manipulated *via* the corresponding parameters, which show a more flexible intensity control or phase control for the superposition modes. Third, unlike in solid-state systems [4–6], nonlinear effects are highly efficient and require only low light intensities in atomic vapors, which is convenient for the experimental realization of our scheme.

Before ending this section, it is worthwhile to briefly discuss the possible experimental realization of our scheme. Such an atomic structure can be realized in cold ^{85}Rb atoms. The designated states can be chosen as: $|0\rangle = |5S_{1/2}, F = 1\rangle$, $|1\rangle = |5S_{1/2}, F = 2\rangle$, $|2\rangle = |5P_{3/2}\rangle$, $|3\rangle = |5D_{5/2}\rangle$ and $|4\rangle = |nP_{3/2}\rangle$ ($n > 10$). Three transitions are $|5S_{1/2}, F = 1\rangle \leftrightarrow |5P_{3/2}\rangle$ at 780 nm, $|5P_{3/2}\rangle \leftrightarrow |5D_{5/2}\rangle$ at 776 nm, $|5D_{5/2}\rangle \leftrightarrow |63P_{3/2}\rangle$ at 1260 nm, and a Rydberg transition generated the FWM field $|5S_{1/2}, F = 1\rangle \leftrightarrow |63P_{3/2}\rangle$ at 300 nm.

4 CONCLUSION

In summary, we have studied the spatial manipulation *via* four-wave mixing (FWM) in a five-level atomic system. Interestingly, by adjusting the detunings, one can effectively modulate the phase and intensity of the FWM field when the radial index is considered. More importantly, we show the superposition modes created by the interference between the FWM field and a same-frequency Gaussian beam, which show many interesting properties. So our results may be helpful to investigate the interactions between OAM light and quantum media [13, 14].

DATA AVAILABILITY STATEMENT

The original contributions presented in the study are included in the article/Supplementary material, further inquiries can be directed to the corresponding author.

AUTHOR CONTRIBUTIONS

The author confirms being the sole contributor of this work and has approved it for publication.

ACKNOWLEDGMENTS

This work is supported by the key project of continuing education and teaching reform of Department of Education of Anhui Province (2019jxjj39) and the key project of research and development of Anhui Province (NO. 202004a05020043).

REFERENCES

1. Allen L, Beijersbergen MW, Spreeuw RJC, Woerdman JP. Orbital Angular Momentum of Light and the Transformation of Laguerre-Gaussian Laser Modes. *Phys Rev A* (1992) 45:8185. doi:10.1103/physreva.45.8185
2. Qiu J, Wang Z, Ding D, Huang Z, Yu B. Control of Space-dependent Four-Wave Mixing in a Four-Level Atomic System. *Phys Rev A* (2020) 102:033516. doi:10.1103/physreva.102.033516
3. Yu C, Wang Z. Engineering Helical Phase via Four-Wave Mixing in the Ultraslow Propagation Regime. *Phys Rev A* (2021) 103:013518. doi:10.1103/physreva.103.013518
4. Zhang Y, Wang Z, Qiu J, Hong Y, Yu B. Spatially Dependent Four-Wave Mixing in Semiconductor Quantum wells. *Appl Phys Lett* (2019) 115:171905. doi:10.1063/1.5121275
5. Wang Z, Zhang Y, Paspalakis E, Yu B. Efficient Spatiotemporal-Vortex Four-Wave Mixing in a Semiconductor Nanostructure. *Phys Rev A* (2020) 102:063509. doi:10.1103/physreva.102.063509
6. Qiu J, Wang Z, Ding D, Li W, Yu B. Highly Efficient Vortex Four-Wave Mixing in Asymmetric Semiconductor Quantum wells. *Opt Express* (2020) 28(3):2975–86. doi:10.1364/oe.379245
7. Gan S. Spatial Vortex Four-Wave Mixing in a Five-Level Atomic System. *Laser Phys* (2021) 31:055401. doi:10.1088/1555-6611/abee8e
8. Wu Y, Payne MG, Hagley EW, Deng L. Efficient Multiwave Mixing in the Ultraslow Propagation Regime and the Role of Multiphoton Quantum Destructive Interference. *Opt Lett* (2004) 29:2294. doi:10.1364/ol.29.002294
9. Wu Y, Saldana J, Zhu Y. Large Enhancement of Four-Wave Mixing by Suppression of Photon Absorption from Electromagnetically Induced Transparency. *Phys Rev A* (2003) 67:013811. doi:10.1103/physreva.67.013811
10. Hong Y, Wang Z, Ding D, Yu B. Ultraslow Vortex Four-Wave Mixing via Multiphoton Quantum Interference. *Opt Express* (2019) 27:29863. doi:10.1364/oe.27.029863
11. Chen J, Wang Z, Yu B. Spatially Dependent Hyper-Raman Scattering in Five-Level Cold Atoms. *Opt Express* (2021) 29(7):10914–22. doi:10.1364/oe.420015
12. Wu Y, Yang X. Highly Efficient Four-Wave Mixing in Double-Λsystem in Ultraslow Propagation Regime. *Phys Rev A* (2004) 70:053818. doi:10.1103/physreva.70.053818
13. Qiu J, Wang Z, Yu B. Generation of New Structured Beams via Spatially Dependent Transparency. *Quan Inf Process* (2019) 18:1. doi:10.1007/s11128-019-2278-6
14. Zhang K, Wang W, Liu S, Pan X, Du J, Lou Y, et al. Reconfigurable Hexapartite Entanglement by Spatially Multiplexed Four-Wave Mixing Processes. *Phys Rev Lett* (2020) 124:090501. doi:10.1103/physrevlett.124.090501

Conflict of Interest: The author declares that the research was conducted in the absence of any commercial or financial relationships that could be construed as a potential conflict of interest.

Publisher's Note: All claims expressed in this article are solely those of the authors and do not necessarily represent those of their affiliated organizations, or those of the publisher, the editors and the reviewers. Any product that may be evaluated in this article, or claim that may be made by its manufacturer, is not guaranteed or endorsed by the publisher.

frontiers in Physics

ORIGINAL RESEARCH
published: 22 March 2022
doi: 10.3389/fphy.2022.847409

Quantum Phases of Time Order in Many-Body Ground States

Tie-Cheng Guo[1]* *and Li You*[1,2]*

[1]State Key Laboratory of Low Dimensional Quantum Physics, Department of Physics, Tsinghua University, Beijing, China, [2]Frontier Science Center for Quantum Information, Beijing, China

Understanding phases of matter is of both fundamental and practical importance. Prior to the widespread appreciation and acceptance of topological order, the paradigm of spontaneous symmetry breaking, formulated along the Landau–Ginzburg–Wilson (LGW) dogma, is central to understanding phases associated with order parameters of distinct symmetries and transitions between phases. This work proposes to identify ground-state phases of the quantum many-body system in terms of *time order*, which is operationally defined by the appearance of the non-trivial temporal structure in the two-time auto-correlation function of a symmetry operator (order parameter) while the system approaches thermodynamic limit. As a special case, the (symmetry protected) *time crystalline order* phase detects continuous time crystal (CTC). We originally discover the physical meaning of CTC's characteristic period and amplitude. Time order phase diagrams for spin-1 atomic Bose–Einstein condensate (BEC) and quantum Rabi model are fully worked out. In addition to time-crystalline order, the intriguing phase of time-functional order is discussed in two non-Hermitian interacting spin models.

Keywords: time order, time crystal, quantum phase, Bose–Einstein condensate, non-Hermitian many-body physics, fully connected model, exotic phase

OPEN ACCESS

Edited by:
Weibin Li,
University of Nottingham,
United Kingdom

Reviewed by:
Yongqiang Li,
National University of Defense Technology, China
Yunbo Zhang,
Zhejiang Sci-Tech University, China

***Correspondence:**
Tie-Cheng Guo
gtc16@tsinghua.org.cn
Li You
lyou@mail.tsinghua.edu.cn

Specialty section:
This article was submitted to Quantum Engineering and Technology, a section of the journal Frontiers in Physics

Received: *02 January 2022*
Accepted: *24 January 2022*
Published: *22 March 2022*

Citation:
Guo T-C and You L (2022) Quantum Phases of Time Order in Many-Body Ground States. Front. Phys. 10:847409. doi: 10.3389/fphy.2022.847409

1 INTRODUCTION

A consistent theme for studying the many-body system, particularly in condensed matter physics, concerns the classification of phases and their associated phase transitions [20, 52, 68]. In the celebrated Landau–Ginzburg–Wilson (LGW) paradigm [35, 70], spontaneous symmetry breaking plays a central role with order parameters characterizing different phases of matter possessing respective broken symmetries. Other schemes for classifying phases as well as their associated transitions are, however, beyond the Landau–Ginzburg–Wilson paradigm, which are by now well accepted since first established decades ago [53, 63, 64]. For example, topological order, which classifies the gapped quantum many-body system, constitutes a topical research direction [63, 64, 66, 67]. Our current understanding categorizes gapped systems into gapped liquid phases [74] and gapped non-liquid phases, with the former broadly including phases of topological order [63, 64], symmetry-enriched topological order [9, 12, 25, 65], and symmetry-protected trivial order [10, 11, 23], while the recently discussed fracton phases [55, 56, 60] belong to the latter of gapped non-liquid phases.

Temporal properties of phases are also worthy of investigations as exemplified by many recent studies [41, 50, 69]. For instance, time crystal (TC) or perpetual temporal dependence in a many-body ground state that breaks spontaneously time translation symmetry (TTS) constitutes an exciting new phenomenon. First proposed by Wilczek [69] for quantum systems and followed by Shapere and Wilczek [54] for classical systems in 2012, TC in their original sense is unfortunately

ruled out by Bruno's no-go theorem the following year [3, 42]. Watanabe and Oshikawa (WO) reformulate the idea of quantum TC, and present a refined no-go theorem for many-body systems without too long-range interactions [62]. Continued efforts are directed at searching for continuous time crystal in open systems [4, 5, 30] and classical driven-diffusive systems [28]. Most recent efforts on this topic are directed toward non-equilibrium discrete/Floquet TC breaking discrete TTS [16, 17, 31, 51, 61, 72], particularly in systems with disorder that facilitate many-body localizations [61, 72], in addition to clean systems [19, 27, 39, 49]. Ongoing studies are further extended to open systems with Floquet driving in the presence of dissipation [14, 21, 22, 37, 46], with experimental investigations reported for a variety of systems [2, 13, 43, 47, 48, 57, 75]. A recent study addresses TC and its associated physics along the imaginary time axis [6].

We introduce *time order* in this work as the essential element for a new perspective to identify and categorize quantum many-body phases, based on different ground-state temporal patterns. Each quantum many-body Hamiltonian $\hat{H}$ comes with its evolution or time translation operator $e^{-i\hat{H}t}$. When continuous time translation symmetry is broken for operator $e^{-i\hat{H}t}$, akin to the breaking of continuous spatial translation symmetry for operator $e^{-i\vec{k}\cdot\vec{r}}$, time crystals arise in direct analogy to spatial crystals [69]. The message we hope to convey here in this study is rooted on the dual between $\hat{H}$ and $e^{-i\hat{H}t}$, which we argue quite generally establishes a solid foundation for time order and provides further information concerning ground-state quantum phases based on time domain properties. Different quantum many-body states with the same temporal patterns are classified into the same time order phases, of which continuous TC (CTC), a ground state with periodic time dependence breaking continuous TTS as originally proposed in Refs. [54, 69], belongs to one of them.

We will adopt the WO definition of CTC based on two-time auto-correlation function of an operator. It was first outlined in the now famous no-go theorem work [62], and it establishes a general and rigorous subtype of CTC. Recently, Kozin and Kyriienko claim to have realized such a genuine ground-state CTC in a multi-spin model with long-range interaction [33], buttressing much confidence to the search for exotic CTCs. The operational definition that we introduced for time order encompasses WO CTC as one type of time order phases. We will also explore and elaborate a variety of possible exotic phases.

2 RESULTS

2.1 Time Order

We argue that ground-state temporal properties of a quantum many-body system can be used to characterize or classify its phases. Hence, the concept of *time order* can be introduced analogous to an order parameter by bestowing it in the non-trivial temporal dependence. To exemplify the essence of the associated physics, we shall present an operational definition for *time order* and accordingly work out the exhaustive list of all allowed phases. According to the WO proposal [62], a witness to CTC is the following two-time (or unequal time) auto-correlation function (with respect to the ground state):

$$\lim_{V\to\infty} \langle \hat{\Phi}(t)\hat{\Phi}(0)\rangle / V^2 \equiv f(t), \tag{1}$$

for operator $\hat{\Phi}(t) \equiv \int_V d^D x \hat{\phi}(\vec{x}, t)$ defined as an integrated order parameter (over D-spatial-dimension), or analogously the volume averaged one,

$$f(t) = \lim_{V\to\infty} \langle \hat{\phi}(t)\hat{\phi}(0)\rangle, \tag{2}$$

with $\hat{\phi}(\vec{x}, t)$ the corresponding local order parameter density operator $\hat{\phi} \equiv \hat{\Phi}/V$.

If $f(t)$ is time periodic in the thermodynamic limit, the system is in a state of CTC. This can be reformulated into an explicit operational protocol by introducing a twisted vector. *For a quantum many-body system with energy eigen-state $|\psi_i\rangle$, if there exists a coarse-grained Hermitian order parameter $\hat{\phi}$, $\hat{\phi}|\psi_i\rangle$ is called the eigen-state twisted vector; more generally, if $\hat{\phi}$ is non-Hermitian, $\hat{\phi}|\psi_i\rangle$ (or $\hat{\phi}^\dagger|\psi_i\rangle$) will be called the right (or left) eigen-state twisted vector.*

The orthonormal set of eigen-wavefunctions $|\psi_i\rangle$ $(i = 0, 1, 2, \cdots)$ for a system described by Hamiltonian $\hat{H}$ is arranged in increasing eigen-energies ϵ_i with $i = 0$ denoting the ground state. When the coarse-grained order parameter $\hat{\phi}$ is Hermitian, the ground-state twisted vector $|v\rangle$ can be expanded $|v\rangle \equiv \hat{\phi}(0)|\psi_0\rangle = \sum_{i=0}^{\infty} a_i|\psi_i\rangle$ into the eigen-basis. With the help of the Schrödinger equation $i\partial|\psi(t)\rangle/\partial t = \hat{H}|\psi(t)\rangle$ ($\hbar = 1$ assumed throughout) for the system wave function $|\psi(t)\rangle$, we obtain the following equation:

$$\begin{aligned} f(t) &= \lim_{V\to\infty} \langle\psi_0|e^{i\hat{H}t}\hat{\phi}(0)e^{-i\hat{H}t}\hat{\phi}(0)|\psi_0\rangle \\ &= \lim_{V\to\infty} e^{i\epsilon_0 t}\langle v|e^{-i\hat{H}t}|v\rangle \\ &= \lim_{V\to\infty} \sum_{j=0}^{\infty} \eta_j e^{-i(\epsilon_j-\epsilon_0)t}, \end{aligned} \tag{3}$$

where $\eta_j \equiv |a_j|^2$ denotes weights of the ground-state twisted vector, η_0 the corresponding ground-state weight, and η_j (with $j > 0$) the excited-state weight.

When the coarse-grained order parameter $\hat{\phi}$ is non-Hermitian, we use $|v^{(l)}\rangle$ and $|v^{(r)}\rangle$ to denote, respectively, the left and right ground-state twisted vectors and expand them analogously in the eigen-basis to arrive at $|v^{(l)}\rangle \equiv \hat{\phi}^\dagger|\psi_0\rangle = \sum_{i=0}^{\infty} b_i|\psi_i\rangle$ and $|v^{(r)}\rangle \equiv \hat{\phi}|\psi_0\rangle = \sum_{i=0}^{\infty} a_i|\psi_i\rangle$. In this case, we find the following equation:

$$\begin{aligned} f(t) &= \lim_{V\to\infty} \langle\psi_0|e^{i\hat{H}t}\hat{\phi}(0)e^{-i\hat{H}t}\hat{\phi}(0)|\psi_0\rangle \\ &= \lim_{V\to\infty} e^{i\epsilon_0 t}\langle v^{(l)}|e^{-i\hat{H}t}|v^{(r)}\rangle \\ &= \lim_{V\to\infty} \sum_{j=0}^{\infty} \eta_j e^{-i(\epsilon_j-\epsilon_0)t}, \end{aligned} \tag{4}$$

with $\eta_j \equiv b_j^* a_j$ weights of the ground-state twisted vector instead. Similarly, η_0 and η_j $(j > 0)$ denote, respectively, ground- and excited-state weights.

Given an order parameter $\hat{\phi}$, quite generally $f(t)$ is a sum of many harmonic functions with amplitudes η_j and characteristic

TABLE 1 | Classification of the ground-state phases for a quantum many-body system.

Phase		Property of two-time auto-correlator
Time trivial order		$f(t)$ = const. ≠ 0 or $f(t) = 0$, $F(t)$ = const.
Time order	Time crystalline order	$f(t)$ is periodic and non-vanishing
	Time quasi-crystalline order	$f(t)$ is quasiperiodic with beats from two incommensurate frequencies
	Time functional order	$f(t)$ is aperiodic
	Generalized time crystalline order	$f(t) = 0$, $F(t)$ is periodic and non-vanishing
	Generalized time quasi-crystalline order	$f(t) = 0$, $F(t)$ is quasiperiodic with beats from two incommensurate frequencies
	Generalized time functional order	$f(t) = 0$, $F(t)$ is aperiodic

frequencies $\omega_j \equiv \epsilon_j - \epsilon_0$. Non-trivial time dependence of the two-time auto-correlation function is thus imbedded in the energy spectra of H as well as in the weights of the ground-state twisted vector. For CTC order to exist, one of the excited-state weights must be non-vanishing in the thermodynamic limit, or in rare cases, $f(t)$ can include harmonic terms of commensurate frequencies.

If $f(t)$ is a constant, the time dependence will be trivial. However, a subtlety appears when $f(t)$ is vanishingly small with respect to the system size. Since what we are after is the system's explicit temporal behavior or time dependence, it is easily washed out to $f(t) = 0$ by a vanishing norm of the twisted vector. Such a difficulty can be mitigated by multiplying system volume V, that is, using the twisted vector $|v\rangle \to V|v\rangle$, to check if the correlation for the bulk order parameter $F(t) \equiv V^2 f(t)$ exhibits temporal dependence, or vanishes as follows:

$$F(t) = \lim_{V\to\infty} \langle \hat{\Phi}(t)\hat{\Phi}(0)\rangle. \tag{5}$$

When $f(t) = 0$ but $F(t)$ remains a periodic function, the system can still be considered a CTC. Such a remedy surprisingly captures the essence of generalized CTC of Ref. [40].

The analysis presented above can be directly extended to excited states [59]. It is also straightforwardly applicable to non-Hermitian systems, as long as a plausible "ground state" can be identified, for example, by requiring its eigen-energy to possess the largest imaginary part or the smallest norm. Denoting the imaginary part of energy eigen-value E_i as $\mathrm{Im}(E_i)$, a prefactor $\propto e^{\mathrm{Im}(E_i)t}$ then arises in the auto-correlation function, leading to unusual time functional order in the classification of time order.

Therefore, quantum many-body phases can be classified according to *time order*. The two-time auto-correlation function-based complete operational procedure for classifying time order thus extends the definition of WO CTC as provided in Ref. [62]. Our central results can be simply stated as follows: *if $f(t)$ exhibits non-trivial time dependence, then time order exists. If $f(t) = 0$ but $F(t)$ displays non-trivial time dependence instead, then generalized time order exists.*

More specifically, if $f(t)$ = const. is non-zero, the system exhibits time trivial order. The same applies when $f(t) = 0$ and $F(t)$ = const. For all other situations, non-trivial time order prevails. A complete classification for all time order ground-state phases is shown in **Table 1**, according to the temporal behaviors of their auto-correlation functions $f(t)$ or $F(t)$. As discussed in **Section 4**, the above discussion and classification on time order can be extended to finite temperature systems as well.

The operational procedure outlined previously presents a straightforward approach for detecting *time order*, albeit with reference to an order parameter operator. Hence, more appropriately, this approach should be called *order parameter assisted time order* or *symmetry-based (or -protected) time order* to emphasize its reference to symmetry order parameter of a quantum many-body system. The twisted vector facilitates easy calculations to distinguish between different time order phases from time trivial ones, as we illustrate in the following text in terms of a few concrete examples. It is reasonable to expect that transitions between different time order phases can occur, reminiscent of phase transitions in the LGW spontaneous symmetry breaking paradigm.

2.2 Time Order Phase in a Spin-1 Atomic Condensate

A spin-1 atomic Bose–Einstein condensate (BEC) under single spatial mode approximation (SMA) [36, 44, 73] is described by the following Hamiltonian:

$$\begin{aligned}\hat{H} = \frac{c_2}{2N}\left[\left(2\hat{N}_0 - 1\right)\left(\hat{N} - \hat{N}_0\right) + 2\left(\hat{a}_1^\dagger \hat{a}_{-1}^\dagger \hat{a}_0 \hat{a}_0 + \text{h.c.}\right)\right] \\ - p\left(\hat{N}_1 - \hat{N}_{-1}\right) + q\left(\hat{N}_1 + \hat{N}_{-1}\right),\end{aligned} \tag{6}$$

where $\hat{a}_{m_F}(m_F = 0, \pm 1)$ $(\hat{a}_{m_F}^\dagger)$ denotes the annihilation (creation) operator for atom in the ground-state Zeeman manifold $|F = 1, m_F\rangle$ with corresponding number operator $\hat{N}_{m_F} = \hat{a}_{m_F}^\dagger \hat{a}_{m_F}$. The total atom number $\hat{N} = \hat{N}_1 + \hat{N}_0 + \hat{N}_{-1}$ is conserved. p and q are linear and quadratic Zeeman shifts that can be tuned independently [38], while c_2 describes the strength of spin exchange interaction.

The validity of this model is well established based on extensive theoretical [8, 24, 71, 76] and experimental [1, 7, 38, 45] studies of spinor BEC over the years. The fractional population in spin states $|1, 1\rangle$ and $|1, -1\rangle$, $\hat{n}_{\mathrm{sum}} \equiv N_{\mathrm{sum}}/N$, with $N_{\mathrm{sum}} = \hat{N}_1 + \hat{N}_{-1} = N - N_0$, is often chosen as an order parameter [1, 15, 34, 71] with N assuming the role of system size. The ground state twisted vector then becomes $|v\rangle \equiv \hat{n}_{\mathrm{sum}}|\psi_0\rangle$, and

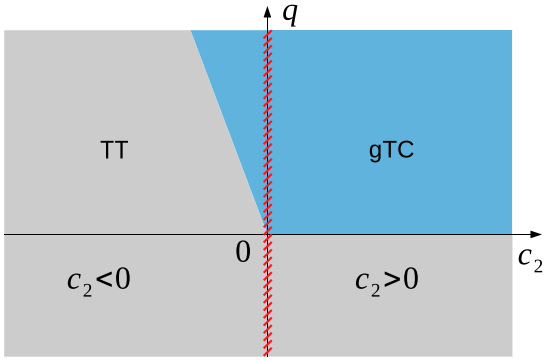

FIGURE 1 | Time order phase diagram for spin-1 atomic BEC, where TT and gTC, respectively, denote time trivial and generalized time crystalline order. The region of (hashed) line segments surrounding $c_2 = 0$ for the non-interacting system is to be excluded.

$$f(t) = \lim_{N\to\infty} \langle \hat{n}_{\rm sum}(t)\hat{n}_{\rm sum}(0)\rangle, \tag{7}$$

$$F(t) = \lim_{N\to\infty} \langle \hat{N}_{\rm sum}(t)\hat{N}_{\rm sum}(0)\rangle. \tag{8}$$

We will concentrate on the zero magnetization $F_z = 0$ subspace and employ exact diagonalization (ED) to calculate eigen-states. $p = 0$ is assumed since F_z is conserved. **Figure 1** illustrates the system's complete time order phase diagram. For ferromagnetic interaction $c_2 < 0$ as with ^{87}Rb atoms, the critical quadratic Zeeman shift $q/|c_2| = 2$ splits the whole region into the time trivial order (TT) phase for smaller q that observes TTS and the generalized time crystalline (gTC) order phase for $q/|c_2| > 2$, where TTS is spontaneously broken. The latter (gTC phase) is found to coincide with the polar phase [71]. Limited by available computation resources, the system sizes we explored with ED remain moderate which prevent us from mapping out the finer details in the immediate neighborhood of $q = 2|c_2|$. Further elaboration of time order properties in this region is therefore needed. On the other hand, for antiferromagnetic interaction $c_2 > 0$ with ^{23}Na atoms, we find $q = 0$ separates TT phase from gTC order. We note here that $q = 2|c_2|$ is the second-order quantum phase transition (QPT) critical point between the polar phase and the broken-axisymmetry phase of the ferromagnetic spin-1 BEC, while $q = 0$ corresponds to the first-order QPT critical point for antiferromagnetic interaction.

More detailed discussions including the dependence of time order phases on system size, possible approaches to detect them, and extension to thermal state phases can be found in **Section 4**.

2.3 Time Order Phase Diagram for Quantum Rabi Model

As a second example, we consider time order phases of the quantum Rabi model described by the Hamiltonian as follows:

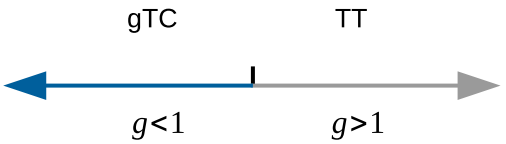

FIGURE 2 | Time order phase diagram for the quantum Rabi model, where TT and gTC, respectively, denote time trivial and generalized time crystalline order.

$$\hat{H}_{\rm Rabi} = \omega_0 \hat{a}^\dagger \hat{a} + \frac{\Omega}{2}\hat{\sigma}_z - \lambda(\hat{a} + \hat{a}^\dagger)\hat{\sigma}_x, \tag{9}$$

where $\hat{\sigma}_{x,z}$ is the Pauli matrix of a two-level system (transition frequency Ω), $\hat{a}(\hat{a}^\dagger)$ is the annihilation (creation) operator for a single bosonic field mode (of frequency ω_0), and λ is their coupling strength.

It is known that the aforementioned model exhibits a QPT to a superradiant state, despite its simplicity [29]. The transition occurs at the critical point $g_c \equiv 1$, with the dimensionless parameter $g \equiv 2\lambda/\sqrt{\omega_0\Omega}$. The equivalent thermodynamic limit is approached by taking $\Omega/\omega_0 \to \infty$. Though the system only has finite components, the QPT herein is well established. According to the studies in Ref. [29], an almost exact effective low-energy Hamiltonian for the normal phase ($g < 1$) is given by the following equation:

$$\hat{H}_{\rm np} = \omega_0 \hat{a}^\dagger \hat{a} - \frac{\omega_0 g^2}{4}(\hat{a} + \hat{a}^\dagger)^2 - \frac{\Omega}{2}, \tag{10}$$

whose low-energy eigen-states are $|\phi^m_{\rm np}(g)\rangle = \hat{\mathcal{S}}[r_{\rm np}(g)]|m\rangle|\downarrow\rangle$ for $g \le 1$, with $\hat{\mathcal{S}}[x] = \exp[x(\hat{a}^{\dagger 2} - \hat{a}^2)/2]$ and $r_{\rm np}(g) = -[\ln(1 - g^2)]/4$, and the energy eigen-values are $E^m_{\rm np}(g) = m\epsilon_{\rm np}(g) + E_{\rm G,np}(g)$, with $\epsilon_{\rm np}(g) = \omega_0\sqrt{1-g^2}$ and $E_{\rm G,np}(g) = [\epsilon_{\rm np}(g) - \omega_0]/2 - \Omega/2$. For the superradiant phase ($g > 1$), the effective low energy Hamiltonian becomes

$$\hat{H}_{\rm sp} = \omega_0 \hat{a}^\dagger \hat{a} - \frac{\omega_0}{4g^4}(\hat{a} + \hat{a}^\dagger)^2 - \frac{\Omega}{4}(g^2 + g^{-2}), \tag{11}$$

whose eigen-states are given by $|\phi^m_{\rm sp}(g)\rangle_\pm = \hat{\mathcal{D}}[\pm\alpha_g]\hat{\mathcal{S}}[r_{\rm sp}(g)]|m\rangle\Downarrow^\pm\rangle$, with $r_{\rm sp}(g) = -[\ln(1 - g^{-4})]/4$, $\alpha_g = \sqrt{(\Omega/4g^2\omega_0)(g^4-1)}$, and $\hat{\mathcal{D}}[\alpha] = e^{\alpha(\hat{a}^\dagger - \hat{a})}$. The displacement-dependent spin states are $\Downarrow^\pm\rangle = \mp\sqrt{(1-g^{-2})/2}|\uparrow\rangle + \sqrt{(1+g^{-2})/2}|\downarrow\rangle$, while the energy eigen-values take the form $E^m_{\rm sp}(g) = m\epsilon_{\rm sp}(g) + E_{\rm G,sp}(g)$, with $\epsilon_{\rm sp}(g) = \omega_0\sqrt{1-g^{-4}}$ and $E_{\rm G,sp}(g) = [\epsilon_{\rm sp}(g) - \omega_0]/2 - \Omega(g^2 + g^{-2})/4$. More details can be found in the supplementary material of Ref. [29].

For this model, the scaled average cavity photon number $\hat{n}_c = \omega_0\hat{a}^\dagger\hat{a}/\Omega$ is a suitable order parameter with Ω/ω_0 assuming the role of system size. The corresponding bulk order parameter then becomes $\hat{N}_c = \hat{a}^\dagger\hat{a}$ or the average cavity photon number, and

$$\begin{aligned} f(t) &= \lim_{\Omega/\omega_0\to\infty} \langle \hat{n}_c(t)\hat{n}_c(0)\rangle, \\ F(t) &= \lim_{\Omega/\omega_0\to\infty} \langle \hat{N}_c(t)\hat{N}_c(0)\rangle. \end{aligned} \tag{12}$$

For $g < 1$, we find

$$f(t) = 0,$$
$$F(t) = \eta_0 + \eta_2 e^{-i(2\epsilon_{np})t}, \tag{13}$$

respectively, where $\eta_0 = \sinh^4(r_{np})$ and $\eta_2 = \cosh^2(r_{np})\sinh^2(r_{np})$. For $g > 1$, we obtain the following equation:

$$f(t) = \frac{(g^2 - g^{-2})^2}{16}. \tag{14}$$

The time order phase diagram is shown in **Figure 2**. When $g < 1$, the system ground state corresponds to a generalized time crystalline order phase, while the system exhibits time trivial order when $g > 1$. Despites such a simple model composed of a two-level system and a bosonic field mode, the ground state of the quantum Rabi model displays an intriguing temporal phase structure accompanied by a finite-component quantum phase transition.

2.4 Non-Hermitian Many-Body Interaction Model

Finally, we consider two effective models with many-body spin–spin interaction and non-Hermitian effects. The first is described by the Hamiltonian:

$$\hat{H} = -\frac{1}{N(N-1)} \sum_{1 \le i < j \le N} (\lambda + i\gamma)\sigma_1^x \sigma_2^x \cdots \sigma_{(i)}^y \cdots \sigma_{(j)}^y \cdots \sigma_N^x, \tag{15}$$

with two σ^y operators at sites i and j in a string of otherwise σ^x N-body spin interaction. $1/[N(N-1)]$ is the normalization factor, λ is the spin interaction strength, and γ represents an effective dissipation rate. $\lambda > 0$ and $\gamma \ge 0$ are both real numbers.

We observe that the Greenberger–Horne–Zeilinger (GHZ) states

$$|G_\pm\rangle = \frac{1}{\sqrt{2}}\left(|0\rangle^{\otimes N} \pm |1\rangle^{\otimes N}\right), \tag{16}$$

correspond to two non-degenerate system eigen-states with eigen-energies $\pm(\lambda + i\gamma)/2$. The spectra of this model system are bounded inside the circle of radius $\sqrt{\lambda^2 + \gamma^2}/2$ in the complex plane. The eigen-state whose eigen-value has the largest imaginary part is taken as the ground state, or $|\mathrm{GS}\rangle = |G_+\rangle$ with eigen-energy $\epsilon_0 = (\lambda + i\gamma)/2$. The highest excited state is $|G_-\rangle$, whose corresponding eigen-energy is $\epsilon_{2^N-1} = -(\lambda + i\gamma)/2$.

An appropriate order parameter operator in this case becomes the average magnetization $\hat{m} = \sum_{i=1}^N \sigma_i^z/N$. The twisted vector becomes $|v\rangle = \hat{m}|\mathrm{GS}\rangle = |G_-\rangle$, and the auto-correlator can be easily worked out to be $f(t) = \lim_{N\to\infty}\langle \hat{m}(t)\hat{m}(0)\rangle = e^{-i\lambda t}e^{\gamma t}$. When $\gamma = 0$, the system ground state exists time-crystalline order phase and corresponds to a continuous time crystal [33]. When $\gamma \neq 0$, the system exhibits time functional order, with an exploding $f(t)$ as time evolves.

A second non-Hermitian model Hamiltonian is given by

$$\hat{H} = (\lambda + i\gamma)\left(\sigma_1^x \sigma_2^x \cdots \sigma_{[N/2]}^x - \sigma_{[N/2]+1}^x \cdots \sigma_N^x\right) - \sum_{j=1}^N \sigma_j^z \sigma_{j+1}^z, \tag{17}$$

where $[\cdot]$ denotes the integer part, $\boldsymbol{\sigma}_{N+1} \equiv \boldsymbol{\sigma}_1$ corresponds to the periodic boundary condition, and λ and γ are spin-string interaction strength and dissipation strength, respectively, as in the previous model, and are real numbers. This Hamiltonian contains $[(N+1)/2]$-body interaction terms and supports GHZ state $|G_+\rangle$ as a non-degenerate excited state [18] with eigen-energy $\epsilon_+ = -N$. The other two eigen-states of concern are $|\Psi^{(\pm)}\rangle \equiv (\alpha_1|G_-\rangle + \alpha_2|\tilde{G}_{-\mathcal{I}}\rangle)/\sqrt{|\alpha_1|^2 + |\alpha_2|^2}$ with $\alpha_1 = 1$ and $\alpha_2 = -(N + \epsilon^{(\pm)})/2(\lambda + i\gamma)$, where

$$|\tilde{G}_{-\mathcal{I}}\rangle = \frac{1}{\sqrt{2}}\left(|0\rangle_1 \cdots |0\rangle_{[N/2]}|1\rangle_{[N/2]+1} \cdots |1\rangle_N - |1\rangle_1 \cdots |1\rangle_{[N/2]}|0\rangle_{[N/2]+1} \cdots |0\rangle_N\right). \tag{18}$$

The eigen-energies for $|\Psi^{(\pm)}\rangle$ are given by $\epsilon^{(\pm)} = -N + 2 \pm 2\sqrt{1 + (\lambda + i\gamma)^2}$, with more details of the derivation given in **Section 4**. For the same order parameter operator $\hat{m}$, we find $\hat{m}|\Psi_0\rangle \overset{N\to\infty}{\longrightarrow} \alpha_1|G_+\rangle/\sqrt{|\alpha_1|^2 + |\alpha_2|^2}$.

At $\gamma = 0$, the above non-Hermitian Hamiltonian **Eq. 17** reduces to a Hermitian one, whose ground state $|\Psi_0\rangle$ corresponds to the one with smaller ϵ from $|\Psi^{(-)}\rangle$ and $|\Psi^{(+)}\rangle$, or $\epsilon_0 = -N - 2(\sqrt{1 + \lambda^2} - 1)$. The ground state $|\Psi_0\rangle$ for this non-Hermitian system is therefore chosen from $|\Psi^{(-)}\rangle$ or $|\Psi^{(+)}\rangle$ to be the one that deforms into the right Hermitian case one when γ approaches zero. However, the criteria for the ground state energy ϵ_0 correspond to choosing the smaller one from $\epsilon^{(\pm)}$ when ϵ is real and choosing the one with the larger imaginary part when ϵ is complex.

Therefore, we directly obtain the following equation:

$$f(t) = \lim_{N\to\infty}\langle \hat{m}(t)\hat{m}(0)\rangle = \frac{|\alpha_1|^2}{|\alpha_1|^2 + |\alpha_2|^2} e^{-i(\epsilon_+ - \epsilon_0)t}. \tag{19}$$

When $\lambda \neq 0$ and $\gamma \neq 0$, the system exists in *time functional order phase* and again results from the non-Hermitian Hamiltonian. When $\lambda \neq 0$ but $\gamma = 0$, the auto-correlation function reduces to

$$f(t) = \frac{1}{2}\left(1 + \frac{1}{\sqrt{1 + \lambda^2}}\right) e^{-2i(\sqrt{1+\lambda^2} - 1)t}, \tag{20}$$

as for a genuine time crystal of the WO type exhibiting time crystalline order. When $\lambda = 0$ and $0 < |\gamma| \le 1$, we find

$$f(t) = \frac{1}{2}(1 + \sqrt{1 - \gamma^2})e^{-2i(\sqrt{1-\gamma^2} - 1)t}. \tag{21}$$

The system ground state again exhibits time-crystalline order. When $\lambda = 0$ and $|\gamma| > 1$, we obtain

$$f(t) = \frac{1}{2} e^{2it} e^{-2\sqrt{\gamma^2 - 1}\ t}, \tag{22}$$

by choosing $\epsilon_0 = -N + 2 + 2i\sqrt{\gamma^2 - 1}$ as the ground state eigen-energy from the two eigen-values $-N + 2 \pm 2i\sqrt{\gamma^2 - 1}$. The system ground state now exhibits time functional order phase, with a decaying $f(t)$ as time evolves. When $\lambda = \gamma = 0$,

$$f(t) = 1, \tag{23}$$

the ground state reduces to the time trivial order phase.

The above two non-Hermitian models represent direct generalizations of the Hermitian system as considered in

Refs. [18, 33]. While slightly more complicated, they remain sufficiently simple for compact analytical treatment, thus helping to reveal interesting and clear physical meanings of the underlying time order.

2.5 Some Remarks About Continuous Time Crystal

According to the WO no-go theorem [62], $f(t)$ for the ground state or the Gibbs ensemble of a general many-body Hamiltonian whose interactions are not-too-long ranged exhibits no temporal dependence; hence, it belongs to time trivial order according to our classification scheme. At first sight, this seems to sweep many important models of condensed matter physics into the same boring class of the time trivial order phase. However, it remains to explore, for instance, many-body systems with more than two-body (or k-body) interactions, or non-Hermitian systems, which might support the existence of CTC. Inspired by the recent results on CTC [33], we believe more time crystalline phases will be uncovered and further understanding will be gained in the future.

The two-time auto-correlation function $f(t)$ measures the CTC phase as in earlier studies [33, 62], while both auto-correlation functions $f(t)$ and $F(t)$ together define different time-order phases we propose in this work. The absence of the local temporal behavior $f(t) = 0$ does not imply the absence of any temporal property in the bulk, when $F(t)$ could have various temporal behaviors. Based on this, our operational definitions of time order are developed. We also extend the scope of CTC to include both TC order and gTC order phases. This distinction between $f(t)$ and $F(t)$ gives more insights into quantum many-body phases.

As emphasized earlier, continuous time crystal results from spontaneously breaking continuous time translation symmetry. Due to the genuine time periodicity contained in CTC, it might be possible to explore and design *new types of clocks* based on macroscopic many-body systems, as the time period is directly related to energy spectra, and whose physical meaning is clearly the same as for atomic clock states. Furthermore, they are not affected by finite size effect in contrast to periodicity in DTC.

3 DISCUSSION AND CONCLUSION

While ground-state phases of a quantum many-body system are mostly classified with their Hamiltonian based on the following two paradigms: LGW symmetry breaking order parameter or topological order, this work proposes to study phases from time dimension using *time order* or more specifically with the proposed symmetry-based time order. Compared to the recent progress and understanding gained for topological order [66, 67], one could try to develop a framework for *entanglement-based time order* instead of the *symmetry-based time order* we employ here in this study. Quantum entanglement in a many-body system is responsible for topological order, whose origin lies at the tensor product structure of the quantum many-body Hilbert space $\mathcal{H}_{\text{tot}} = \otimes_i \mathcal{H}_i$ with $\mathcal{H}_i$ the finite-dimensional Hilbert space for site-i. An *entanglement-based time order* therefore calls for a combined investigation to exploit quantum entanglement and temporal properties of a quantum many-body system.

Through *time order*, one focuses on temporal structure of the evolution operator $e^{-i\hat{H}t}$. The *symmetry-based time order* therefore unifies the LGW paradigm with the concept of *time order*, while an *entanglement-based time order* could amalgamate the topological order paradigm (or entanglement beyond that) with time order. For this to happen, a more basic definition for *time order* will be required, which will likely expand into further in-depth investigations.

In conclusion, understanding the phases of matter constitutes a cornerstone of contemporary physics. Capitalizing on the concept of CTC for the many-body ground state with perpetual time dependence, this study argues that information from time domain can be employed to classify the quantum phase as well, which provides a new perspective toward the understanding of ground-state time dependence, significantly beyond existing studies on CTC. We introduce time order, provide its operational definition in terms of two-time auto-correlation function of an appropriate symmetry order operator, bestow physical meaning to characteristic frequencies and amplitudes of the correlation function, and present a complete classification of time order phases. Time order phase diagrams for a spin-1 BEC system and the quantum Rabi model are fully worked out. Interesting time order phases in non-Hermitian spin models with multi-body interaction are presented. In addition to the time crystalline order which already attracts broad attention from its studies in terms of CTC, other phases we identify, for example, time quasi-crystalline order and time functional order, represent exciting new possibilities.

4 METHODS AND CALCULATION DETAILS

Here, in this section, we provide more supporting material for our main results and related details for the aforementioned presentation. It is organized as follows: in **Section 4.1**, we extend the discussion of time order to finite temperature; in **Section 4.2**, we present calculation details related to the spin-1 atomic BEC example considered and give intriguing results for finite temperature scenario in spin-1 BEC; in **Section 4.3**,as a more straightforward approach to understand numerical results, we present a variational approach for treating the polar ground state of a spin-1 BEC. Finally, we give the details about ground state and eigen-energy calculation in the non-Hermitian quantum many-body model with multi-body interaction in **Section 4.4**.

4.1 Time Order at Finite Temperature

At finite temperature T, excited states will be populated, which can be taken into account with the Gibbs ensemble $\hat{\rho} \equiv e^{-\beta\hat{H}}/Z$, where $Z \equiv \text{Tr}\, e^{-\beta\hat{H}}$ denotes the partition function and $\beta \equiv 1/T$ the inverse temperature. We then find

$$
\begin{aligned}
f(t) &\to \lim_{V\to\infty} \mathrm{Tr}\left(e^{i\hat{H}t}\hat{\phi}(0)e^{-i\hat{H}t}\hat{\phi}(0)\hat{\rho}\right) \\
&= \lim_{V\to\infty} \sum_{k=0}^{\infty} \langle\psi_k|e^{i\hat{H}t}\hat{\phi}(0)e^{-i\hat{H}t}\hat{\phi}(0)\frac{e^{-\beta\hat{H}}}{Z}|\psi_k\rangle \\
&= \lim_{V\to\infty} \sum_{k=0}^{\infty} \frac{1}{Z}e^{i\epsilon_k t-\beta\epsilon_k}\langle\nu_k|e^{-i\hat{H}t}|\nu_k\rangle \\
&= \lim_{V\to\infty} \sum_{k=0}^{\infty}\sum_{j=0}^{\infty} \frac{1}{Z}c_{jk}e^{-\beta\epsilon_k}e^{-i(\epsilon_j-\epsilon_k)t},
\end{aligned}
\tag{24}
$$

where $|\nu_k\rangle$ is the eigen-state twisted vector for $|\psi_k\rangle$ and c_{jk} is its associated weight. Analogously, for the non-Hermitian case, we find

$$
\begin{aligned}
f(t) &= \lim_{V\to\infty} \sum_{k=0}^{\infty} \frac{1}{Z}e^{i\epsilon_k t-\beta\epsilon_k}\langle\nu_k^{(l)}|e^{-i\hat{H}t}|\nu_k^{(r)}\rangle \\
&= \lim_{V\to\infty} \sum_{k=0}^{\infty}\sum_{j=0}^{\infty} \frac{1}{Z}c_{jk}e^{-\beta\epsilon_k}e^{-i(\epsilon_j-\epsilon_k)t},
\end{aligned}
\tag{25}
$$

where $|\nu_k^{(l)}\rangle$ and $|\nu_k^{(r)}\rangle$ are the left and right twisted vectors for eigen-state $|\psi_k\rangle$, respectively, and c_{jk} is the corresponding weight.

It is easily noted that $f(t)$ at finite temperature contains contributions from all eigen-states of the quantum many-body system $\hat{H}$, with a temperature-dependent weight factor for different energy levels, but $f(t)$ remains to include contributions from different periodic functions. Hence, the quantum phase classification task essentially remains the same (including its possible reference to $F(t)$) as is shown in **Table 1** for the ground state. At finite temperature, due to thermal excitations to the ground state, the temporal behavior will be more complex, thus opening up for more interesting possibilities, for example, to control *time order* phases and to study crossover or driven phase transitions between different time order phases.

4.2 Time Order in a Spin-1 Atomic BEC

For typical interaction parameters of a spin-1 BEC (e.g., of ground state ^{87}Rb or ^{23}Na atoms) in a tight trap, spin domain formation is energetically suppressed when the atom number is not too large as spin-dependent interaction strength is much weaker than spin-independent interaction [26, 32, 36, 58]. This facilitates a single-spatial-mode approximation (SMA) by assuming all spin states share the same spatial wave function $\phi(\boldsymbol{r})$, which effectively decouples the spatial degrees of freedom from the spin and results in the Hamiltonian [36, 44] in **Eq. 6** for the model many-body system, where $\hat{a}_{m_F}(m_F = 0, \pm 1)$ is the annihilation operator of the ground manifold state $|F = 1, m_F\rangle$ with corresponding number operator $\hat{N}_{m_F} = \hat{a}^{\dagger}_{m_F}\hat{a}_{m_F}$. p and q are linear and quadratic Zeeman shifts which could be tuned independently in experiments [38], while c_2 denotes the spin exchange interaction strength. Unless otherwise noted, we will take $|c_2| = 1$ as unit of energy in this work. The total particle number operator $\hat{N} = \hat{N}_1 + \hat{N}_0 + \hat{N}_{-1}$ and the longitudinal magnetization operator $\hat{F}_z = \hat{N}_1 - \hat{N}_{-1}$ are both conserved. Thus, linear Zeeman shift can be set to $p = 0$ effectively.

As discussed in the main text, a suitable order parameter for this model system is $\hat{n}_{\mathrm{sum}} \equiv \hat{N}_{\mathrm{sum}}/N$ ($\hat{N}_{\mathrm{sum}} = \hat{N}_1 + \hat{N}_{-1} = N - \hat{N}_0$), which measures the fractional atomic population in the states $|1, 1\rangle$ and $|1, -1\rangle$, and N assumes the role of system size. Following our formulation and denoting the system energy eigen-state by $|\psi_i\rangle$ ($i = 0, 1, 2, \cdots$) with increasing eigen-energy ϵ_i, the ground-state twisted vector becomes $|\nu\rangle \equiv \hat{n}_{\mathrm{sum}}|\psi_0\rangle = \sum_{i=0}^{\infty} a_i|\psi_i\rangle$, with $a_i = \langle\psi_i|\nu\rangle$ its expansion coefficient on the eigen-state $|\psi_i\rangle$. We find

$$
f(t) = \lim_{N\to\infty}\langle\hat{n}_{\mathrm{sum}}(t)\hat{n}_{\mathrm{sum}}(0)\rangle = \lim_{N\to\infty}\sum_{j=0}^{\infty} b_j e^{-i(\epsilon_j-\epsilon_0)t}, \tag{26}
$$

where $b_j \equiv |a_j|^2$ is the weight of the ground-state twisted vector, $b \equiv \sum_{j=0}^{\infty} b_j$ the total weight, and

$$
F(t) = \lim_{N\to\infty}\langle\hat{N}_{\mathrm{sum}}(t)\hat{N}_{\mathrm{sum}}(0)\rangle = \lim_{N\to\infty}\sum_{j=0}^{\infty} B_j e^{-i(\epsilon_j-\epsilon_0)t}, \tag{27}
$$

where $A_i = N\langle\psi_i|\nu\rangle$, $B_j \equiv |A_j|^2$ is the weight of the enlarged ground state twisted vector, and $B \equiv \sum_{j=0}^{\infty} B_j$ the total weight.

Our study below is for the zero magnetization $F_z = 0$ subspace and employs exact diagonalization (ED) to calculate eigen-states as well as eigen-energies. The overall time order phase diagram for spin-1 BEC is shown in **Figure 1**. For ferromagnetic interaction $c_2 < 0$, the critical quadratic Zeeman energy $q/|c_2| = 2$ splits the whole region into the time trivial order (TT) phase for smaller q that observes TTS, and the generalized time crystalline (gTC) order phase for $q/|c_2| > 2$ where TTS is spontaneously broken. The latter (gTC phase) is found to coincide with the ground-state polar phase. The available computation resource limits the calculation to a finite system size, which prevents us from mapping out the exact details in the immediate neighborhood of $q = 2$, where further elaboration is needed for its time order properties. On the other hand, for antiferromagnetic interactions, we find $q = 0$ separates TT phase from gTC order.

In **Figure 3**, the weights for the ground state as well as for the low-lying excited states are shown as functions of q for a typical system size of $N = 10\,000$. Only the ground-state weight b_0 is non-vanishing in the $q < 2$ ($q < 0$) region for ferromagnetic (antiferromagnetic) interactions, but total weight b is zero in the $q > 2$ ($q > 0$) region for ferromagnetic (antiferromagnetic) interaction, which prompts us to examine further the enlarged weights B_i corresponding to the bulk order parameter. For ground and the first excited states, the volume enlarged weights $B_{0,1}$ are found to be non-vanishing, although both decrease as q increases and grow with N as q approaches $q = 2$ ($q = 0$) for ferromagnetic (antiferromagnetic) interaction. However, as mentioned above, limited to a system size of $N = 10\,000$ by computation resource in the ED calculation, we cannot exactly map out the behavior near $q = 2$ ($q = 0$) for ferromagnetic (antiferromagnetic) interaction. This consequently leaves empty for q in region [2.0, 2.02] ([0, 0.01]) for ferromagnetic (antiferromagnetic) interaction.

The dependence on system size N is clearly revealed by **Figure 4**, with the enlarged weights in the gTC regime attaining fixed values as the system approaches thermodynamic limit ($N \to \infty$). In regions away from $q = 2$ ($q = 0$) for ferromagnetic (antiferromagnetic) interaction, ED numerics can always approach thermodynamic limit, except for

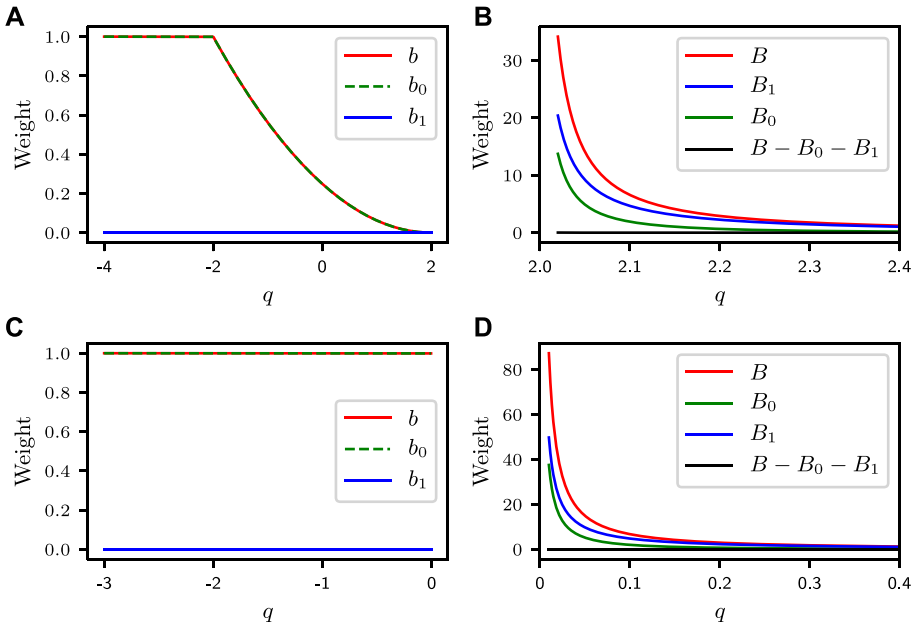

FIGURE 3 | Weights of ground-state twisted vector in the ground and low-lying excited states as functions of q at system size $N = 10\,000$. The upper panel is for ferromagnetic interaction, where weights b_i for $q < 2$ are shown in **(A)**, while weights B_i for $q > 2$ are shown in **(B)**. The lower panel is for antiferromagnetic interaction, where weights b_i for $q < 0$ are shown in **(C)**, while weights B_i for $q > 0$ are shown in **(D)**.

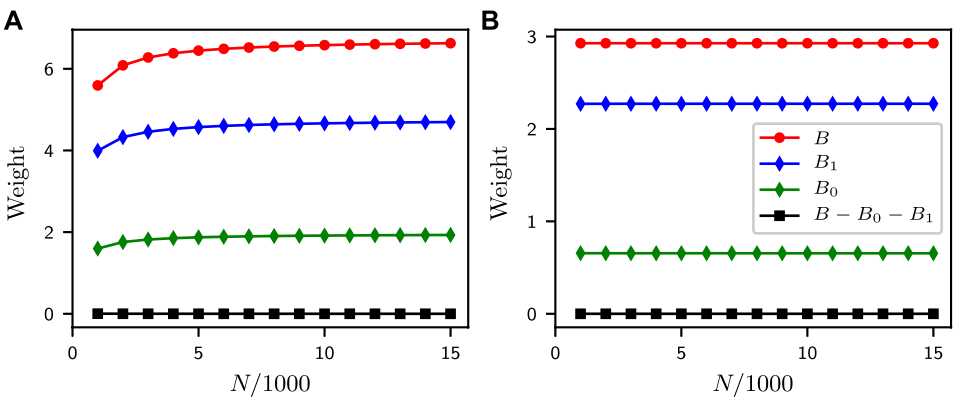

FIGURE 4 | Weights of ground-state twisted vector in the ground and low-lying excited states as functions of system size N at $q = 2.1$ for ferromagnetic interaction **(A)** and at $q = 0.2$ for antiferromagnetic interaction **(B)**.

the immediate neighborhood near $q = 2$ ($q = 0$), where we infer with confidence the tendencies to divergence of the weights $B_{0,1}$ as q approaches $q = 2$ ($q = 0$).

The time evolution of two-time auto-correlation function $F(t)$ is plotted in **Figures 5A,C** for ferromagnetic and for antiferromagnetic interactions, while **Figures 5B,D** display energy gaps between ground and the first excited states as a function of q for ferromagnetic and antiferromagnetic interactions, respectively, at a system size of $N = 5000$. The behavior of $F(t)$ is quantitatively consistent with that of the weights $B_i(q)$ ($i = 0, 1$) shown in **Figure 3** and the energy gap $\epsilon_1 - \epsilon_0$ shown in **Figures 5B,D**.

At finite temperature, excited states come into play by also contributing to the correlation function. We find the gTC order hosted in the polar phase persists for both ferromagnetic and antiferromagnetic interactions. The corresponding time evolution and Fourier transform of $F(t)$ are shown in **Figure 6**, calculated for $N = 500$ at a temperature of $\beta \equiv 1/T = 1$. The Fourier transform is performed for Re(F) over $t = [0, 1000]$ with the zero frequency (DC) component subtracted or for Im(F). The upper (lower) panel corresponds to ferromagnetic (antiferromagnetic) interaction at $q = 3$ ($q = 2$). For ferromagnetic interaction, two distinct frequency components are clearly identified for $q = 3$, associated with the two different energy level gaps. The beautiful beat pattern for

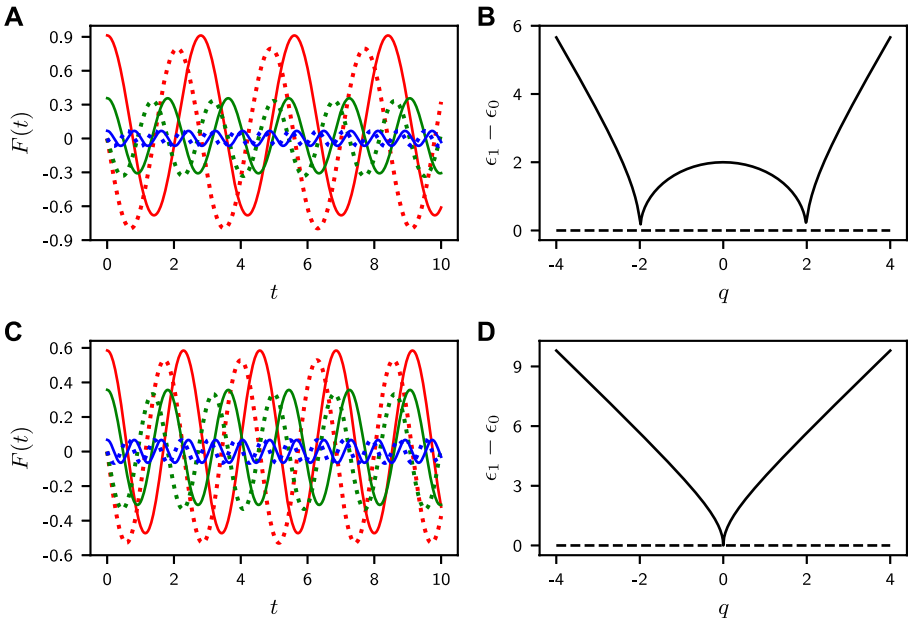

FIGURE 5 | $F(t)$ for different q as a function of time t. The solid and dotted lines correspond to Re(F) and Im(F), respectively. The red, green, and blue lines correspond to $q = 2.5$, $q = 3$, and $q = 5$, respectively, for ferromagnetic interaction **(A)**. The red, green, and blue lines correspond to $q = 0.7$, $q = 1$, and $q = 3$, respectively for antiferromagnetic interaction **(C)**. The energy gap between ground and the first excited state $\epsilon_1 - \epsilon_0$ as a function of q for ferromagnetic **(B)** and antiferromagnetic interactions **(D)**, at system size $N = 5000$.

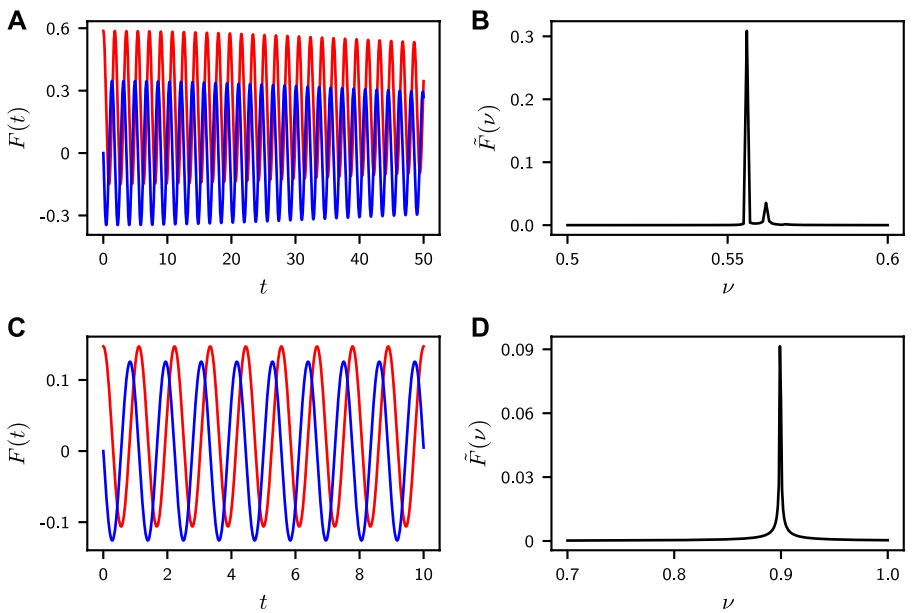

FIGURE 6 | $F(t)$ as a function of time t at $q = 3$ for ferromagnetic interaction **(A)** and $q = 2$ for antiferromagnetic interaction **(C)**. The red and blue solid lines, respectively, correspond to Re(F) and Im(F). The Fourier transform spectrum $\tilde{F}(\nu)$ of Re(F) or Im(F) with $\nu = 1/T$ the frequency, T the period, for ferromagnetic **(B)** and antiferromagnetic **(D)** interactions, at temperature $\beta = 1$ and system size $N = 500$.

$F(t)$ would appear, while we only show the short time behavior in **Figure 6** (*a*). Thus, the gTC phase remains at a finite temperature. Moreover, we also find a generalized time quasi-crystalline order phase assuming the two frequencies are incommensurate, by fine-tuning their corresponding energy gaps such that the relation $\Delta_1/\Delta_2 = m_1/m_2$ with m_1 and m_2 being co-primes is not satisfied. The gTC

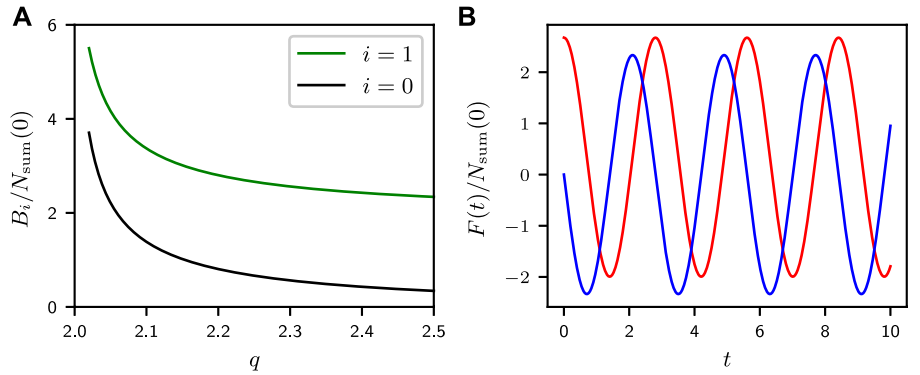

FIGURE 7 | (A) $B_i/N_{\rm sum}(0)$ as a function of q for ferromagnetic interaction. **(B)** $F(t)/N_{\rm sum}(0)$ as a function of time t at $q = 2.5$ for ferromagnetic interaction. The red and blue solid lines correspond to the real and imaginary part of $F(t)/N_{\rm sum}(0)$, respectively.

phase at finite temperature here is robust which is in contrast to the melting behavior of continuous time crystal (CTC) shown in Ref. [33].

Finally, we hope to address the critical question about how could this time order, sort of a perpetual time dependence, can be observed. We note the bulk two-time auto-correlation function introduced $F(t) = \lim_{N\to\infty}\langle \hat{N}_{\rm sum}(t)\hat{N}_{\rm sum}(0)\rangle$ denotes nothing but the ground-state (averaged) conditional outcome of measuring $N_{\rm sum}(t)$ at t after starting with $N_{\rm sum}(0)$ initially. The dynamics of $F(t)$ follows that of $N_{\rm sum}(t)$ as in the quantum regression theorem. Given the system is well controlled, highly reproducible, one can simply detect $F(t)$ by measuring $N_{\rm sum}(t)$, although for each measurement at an instant t, a condensate is destroyed, and a follow-up one will have to be prepared as closely as possible in every respects (through selection and post-selection) and be measured at a different $t' > t$. Thus, a plausible way to detect the ground-state time dependence will require reconstructing the time dependence of $F(t)/N_{\rm sum}(0)$. As long as the oscillation amplitude is more than a few percent, it will be easily observable with not too much difficulty, although such a reconstruction will still be difficult as $N_{\rm sum}(0)$ can be rather small compared to $N_0 \sim N$ in the polar state. Alternatively, one can perhaps start from a twin-Fock state, that is, by preparing an initial state with $N_{\rm sum}(0) \sim N$.

In **Figure 7A**, we show the behavior of oscillation amplitude for $F(t)/N_{\rm sum}(0)$. The time dependence of $F(t)/N_{\rm sum}(0)$ at $q = 2.5$ for ferromagnetic interaction is shown in **Figure 7B**.

4.3 A Variational Polar State for Ferromagnetic Spin-1 BEC

One might naively expect that nothing particularly interesting could happen in the polar phase of a ferromagnetic spin-1 BEC, where essentially all atoms reside in the single particle state $|1, 0\rangle$. Nevertheless, due to the competition between spin exchange interaction c_2 and quadratic Zeeman shift q, the ground state of our system differs from $|N_1 = 0, N_0 = N, N_{-1} = 0\rangle$, which can be affirmed based on a simple variational analytical calculation given in this section.

We use the number-state basis $|N_1, N_0, N_{-1}\rangle \equiv |[N], M, k\rangle$, where N_{m_F} denotes the occupation number of the m_F magnetic state, $M \equiv N_1 - N_{-1}$, and $k \equiv N_{-1}$. We take the following ground-state variational ansatz $|\psi_0\rangle = \frac{1}{\sqrt{1+|a|^2}}(|0, N, 0\rangle + a|1, N-2, 1\rangle)$ for the polar state of ferromagnetic spin-1 BEC, where $a = re^{i\phi}$ is a (complex) variational parameter with r and ϕ as real parameters. From **Eq. 6** and (assumed) $p = 0$, the ground-state energy follows from

$$\begin{aligned} E &= \frac{\langle\psi_0|H|\psi_0\rangle}{\langle\psi_0|\psi_0\rangle} \\ &= \frac{1}{1+a^*a}\left[\left(\frac{c_2(2N-5)}{N} + 2q\right)a^*a + c_2\sqrt{\frac{N-1}{N}}(a^* + a)\right] \\ &= \frac{1}{1+r^2}\left[\left(\frac{c_2(2N-5)}{N} + 2q\right)r^2 + 2c_2\sqrt{\frac{N-1}{N}}\,r\cos(\phi)\right]. \end{aligned} \tag{28}$$

We see the extreme value (the minimum) of E is reached when $\cos(\phi) = \pm 1$, that is, for a real variational parameter a, which will be assumed from now on. This gives the following equation:

$$E = \frac{x_1 a^2 + x_2 a}{1 + a^2}, \tag{29}$$

with $x_1 = \frac{c_2(2N-5)}{N} + 2q$ and $x_2 = 2c_2\sqrt{\frac{N-1}{N}}$. The derivative of the energy function $E(a)$ is as follows:

$$E'(a) = \frac{-x_2 a^2 + 2x_1 a + x_2}{(1+a^2)^2}, \tag{30}$$

which determines the locations for the extreme values.

$$\begin{aligned} a_\pm = &\frac{1}{2c_2\sqrt{N(N-1)}} \\ &\left[c_2(2N-5) + 2Nq \pm N\sqrt{\frac{c_2^2(8N^2-24N+25)}{N^2} + \frac{4c_2 q(2N-5)}{N} + 4q^2}\right], \end{aligned} \tag{31}$$

and the corresponding extreme values are as follows:

$$\begin{aligned} E_\pm = c_2 + q \pm \frac{1}{2}\sqrt{4q^2 + 8c_2 q + 8c_2^2 + \frac{-24c_2^2 - 10c_2 q}{N} + \frac{25c_2^2}{N^2}} \\ - \frac{5c_2}{2N}. \end{aligned} \tag{32}$$

In the thermodynamic limit $N \to \infty$, they reduce, respectively, to $a_{\pm} = 1 + \frac{q}{c_2} \pm \frac{\sqrt{2c_2^2+2c_2q+q^2}}{c_2}$ and $E_{\pm} = c_2 + q \pm \sqrt{2c_2^2 + 2c_2q + q^2}$. The left and right asymptotic value for the energy function $E(a)$ is therefore

$$E(a) = c_2\left(2 - \frac{5}{N}\right) + 2q, \quad (\text{when } a \to \pm\infty). \tag{33}$$

For ferromagnetic interaction ($c_2 < 0$), E_- assumes the minimum, which corresponds to the ground state $|\psi_0\rangle = \frac{1}{\sqrt{1+a_-^2}}(|0, N, 0\rangle + a_-|1, N-2, 1\rangle)$ with $N_{\text{sum}} = 2a_-^2/(1+a_-^2)$, and $a_- = 1 + \frac{q}{c_2} - \frac{\sqrt{2c_2^2+2c_2q+q^2}}{c_2}$ in the thermodynamic limit $N \to \infty$.

Despite the vanishing order parameter n_{sum} in the polar phase (here the gTC order phase from the time order perspective), the enlarged quantity N_{sum} retains a finite value. Hence, the physics we present here clearly belongs to the realm of quantum effects, beyond the reach of mean-field theory.

4.4 The Non-Hermitian Spin Model With Multi-Body Interaction

The non-Hermitian quantum many-body model Hamiltonian is

$$\hat{H} = \hat{H}_0 + (\lambda + \gamma\mathrm{i})\hat{H}_1, \tag{34}$$

with

$$\begin{aligned} \hat{H}_0 &= -\sum_{j=1}^{N} \sigma_j^z \sigma_{j+1}^z, \\ \hat{H}_1 &= \sigma_1^x \sigma_2^x \cdots \sigma_{[N/2]}^x - \sigma_{[N/2]+1}^x \cdots \sigma_N^x, \end{aligned} \tag{35}$$

where $[\cdot]$ denotes the integral part, $\boldsymbol{\sigma}_{N+1} \equiv \boldsymbol{\sigma}_1$, λ, and γ are spin-string interaction strength and dissipation strength, respectively. λ and γ are both real numbers. i is the imaginary unit. $\sigma^{x,y,z}$ are Pauli operators. N is the qubit number of the system. The Hamiltonian has the $[(N+1)/2]$-body interaction term and supports the GHZ state $|G_+\rangle$ as a non-degenerate excited state.

First, the Greenberger–Horne–Zeilinger (GHZ) states are denoted as follows:

$$|G_{\pm}\rangle = \frac{1}{2}(|0\rangle^{\otimes N} \pm |1\rangle^{\otimes N}), \tag{36}$$

and

$$\begin{aligned} &|\tilde{G}_{-,\mathcal{I}}\rangle = \\ &\frac{1}{\sqrt{2}}(|0\rangle_1 \cdots |0\rangle_{[N/2]} |1\rangle_{[N/2]+1} \cdots |1\rangle_N - |1\rangle_1 \cdots |1\rangle_{[N/2]} |0\rangle_{[N/2]+1} \cdots |0\rangle_N), \end{aligned} \tag{37}$$

where $\mathcal{I} = ([N/2]+1, [N/2]+2, \ldots, N)$ is a multi-index.

We immediately know that $|G_{\pm}\rangle$ is the degenerate ground state of the ferromagnetic Ising Hamiltonian $\hat{H}_0$ with eigen-energy $E_{(0)} = -N$, $|\tilde{G}_{-,\mathcal{I}}\rangle$ is the excited state of $\hat{H}_0$ with eigen-energy $E_{(1)} = -N+4$.

The action of $\widehat{H_1}$ on $|G_-\rangle$ ($|\tilde{G}_{-,\mathcal{I}}\rangle$) gives $|\tilde{G}_{-,\mathcal{I}}\rangle$ ($|G_-\rangle$) with a multiplicative factor −2.

$$\begin{aligned} \hat{H}_1|G_-\rangle &= -2|\tilde{G}_{-,\mathcal{I}}\rangle, \\ \hat{H}_1|\tilde{G}_{-,\mathcal{I}}\rangle &= -2|G_-\rangle. \end{aligned} \tag{38}$$

Then we know the two eigen-states of $\hat{H}$ are a superposition of $|G_-\rangle$ and $|\tilde{G}_{-,\mathcal{I}}\rangle$, and can be written as

$$|\Psi\rangle = \alpha_1|G_-\rangle + \alpha_2|\tilde{G}_{-,\mathcal{I}}\rangle, \tag{39}$$

where $\alpha_{1,2}$ are the undetermined coefficients. By substituting into the Schrödinger equation $\hat{H}\Psi\rangle = \epsilon|\Psi\rangle$, we get

$$\epsilon^2 - (E_{(0)} + E_{(1)})\epsilon + (E_{(0)}E_{(1)} - 4(\lambda+\gamma\mathrm{i})^2) = 0, \tag{40}$$

$$2(\lambda+\gamma\mathrm{i})\alpha_2 = (E_{(0)} - \epsilon)\alpha_1. \tag{41}$$

We obtain the eigen-energy $\epsilon^{(\pm)} = \frac{1}{2}[E_{(0)} + E_{(1)} \pm \sqrt{(E_{(1)} - E_{(0)})^2 + 16(\lambda+\gamma\mathrm{i})^2}]$. Choosing $\alpha_1 = 1$, we have $\alpha_2 = \frac{E_{(0)}-\epsilon}{2(\lambda+\gamma\mathrm{i})}$. Imposing the normalization condition, we have the following equation:

$$|\Psi^{(\pm)}\rangle = \frac{\alpha_1}{\sqrt{|\alpha_1|^2 + |\alpha_2|^2}}|G_-\rangle + \frac{\alpha_2}{\sqrt{|\alpha_1|^2 + |\alpha_2|^2}}|\tilde{G}_{-,\mathcal{I}}\rangle. \tag{42}$$

If $\gamma = 0$, the Hamiltonian is Hermitian, and we have the ground state $|\Psi_0\rangle \equiv |\Psi^{(-)}\rangle$ with energy $\epsilon_0 \equiv \epsilon^{(-)} = -N - 2(\sqrt{1+\lambda^2} - 1)$ (see more details about the Hermitian version of the system in Ref. [18]). Here, we choose the eigen-state from $\{|\Psi^{(+)}\rangle, |\Psi^{(-)}\rangle\}$ as the ground state $|\Psi_0\rangle$ of our generalized non-Hermitian system, for it deforms into the ground state of the Hermitian case when γ approaches zero. If ϵ is real, then ground-state energy ϵ_0 corresponds to the smaller one from $\epsilon^{(\pm)}$. However, ground-state energy ϵ_0 corresponds to the one with the larger imaginary part when ϵ is a complex number. Ground state $|\Psi_0\rangle$ is obtained straightforwardly.

For the GHZ state $|G_+\rangle$, we can know it is a non-degenerate excited state with energy $\epsilon_+ = -N$, for

$$\hat{H}_1|G_+\rangle = 0. \tag{43}$$

DATA AVAILABILITY STATEMENT

The raw data supporting the conclusions of this article will be made available by the authors, without undue reservation.

AUTHOR CONTRIBUTIONS

T-CG proposed and conducted the research, LY supervised the research, and T-CG, LY discussed the results and wrote the manuscript.

FUNDING

This work is supported by the National Key R&D Program of China (grant no. 2018YFA0306504), the National Natural Science Foundation of China (NSFC) (grants nos. 11 654001 and U1930201), and the Key-Area Research and Development Program of GuangDong Province (grant no. 2019B030330001).

ACKNOWLEDGMENTS

T-CG thanks Qi Liu and Ming Xue for their helpful discussion about spinor Bose–Einstein condensate.

REFERENCES

1. Anquez M, Robbins BA, Bharath HM, Boguslawski M, Hoang TM, Chapman MS Quantum Kibble-Zurek Mechanism in a Spin-1 Bose-Einstein Condensate. *Phys Rev Lett* (2016) 116:155301. doi:10.1103/physrevlett.116.155301
2. Autti S, Eltsov VB, Volovik GE Observation of a Time Quasicrystal and its Transition to a Superfluid Time crystal. *Phys Rev Lett* (2018) 120:215301. doi:10.1103/PhysRevLett.120.215301
3. Bruno P Impossibility of Spontaneously Rotating Time Crystals: A No-Go Theorem. *Phys Rev Lett* (2013) 111:070402. doi:10.1103/PhysRevLett.111.070402
4. Buča B, Tindall J, Jaksch D Non-stationary Coherent Quantum many-body Dynamics through Dissipation. *Nat Commun* (2019) 10:1730. doi:10.1038/s41467-019-09757-y
5. Buča B, Jaksch D Dissipation Induced Nonstationarity in a Quantum Gas. *Phys Rev Lett* (2019) 123:260401. doi:10.1103/PhysRevLett.123.260401
6. Cai Z, Huang Y, Vincent Liu W Imaginary Time crystal of thermal Quantum Matter. *Chin Phys. Lett.* (2020) 37:050503. doi:10.1088/0256-307x/37/5/050503
7. Chang M-S, Hamley CD, Barrett MD, Sauer JA, Fortier KM, Zhang W, et al. Observation of Spinor Dynamics in Optically TrappedRb87Bose-Einstein Condensates. *Phys Rev Lett* (2004) 92:140403. doi:10.1103/physrevlett.92.140403
8. Chang M-S, Qin Q, Zhang W, You L, Chapman MS Coherent Spinor Dynamics in a Spin-1 Bose Condensate. *Nat Phys* (2005) 1:111–6. doi:10.1038/nphys153
9. Chen X, Burnell FJ, Vishwanath A, Fidkowski L Anomalous Symmetry Fractionalization and Surface Topological Order. *Phys Rev X* (2015) 5:041013. doi:10.1103/PhysRevX.5.041013
10. Chen X, Gu Z-C, Liu Z-X, Wen X-G Symmetry Protected Topological Orders and the Group Cohomology of Their Symmetry Group. *Phys Rev B* (2013) 87:155114. doi:10.1103/PhysRevB.87.155114
11. Chen X, Liu Z-X, Wen X-G Two-dimensional Symmetry-Protected Topological Orders and Their Protected Gapless Edge Excitations. *Phys Rev B* (2011) 84:235141. doi:10.1103/PhysRevB.84.235141
12. Cheng M, Gu Z-C, Jiang S, Qi Y Exactly Solvable Models for Symmetry-Enriched Topological Phases. *Phys Rev B* (2017) 96:115107. doi:10.1103/PhysRevB.96.115107
13. Choi S, Choi J, Landig R, Kucsko G, Zhou H, Isoya J, et al. Observation of Discrete Time-Crystalline Order in a Disordered Dipolar many-body System. *Nature* (2017) 543:221–5. doi:10.1038/nature21426
14. Cosme JG, Skulte J, Mathey L Time Crystals in a Shaken Atom-Cavity System. *Phys Rev A* (2019) 100:053615. doi:10.1103/PhysRevA.100.053615
15. Damski B, Zurek WH Dynamics of a Quantum Phase Transition in a Ferromagnetic Bose-Einstein Condensate. *Phys Rev Lett* (2007) 99:130402. doi:10.1103/PhysRevLett.99.130402
16. Else DV, Bauer B, Nayak C. Floquet Time Crystals. *Phys Rev Lett* (2016) 117:090402. doi:10.1103/PhysRevLett.117.090402
17. Else DV, Monroe C, Nayak C, Yao NY Discrete Time Crystals. *Annu Rev Condens Matter Phys* (2020) 11:467–99. doi:10.1146/annurev-conmatphys-031119-050658
18. Facchi P, Florio G, Pascazio S, Pepe FV Greenberger-horne-zeilinger States and Few-Body Hamiltonians. *Phys Rev Lett* (2011) 107:260502. doi:10.1103/PhysRevLett.107.260502
19. Fan C-h., Rossini D, Zhang H-X, Wu J-H, Artoni M, La Rocca GC Discrete Time crystal in a Finite Chain of Rydberg Atoms without Disorder. *Phys Rev A* (2020) 101:013417. doi:10.1103/PhysRevA.101.013417
20. Fradkin E *Field Theories of Condensed Matter Physics*. 2nd ed. Oxford, UK: Oxford University Press (2004).
21. Gambetta FM, Carollo F, Marcuzzi M, Garrahan JP, Lesanovsky I Discrete Time Crystals in the Absence of Manifest Symmetries or Disorder in Open Quantum Systems. *Phys Rev Lett* (2019) 122:015701. doi:10.1103/PhysRevLett.122.015701
22. Gong Z, Hamazaki R, Ueda M Discrete Time-Crystalline Order in Cavity and Circuit Qed Systems. *Phys Rev Lett* (2018) 120:040404. doi:10.1103/PhysRevLett.120.040404
23. Gu Z-C, Wen X-G Tensor-entanglement-filtering Renormalization Approach and Symmetry-Protected Topological Order. *Phys Rev B* (2009) 80:155131. doi:10.1103/PhysRevB.80.155131
24. Guzman J, Jo G-B, Wenz AN, Murch KW, Thomas CK, Stamper-Kurn DM Long-time-scale Dynamics of Spin Textures in a Degenerate $F = 1^{87}$rb Spinor Bose Gas. *Phys Rev A* (2011) 84:063625. doi:10.1103/physreva.84.063625
25. Heinrich C, Burnell F, Fidkowski L, Levin M Symmetry-enriched String Nets: Exactly Solvable Models for Set Phases. *Phys Rev B* (2016) 94:235136. doi:10.1103/PhysRevB.94.235136
26. Ho T-L Spinor Bose Condensates in Optical Traps. *Phys Rev Lett* (1998) 81:742–5. doi:10.1103/PhysRevLett.81.742
27. Huang B, Wu Y-H, Liu WV Clean Floquet Time Crystals: Models and Realizations in Cold Atoms. *Phys Rev Lett* (2018) 120:110603. doi:10.1103/PhysRevLett.120.110603
28. Hurtado-Gutiérrez R, Carollo F, Pérez-Espigares C, Hurtado PI Building Continuous Time Crystals from Rare Events. *Phys Rev Lett* (2020) 125:160601. doi:10.1103/PhysRevLett.125.160601
29. Hwang M-J, Puebla R, Plenio MB Quantum Phase Transition and Universal Dynamics in the Rabi Model. *Phys Rev Lett* (2015) 115:180404. doi:10.1103/PhysRevLett.115.180404
30. Iemini F, Russomanno A, Keeling J, Schirò M, Dalmonte M, Fazio R Boundary Time Crystals. *Phys Rev Lett* (2018) 121:035301. doi:10.1103/PhysRevLett.121.035301
31. Khemani V, Lazarides A, Moessner R, Sondhi SL Phase Structure of Driven Quantum Systems. *Phys Rev Lett* (2016) 116:250401. doi:10.1103/PhysRevLett.116.250401
32. Koashi M, Ueda M Exact Eigenstates and Magnetic Response of Spin-1 and Spin-2 Bose-Einstein Condensates. *Phys Rev Lett* (2000) 84:1066–9. doi:10.1103/PhysRevLett.84.1066
33. Kozin VK, Kyriienko O Quantum Time Crystals from Hamiltonians with Long-Range Interactions. *Phys Rev Lett* (2019) 123:210602. doi:10.1103/PhysRevLett.123.210602
34. Lamacraft A Quantum Quenches in a Spinor Condensate. *Phys Rev Lett* (2007) 98:160404. doi:10.1103/physrevlett.98.160404
35. Landau LD, Lifshitz E *Statistical Physics*. Oxford, UK: Butterworth-Heinemann (1999).
36. Law CK, Pu H, Bigelow NP Quantum Spins Mixing in Spinor Bose-Einstein Condensates. *Phys Rev Lett* (1998) 81:5257–61. doi:10.1103/PhysRevLett.81.5257
37. Lazarides A, Roy S, Piazza F, Moessner R Time Crystallinity in Dissipative Floquet Systems. *Phys Rev Res* (2020) 2:022002. doi:10.1103/PhysRevResearch.2.022002
38. Luo XY, Zou YQ, Wu LN, Liu Q, Han MF, Tey MK, et al. Deterministic Entanglement Generation from Driving through Quantum Phase Transitions. *Science* (2017) 355:620–3. doi:10.1126/science.aag1106
39. Machado F, Else DV, Kahanamoku-Meyer GD, Nayak C, Yao NY Long-range Prethermal Phases of Nonequilibrium Matter. *Phys Rev X* (2020) 10:011043. doi:10.1103/PhysRevX.10.011043
40. Medenjak M, Buča B, Jaksch D Isolated Heisenberg Magnet as a Quantum Time crystal. *Phys Rev B* (2020) 102:041117. doi:10.1103/PhysRevB.102.041117
41. Mierzejewski M, Giergiel K, Sacha K Many-body Localization Caused by Temporal Disorder. *Phys Rev B* (2017) 96:140201. doi:10.1103/PhysRevB.96.140201
42. Nozières P Time Crystals: Can Diamagnetic Currents Drive a Charge Density Wave into Rotation? *Europhysics Lett* (2013) 103:57008. doi:10.1209/0295-5075/103/57008
43. Pal S, Nishad N, Mahesh TS, Sreejith GJ Temporal Order in Periodically Driven Spins in star-shaped Clusters. *Phys Rev Lett* (2018) 120:180602. doi:10.1103/PhysRevLett.120.180602
44. Pu H, Law CK, Raghavan S, Eberly JH, Bigelow NP Spin-mixing Dynamics of a Spinor Bose-Einstein Condensate. *Phys Rev A* (1999) 60:1463–70. doi:10.1103/PhysRevA.60.1463
45. Qiu LY, Liang HY, Yang YB, Yang HX, Tian T, Xu Y, et al. Observation of Generalized Kibble-Zurek Mechanism across a First-Order Quantum Phase Transition in a Spinor Condensate. *Sci Adv* (2020) 6:eaba7292. doi:10.1126/sciadv.aba7292

46. Riera-Campeny A, Moreno-Cardoner M, Sanpera A Time Crystallinity in Open Quantum Systems. *Quantum* (2020) 4:270. doi:10.22331/q-2020-05-25-270
47. Rovny J, Blum RL, Barrett SE P31 NMR Study of Discrete Time-Crystalline Signatures in an Ordered crystal of Ammonium Dihydrogen Phosphate. *Phys Rev B* (2018) 97:184301. doi:10.1103/PhysRevB.97.184301
48. Rovny J, Blum RL, Barrett SE Observation of Discrete-Time-crystal Signatures in an Ordered Dipolar many-body System. *Phys Rev Lett* (2018) 120:180603. doi:10.1103/PhysRevLett.120.180603
49. Russomanno A, Iemini F, Dalmonte M, Fazio R Floquet Time crystal in the Lipkin-Meshkov-Glick Model. *Phys Rev B* (2017) 95:214307. doi:10.1103/PhysRevB.95.214307
50. Sacha K Anderson Localization and mott Insulator Phase in the Time Domain. *Sci Rep* (2015) 5:10787. doi:10.1038/srep10787
51. Sacha K Modeling Spontaneous Breaking of Time-Translation Symmetry. *Phys Rev A* (2015) 91:033617. doi:10.1103/physreva.91.033617
52. Sachdev S *Quantum Phase Transitions*. Cambridge: Cambridge University Press (1999).
53. Senthil T, Vishwanath A, Balents L, Sachdev S, Fisher MPA Deconfined Quantum Critical Points. *Science* (2004) 303:1490–4. doi:10.1126/science.1091806
54. Shapere A, Wilczek F Classical Time Crystals. *Phys Rev Lett* (2012) 109:160402. doi:10.1103/physrevlett.109.160402
55. Shirley W, Slagle K, Chen X Universal Entanglement Signatures of Foliated Fracton Phases. *Scipost Phys* (2019) 6:15. doi:10.21468/SciPostPhys.6.1.015
56. Shirley W, Slagle K, Wang Z, Chen X Fracton Models on General Three-Dimensional Manifolds. *Phys Rev X* (2018) 8:031051. doi:10.1103/PhysRevX.8.031051
57. Smits J, Liao L, Stoof HTC, van der Straten P Observation of a Space-Time crystal in a Superfluid Quantum Gas. *Phys Rev Lett* (2018) 121:185301. doi:10.1103/PhysRevLett.121.185301
58. Stamper-Kurn DM, Ueda M Spinor Bose Gases: Symmetries, Magnetism, and Quantum Dynamics. *Rev Mod Phys* (2013) 85:1191–244. doi:10.1103/RevModPhys.85.1191
59. Syrwid A, Zakrzewski J, Sacha K Time crystal Behavior of Excited Eigenstates. *Phys Rev Lett* (2017) 119:250602. doi:10.1103/PhysRevLett.119.250602
60. Vijay S, Haah J, Fu L Fracton Topological Order, Generalized Lattice Gauge Theory, and Duality. *Phys Rev B* (2016) 94:235157. doi:10.1103/PhysRevB.94.235157
61. von Keyserlingk CW, Khemani V, Sondhi SL Absolute Stability and Spatiotemporal Long-Range Order in Floquet Systems. *Phys Rev B* (2016) 94:085112. doi:10.1103/PhysRevB.94.085112
62. Watanabe H, Oshikawa M Absence of Quantum Time Crystals. *Phys Rev Lett* (2015) 114:251603. doi:10.1103/physrevlett.114.251603
63. Wen XG Vacuum Degeneracy of Chiral Spin States in Compactified Space. *Phys Rev B* (1989) 40:7387–90. doi:10.1103/PhysRevB.40.7387
64. Wen XG Topological Orders in Rigid States. *Int J Mod Phys B* (1990) 04:239–71. doi:10.1142/S0217979290000139
65. Wen XG Quantum Orders and Symmetric Spin Liquids. *Phys Rev B* (2002) 65:165113. doi:10.1103/physrevb.65.165113
66. Wen XG Colloquium : Zoo of Quantum-Topological Phases of Matter. *Rev Mod Phys* (2017) 89:041004. doi:10.1103/RevModPhys.89.041004
67. Wen XG. Choreographed Entanglement Dances: Topological States of Quantum Matter. *Science* (2019) 363:eaal3099. doi:10.1126/science.aal3099
68. Wen XG *Quantum Field Theory of Many-Body Systems*. Oxford, UK: Oxford University Press (2004).
69. Wilczek F Quantum Time Crystals. *Phys Rev Lett* (2012) 109:160401. doi:10.1103/PhysRevLett.109.160401
70. Wilson K, Kogut J The Renormalization Group and the ε Expansion. *Phys Rep* (1974) 12:75–199. doi:10.1016/0370-1573(74)90023-4
71. Xue M, Yin S, You L Universal Driven Critical Dynamics across a Quantum Phase Transition in Ferromagnetic Spinor Atomic Bose-Einstein Condensates. *Phys Rev A* (2018) 98:013619. doi:10.1103/PhysRevA.98.013619
72. Yao NY, Potter AC, Potirniche ID, Vishwanath A Discrete Time Crystals: Rigidity, Criticality, and Realizations. *Phys Rev Lett* (2017) 118:030401. doi:10.1103/PhysRevLett.118.030401
73. Yi S, Müstecaplıoğlu ÖE, Sun CP, You L Single-mode Approximation in a Spinor-1 Atomic Condensate. *Phys Rev A* (2002) 66:011601. doi:10.1103/PhysRevA.66.011601
74. Zeng B, Wen XG Gapped Quantum Liquids and Topological Order, Stochastic Local Transformations and Emergence of Unitarity. *Phys Rev B* (2015) 91:125121. doi:10.1103/PhysRevB.91.125121
75. Zhang J, Hess PW, Kyprianidis A, Becker P, Lee A, Smith J, et al. Observation of a Discrete Time crystal. *Nature* (2017) 543:217–20. doi:10.1038/nature21413
76. Zhang W, Sun B, Chapman M, You L Localization of Spin Mixing Dynamics in a Spin-1 Bose-Einstein Condensate. *Phys Rev A* (2010) 81:033602. doi:10.1103/physreva.81.033602

Conflict of Interest: The authors declare that the research was conducted in the absence of any commercial or financial relationships that could be construed as a potential conflict of interest.

Publisher's Note: All claims expressed in this article are solely those of the authors and do not necessarily represent those of their affiliated organizations, or those of the publisher, the editors, and the reviewers. Any product that may be evaluated in this article, or claim that may be made by its manufacturer, is not guaranteed or endorsed by the publisher.

frontiers | Frontiers in Physics

ORIGINAL RESEARCH
published: 19 April 2022
doi: 10.3389/fphy.2022.877859

Coherent Control of Perfect Optical Vortex Through Four-Wave Mixing in an Asymmetric Semiconductor Double Quantum Well

Xu Deng, Tao Shui and Wen-Xing Yang**

School of Physics and Optoelectronic Engineering, Yangtze University, Jingzhou, China

A scheme for the coherent control of perfect optical vortex (POV) in an asymmetric semiconductor double quantum well (SDQW) nanostructure is proposed by exploiting the tunneling-induced highly efficient four-wave mixing (FWM). The orbital angular momentum (OAM) is completely transferred from a unique POV mode to the generated FWM field. Using experimentally achievable parameters, we identify the conditions under which resonant tunneling allows us to improve the quality of the vortex FWM field and engineer helical phase wave front beyond what is achievable in the absence of resonant tunneling. Furthermore, we find that the intensity and phase patterns of the vortex FWM field are sensitive to the detuning of the probe field but rather robust against the detuning of the coupling field. Subsequently, we perform the coaxial interference between the vortex FWM field and a same-frequency POV beam and show interesting interference properties, which allow us to measure the topological charge of the output POV beam. Our result may find potential applications in quantum technologies based on POV in solids.

Keywords: perfect optical vortex, coherent control, resonant tunneling, four-wave mixing, quantum well

OPEN ACCESS

Edited by:
Guangling Cheng,
East China Jiaotong University, China

Reviewed by:
Yandong Peng,
Shandong University of Science and Technology, China
Chunling Ding,
Wuhan Institute of Technology, China

****Correspondence:***
Tao Shui
ahushuitao@126.com
Wen-Xing Yang
wenxingyang2@126.com

Specialty section:
This article was submitted to Quantum Engineering and Technology, a section of the journal Frontiers in Physics

Received: *17 February 2022*
Accepted: *16 March 2022*
Published: *19 April 2022*

Citation:
Deng X, Shui T and Yang W-X (2022) Coherent Control of Perfect Optical Vortex Through Four-Wave Mixing in an Asymmetric Semiconductor Double Quantum Well. Front. Phys. 10:877859. doi: 10.3389/fphy.2022.877859

1 INTRODUCTION

In the past several decades, the study of optical vortices has been one of the hot spots in optics due to their potential applications in particle manipulation [1, 2], optical communication [3, 4], and quantum information processing [5–16]. Note that an optical vortex beam with a helical phase factor $e^{il\theta}$ carries OAM of $l\hbar$ per photon, where l and θ are the topological charge (TC) and azimuthal angle, respectively [17–19]. Conventional optical vortex beams such as Laguerre–Gaussian (LG) beam [20], Bessel–Gauss (BG) beam [21], and high-order Bessel beam [22] exhibit the concentric ring intensity pattern at the transverse distribution. However, the ring radii of this kind of optical vortices is proportional to TCs, which make them face difficulties in actual applications requiring a small vortex diameter and a large topological charge [3] or spatial superposition of vortex beams with different TCs [4]. In order to overcome this challenge, Ostrovsky et al. first proposed the concept of the POV beam, whose ring radius is completely independent of its TC [23]. Since then, significant efforts have been made to explore the generation and detection of the POV beam [24–28]. For instance, different kinds of POV beams have been experimentally generated *via* using spatial light modulator [28, 29], polymer-based phase plate [30], strongly scattering media [31], single-layer dielectric metasurface [32], etc. *In situ* measurements for TC of POV beams have been realized *via* exploiting the phase shift method [33], optical modal decomposition [34], and hybrid angular gradient phase grating [35].

Quite recently, Dai et al put forward a scheme for the fractional OAM conversion of an asymmetric POV beam by using second-harmonic generation [31].

On the other hand, based on the combination of electromagnetically induced transparency (EIT) and standing waves, spatially dependent light-matter interaction has led to many interesting quantum optical phenomena such as atom localization [36, 37], electromagnetically induced grating [38], and controllable photonic band gaps [39]. In 2015, Radwell et al experimentally observed spatially dependent electromagnetically induced transparency *via* utilizing optical vortex beams to drive cold rubidium atoms [40]. Subsequently, numerous schemes for the spatially dependent light-matter interaction induced by LG beams have been proposed in cold atomic ensembles [41], rare-earth–doped crystal [42], two-dimensional array of metal-coated dielectric nanosphere [43], semiconductor quantum dots [44], and molecular magnets [45]. Meanwhile, many intriguing quantum optical phenomena have been discovered such as vortex-induced spatial absorption [46, 47], spatially structured Kerr nonlinearity [39], ultraprecise Rydberg atomic localization [48], vortex four-wave mixing (FWM) [44, 45, 49, 50, 51, 52], and spatially dependent hyper Raman scattering [53]. Recently, semiconductor quantum wells (SQWs) have been exploited to explore the transfer and control of mid-infrared LG beams due to their inherent advantages such as high nonlinear optical coefficient and large electric dipole moments of intersubband transitions [54, 55, 56]. As far as we know, no reports have been proposed for the investigation of the conversion and manipulation of a POV beam in SDQWs.

In this study, we investigate the conversion and manipulation of a POV beam in an asymmetric SDQW nanostructure *via* resonant tunneling. The OAM of a unique POV mode can be completely transferred to the generated FWM field *via* the tunneling-induced highly efficient FWM process. Differing from previous studies in solids [44, 54, 55, 56], the distinguishing features of this scheme are given as follows: First and foremost, we are interested in showing the conversion and manipulation of the mid-infrared perfect optical vortex (POV) beam, which has different vortex characteristics from LG beams in Refs. [54, 55, 56]. Second, our scheme combines the advantages of the four-level ladder-type scheme [55] and tunneling-induced constructive interference [57, 58]. With resonant tunneling, the FWM field is closer to an ideal POV beam, which is a significant advantage of our scheme compared with Ref. [55]. Third, the detunings of probe and coupling fields have different influences on the intensity and phase of the FWM field. Differing from previous schemes [54, 55, 56], the vortex properties of the FWM field are rather robust against the detuning of the strong continuous-wave (CW) coupling field. Furthermore, we show the coaxial interference between the vortex FWM field and a same-frequency POV beam and focus on the influence of the TC of the vortex FWM field on the interference pattern. The interference results illustrate that the interference intensity and phase patterns are determined by the TC of the FWM field, which allows us to measure the TC of the generated POV field.

2 MODELS AND EQUATIONS

As shown in **Figure 1A**, we consider an n-doped asymmetric SDQW nanostructure, which can be grown by molecular-beam epitaxy (MBE) on a semi-insulating GaAs substrate [59]. After a buffer layer, the active region shown in **Figure 1A** is grown. It consists of a 118 A° wide deep well layer (GaAs) and a 130 A° wider shallow well layer ($Al_{0.10}Ga_{0.90}As$). The two well layers are separated by a 32 A° wide thin potential barrier ($Al_{0.485}Ga_{0.515}As$). Then, the growth is finished with a thick capping layer. The corresponding electron wave functions are shown *via* color-coded solid lines, and the energy levels are shown *via* blue dashed lines. The electron motion in the z-direction is limited by the potential barrier of the SDQW and obeys the one-dimensional effective mass Schrödinger equation, that is, $[\frac{\hbar^2}{2m^*}\frac{d^2}{dz^2} + V(z)]\psi(z) = E_z\psi(z)$, where $m^\star$ and $\psi(z)$ represent the effective mass and wave function of the moving electrons. It is worth noting that $|\psi(z)|^2$ represents the probability of finding the electrons. In this SDQW nanostructure, the energy of the ground subband $|1\rangle$ in the right side of the deep well is 25.5 meV. Two closely spaced delocalized subbands $|2\rangle$ and $|3\rangle$ with energies 101.8 and 106.9 meV are separated by resonant tunneling. Their corresponding wave functions are asymmetric and symmetric combinations of $|sg\rangle$ and $|de\rangle$, that is, $|2\rangle = (|sg\rangle - |de\rangle)/\sqrt{2}$ and $|3\rangle = (|sg\rangle + |de\rangle)/\sqrt{2}$. Two upper subbands $|4\rangle$ and $|5\rangle$ with eigen-energies of 259.5 and 374.1 meV are coupled by a continuous-wave (CW) driving field Ω_d (central frequency ω_d and wave vector $\vec{k}_d$). A weak probe field Ω_p (central frequency ω_p and wave vector $\vec{k}_p$) couples the ground subband $|1\rangle$ and two short-lived subbands $|2\rangle$ and $|3\rangle$, while a CW control field Ω_c (central frequency ω_c and wave vector $\vec{k}_c$) couples the subband $|4\rangle$ and the subbands $|2\rangle$ and $|3\rangle$, respectively. In this SDQW nanostructure, the pulse probe field and CW coupling and driving fields would induce two FWM processes $|1\rangle \rightarrow |2\rangle \rightarrow |4\rangle \rightarrow |5\rangle \rightarrow |1\rangle$ and $|1\rangle \rightarrow |3\rangle \rightarrow |4\rangle \rightarrow |5\rangle \rightarrow |1\rangle$, and then generate a pulse FWM field Ω_m (central frequency ω_m and wave vector $\vec{k}_m$) (see **Figures 1B,C**). In our proposal, the driving field Ω_d is a POV beam, which can be obtained through Fourier transformation of a BG beam [28]. Thus, the driving field Ω_d can be written as

$$\Omega_d(r,\theta) = \Omega_{d0}\Omega(r)e^{il\theta}, \tag{1}$$

where $\Omega(r) = i^{l-1}\frac{w_g}{w_0}e^{-(r-R)^2/w_0^2}$, Ω_{d0} is the initial Rabi frequency of the driving field, r is the radius, and θ is the azimuthal angle. w_0 ($= 2f/(k_d w_g)$) and R are the half width and radius of the ring of the POV beam, respectively, f is the focal length of the Fourier lens, and w_g is the beam waist of the initial BG beam.

In the interaction picture and under the rotating-wave approximation, the Hamiltonian of this system is given by:

$$H_I = -\hbar\begin{pmatrix} 0 & \Omega_p^\star e^{-ik_p z} & \alpha\Omega_p^\star e^{-ik_p z} & 0 & \Omega_m^\star e^{-ik_m z} \\ \Omega_p e^{ik_p z} & \Delta_p & 0 & \Omega_c^\star e^{-ik_c z} & 0 \\ \alpha\Omega_p e^{ik_p z} & 0 & \Delta_p - \delta & \beta\Omega_c^\star e^{-ik_c z} & 0 \\ 0 & \Omega_c e^{ik_c z} & \beta\Omega_c e^{ik_c z} & \Delta_p + \Delta_c & \Omega_d^\star e^{-ik_d z} \\ \Omega_m e^{ik_m z} & 0 & 0 & \Omega_d e^{ik_d z} & \Delta_m \end{pmatrix}, \tag{2}$$

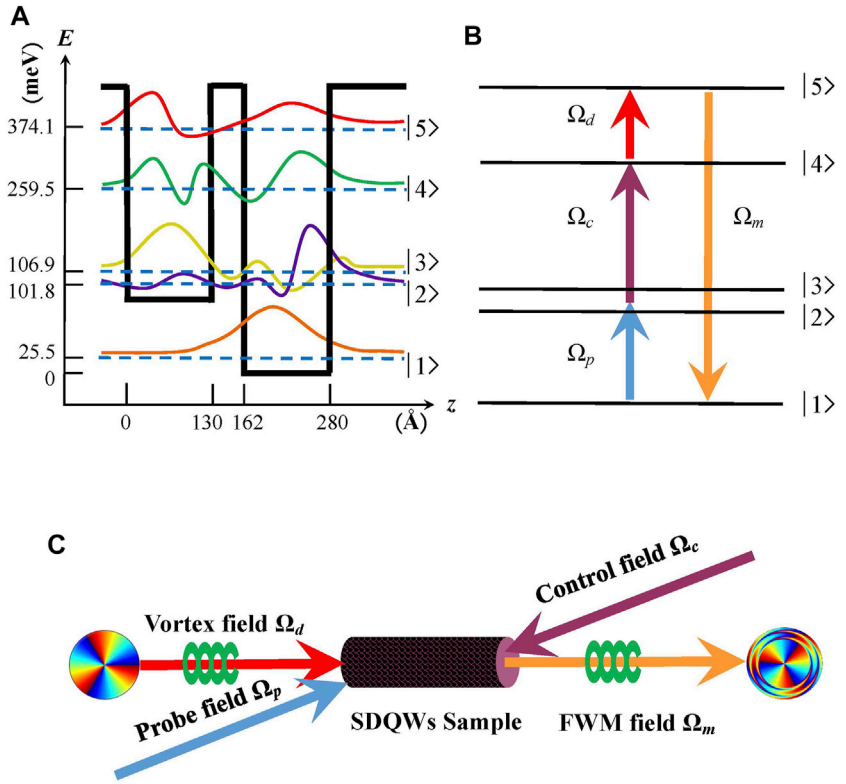

FIGURE 1 | (A,B) Schematic of diagram of an asymmetric SDQW nanostructure with five subbands. The solid curves represent the schematics of the corresponding electronic wave functions. **(C)** A simple block diagram of the SDQW nanostructure sample with four optical fields, in which the driving field is a POV beam.

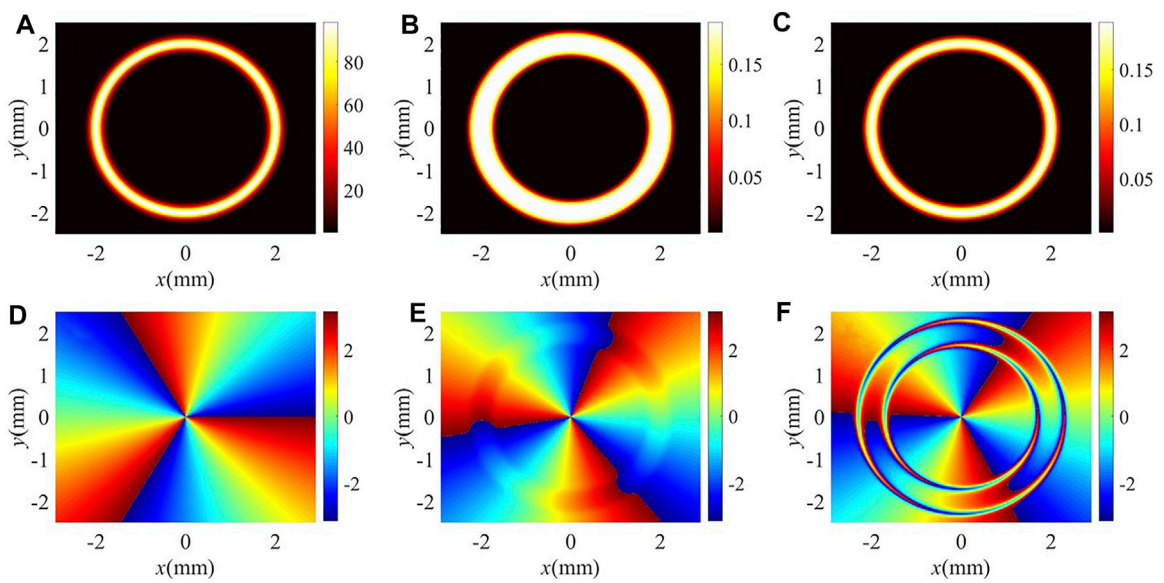

FIGURE 2 | (A,D) Intensity and phase profiles of the drive field with POV. **(B,C)** Intensity and **(E,F)** phase profiles of the FWM field for different values of α, β, and δ: **(B,E)** $\alpha = \beta = 0$, $\delta = 0$ meV; **(C,F)** $\alpha = -0.11$, $\beta = 0.98$, $\delta = 5.1$ meV. The other parameters are $\zeta_p = \zeta_m = 9.2 \times 10^{-3}$ meV/μm, $L = 100$ μm, $l = 3$, $w_g = 200$ μm, $\lambda = 10.83$ μm, $R = 2$ mm, $f = 11.69$ mm, $\Omega_p = 1$ meV, $\Omega_c = 14$ meV, $\Omega_{d0} = 10$ meV, $\Delta_p = 16$ meV, and $\Delta_c = \Delta_m = 0$ meV.

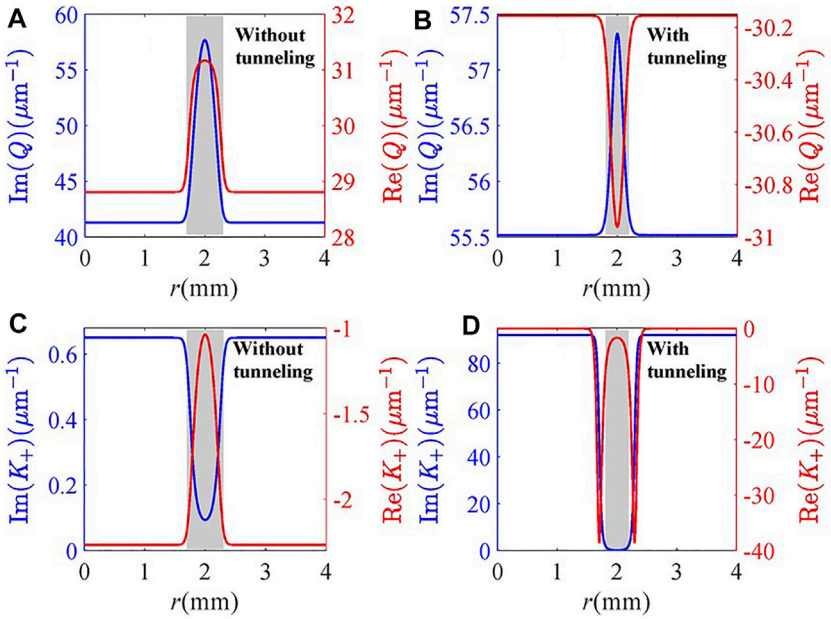

FIGURE 3 | Real and imaginary parts of **(A,B)** Q and **(C,D)** K_+ versus radius r for different values of α, β, and δ: **(A,C)** $\alpha = \beta = 0$, $\delta = 0$ meV; **(B,D)** $\alpha = -0.11$, $\beta = 0.98$, $\delta = 5.1$ meV. Other parameters are the same as in **Figure 2**.

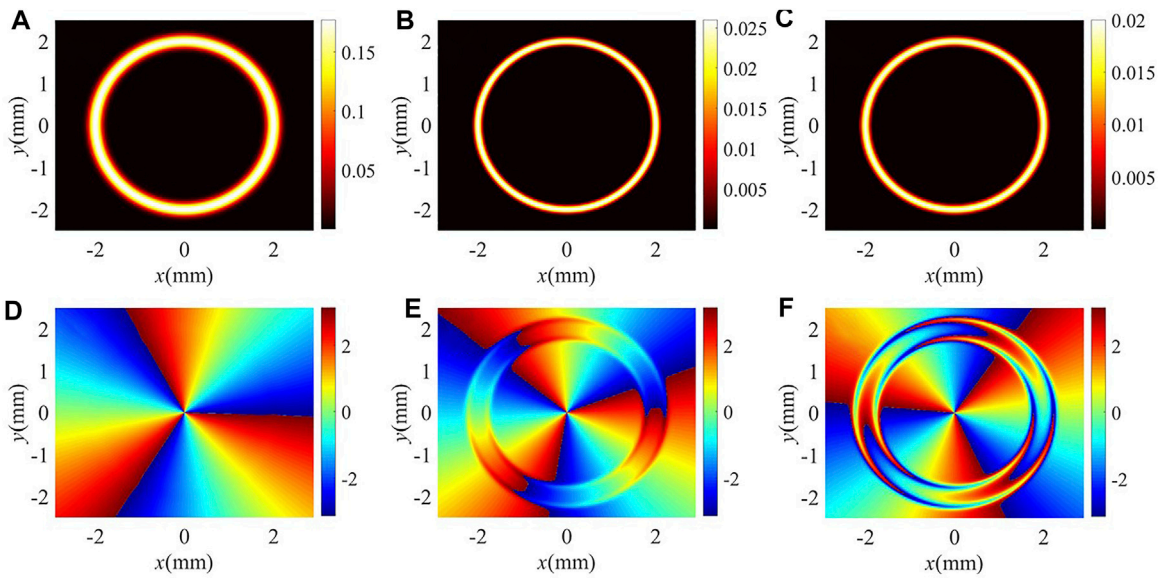

FIGURE 4 | (A–C) Intensity and **(D–F)** phase profiles of the FWM field for different probe detuning Δ_p: **(A,D)** $\Delta_p = -4$ meV; **(B,E)** $\Delta_p = 4$ meV; **(C,F)** $\Delta_p = 8$ meV. Other parameters are the same as in **Figure 2C**.

where$\Omega_p = \vec{\mu}_{21} \cdot \vec{E}_p/(2\hbar), \Omega_c = \vec{\mu}_{42} \cdot \vec{E}_c/(2\hbar), \Omega_d = \vec{\mu}_{54} \cdot \vec{E}_d/(2\hbar)$, and $\Omega_m = \vec{\mu}_{51} \cdot \vec{E}_m/(2\hbar)$ represent one-half of the Rabi frequencies for the respective transitions. $\vec{\mu}_{21}, \vec{\mu}_{42}, \vec{\mu}_{54}$ and $\vec{\mu}_{51}$ are the corresponding dipole matrix elements. $\Delta_{p(c,m)} = \omega_{p(c,m)} - (\omega_{2(4,5)} - \omega_{1(2,1)})$ denote the detuning of the corresponding fields. $\delta \approx 5.1$ meV indicates the strength of the resonant tunneling between subbands $|3\rangle$ and $|2\rangle$. $\alpha = \vec{\mu}_{31}/\vec{\mu}_{21}$ is the ratio between the subband transition dipole moments $\{\vec{\mu}\}\_\{31\}$ and $\{\vec{\mu}\}\_\{21\}$. $\beta = \vec{\mu}_{43}/\vec{\mu}_{42}$ is the ratio between the subband transition dipole moments $\{\vec{\mu}\}\_\{43\}$ and $\{\vec{\mu}\}\_\{42\}$.

Defining the electronic energy state as $|\Psi(t)\rangle = A_1|1\rangle + A_2 e^{ik_p z}|2\rangle + A_3 e^{ik_p z}|3\rangle + A_4 e^{i(k_p+k_c)z}|4\rangle + A_5 e^{ik_m z}|5\rangle$,

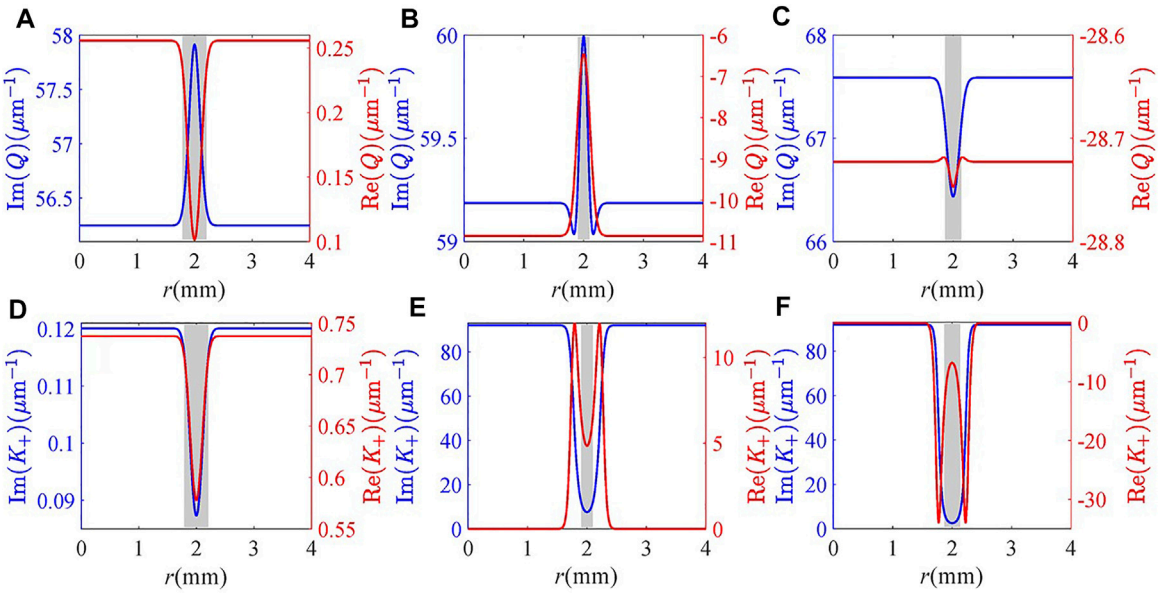

FIGURE 5 | Real and imaginary parts of **(A–C)** Q and **(D–F)** K_+ versus radius r for different probe detuning Δ_p: **(A,D)** $\Delta_p = -4$ meV; **(B,E)** $\Delta_p = 4$ meV; **(C,F)** $\Delta_p = 8$ meV. Other parameters are the same as in **Figure 2C**.

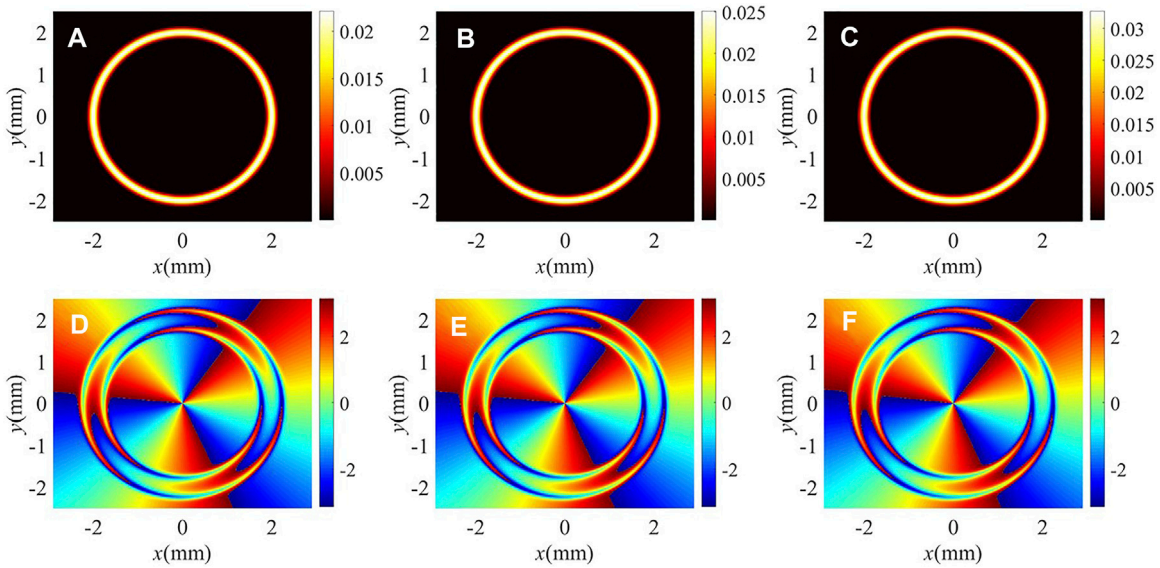

FIGURE 6 | (A–C) Intensity and **(D–F)** phase profiles of the FWM field for different coupling detuning Δ_c: **(A,D)** $\Delta_c = 4$ meV; **(B,E)** $\Delta_c = 8$ meV; **(C,F)** $\Delta_c = 16$ meV. Other parameters are the same as in **Figure 4C**.

using the Schrödinger equation $i\hbar\partial|\Psi(t)\rangle/\partial t = H_I|\Psi(t)\rangle$, the equations of motion for the probability amplitude A_j ($j = 1 \sim 5$) of the electronic wave functions can be obtained as

$$\frac{\partial A_2}{\partial t} = i\left(\Delta_p + i\gamma_2\right)A_2 + i\Omega_p A_1 + i\Omega_c^{\star} A_4, \tag{3}$$

$$\frac{\partial A_3}{\partial t} = i\left(\Delta_p - \delta + i\gamma_3\right)A_3 + i\alpha\Omega_p A_1 + i\beta\Omega_c^{\star} A_4, \tag{4}$$

$$\frac{\partial A_4}{\partial t} = i\left(\Delta_p + \Delta_c + i\gamma_4\right)A_4 + i\Omega_c A_2 + i\beta\Omega_c A_3 + i\Omega_d^{\dagger} e^{-i\Delta kz} A_5, \tag{5}$$

$$\frac{\partial A_5}{\partial t} = i\left(\Delta_m + i\gamma_5\right)A_5 + i\Omega_m A_1 + i\Omega_d e^{i\Delta kz} A_4, \tag{6}$$

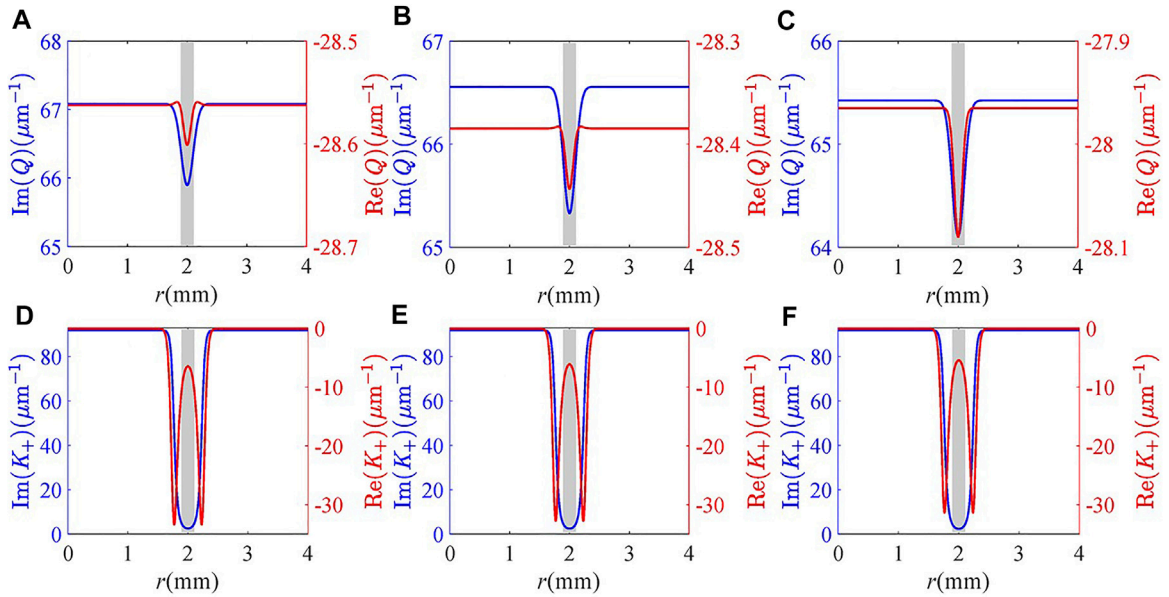

FIGURE 7 | Real and imaginary parts of **(A–C)** Q and **(D–F)** K_+ versus radius r for different coupling detuning Δ_c: **(A,D)** Δ_c = 4 meV; **(B,E)** Δ_c = 8 meV; **(C,F)** Δ_c = 16 meV. Other parameters are the same as in **Figure 4C**.

where γ_i (i = 2, 3, 4, 5) is added phenomenologically to describe the overall decay rate of the subbands $|i\rangle$, (i = 2, 3, 4, 5). In order to simplify the calculation, we assume the phase matching condition, that is, $\Delta\vec{k} = \vec{k}_p + \vec{k}_c + \vec{k}_d - \vec{k}_m = 0$, is satisfied.

The following Maxwell equations describe the propagation equations of the probe and FWM fields:

$$\frac{\partial\Omega_p(z,t)}{\partial z} + \frac{1}{c}\frac{\partial\Omega_p(z,t)}{\partial t} = i\frac{c}{2\omega_p}\nabla_\perp^2\Omega_p + i\zeta_p(A_2 + \alpha A_3)A_1^\star, \quad (7)$$

$$\frac{\partial\Omega_m(z,t)}{\partial z} + \frac{1}{c}\frac{\partial\Omega_m(z,t)}{\partial t} = i\frac{c}{2\omega_m}\nabla_\perp^2\Omega_m + i\zeta_m A_5 A_1^\star, \quad (8)$$

where $\zeta_p = \zeta_{21(31)} = 2N\omega_p|\mu_{21(31)}|^2/(\hbar\varepsilon_0 c)$, $\zeta_m = \zeta_{51} = 2N\omega_m|\mu_{51}|^2/(\hbar\varepsilon_0 c)$ are two constants, which are related to the frequently used oscillator strengths of the subband transitions $|1\rangle \leftrightarrow |2\,(3)\rangle$ and $|1\rangle \leftrightarrow |5\rangle$. N is the electron sheet density. The transverse derivatives $\nabla_\perp^2\Omega_{p(m)}$ on the right-hand sides of **Eqs 7**, **8** account for light diffraction [51]. When the propagation distance is much smaller than the Rayleigh length, that is, $\pi w_0^2/\lambda_m \gg L$, light diffraction can be neglected. In this study, $w_0 \approx 200\ \mu$m, $\lambda_m = 3.56\ \mu$m, and $L = 100\ \mu$m are chosen so that $\pi w_0^2/\lambda_m \approx 3.53 \times 10^4\ \mu\text{m} \gg L$. Therefore, it is reasonable to ignore diffraction in the following analysis.

In the limit of the weak probe and FWM fields, most of the electrons remain in the subband $|1\rangle$, that is, $|A_1|^2 \approx 1$. Taking Fourier transform of **Eqs 3–6** and **7**, **8**, we obtain

$$d_2\tilde{A}_2 + \Omega_c^\star\tilde{A}_4 + \tilde{\Omega}_p = 0, \quad (9)$$

$$d_3\tilde{A}_3 + \beta\Omega_c^\star\tilde{A}_4 + \alpha\tilde{\Omega}_p = 0, \quad (10)$$

$$\Omega_c\tilde{A}_2 + \beta\Omega_c\tilde{A}_3 + d_4\tilde{A}_4 + \Omega_d^\star\tilde{A}_5 = 0, \quad (11)$$

$$\Omega_d\tilde{A}_4 + d_5\tilde{A}_5 + \tilde{\Omega}_m = 0, \quad (12)$$

$$\frac{\partial\tilde{\Omega}_p}{\partial z} - i\frac{\omega}{c}\tilde{\Omega}_p = i\zeta_p\left(\tilde{A}_2 + \alpha\tilde{A}_3\right), \quad (13)$$

$$\frac{\partial\tilde{\Omega}_m}{\partial z} - i\frac{\omega}{c}\tilde{\Omega}_m = i\zeta_m\tilde{A}_5, \quad (14)$$

where $d_2 = \omega + \Delta_p + i\gamma_2$, $d_3 = \omega + \Delta_p - \delta + i\gamma_3$, $d_4 = \omega + \Delta_p + \Delta_c + i\gamma_4$, $d_5 = \omega + \Delta_m + i\gamma_5$, ω is the Fourier variable. $\tilde{A}_j$ (j = 2, 3, 4, 5) and $\tilde{\Omega}_{p(m)}$ are the Fourier transforms of A_j (j = 2, 3, 4, 5) and $\Omega_{p(m)}$, respectively. By solving **Eqs 9–12**, it is easy to obtain the following relations:

$$\tilde{A}_2 + \alpha\tilde{A}_3 = \left(D_{p1}\tilde{\Omega}_p + D_{m1}\tilde{\Omega}_m\right)\Big/ D, \quad (15)$$

$$\tilde{A}_5 = \left(D_{p2}\tilde{\Omega}_p + D_{m2}\tilde{\Omega}_m\right)\Big/ D, \quad (16)$$

where $D_{p1} = D_{p1}(\omega)$, $D_{p2} = D_{p2}(\omega)$, $D_{m1} = D_{m1}(\omega)$, $D_{m2} = D_{m2}(\omega)$, $D = D(\omega)$, $D_{p1}(\omega) = d_5\,(\alpha - \beta)^2|\Omega_c|^2 - (d_2\alpha^2 + d_3)\,(d_4d_5 - |\Omega_d|^2)$, $D_{p2}(\omega) = -(d_2\alpha\beta + d_3)\Omega_c\Omega_d$, $D_{m1}(\omega) = -(d_2\alpha\beta + d_3)\Omega_c^\star\Omega_d^\star$, $D_{m2}(\omega) = -d_2d_3d_4 + (d_2\beta^2 + d_3)|\Omega_c|^2$, and $D(\omega) = d_2d_3\,(d_4d_5 - |\Omega_d|^2) - d_5\,(d_2\beta^2 + d_3)|\Omega_c|^2$.

By substituting **Eqs 15**, **16** into **Eqs 13**, **14** and using the initial condition $\tilde{\Omega}_m(z = 0, \omega; x, y) = 0$, the expression of the generated FWM field can be obtained as

$$\tilde{\Omega}_m(z,\omega;x,y) = \tilde{\Upsilon}(\omega)\tilde{\Omega}_p(z = 0,\omega;x,y)\left[e^{iK_+(\omega)}z - e^{iK_-(\omega)}z\right], \quad (17)$$

where $K_\pm(\omega) = \omega/c + (\zeta_pD_{p1} + \zeta_mD_{m2})/(2D) \pm \sqrt{G(\omega)}/(2D) = K_\pm(0) + K_\pm^{(1)}\omega + O(\omega^2)$, $\tilde{\Upsilon}(\omega) = \zeta_mD_{p2}/\sqrt{G(\omega)} = \tilde{\Upsilon}(0) + O(\omega)$ with $G(\omega) = (\zeta_pD_{p1} - \zeta_mD_{m2})^2 + 4\zeta_p\zeta_mD_{p2}D_{m1}$. From **Eq. 17**, we

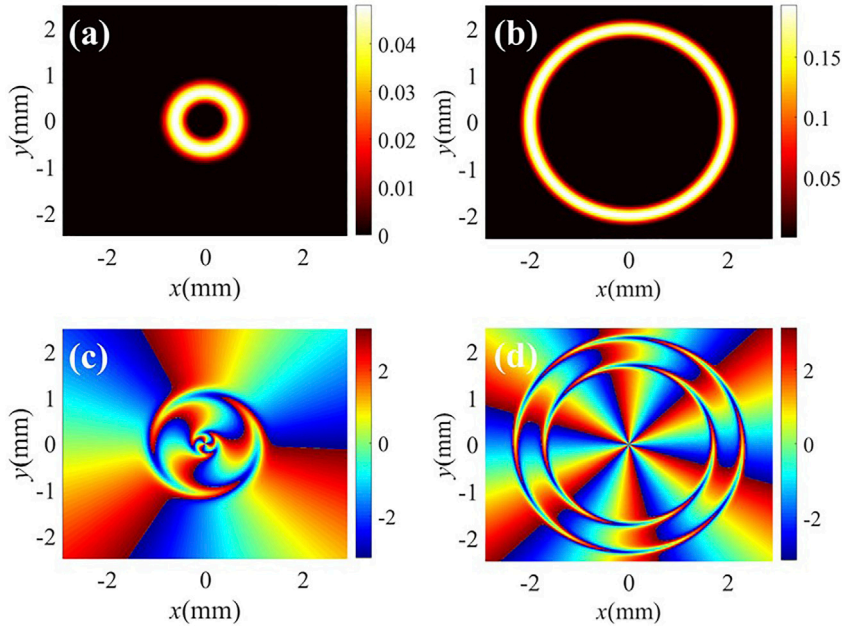

FIGURE 8 | (A,B) Intensity and **(C,D)** phase profiles of the FWM field for different beams. **(A,C)** LG beam with $p = 0$, $l = 3$, and $w_{LG} = 0.5$ mm; **(B,D)** POV beam with $l = 6$. Other parameters are the same as in **Figure 2C**.

readily observe that there exist two modes described by the dispersion relations $K_+(\omega)$ and $K_-(\omega)$, respectively. By seeking the approximated inverse Fourier transform with the approximation of neglecting both $O(\omega)$ in $\tilde{\Upsilon}(\omega)$ and $O(\omega^2)$ in $K_\pm(\omega)$, it is straightforward to obtain

$$\Omega_m(z,t;x,y) = \tilde{\Upsilon}(0)\left[\Omega_p(\eta_+)e^{iK_+z} - \Omega_p(\eta_-)e^{iK_-z}\right], \quad (18)$$

where $K_\pm = K_\pm(0)$, $\eta_\pm = t - z/V_{g\pm}$, and $V_{g\pm} = 1/\mathrm{Re}[K_\pm^{(1)}]$ is the group velocity of $K_\pm$ mode. $\mathrm{Re}(K_\pm)$ and $\mathrm{Im}(K_\pm)$ represent the phase shift per unit length and absorption coefficient of $K_\pm$ mode, respectively. In the adiabatic regime, the absorption coefficient $\mathrm{Im}(K_-)$ is much greater than $\mathrm{Im}(K_+)$ [58], which indicates that the K_- mode is absorbed quickly and only the K_+ mode remains after a short propagation distance L. Therefore, $\mathrm{Re}(K_+)$ and $\mathrm{Im}(K_+)$ are called as the modal phase shift per unit length and absorption coefficient for the remaining K_+ mode, respectively. By neglecting the K_- mode, the generated FWM field after a short propagation distance L can be given as

$$\Omega_m(L,t;x,y) = S\Omega_c\Omega_{d0}\Omega(r)\Omega_p(\eta_+)e^{il\theta}e^{iK_+L}, \quad (19)$$

with

$$S = -\zeta_m\left[\alpha\beta\Delta_p + \Delta_p - \delta + i(\alpha\beta\gamma_2 + \gamma_3)\right]/\sqrt{G(0)}. \quad (20)$$

It is worth noting that the modulation term S, which is independent of the propagation distance L, can also influence the output of the FWM field, that is, the modulation term S appears once the FWM process takes place. Thus, S is the inherent attribute for the SDQW-based FWM system. S is a complex function of the radial position r due to the existence of the POV driving field and can modify the intensity and phase patterns of the generated FWM field. In order to compare with the modal phase shift $\mathrm{Re}(K_+)$ and modal absorption $\mathrm{Im}(K_+)$, we introduce a factor Q to replace S by setting $S = e^{iQL} = e^{i\,\mathrm{Re}(Q)L - \mathrm{Im}(Q)L}$. In this sense, the inherent phase shift and absorption induced by S can be represented by $\mathrm{Re}(Q)$ and $\mathrm{Im}(Q)$. Thus, $\mathrm{Re}(Q)$ and $\mathrm{Im}(Q)$ are called as the inherent phase shift per unit length and absorption coefficient of the SDQW-based FWM system. Using $K_+ = \mathrm{Re}(K_+) + i\,\mathrm{Im}(K_+)$, **Eq. 19** can be rewritten as

$$\Omega_m(L,t;x,y) = \Omega_c\Omega_{d0}\Omega(r)\Omega_p(\eta_+)e^{-[\mathrm{Im}(Q)+\mathrm{Im}(K_+)]L}e^{il\theta+i[\mathrm{Re}(Q)+\mathrm{Re}(K_+)]L}, \quad (21)$$

where the intensity of the vortex FWM field is $\propto |\Omega_c\Omega_{d0}\Omega(r)\Omega_p(\eta_+)e^{-[\mathrm{Im}(Q)+\mathrm{Im}(K_+)]L}|^2$, while the factor $e^{il\theta+i[\mathrm{Re}(Q)+\mathrm{Re}(K_+)]L}$ reflects the phase wave front of the vortex FWM field. In **Eq. 21**, $\mathrm{Im}(K_+)L$, $\mathrm{Im}(Q)L$, and $\mathrm{Re}(Q)L$ should be dimensionless. In our proposal, the unit of the propagation distance L is μm. Therefore, the units of the absorption coefficients and the phase shifts per unit length are $\mu\mathrm{m}^{-1}$.

3 RESULTS AND DISCUSSIONS

In this section, the focus is on investigating the coherent control of the generated POV beam *via* FWM process in an asymmetric SDQW nanostructure. As we know, the structure of a SQW determines its properties such as resonant tunneling and subband decay rates. In other words, these properties of the SQW are determined once it is fabricated. Thus, the values of the decay rates may be different for the cases with and without resonant tunneling. In the proposed asymmetric SDQW nanostructure, resonant tunneling exists, that is, $\alpha = -0.11$, $\beta = 0.98$, and $\delta = 5.1$ meV, and the decay rates are $\gamma_2 = \gamma_3 = 1$ meV and $\gamma_4 = \gamma_5 = 0.1$ meV [58]. For comparative analysis, we consider the case

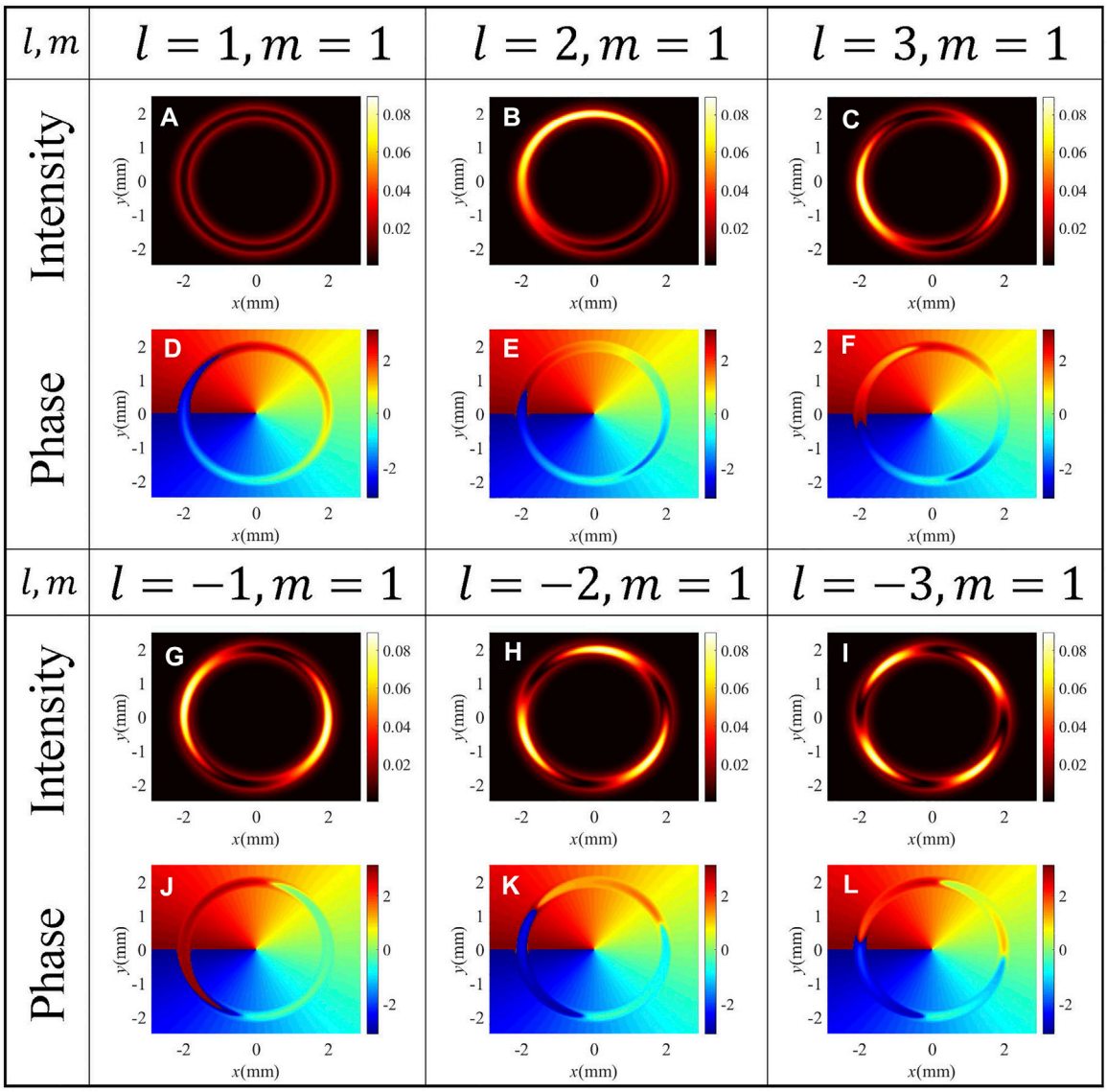

FIGURE 9 | Interference intensity [**(A–C)** and **(G–I)**] and phase [**(D–F)** and **(J–L)**] profiles of different values of TC of the FWM field. $\Omega_{G0} = 0.16$ meV, $m = 1$, and other parameters are the same as in **Figure 4C**.

without resonant tunneling by directly taking $\alpha = \beta = 0$ and $\delta = 0$. This approach has been used to investigate tunneling-induced highly efficient FWM [57,58].

The influence of the resonant tunneling on the intensity and phase of the generated FWM field is explored first. Here, the driving field $\Omega_d(r, \theta)$ is a POV beam with the TC $l = 3$, and the corresponding intensity and phase profiles are plotted in **Figures 2A,D**, respectively. The intensity distribution of the driving field in **Figure 2A** exhibits a ring pattern at the radial position $r =$ 2 mm with a full width at half maximum (FWHM) of $\Delta\omega_H =$ 0.402 mm. Meanwhile, the helical phase profile in **Figure 2D** displays three periods along the azimuthal direction, and the phase of each period is 2π. Based on **Eq. 21**, the intensity and phase profiles of the generated FWM field are also plotted in **Figure 2**. As shown in **Figures 2B,E**, in the absence of resonant tunneling, that is, $\alpha = \beta = 0$ and $\delta = 0$, the intensity distribution also displays a ring pattern at $r = 2$ mm with an increased FWHM of $\Delta\omega_H = 0.606$ mm (see **Figure 2B**), while the helical phase twists in the clockwise direction [see **Figure 2E**]. When considering the existence of resonant tunneling, that is, $\alpha = -0.11$, $\beta = 0.98$ and $\delta =$ 5.1 meV [58], as shown in **Figures 2C,F**, the intensity of the vortex FWM field is almost unchanged, and FWHM of the intensity pattern decreases from 0.606 to 0.384 mm, while the helical phase twists in the opposite direction compared with the case in **Figures 2B,E**. More interestingly, the phase distortion is significantly enhanced at two edges of the intensity pattern. For a POV beam, the FWHM of the intensity pattern can be adopted in appraising the quality of POV, where $\Delta\omega_H = 0$ corresponds to an

ideal POV beam [23]. The direct comparison between the aforementioned two cases implies that the resonant tunneling makes the generated vortex FWM field closer to an ideal POV beam and modifies the wave front of the helical phase. Actually, the resonant tunneling can lead to the symmetric and asymmetric wave functions of subbands $|2\rangle$ and $|3\rangle$ in the SDQW nanostructure (i.e., $\alpha\beta < 0$). Therefore, the optical nonlinear properties of the SDQW nanostructure can be modified by the resonant tunneling, which results in the different findings in **Figure 2**.

In order to inspect the effect of the resonant tunneling, the radial distributions of the imaginary and real parts of Q and K_+ are plotted in **Figure 3**. Note that the inherent absorption Im(Q) and modal absorption Im (K_+) at $r = 2$ mm determine the output intensity of the vortex FWM field. Without and with resonant tunneling, the total absorption coefficients at $r = 2$ mm are 57.77 μm^{-1} and 57.56 μm^{-1}, respectively. In the two cases, the total absorption coefficients are nearly equal so that the intensity of the FWM field remains nearly constant. In addition, the inherent absorption Im(Q) and modal absorption Im (K_+) determine the intensity distribution of the generated vortex FWM field, while the inherent phase shift Re(Q) and modal phase shift Re(K_+) determine the wave front distribution of the helical phase. Without the resonant tunneling, the inherent absorption Im(Q) dominates in tailoring the intensity profile of the FWM field [see blue lines in **Figures 3A,C**]. The ring pattern of the FWM field becomes flat in the vortex transfer processing due to the existence of the strong inherent absorption peak at $r = 2$ mm. Thus, the FWHM of the vortex FWM field increases compared with the driving field with POV. The appearance of peaks of both the inherent and modal phase shifts at $r = 2$ mm results in the helical phase twisted in the clockwise direction (see red lines in **Figures 3A,C**). With the resonant tunneling, the FWM field suffers stronger inherent and modal absorption at two edges of the intensity pattern (see blue lines in **Figures 3B,D**). In this case, the edge energy of the vortex FWM field can be easily dissipated, resulting in the width of the intensity pattern becoming narrower. The double-valley pattern of the dominated modal phase shift around $r = 2$ mm gives rise to two tremendous distortions in the anticlockwise direction (see red lines in **Figures 3B,D**).

We then examine in **Figure 4** the influence of the detuning Δ_p of the probe field on the intensity and helical phase of the vortex FWM field in the presence of the resonant tunneling. The corresponding radial distributions of the imaginary and real parts of Q and K_+ are shown in **Figure 5**. One can find that the total absorption (including inherent and modal absorption) at the center of the light ring increases when increasing Δ_p from −4 to 8 meV (see blue lines in **Figure 5**). Correspondingly, the intensity of the vortex FWM field decreases (see **Figures 4A–C**). In the case of $\Delta_p = -4$ meV, one can find from **Figures 4A,D** that the FWHM of the light ring is wide ($\Delta\omega_H = 0.416$ mm) while the distortion of the helical phase is almost invisible. The reason is that the vortex FWM field suffers a strong inherent absorption at the center of the light ring and a small total phase shift (including inherent and modal phase shifts) (**Figures 5A,D**). When the probe detuning is varied from −4 to 4 meV, the vortex FWM field suffers stronger inherent and modal absorption at the edges of the intensity pattern (see **Figure 5B**), and there are single peaks of inherent phase shift and double peaks of modal phase shift (**Figure 5E**). Therefore, the FWHM of the intensity pattern decreases to 0.196 mm (**Figure 4B**), and the helical phase twists in the clockwise direction (**Figure 4E**). More importantly, the twisted helical phase wave front is flat because of complementation between inherent and modal phase shifts. As the probe detuning increases to 8 meV, as shown in **Figures 4C,F**, **5C,F**, the FWHM of the intensity slightly increases to 0.264 mm due to the wider transparent window in modal absorption spectrum. Meanwhile, the helical phase twists anticlockwise because of the existence of a single valley of inherent phase shift and double valleys of modal phase shift. Therefore, one can conclude that the detuning of the probe field can manipulate the helical phase wave front of the generated FWM field in an effective manner.

We further investigate the dependence of the intensity and helical phase of the vortex FWM field on the detuning Δ_c of the coupling field in **Figures 6**, **7**. It can be seen from **Figure 6** that the intensity, width, and phase of the vortex FWM field are not very sensitive to the coupling detuning Δ_c. The results can be explained that the impact of the coupling detuning on the absorption and phase properties of the FWM field is weak. At the center of the light ring, the modal absorption remains unchanged and the inherent absorption decreases slowly with the increase of Δ_c (see blue lines in **Figure 7**), so we can find that the intensity of the vortex FWM field increases limitedly in **Figures 6A–C**. However, the FWHM of the intensity pattern is kept at 0.216 mm because of the strong inherent and modal absorption at the two edges of the intensity pattern. At the same time, the modal phase shift dominates in modulating the helical phase wave front of the FWM field (see red lines in **Figure 7**). As shown in **Figures 6D–F**, the near-identical double valleys of the modal phase shift result in almost the same double distortions for the helical phase wave front. Therefore, the generated vortex FWM field has good robustness on the detuning of the coupling field.

Now, we analyze the influence of the conventional LG beam and POV beam with higher order TC on the intensity and phase patterns of the vortex FWM field in **Figure 8**. In the former case, we select the traditional single-ring LG beam $\Omega_d = \Omega_{d0}\frac{1}{\sqrt{|l|!}}(\frac{\sqrt{2}r}{w_{LG}})^{|l|}L_p^{|l|}(\frac{2r^2}{w_{LG}^2})e^{-\frac{r^2}{w_{LG}^2}}e^{il\theta}$ with radial index $p = 0$ and TC $l = 3$ in Ref.[45] as the OAM driving field and plot the intensity and phase profiles of the FWM field in **Figures 8A,C**. Compared with the case shown in **Figures 2C,F**, we can find that both the intensity and ring radius of the FWM field greatly decrease (**Figure 8A**). In addition, the helical phase wave front also suffers double distortion at the two edges of the intensity pattern. However, the phase twist in the inner edge is much smaller than that in the outer edge (**Figure 8C**). In the latter case, a POV beam with TC $l = 6$ is treated as the OAM driving field. The intensity and phase profiles of the FWM field are plotted in **Figures 8B,D**, respectively. The direct comparison between **Figures 2C,F**, **8B,D** implies that the intensity patterns and phase distortions of the FWM field remain unchanged, except for the fact that the helical phase profile in **Figure 8D** displays six periods along the azimuthal direction.

We note that, very recently, some theoretical schemes for exploring the vortex FWM process in SQWs have been proposed [54, 55, 56]. In these schemes, SQWs were used to explore the transfer

and control of mid-infrared conventional LG beams [54, 55] and inner–outer ring LG beams [56]. In comparison with these schemes, the major differences in our proposal are the following: First, the main difference between our scheme and Refs. [54, 55, 56] is that we focus on the conversion and manipulation of the mid-infrared POV beam, while previous studies are focused on the control of the mid-infrared LG beams. Second, our scheme takes the advantages of the four-level ladder-type scheme [55] and tunneling-induced constructive interference [57, 58]. For example, resonant tunneling can effectively open the channel for the FWM process and modify the spatial distribution of the FWM field. Third, with the presence of resonant tunneling, both the intensity and phase patterns are insensitive to the detuning of the coupling field. The findings are quite different from the results obtained in Ref. [55], where the intensity pattern and phase distortion strongly depend on the detuning of the corresponding field.

Finally, we perform the coaxial interference between the vortex FWM field and a same-frequency POV beam $\Omega_G(r,\theta) = \Omega_{G0} i^{(m-1)} \frac{w_g}{w_0} e^{im\theta} e^{-(r-R)^2/(4w_0^2)}$ with the topological charge $m = 1$. The interference intensity and phase patterns are displayed in **Figure 9** for different TCs of the vortex FWM field. From **Figure 9**, one can find that the interference patterns are quite different from the case in **Figures 4C,F**. The interference intensity exhibits a double-ring pattern for $l = m = 1$ and a vortex petal-like pattern for $l \neq m = 1$ (**Figures 9A–C,G–I**). Specifically, as TC increases from $l = 1$ to $l = 3$, the number of petals in the intensity pattern increases from 0 to 2, and the rotating direction of petals is clockwise. However, the number of petals increases from 2 to 4 with TC increasing from $l = -1$ to $l = -3$, where the petal-like pattern is rotated in the anticlockwise direction. Meanwhile, the interference phase at the radial position $r = 2$ mm twists in the clockwise direction for $l = 1, 2, 3$ and in the opposite direction for $l = -1, -2, -3$, while the interference phase in the other region is the same as the helical phase of the POV beam Ω_G. From **Figure 9**, one can conclude that the number of intensity petals in the interference intensity spectrum equals to the value of $|l - m|$, and the rotating direction of intensity petals reflects the sign of $l - m$ (i.e., the clockwise and anticlockwise rotation of petals correspond to $l - m > 0$ and $l - m < 0$, respectively). Therefore, we can efficiently realize the measurement for the value and sign of TC of the generated vortex FWM field (i.e., the vortex driving field) *via* observing the interference intensity spectrum.

4 CONCLUSION

We mainly focus on the condition of low temperatures up to 10 K, and have neglected other many-body effects such as the depolarization effect, which renormalizes the free-carrier and carrier-field contributions. These contributions and their interplay have been investigated quite thoroughly in Ref. [60]. Note that due to the low electron sheet density considered here, these effects only give a negligible correction.

In conclusion, a scheme for transferring and manipulating POV in an asymmetric SDQW nanostructure is theoretically suggested. The OAM of a unique POV mode is completely transferred to the generated FWM field *via* a tunneling-induced highly efficient FWM process. It is demonstrated that resonant tunneling plays an important role in the manipulation of the intensity and phase distribution of the vortex FWM field. With the presence of resonant tunneling, the generated FWM field is closer to an ideal POV beam and exhibits an enhanced phase distortion at two edges of the intensity pattern. Furthermore, we find that the intensity and phase profiles of the vortex FWM field are sensitive to the detuning of the weak probe field but rather robust against the detuning of the strong coupling field. These results can be reasonably explained *via* the combination of inherent and modal dispersion relation. Subsequently, the coaxial interference between the vortex FWM field and a same-frequency POV beam is studied. It is found that the interference intensity and phase patterns are determined by TC of the vortex FWM field, which allows us to measure TC of the FWM field with POV. Our proposal may provide an avenue for the coherent control of POV and a possibility for the TC measurement of a POV beam.

DATA AVAILABILITY STATEMENT

The raw data supporting the conclusion of this article will be made available by the authors, without undue reservation.

AUTHOR CONTRIBUTIONS

The idea was first conceived by W-XY. XD was responsible for the physical model, numerical calculations, and writing most of the manuscript. TS contributed to writing the manuscript and verified the calculated results.

FUNDING

The National Natural Science Foundation of China (11774054, 12075036, 12104067); the Science and Technology Research Project of Education Department of Hubei Province (Q20211314).

ACKNOWLEDGMENTS

XD thanks Chun Meng, Yi Song, and Tong Zhang for helpful discussions.

REFERENCES

1. Arita Y, Chen M, Wright EM, Dholakia K. Dynamics of a Levitated Microparticle in Vacuum Trapped by a Perfect Vortex Beam: Three-Dimensional Motion Around a Complex Optical Potential. *J Opt Soc Am B* (2017) 34:C14–C19. doi:10.1364/josab.34.000c14
2. Liang Y, Lei M, Yan S, Li M, Cai Y, Wang Z, et al. Rotating of Low-Refractive-index Microparticles with a Quasi-Perfect Optical Vortex. *Appl Opt* (2018) 57: 79–84. doi:10.1364/AO.57.000079
3. Yan H, Zhang E, Zhao B, Duan K. Free-space Propagation of Guided Optical Vortices Excited in an Annular Core Fiber. *Opt Express* (2012) 20:17904–15. doi:10.1364/OE.20.017904
4. Li S, Wang J. Multi-orbital-angular-momentum Multi-Ring Fiber for High-Density Space-Division Multiplexing. *IEEE Photon J* (2013) 5:7101007. doi:10.1109/jphot.2013.2272778
5. Leach J, Jack B, Romero J, Jha A, Yao A, Franke-Arnold S, et al. Quantum Correlations in Optical Angle-Orbital Angular Momentum Variables. *Science* (2010) 329:662–5. doi:10.1126/science.1190523
6. Fickler R, Lapkiewicz R, Plick W, Krenn M, Schaeff C, Ramelow S, et al. Quantum Entanglement of High Angular Momenta. *Science* (2012) 338:640–3. doi:10.1126/science.1227193
7. Ding D, Zhou Z, Shi B, Guo G. Single-photon-level Quantum Image Memory Based on Cold Atomic Ensembles. *Nat Commun* (2013) 4:2527. doi:10.1038/ncomms3527
8. Nicolas A, Veissier L, Giner L, Giacobino E, Maxein D, Laurat J. Quantum Memory for Orbital Angular Momentum Photonic Qubits. *Nat Photon* (2014) 8:234–8. doi:10.1038/nphoton.2013.355
9. Parigi V, D'Ambrosio V, Arnold C, Marrucci L, Sciarrino F, Laurat J. Storage and Retrieval of Vector Beams of Light in a Multiple-Degree-Of-freedom Quantum Memory. *Nat Commun* (2015) 6:706. doi:10.1038/ncomms8706
10. Wang X, Luo Y, Huang H, Chen M, Su Z, Liu C, et al. 18-qubit Entanglement with Six Photons' Three Degrees of freedom. *Phys Rev Lett* (2018) 120:260502. doi:10.1103/PhysRevLett.120.260502
11. Luo Y, Zhong H, Erhard M, Wang X, Peng L, Krenn M, et al. Quantum Teleportation in High Dimensions. *Phys Rev Lett* (2019) 123:070505. doi:10.1103/PhysRevLett.123.070505
12. Pan X, Yu S, Zhou Y, Zhang K, Zhang K, Lv S, et al. Orbital-angular-momentum Multiplexed Continuous-Variable Entanglement from Four-Wave Mixing in Hot Atomic Vapor. *Phys Rev Lett* (2019) 123:070506. doi:10.1103/PhysRevLett.123.070506
13. Zhang S, Zhou Y, Mei Y, Liao K, Wen Y, Li J, et al. δ-Quench Measurement of a Pure Quantum-State Wave Function. *Phys Rev Lett* (2019) 123:190402. doi:10.1103/PhysRevLett.123.190402
14. Li S, Pan X, Ren Y, Liu H, Yu S, Jing J. Deterministic Generation of Orbital-Angular-Momentum Multiplexed Tripartite Entanglement. *Phys Rev Lett* (2020) 124:083605. doi:10.1103/PhysRevLett.124.083605
15. Zhang K, Wang W, Liu S, Pan X, Du J, Lou Y, et al. Reconfigurable Hexapartite Entanglement by Spatially Multiplexed Four-Wave Mixing Processes. *Phys Rev Lett* (2020) 124:090501. doi:10.1103/PhysRevLett.124.090501
16. Liu S, Lou Y, Jing J. Orbital Angular Momentum Multiplexed Deterministic All-Optical Quantum Teleportation. *Nat Commun* (2020) 11:3875. doi:10.1038/s41467-020-17616-4
17. Allen L, Beijersbergen MW, Spreeuw RJC, Woerdman JP. Orbital Angular Momentum of Light and the Transformation of Laguerre-Gaussian Laser Modes. *Phys Rev A* (1992) 45:8185–9. doi:10.1103/physreva.45.8185
18. Padgett M, Courtial J, Allen L. Light's Orbital Angular Momentum. *Phys Today* (2004) 57:35–40. doi:10.1063/1.1768672
19. Molina-Terriza G, Torres J, Torner L. Twisted Photons. *Nat Phys* (2007) 3: 305–10. doi:10.1038/nphys607
20. Allen L, Padgett MJ, Babiker M. Iv the Orbital Angular Momentum of Light. *Prog Opt* (1999) 39:291–372. doi:10.1016/S0079-6638(08)70391-3
21. Gori F, Guattari G, Padovani C. Bessel-gauss Beams. *Opt Commun* (1987) 64: 491–5. doi:10.1016/0030-4018(87)90276-8
22. Sepulveda K, Chávez V, Cerda S, Arlt J, Dholakia K. Orbital Angular Momentum of a High-Order Bessel Light Beam. *J Opt B Quan Semiclass. Opt* (2002) 4:S82. doi:10.1088/1464-4266/4/2/373
23. Ostrovsky A, Rickenstorff-Parrao C, Arrizón V. Generation of the "Perfect" Optical Vortex Using a Liquid-crystal Spatial Light Modulator. *Opt Lett* (2013) 38:534–6. doi:10.1364/OL.38.000534
24. Kotlyar V, Kovalev A, Porfirev A. Optimal Phase Element for Generating a Perfect Optical Vortex. *J Opt Soc Am* (2016) 33:2376–84. doi:10.1364/JOSAA.33.002376
25. Karahroudi M, Parmoon B, Qasemi M, Mobashery A, Saghafifar H. Generation of Perfect Optical Vortices Using a Bessel-Gaussian Beam Diffracted by Curved fork Grating. *Appl Opt* (2017) 56:5817–23. doi:10.1364/AO.56.005817
26. Jabir M, Chaitanya NA, Aadhi A, Samanta G. Generation of "Perfect" Vortex of Variable Size and its Effect in Angular Spectrum of the Down-Converted Photons. *Sci Rep* (2016) 6:21977. doi:10.1038/srep21877
27. Garcia-Garcia J, Rickenstorff-Parrao C, Ramos-Garcia R, Arrizon V, Ostrovsky A. Simple Technique for Generating the Perfect Optical Vortex. *Opt Lett* (2014) 39:5305–8. doi:10.1364/OL.39.005305
28. Vaity P, Rusch L. Perfect Vortex Beam: Fourier Transformation of a Bessel Beam. *Opt Lett* (2015) 40:597–600. doi:10.1364/OL.40.000597
29. Du Y, Liu D, Fu S, Wang Y, Qin Y. Reconfigurable Generation of Double-Ring Perfect Vortex Beam. *Opt Express* (2021) 29:17353–64. doi:10.1364/OE.424664
30. Guo Z, Liu H, Xiang L, Chen L, Yang J, Wen J, et al. Generation of Perfect V Ortex Beams with Polymer-Based Phase Plate. *IEEE Photon Technol Lett* (2020) 32:565–8. doi:10.1109/LPT.2020.2985745
31. Dai K, Miller J, Li W, Watkins R, Johnson E. Fractional Orbital Angular Momentum Conversion in Second-Harmonic Generation with an Asymmetric Perfect Vortex Beam. *Opt Lett* (2021) 46:3332–5. doi:10.1364/OL.428859
32. Zhou Q, Liu M, Zhu W, Chen L, Ren Y, Lezec H, et al. Generation of Perfect Vortex Beams by Dielectric Geometric Metasurface for Visible Light. *Laser Photon Rev* (2021) 15:2100390. doi:10.1002/lpor.202100390
33. Ma H, Li X, Tai Y, Li H, Wang J, Tang M, et al. *In Situ* measurement of the Topological Charge of a Perfect Vortex Using the Phase Shift Method. *Opt Lett* (2017) 42:135–8. doi:10.1364/OL.42.000135
34. Pinnell J, Rodríguez-Fajardo V, Forbes A. Quantitative Orbital Angular Momentum Measurement of Perfect Vortex Beams. *Opt Lett* (2019) 44: 2736–9. doi:10.1364/ol.44.002736
35. Chu C, Gao S, Liu Z, Tu J, Yang J, Hao C, et al. Hybrid Angular Gradient Phase Grating for Measuring the Orbital Angular Momentum of Perfect Optical Vortex Beams. *IEEE Photon J* (2020) 12:1. doi:10.1109/jphot.2020.2986266
36. Jiang X, Li J, Sun X. Two-dimensional Atom Localization Based on Coherent Field Controlling in a Five-Level M-type Atomic System. *Opt Express* (2017) 25:31678–87. doi:10.1364/OE.25.031678
37. Tian Y, Wang X, Yang W, Shui T, Li L, Li X, et al. High-precision Three Dimensional Atom Localization via Multiphoton Quantum Destructive Interference. *Opt Express* (2020) 28:25308–18. doi:10.1364/OE.396973
38. Zhou F, Qi Y, Sun H, Chen D, Yang J, Niu Y, et al. Electromagnetically Induced Grating in Asymmetric Quantum wells via Fano Interference. *Opt Express* (2013) 21:12249–59. doi:10.1364/oe.21.012249
39. Che J, Zhao P, Ma D, Zhang Y. Kerr-nonlinearity-modulated Dressed Vortex Four-Wave Mixing from Photonic Band gap. *Opt Express* (2020) 28:18343–50. doi:10.1364/oe.395426
40. Radwell N, Clark T, Piccirillo B, Barnett S, Franke-Arnold S. Spatially Dependent Electromagnetically Induced Transparency. *Phys Rev Lett* (2015) 114:123603. doi:10.1103/PhysRevLett.114.123603
41. Han L, Cao M, Liu R, Liu H, Guo W, Wei D, et al. Identifying the Orbital Angular Momentum of Light Based on Atomic Ensembles. *EPL* (2012) 99: 34003. doi:10.1209/0295-5075/99/34003
42. Wang L, Zhang X, Li A, Kang Z, Wang H, Gao J. Controlled-Not Gate with Orbital Angular Momentum in a Rare-Earth-Ion-Doped Solid. *J Lumin* (2020) 228:117628. doi:10.1016/j.jlumin.2020.117628
43. Hamedi H, Yannopapas V, Paspalakis E. Spatially Structured Optical Effects in a Four-Level Quantum System Near a Plasmonic Nanostructure. *Ann Phys* (2021) 533:2100117. doi:10.1002/andp.202100117
44. Rahmatullah, Abbas M, Ziauddin, Qamar S. Spatially Structured Transparency and Transfer of Optical Vortices via Four-Wave Mixing in a Quantum-Dot Nanostructure. *Phys Rev A* (2020) 101:023821. doi:10.1103/PhysRevA.101.023821

45. Mahdavi M, Sabegh Z, Hamedi H, Mahmoudi M. Orbital Angular Momentum Transfer in Molecular Magnets. *Phys Rev B* (2021) 104:094432. doi:10.1103/PhysRevB.104.094432
46. Hamedi H, Kudriasov V, Ruseckas J, Juzeliunas G. Azimuthal Modulation of Electromagnetically Induced Transparency Using Structured Light. *Opt Express* (2018) 26:28249–62. doi:10.1364/OE.26.028249
47. Dai X, Hao X, Jin R, Peng C, Ding C. Controllable Probe Absorption Spectrum via Vortex Beams Excitation in a Cascaded Atomic System. *J Appl Phys* (2021) 129:224303. doi:10.1063/5.0050488
48. Jia N, Qian J, Kirova T, Juzeliunas G, Hamedi H. Ultraprecise Rydberg Atomic Localization Using Optical Vortices. *Opt Express* (2020) 28:36936–52. doi:10.1364/OE.411130
49. Yu C, Wang Z. Engineering Helical Phase via Four-Wave Mixing in the Ultraslow Propagation Regime. *Phys Rev A* (2021) 103:013518. doi:10.1103/PhysRevA.103.013518
50. Qiu J, Wang Z, Ding D, Huang Z, Yu B. Control of Space-dependent Four-Wave Mixing in a Four-Level Atomic System. *Phys Rev A* (2020) 102:033516. doi:10.1103/PhysRevA.102.033516
51. Hamedi H, Ruseckas J, Juzeliūnas G. Exchange of Optical Vortices Using an Electromagnetically-Induced-Transparency–Based Four-Wave-Mixing Setup. *Phys Rev A* (2018) 98:013840. $\\bar{\\mathrm{u}}$. doi:10.1103/physreva.98.013840
52. Hong Y, Wang Z, Ding D, Yu B. Ultraslow Vortex Four-Wave Mixing via Multiphoton Quantum Interference. *Opt Express* (2019) 27:29863–74. doi:10.1364/OE.27.029863
53. Chen J, Wang Z, Yu B. Spatially Dependent Hyper-Raman Scattering in Five-Level Cold Atoms. *Opt Express* (2021) 29:10914–22. doi:10.1364/oe.420015
54. Qiu J, Wang Z, Ding D, Li W, Yu B. Highly Efficient Vortex Four-Wave Mixing in Asymmetric Semiconductor Quantum wells. *Opt Express* (2020) 28:2975–86. doi:10.1364/OE.379245
55. Zhang Y, Wang Z, Qiu J, Hong Y, Yu B. Spatially Dependent Four-Wave Mixing in Semiconductor Quantum wells. *Appl Phys Lett* (2019) 115:171905. doi:10.1063/1.5121275
56. Wang Z, Zhang Y, Paspalakis E, Yu B. Efficient Spatiotemporal-Vortex Four-Wave Mixing in a Semiconductor Nanostructure. *Phys Rev A* (2020) 102:063509. doi:10.1103/PhysRevA.102.063509
57. Sun H, Fan S, Zhang H, Gong S. Tunneling-induced High-Efficiency Four-Wave Mixing in Asymmetric Quantum wells. *Phys Rev B* (2013) 87:235310. doi:10.1103/PhysRevB.87.235310
58. Sun D, Zhang H, Sun H, Li X, Li H. Tunneling-induced Highly Efficient Four-Wave Mixing in Asymmetric Double Quantum wells. *Laser Phys Lett* (2018) 15:045208. doi:10.1088/1612-202X/aaa9c8
59. Schmidt H, Campman K, Gossard A, Imamolu A. Tunneling Induced Transparency: Fano Interference in Intersubband Transitions. *Appl Phys Lett* (1997) 70:3455–7. doi:10.1063/1.119199
60. Shih T, Reimann K, Woerner M, Elsaesser T, Waldmüller I, Knorr A, et al. Nonlinear Response of Radiatively Coupled Intersubband Transitions of Quasi-Two-Dimensional Electrons. *Phys Rev B* (2005) 72:195338. doi:10.1103/physrevb.72.195338

Conflict of Interest: The authors declare that the research was conducted in the absence of any commercial or financial relationships that could be construed as a potential conflict of interest.

frontiers | Frontiers in Physics

ORIGINAL RESEARCH
published: 27 April 2022
doi: 10.3389/fphy.2022.892542

Electric Field Tuned Dipolar Interaction Between Rydberg Atoms

Yuechun Jiao[1,2], Jingxu Bai[1], Rong Song[1], Shanxia Bao[3], Jianming Zhao[1,2]* and Suotang Jia[1,2]*

[1]State Key Laboratory of Quantum Optics and Quantum Optics Devices, Institute of Laser Spectroscopy, Shanxi University, Taiyuan, China, [2]Collaborative Innovation Center of Extreme Optics, Shanxi University, Taiyuan, China, [3]Department of Physics, Institute of Theoretical Physics, Shanxi Datong University, Datong, China

We demonstrated a tuned dipole interaction between Rydberg atoms by employing a controllable electric field in a cold cesium ensemble. The $|nP_{3/2}\rangle$ (n = 38–40) Rydberg pairs are prepared with a three-photon scheme and detected *via* the state-selective field ionization technique. A weak DC electric field is used to tune the Rydberg pair interaction from the van der Waals interaction regime to the dipole–dipole interaction regime. The Förster resonant interaction and an adiabatic resonance energy transfer between the nP and nS Rydberg states are attained by precisely tuning the electric field. Rydberg excitation blockade with and without the electric field is investigated by changing the excitation pulse duration, which demonstrates that the dipole interaction–induced blockade effect is stronger than the van der Waals interaction–induced blockade effect. The precise control of the Rydberg interaction is of great significance to the coherent interaction in many-body systems and non-radiative collision processes.

Keywords: Rydberg atoms, dipolar interactions, resonance energy transfer, Stark effect, blockade

OPEN ACCESS

Edited by:
Weibin Li,
University of Nottingham,
United Kingdom

Reviewed by:
Xiao-Feng Shi,
Xidian University, China
Jie Song,
Harbin Institute of Technology, China

****Correspondence:***
Yuechun Jiao
ycjiao@sxu.edu.cn
Jianming Zhao
zhaojm@sxu.edu.cn

Specialty section:
This article was submitted to Quantum Engineering and Technology, a section of the journal Frontiers in Physics

Received: *09 March 2022*
Accepted: *30 March 2022*
Published: *27 April 2022*

Citation:
Jiao Y, Bai J, Song R, Bao S, Zhao J and Jia S (2022) Electric Field Tuned Dipolar Interaction Between Rydberg Atoms. Front. Phys. 10:892542. doi: 10.3389/fphy.2022.892542

1 INTRODUCTION

Rydberg atom, one electron placed in a highly energetic excited state is a kind of exotic atom that has attracted more and more attention in atomic and molecular physics in recent years. A Rydberg atom has a huge orbital radius ($\propto n^2$, n is the principal quantum number), a large polarizability ($\propto n^7$), a strong interaction between Rydberg atoms ($\propto n^{11}$) [1], and so on. Due to these properties, the Rydberg atom is very popular both for investigation of the blockade effect and single photon source [2,3] and single photon transistor [4] and for the microwave field measurement and the field sensor [5–10].

In addition, Rydberg levels can be tuned by the external field to the Förster resonant regime, where the Rydberg atoms display strong dipole–dipole interaction and dipole blockade [11,12]. At the Förster resonance, the non-radiative redistribution of the electronic state between two particles coupled by the dipole–dipole interaction is of great importance for a variety of phenomena. For the Rydberg pair state, the initial prepared Rydberg atom can adiabatically transfer to a nearby state without a change in the kinetic energy, which is called the resonance energy transfer (RET). The dipole interaction and the RET play a very important role in atomic and molecular dynamics and multi-body interactions [13]. This kind of resonant interaction has been studied extensively, for example, the strong interaction between Rydberg atoms under an electric field [14–17], the exploration, and analysis of the multi-body [13] and the few-body interaction [18,19], an optical nonlinearity in cold atom systems [20], and an atomic interference [21]. In recent years, the resonant

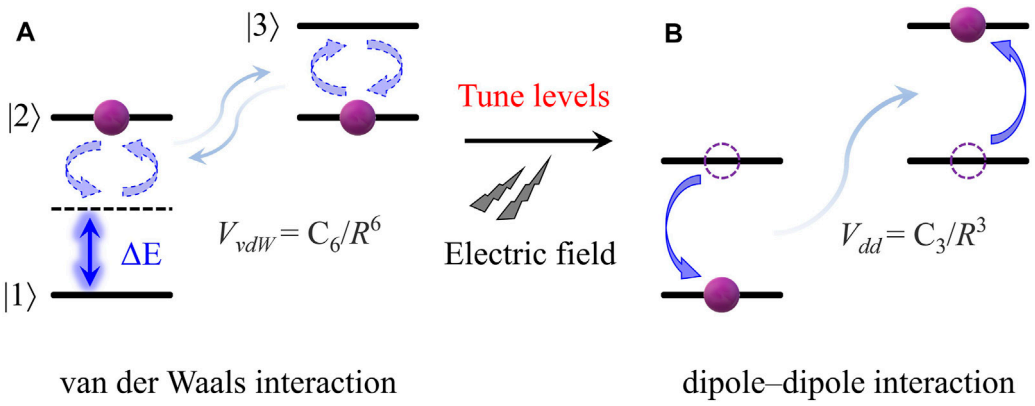

FIGURE 1 | (color online). **(A)** Scheme of the van der Waals interaction between Rydberg atomic pairs. Two atoms initially prepared in the same Rydberg state $|2\rangle$, $|1\rangle$, and $|3\rangle$ are the dipole allowed near states. ΔE indicates the energy defect between $|3\rangle - |2\rangle$ and $|2\rangle - |1\rangle$. For the case of $\Delta E \neq 0$, the Rydberg pair displays the van der Waals interaction, which scales as R^{-6}. **(B)** Scheme of the dipole–dipole interaction. The weak DC electric field is used to tune the Rydberg level to the Förster resonance. For the case of $\Delta E = 0$, the Rydberg pair displays the dipole–dipole interaction, which scales as R^{-3}.

dipole interaction between neutral pairs of atoms, particularly the dipole interaction between Rydberg atoms, has been used to investigate quantum gates [22–24], quantum simulation, and computing [25,26].

In this work, we prepared the $|nP_{3/2}\rangle$ ($n = 38$–40) Rydberg pair with the three-photon scheme in the cold cesium atoms. A weak DC electric field is used to tune the Rydberg pair interaction from the van der Waals interaction regime to the dipole–dipole interaction regime. At the Förster resonance, we achieved an adiabatic resonance energy transfer between the nP and nS Rydberg states by means of controlling the dipolar interaction tuned by an electric field. Rydberg excitation with and without the DC field and the blockade effect are investigated by changing the excitation pulse duration, which demonstrates that the dipole interaction–induced blockade effect is stronger than the van der Waals interaction–induced blockade effect.

2 INTERACTIONS BETWEEN RYDBERG ATOMS

As mentioned earlier, the Rydberg atom has a strong long-range interaction and a large dipole transition matrix element because of its huge polarizability. Considering a pair of Rydberg atoms, the Hamiltonian can be expressed as,

$$H = H_0 + \hat{V}_{int}, \tag{1}$$

where, $H_0 = H_A + H_B$ is the Hamiltonian of the bare atoms A and B, $\hat{V}_{int}$ is the interaction potential between atoms. The interaction potential can be written as a Laurent series with the atomic distance R,

$$\hat{V}_{int} = -\sum_{n=1}^{\infty} \frac{C_n}{R^n}, \tag{2}$$

with C_n as the dispersion coefficient. We assumed that two atoms are initially in the same Rydberg state $|2\rangle$, as shown in **Figure 1A**. The state $|2\rangle$ can transition to the state $|1\rangle$ ($|3\rangle$) by emitting (absorbing) a photon. The energy level is E_i ($i = 1,2,3$), and the energy defect of the atomic pair is defined as $\Delta E = 2E_2 - (E_1 + E_3)$. We take the pair state of $\{|2\rangle|2\rangle\}$ ($|nP\rangle|nP\rangle$) and $\{|1\rangle|3\rangle\}$ ($|nS\rangle|n'S\rangle$) as our basis vectors and further diagonalize the Hamiltonian to obtain the eigen energy,

$$E_{\pm} = -\frac{\Delta E}{2} \pm \sqrt{\left(\frac{\Delta E}{2}\right) + \left(\frac{\vec{\mu}_1 \cdot \vec{\mu}_2}{R^3}\right)^2}, \tag{3}$$

where $\vec{\mu}_1$ ($\vec{\mu}_2$) represents the transition dipole moment of $|2\rangle \rightarrow |1\rangle$ ($|2\rangle \rightarrow |3\rangle$). Usually, 1) when $|\Delta E| \gg |\mu_1\mu_2/R^3|$, the Rydberg pair mainly displays the van der Waals interaction, and the related interaction potential is $V_{vdW} = C_6/R^6$ ($C_6 \sim n^{11}$)(**Figure 1A**). 2) When $|\Delta E| \ll |\mu_1\mu_2/R^3|$, the Rydberg pair shows the strong dipole–dipole interaction, and the interaction potential is $V_{dd} = C_3/R^3$ (**Figure 1B**). For $|38P_{3/2}, m_j = 3/2\ (1/2)\rangle$ state used in this work, the calculated $C_3 = 0.56\ (0.37)$ GHz $\cdot\ \mu m^3$ and the mean of C_6 in all directions are $1.62\ (1.40)$ GHz $\cdot\ \mu m^3$, respectively. Both the van der Waals and the dipole–dipole interaction of Rydberg atoms can block further excitation of the nearby atom, resulting in the blockade effect. Under the condition of $\Delta E = 0$ ($E_3 - E_2 = E_2 - E_1$), one initial atom in $|2\rangle$ state can transfer to $|3\rangle$ state by absorbing a photon that is emitted by the $|2\rangle \rightarrow |1\rangle$ transition of the other atom, which is called the resonance energy transfer (RET).

In view of Rydberg wave functions and parity conservation, the selection rules of $\Delta l = \pm 1$ (l, the orbital quantum number) and $\Delta m_j = 0, \pm 1$ (m_j, the total angular momentum quantum number) for the electric dipole moment operator are considered. For a cesium atom in this work, we chose the initial $|nP_{3/2}\rangle$ state excited by the three-photon excitation; the form of resonance energy transfer is usually expressed as

$$nP_{3/2} + nP_{3/2} \rightarrow nS_{1/2} + (n+1)S_{1/2}. \tag{4}$$

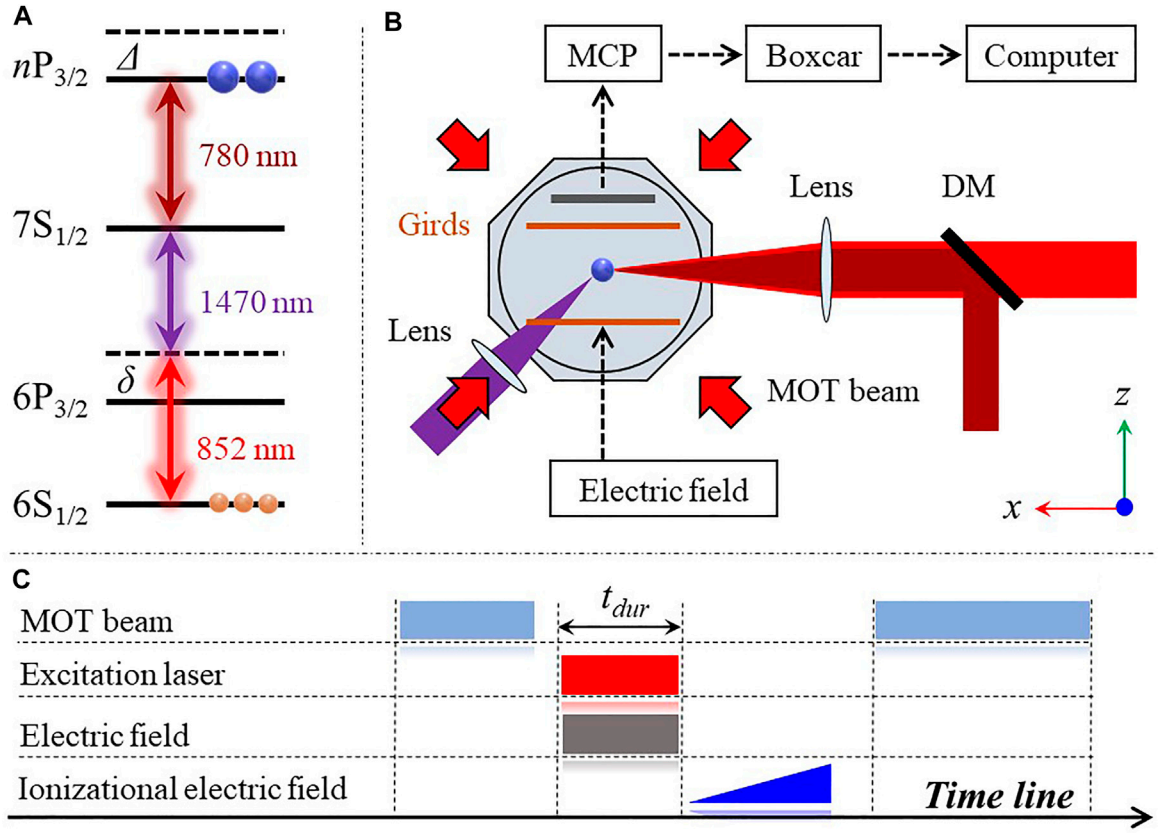

FIGURE 2 | (color online). **(A)** Three-photon excitation diagram of the Rydberg state. The first photon from the 852 nm (red) laser drives the lower transition $|6S_{1/2}\rangle \rightarrow |6P_{3/2}\rangle$, whose frequency is blue detuned δ from the intermediate state. The second photon, 1,470-nm (dark purple) laser couples the intermediate transition of $|6P_{3/2}\rangle \rightarrow |7S_{1/2}\rangle$. The third photon, 780-nm (dark red) laser achieves the Rydberg state *via* the up transition $|7S_{1/2}\rangle \rightarrow |nP_{3/2}\rangle$. Yellow and blue balls represent the ground and Rydberg state atoms, respectively. **(B)** Schematic diagram of the experiment. Three excitation lasers cross through the MOT center. The ions of Rydberg atoms are detected with a MCP detector, analyzed with a boxcar, and recorded by a computer. The ramp (DC) electric field is applied to the grids located in the *z* direction for the field ionization (the manipulation of the Rydberg interaction). Other grids in *x* – and *y* – directions are not shown here. **(C)** Timing sequence. After switching off the MOT beam, the Rydberg excitation pulse with duration of 6 μs is switched on for preparing Rydberg atoms. During the Rydberg excitation, a weak DC electric field is applied to tune the interaction between Rydberg atoms. After the Rydberg excitation, a ramp electric field is applied that is used to selectively ionize the Rydberg atoms. DM: dichroic mirror.

Based on the Stark shift and splitting of the Rydberg state, we tuned the Rydberg level by applying the external DC electric field to obtain $\Delta E = 0$ and the RET condition. Following Zimmerman's method [27], we numerically resolved the radial equation of the cesium atom and obtained the Stark map of the cesium Rydberg atom. From the Stark map, we extracted the Stark shift of $|nS_{1/2}\rangle$ and $|nP_{3/2}\rangle$ levels and obtained the energy defect of the Rydberg pair and, further, the Förster resonant electric field. For details, refer **Section 4**.

3 EXPERIMENT SCHEME AND SETUP

Our experiment is performed in a standard magneto-optical trap (MOT), where a cold cloud of Cs atoms is trapped in the center of a metal MOT with a density of 10^{10} cm^{-3}. The $|nP_{3/2}\rangle$ Rydberg state is excited by the three-photon excitation scheme. The experimental setup and three-photon excitation are displayed in **Figure 2**. Three photons at 852 nm, 1,470 nm and 780 nm lasers are used to realize the Rydberg transition of $|6S_{1/2}\rangle \rightarrow |6P_{3/2}\rangle \rightarrow |7S_{1/2}\rangle \rightarrow |nP_{3/2}\rangle$. The first photon couples the lower transition of $|6S_{1/2}(F = 4)\rangle \rightarrow |6P_{3/2}(F' = 5)\rangle$ with the detuning of $\delta = +110$ MHz and the Rabi frequency of $\Omega_{852} = 2\pi \times 45$ MHz; the second photon drives the intermediate transition of $|6P_{3/2}(F' = 5)\rangle \rightarrow |7S_{1/2}(F'' = 4)\rangle$ with the Rabi frequency of $\Omega_{1470} = 2\pi \times 80$ MHz, while the third photon achieves the Rydberg transition of $|7S_{1/2}\rangle \rightarrow |nP_{3/2}\rangle$ with the Rabi frequency of $\Omega_{780} = 2\pi \times 10$ MHz.

The experimental setup is shown in **Figure 2B**. Cesium atoms are trapped in the center of a metal MOT *via* the laser cooling and trap technique. The MOT density is measured with the shadow image. The first photon, 852 nm, and the third photon, 780 nm, lasers with a waist of ~ 80 μm are co-propagated through the MOT center along the *x*-axis after being combined by a dichroic mirror (DM), whereas, the second photon 1,470 nm lasers with a beam waist of 800 μm is crossed with the first photon laser at the

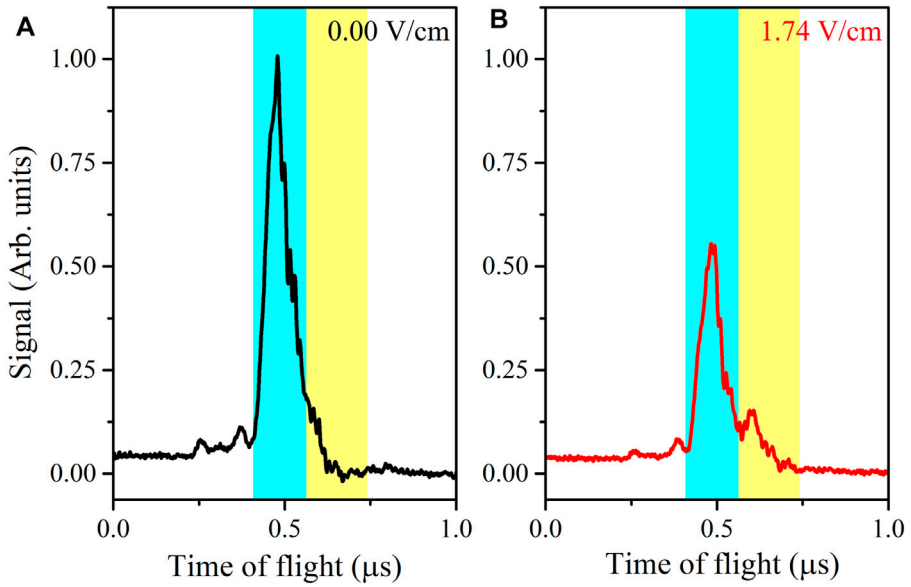

FIGURE 3 | (color online). Time of flight spectrum of the $|38P_{3/2}\rangle$ state with a DC field of 0 V/cm **(A)** and 1.74 V/cm **(B)**. The blue and yellow shadows mark the positions of the $|38P_{3/2}\rangle$ and $|38S_{1/2}\rangle$ states, respectively. The initial $|38P_{3/2}\rangle$ atoms transfer to $|38S_{1/2}\rangle$ due to the Förster resonant dipole interaction within the electric field of 1.74 V/cm.

center of the atom cloud, forming the cylindrical excitation region. Three pairs of girds (only one pair of grid is shown in **Figure 2**) are placed on either side of the MOT along three directions, which are used to apply the electric field for the state-selective field ionization of Rydberg atoms and compensate for the stray electric field. The resultant Rydberg ions are accelerated to the microchannel plate (MCP) detector. The Rydberg signal the MCP detects is analyzed with a boxcar and recorded with a computer.

The experiment is performed within 100 μs, during which the cooling light is turned off, see the timing sequence of **Figure 2C**. During the Rydberg excitation, we apply a weak DC electric field to tune the Rydberg level and further the interaction between Rydberg atoms. After the Rydberg excitation, we apply a ramp electric field for the state selective field, ionizing the initial prepared Rydberg atoms and the production due to the RET process.

4 EXPERIMENTAL RESULTS

In the experiment, we used the three-photon scheme to excite the $|nP_{3/2}\rangle$ Rydberg state; refer **Figure 2A**. The frequencies of the first (852 nm) and the second (1,470 nm) lasers are locked with a method of a saturated absorption spectrum (SAS) and an optical-optical double-resonance spectrum (OODRS), respectively. The frequency of the third (780 nm) laser is scanned at a speed of 4 mHz. In **Figure 3**, we present the time of flight (TOF) spectra of the $|38P_{3/2}\rangle$ state without (**Figure 3A**) and with (**Figure 3B**) an electric field of 1.74 V/cm. The peak at 0.5 μs comes from the initially excited $|38P_{3/2}\rangle$ state, which is marked with the blue gate. In **Figure 3B**, we clearly observed that the small peak appears at later time, marked with the yellow gate, which mainly comes from the $|38S_{1/2}\rangle$ state. The $|38S_{1/2}\rangle$ state is produced due to the RET process as the $|38S_{1/2}\rangle$ state can only be populated at an external field of ~ 1.74 V/cm, where the energy defect is $\Delta E \approx 0$. It should be noted that $|39S_{1/2}\rangle$ would accompany the $|38S_{1/2}\rangle$ state during the RET process and appear before the blue gate. However, in **Figure 3B**, we can see the variation of the front wing of the TOF spectrum but not a clear $|39S_{1/2}\rangle$ signal due to our ramp electric field with a fast ramp time. In addition, it is also seen that in the presence of the electric field, the signal of the $|38P_{3/2}\rangle$ state in the blue gate is about 50% of the field free signal; we attribute the decrease of the signal of the $|38P_{3/2}\rangle$ state to the dipole blockade effect due to the strong dipole interaction at the Förster resonance. It is noted that the small peaks before the blue gate may be attributed to auto-ionization during the Rydberg excitation and the high angular momentum Rydberg states, which are beyond the scope of this work.

To better understand the RET process and qualitative analysis of the observed signals, in **Figure 4A**, we present the Stark map near n = 34, 35 manifolds including $|38P_{3/2}\rangle$, $|38S_{1/2}\rangle$, $|39S_{1/2}\rangle$ states for $|m_j| = 1/2$ (red solid line) and 3/2 (blue solid line). The vertical dashed lines mark the Förster resonance electric fields, 1.60 V/cm for $m_j = 1/2$ and 1.74 V/cm for $m_j = 3/2$, where the energy defect $\Delta E \simeq 0$. Therefore, although the dipole interaction can couple $|38P_{3/2}\rangle$ to a bunch of states, the Förster resonance process occurs only for the specific pair of states under the specific electric field value. The signal of $|38S_{1/2}\rangle$ in the yellow gate of **Figure 3B** is generated from the $|38P_{3/2}\rangle$ Förster resonant transfer. We conducted a series of measurements and recorded the $|38S_{1/2}\rangle$ signal in the yellow gate by changing the frequency of the 780 nm laser and DC electric fields. In **Figure 4B**, we present a contour plot of the $|38S_{1/2}\rangle$ state transferred from $|38P_{3/2}\rangle$ as a

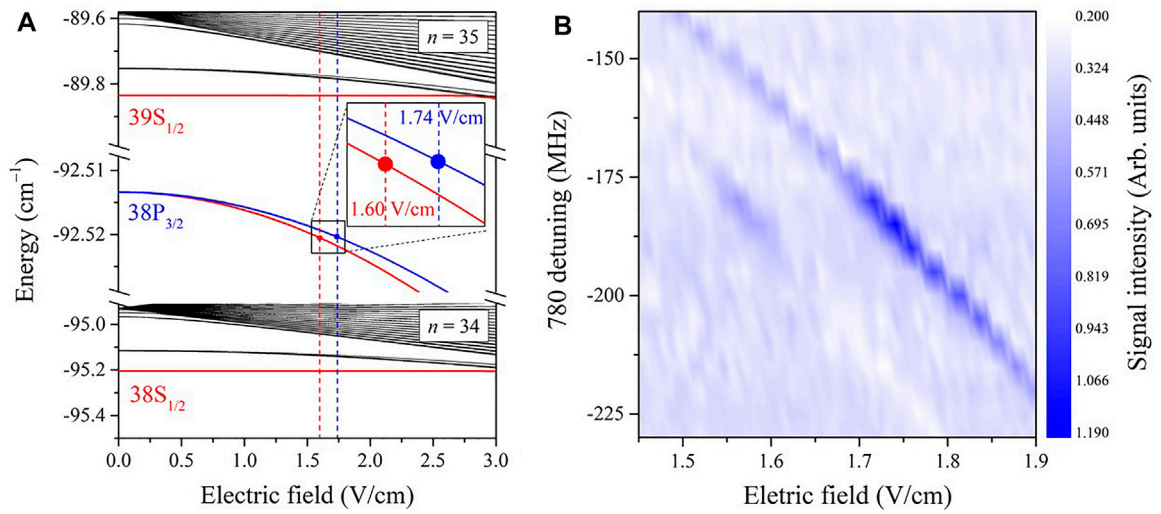

FIGURE 4 | (color online). **(A)** Calculations of the Stark map near n = 34 and 35 manifolds. In the electric field, the $|38P_{3/2}\rangle$ state shifts and splits into two Stark lines, forming two Förster resonant points at the electric field 1.60 V/cm and 1.74 V/cm, respectively, as shown with the black square. The inset shows the enlargement of the square marked region. **(B)** Contour plot of the $|38S_{1/2}\rangle$ state transferred from the initial $|38P_{3/2}\rangle$ state as a function of the DC electric field and the 780-nm laser detuning Δ_{780}. The signal of the $|38S_{1/2}\rangle$ state can be observed at the electric fields of 1.58 ± 0.01 V/cm and 1.74 ± 0.01 V/cm, respectively.

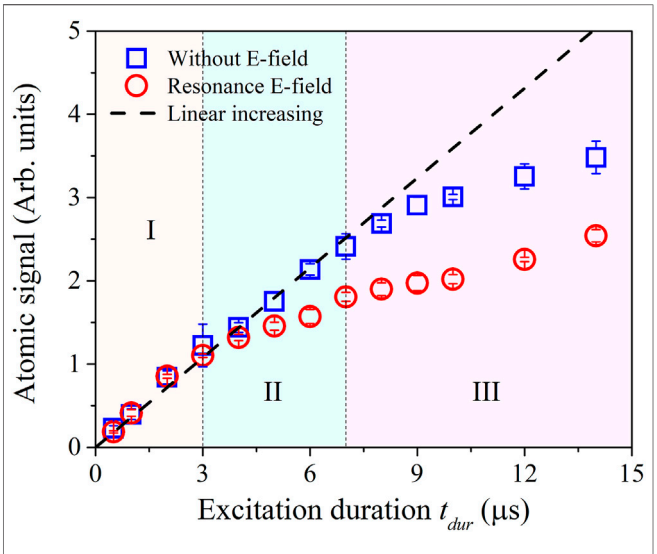

FIGURE 5 | (color online). Measured field ionization signal of $|40P_{3/2}\rangle$ Rydberg state as a function of the excitation duration with (red circles) and without (blue squares) the DC electric field. The black dashed line displays the linear increasing with the excitation duration without any blockade effect. It is seen that blockade behavior is stronger due to the dipole interaction than that due to the van der Waals interaction.

function of the DC electric field and the 780 nm laser detuning Δ_{780}. It is shown that the $|38S_{1/2}\rangle$ signal is very small and reaches maximum only at the field of ~ 1.58 ± 0.01 V/cm and 1.74 ± 0.01 V/cm, showing good agreement with the calculations with a deviation of less than 2%.

As mentioned earlier, the strong interaction between Rydberg atoms can block further excitation of nearby atoms. In the following experiment, we will investigate the blockade effect with and without the electric field. The blockade effect is attained by varying the laser power [11,28] or the excitation pulse duration. In contrast to the previous literature, we changed the duration of the excitation pulse in this work. To observe the blockade effect, we recorded all the signals, including the signals in the blue and yellow gates. In **Figure 5**, we present the measured Rydberg ions of the $|40P_{3/2}\rangle$ state as a function of the excitation pulse duration with (red circles) and without (blue squares) the DC electric field. The dashed line displays the Rydberg signal that linearly increases with the excitation duration without any blockade effect.

Close inspection of **Figure 5** reveals that the Rydberg excitation process can be divided into three regions. I) The first linear region for the excitation duration $t_{dur} < 3\mu s$, where the excited Rydberg signals are almost same and lie in the dashed line, displaying linear increase with the excitation duration for both cases. II) The second region for the excitation duration of $3\mu s \lesssim t_{dur} \lesssim 7\mu s$, where the measured Rydberg signal without the DC field still lies in the dashed line, displaying the linear increase, but the Rydberg signal with the DC field begins to deviate from the dashed line when $t_{dur} > 3\mu s$, and the difference between the signal with and without the DC field increases with the excitation duration. This behavior proves that the dipole interaction $(1/R^3)$–induced blockade effect is much larger than the van der Waals interaction $(1/R^6)$–induced blockade effect. III) The third blockade region for the excitation duration $t_{dur} \gtrsim 7\mu s$, where the Rydberg signal in the absence of the DC field also begins to deviate from the dashed line, showing the blockade effect. In this region, the difference between the signals with and without the DC field does not change much when we increase the excitation duration further because they are both in the blockade region.

Due to the large polarizability, the energy level of the Rydberg state is easily tuned with the external electric field to the Förster resonance, where Rydberg atoms display the strong dipole interaction. The electric field tuned dipole interaction has lots of applications in the non-radiative energy exchange [29], the collective effect [30], the engineering quantum states of matter [31], and so on. The tuning of coherent interactions in many-body systems with an external field has been a promising method. The cold Rydberg gases provide an ideal platform for the quantum simulation of complex many-body problems due to their controllable interactions.

5 CONCLUSION

To conclude, in this work, we have investigated the interaction between $|nP_{3/2}\rangle$ (n = 38–40) Rydberg pairs, excited by the three-photon scheme in the cold cesium atoms. The Rydberg level is tuned by the weak DC field and the resonant energy transfer spectrum due to the Förster resonance is observed. The $|38S_{1/2}\rangle$ state due to the resonant energy transfer as a function of the excitation frequency and the electric field has been obtained and the extracted Förster electric field for $|38P_{3/2}\rangle$ Rydberg atom agrees with the calculated field value. Finally, the blockade effects induced by the van der Waals interaction and the dipole interaction between Rydberg pairs have been studied by changing the excitation duration, which demonstrates that the dipole interaction–induced blockade effect is stronger than the van der Waals interaction–induced blockade effect. Considering the flexible and controllable nature of the electric field, the field tuned dipole interaction plays an important role in the coherent interactions in many-body systems and non-radiative collision processes and collective effects and engineering quantum states of matter.

DATA AVAILABILITY STATEMENT

The raw data supporting the conclusion of this article will be made available by the authors without undue reservation.

AUTHOR CONTRIBUTIONS

JZ designed the study. YJ and JB collected and analyzed the data and wrote the original manuscript. RS, SB, and SJ contributed to the manuscript revision. All authors provided review and comment on the subsequent versions of the manuscript.

FUNDING

This study was supported by the National Key Research and Development Program of China (2017 YFA0304203), the National Natural Science Foundation of China (12120101004, 61835007, and 62175136), the Changjiang Scholars and Innovative Research Team in University of Ministry of Education of China (IRT 17R70), the Graduate Education Innovation Project of Shanxi Province (2021Y017), the Shanxi 1331 Project, and the Scientific and Technological Innovation Program of Higher Education Institutions in Shanxi Province (2020L0479).

REFERENCES

1. Gallagher TF. *Rydberg Atoms*. New York, NY, USA: Cambridge University Press (1994).
2. Ornelas-Huerta DP, Craddock AN, Goldschmidt EA, Hachtel AJ, Wang Y, Bienias P, et al. On-demand Indistinguishable Single Photons from an Efficient and Pure Source Based on a Rydberg Ensemble. *Optica* (2020) 7:813–9. doi:10.1364/optica.391485
3. Peyronel T, Firstenberg O, Liang QY, Hofferberth S, Gorshkov AV, Pohl T, et al. Quantum Nonlinear Optics with Single Photons Enabled by Strongly Interacting Atoms. *Nature* (2012) 488:57–60. doi:10.1038/nature11361
4. Tiarks D, Baur S, Schneider K, Dürr S, Rempe G. Single-photon Transistor Using a Förster Resonance. *Phys Rev Lett* (2014) 113:053602. doi:10.1103/PhysRevLett.113.053602
5. Jiao Y, Han X, Yang Z, Li J, Raithel G, Zhao J, et al. Spectroscopy of Cesium Rydberg Atoms in strong Radio-Frequency fields. *Phys Rev A* (2016) 94:1–7. doi:10.1103/PhysRevA.94.023832
6. Jiao Y, Hao L, Han X, Bai S, Raithel G, Zhao J, et al. Atom-Based Radio-Frequency Field Calibration and Polarization Measurement Using Cesium nD_J Floquet States. *Phys Rev Appl* (2017) 8:1–7. doi:10.1103/PhysRevApplied.8.014028
7. Jing M, Hu Y, Ma J, Zhang H, Zhang L, Xiao L, et al. Atomic Superheterodyne Receiver Based on Microwave-Dressed Rydberg Spectroscopy. *Nat Phys* (2020) 16:911–5. doi:10.1038/s41567-020-0918-5
8. Hao L, Xue Y, Fan J, Bai J, Jiao Y, Zhao J. Precise Measurement of a Weak Radio Frequency Electric Field Using a Resonant Atomic Probe. *Chin Phys B* (2020) 29. doi:10.1088/1674-1056/ab6c49
9. Sedlacek JA, Schwettmann A, Kübler H, Löw R, Pfau T, Shaffer JP. Microwave Electrometry with Rydberg Atoms in a Vapour Cell Using Bright Atomic Resonances. *Nat Phys* (2012) 8:819–24. doi:10.1038/nphys2423
10. Bai J, Fan J, Hao L, Spong NL, Jiao Y, Zhao J. Measurement of the Near Field Distribution of a Microwave Horn Using a Resonant Atomic Probe. *Appl Sci (Switzerland)* (2019) 9:1–9. doi:10.3390/app9224895
11. Vogt T, Viteau M, Zhao J, Chotia A, Comparat D, Pillet P. Dipole Blockade at Förster Resonances in High Resolution Laser Excitation of Rydberg States of Cesium Atoms. *Phys Rev Lett* (2006) 97:6–9. doi:10.1103/PhysRevLett.97.083003
12. Wilk T, Gaëtan A, Evellin C, Wolters J, Miroshnychenko Y, Grangier P, et al. Entanglement of Two Individual Neutral Atoms Using Rydberg Blockade. *Phys Rev Lett* (2010) 104:2–5. doi:10.1103/PhysRevLett.104.010502
13. Mourachko I, Li W, Gallagher TF. Controlled many-body Interactions in a Frozen Rydberg Gas. *Phys Rev A* (2004) 70:1–4. doi:10.1103/PhysRevA.70.031401
14. Gallagher TF, Gounand F, Kachru R, Tran NH, Pillet P. Perturbation of the Ba 6*sng* Series at n =24 by Zero-Field Spectroscopy and Forced Autoionization. *Phys Rev A* (1983) 27:2485–92. doi:10.1103/physreva.27.2485
15. Renn MJ, Anderson WR, Gallagher TF. Resonant Collisions of K Rydberg Atoms. *Phys Rev A* (1994) 49:908–12. doi:10.1103/physreva.49.908
16. Pelle B, Faoro R, Billy J, Arimondo E, Pillet P, Cheinet P. Quasiforbidden Two-Body Förster Resonances in a Cold Cs Rydberg Gas. *Phys Rev A* (2016) 93:1–11. doi:10.1103/PhysRevA.93.023417
17. Zhelyazkova V, Hogan SD. Electrically Tuned Förster Resonances in Collisions of NH_3 with Rydberg He Atoms. *Phys Rev A* (2017) 95:1–6. doi:10.1103/PhysRevA.95.042710
18. Gurian JH, Cheinet P, Huillery P, Fioretti A, Zhao J, Gould PL, et al. Observation of a Resonant Four-Body Interaction in Cold Cesium Rydberg

Atoms. *Phys Rev Lett* (2012) 108:1–5. doi:10.1103/PhysRevLett.108.023005
19. Faoro R, Pelle B, Zuliani A, Cheinet P, Arimondo E, Pillet P. Borromean Three-Body FRET in Frozen Rydberg Gases. *Nat Commun* (2015) 6. doi:10.1038/ncomms9173
20. Firstenberg O, Adams CS, Hofferberth S. Nonlinear Quantum Optics Mediated by Rydberg Interactions. *J Phys B: At Mol Opt Phys* (2016) 49:152003. doi:10.1088/0953-4075/49/15/152003
21. Nipper J, Balewski JB, Krupp AT, Hofferberth S, Löw R, Pfau T. Atomic Pair-State Interferometer: Controlling and Measuring an Interaction-Induced Phase Shift in Rydberg-Atom Pairs. *Phys Rev X* (2012) 2:1–7. doi:10.1103/PhysRevX.2.031011
22. Lukin MD, Fleischhauer M, Cote R, Duan LM, Jaksch D, Cirac JI, et al. Dipole Blockade and Quantum Information Processing in Mesoscopic Atomic Ensembles. *Phys Rev Lett* (2001) 87:37901. doi:10.1103/PhysRevLett.87.037901
23. Isenhower L, Urban E, Zhang XL, Gill AT, Henage T, Johnson TA, et al. Demonstration of a Neutral Atom Controlled-Not Quantum Gate. *Phys Rev Lett* (2010) 104:8–11. doi:10.1103/PhysRevLett.104.010503
24. Müller MM, Murphy M, Montangero S, Calarco T, Grangier P, Browaeys A. Implementation of an Experimentally Feasible Controlled-phase Gate on Two Blockaded Rydberg Atoms. *Phys Rev A* (2014) 89:1–8. doi:10.1103/PhysRevA.89.032334
25. Wu X, Liang X, Tian Y, Yang F, Chen C, Liu YC, et al. A Concise Review of Rydberg Atom Based Quantum Computation and Quantum Simulation. *Chin Phys B* (2021) 30. doi:10.1088/1674-1056/abd76f
26. Altman E, Brown KR, Carleo G, Carr LD, Demler E, Chin C. Quantum Simulators: Architectures and Opportunities. *PRX Quan* (2021) 2:1–19. doi:10.1103/prxquantum.2.017003
27. Zimmerman M, Littman M, Kash M, Kleppner D. Stark Structure of the Rydberg States of Alkali-Metal Atoms. *Phys Rev A* (1979) 20. doi:10.1103/physreva.20.2251
28. Tong D, Farooqi SM, Stanojevic J, Krishnan S, Zhang YP, Côté R, et al. Local Blockade of Rydberg Excitation in an Ultracold Gas. *Phys Rev Lett* (2004) 93:1–4. doi:10.1103/PhysRevLett.93.063001
29. Safinya KA, Delpech JF, Gounand F, Sandner W, Gallagher TF. Resonant Rydberg-Atom-Rydberg-Atom Collisions. *Phys Rev Lett* (1981) 47:405–8. doi:10.1103/PhysRevLett.47.405
30. Comparat D, Pillet P. Dipole Blockade in a Cold Rydberg Atomic Sample [Invited]. *J Opt Soc America B* (2010) 27:A208. doi:10.1364/josab.27.00a208
31. Saffman M, Walker TG, Mølmer K. Quantum Information with Rydberg Atoms. *Rev Mod Phys* (2010) 82:2313–63. doi:10.1103/RevModPhys.82.2313

Conflict of Interest: The authors declare that the research was conducted in the absence of any commercial or financial relationships that could be construed as a potential conflict of interest.

Publisher's Note: All claims expressed in this article are solely those of the authors and do not necessarily represent those of their affiliated organizations, or those of the publisher, the editors, and the reviewers. Any product that may be evaluated in this article, or claim that may be made by its manufacturer, is not guaranteed or endorsed by the publisher.

frontiers | Frontiers in Physics

ORIGINAL RESEARCH
published: 29 April 2022
doi: 10.3389/fphy.2022.893507

The Qubit Fidelity Under Different Error Mechanisms Based on Error Correction Threshold

Kai Li[1,2]*

[1]State Key Laboratory of Magnetic Resonances and Atomic and Molecular Physic, Innovation Academy for Precision Measurement Science and Technology, Chinese Academy of Sciences, Wuhan, China, [2]School of Physical Sciences, University of Chinese Academy of Sciences, Beijing, China

Quantum error correction is a crucial step to realize large-scale universal quantum computing, and the condition for realizing quantum error correction is that the error probability of each operation step must below some threshold. This requires that the qubits' quality and the quantum gates precision can reach a certain level experimentally. We firstly discuss the mechanism of quantum errors: the precision of quantum gates corresponds to unitary operator errors, and the quality of qubits is attributed to decoherence. Then, according to the threshold of the surface code error correction, we proved the minimum of quantum gate fidelity should not be less than $1 - p$ with the error probability p, and found the natural decoherence time of qubits that can be used for error correction. This provides some kind of theoretical supports for qubits preparation and performing quantum operations experimentally.

Keywords: quantum computing, quantum error correction, surface code, decoherence, gate fidelity

OPEN ACCESS

Edited by:
Guangling Cheng,
East China Jiaotong University, China

Reviewed by:
Yonggang Tan,
Luoyang Normal University, China
Hongwei Li,
University of Science and Technology of China, China

***Correspondence:**
Kai Li
kaili@wipm.ac.cn

Specialty section:
This article was submitted to Quantum Engineering and Technology, a section of the journal Frontiers in Physics

Received: *10 March 2022*
Accepted: *25 March 2022*
Published: *29 April 2022*

Citation:
Li K (2022) The Qubit Fidelity Under Different Error Mechanisms Based on Error Correction Threshold. Front. Phys. 10:893507. doi: 10.3389/fphy.2022.893507

1 INTRODUCTION

As one of the Frontier fields in the post-Moore's Law era, quantum computing has received extensive attention from physicists, information scientists, and cryptographers. There are two main reasons. First, The spatial scale of classical computer chips has approached the scale of quantum physics. The classical laws are no longer applicable in such scale, which requiring the support of quantum theory. Second, quantum algorithms based on quantum systems can reduce the computing complexity of difficult problems, to achieve computational acceleration even exponentially, such as Shor's algorithm [1,2], Grover's algorithm [3,4], etc.

However, the main difficulty in the current quantum computing experiments is that it is hard to achieve large-scale qubits integration, because of the decoherence, noise in channels, and crosstalk between qubits, and so on [5,6]. Since practical universal quantum algorithms require large-scale fault-tolerant quantum computing platforms, the current stage in the field of quantum computing is to demonstrate and practicalize the quantum superiority of Noisy Intermediate Scale Qubits quantum computing [7,8]. Quantum error correction is still the most technical step that needs to be overcome and improved. If error correction is not carried out, quantum circuit will accumulate errors until the correct result cannot be obtained. The commonly used error correction scheme that can be implemented at present includes surface code (two-dimensional topological quantum error correction) [9,10]. Gidney et al. estimated that the time to crack 2048-bit RSA by executing the Shor's algorithm on the superconducting circuits platform using the surface code is about 8 h [11], however the qubits overhead reaches 20 millions. Gouzien et al. took advantage of a 3D-guage color code and the ion trap quantum computing to reduce the qubits overhead to 13,436 at the cost of a slight increase in execution time to 177 days [12].

It can be seen that different quantum error correction schemes will have a certain impact on the overhead of quantum circuits, and will also produce different error probability thresholds p_{th}. This threshold p_{th} will further impose a constraint on the fidelity of qubits and quantum operations, which is also the focus of our work. If we want to go further in the development of quantum error correction, we need a more accurate understanding and deeper exploration of the error mechanism of qubits.

Although error correction schemes based on error syndrome detection don't require us to identify the source of errors for each qubit, but only need the statistical probability of errors. However, during the preparation of required qubits and quantum gates, their fidelity and decoherence characteristic time should be used as reference standard. Therefore, according to the error probability threshold required by error correction schemes, after clarifying the error generation mechanism, the theoretical calibration of the corresponding standard is also an important part of overcoming the bottleneck in quantum error correction experiments.

In this work, we explore the different sources of single-qubit errors, and calculate the fidelity of quantum operations and decoherence respectively according to the surface code probability threshold p_{th}. For the single-qubit error correction model, the probability of detecting an error should be a comprehensive characterization of the two error sources. The conclusions of this work provide a theoretical basis for the fidelity criteria of the qubits preparation and quantum operations in experiments.

2 THE SOURCE OF QUBIT ERRORS

As a quantum system existing in the environment, qubits will inevitably interact with the surrounding environment to exchange information. This is a loss of information for qubits, and it will also bring errors to the result of quantum circuits.

We can use the fidelity between the initial and final states of a quantum system to measure the degree of information retention. But since the measurement of fidelity requires ensemble-based measurement methods such as quantum state tomography, it is not suitable to do the fidelity measurement in quantum circuits. Therefore, error correction schemes usually directly use a parity-like error characterization method to monitor errors and avoid destroying data qubits.

Specifically, the model of the interaction between a quantum system and the environment can be described by the operation-sum representation. First, the total state of the quantum system and the environment $\rho = \rho_0 \otimes \rho_{\text{env}}$, ρ_0 represents the initial state density matrix of the quantum system, and ρ_{env} represents the density matrix of the environment. According to the Schmidt purification, the initial state ρ_{env} of the environment can always be written as a pure state, which means $\rho_{\text{env}} = |e_0\rangle\langle e_0|$. Wherein $\{|e_k\rangle\}$ is a set of basis for the environment, and $|e_0\rangle$ is the initial state. Then after the whole system experiences evolution U, the final state of the quantum system $\varepsilon(\rho) = \text{Tr}_{\text{env}}[U(\rho_0 \otimes |e_0\rangle\langle e_0|)U^\dagger]$, that is, ρ experiences the evolution of U, and then the environment is traced to obtain the reduced density matrix of the quantum system,

$$\varepsilon(\rho) = \sum_k |e_k\rangle\langle e_k| \cdot \left[U(\rho_0 \otimes |e_0\rangle\langle e_0|)U^\dagger\right] = \sum_k E_k \rho_0 E_k^\dagger, \quad (1)$$

where $E_k = \langle e_k|U|e_0\rangle$, represents the matrix element of the U under the environmental representation, and acts on the quantum system [13].

For the quantum system, the fidelity F after the evolution is

$$F(\rho_0, \varepsilon(\rho)) = \text{Tr}^2\left(\sqrt{\sqrt{\varepsilon(\rho)}\,\rho_0\sqrt{\varepsilon(\rho)}}\right). \quad (2)$$

In fact, after the partial tracing of the environment Tr_{env}, all we care about is the difference between the initial and final states of the quantum system, that is, what kind of errors will be caused. The details of the evolution process don't need us to care about. The operator E has also become a reduced operator that only acts on the quantum system.

Next, we can judge whether E is unitary or not to classify the errors occurred from the quantum system. For the sake of simplicity, we take one qubit as the quantum system in quantum computing. Specifically, it is divided into two categories:

Unitary operator E. The operator E is unitary and can preserve the trace of the quantum state density matrix. This type of error can keep the qubit still in pure state. We know that under ideal conditions, the quantum state required for quantum computing should be a pure state, and the quantum operation should be a unitary operation[1]. If the introduced error is also a unitary operator, this means that the effect of the error did not decoherent the quantum state. From the perspective of the Bloch sphere, it's just that the state vector produces some unexpected rotations on the spherical surface.

Considering the actual operation, this kind of error mainly comes from the quantum gate. Whether it's because the operator's approximation can't reach 100% accuracy, or because of environmental influences that make the quantum gates behave inaccurately, such kind of errors can be translated into single-qubit rotations on the Bloch sphere.

Non-unitary operator E. The operator E evolves the qubit from a pure state to a mixed state. This type of error can be understood as what we usually say, decoherence. Compared to the first type of error, the effects of decoherence are more common. The damping of amplitude and phase is usually due to the contact of the qubit with the environment (various types of noise). Since the qubit has become a mixed state, part of the information contained in it has changed from the form of quantum superposition to a classical mixture, which has irreversibly leaked into the environment.

From the perspective of the Bloch sphere, the decayed state vector shrinks from the surface to the inside of the sphere. The decay of the state vector can be decomposed into transverse relaxation and longitudinal relaxation [14,15]. For detailed discussion and calculation, please refer to **Section 3.2**.

Although from the perspective of error correction, it seems that we do not need to care about the cause of the errors, but only need to

[1]For the two-qubit operations, we treat the two qubits together as a quantum system. If we consider one of them, it is in a mixed state, but the two-qubit state is still pure.

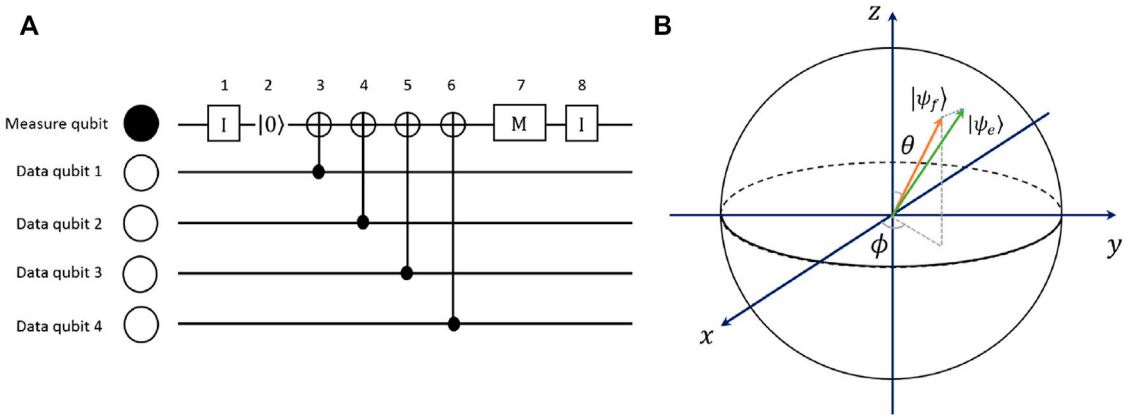

FIGURE 1 | (A) Single cycle logical circuit that detects X errors in the surface code. The solid circles in the circuit represent auxiliary qubits, and the open circles represent data qubits. A single cycle contains 8 steps, including single-qubit gate, initialization, C-NOT gate, and measurement; **(B)** Bloch sphere representation of a single qubit. $|\psi_f\rangle$ represents the quantum state after the ideal quantum operation, $|\psi_e\rangle$ is the final state after the error occurs. The angle between the projection of the $x-y$ plane and the x-axis is the phase angle ϕ, and the angle between the state vector and the z-axis is the polar angle θ.

monitor the errors and take corresponding error correction operations to ensure the reliability of the circuit. However, in experiments, various quantum computing platforms using different materials and principles may have very different qubit properties and types of quantum operations. Our research conclusions can provide a unified theoretical standard for different platforms, and can obtain more precise qubit decoherence fidelity and quantum operation fidelity according to different error correction schemes and error correction standards. Therefore, the research on the error mechanism of qubits is of certain significance.

For the widely used surface code, since the error correction circuit increases the circuit depth and the number of qubits, its error threshold can also be divided into different classes [9]. Specifically, according to the surface code error correction circuit (**Figure 1A**), Fowler et al. divides the error thresholds into $p_{\text{th},0}$, $p_{\text{th},1}$, and $p_{\text{th},2}$. These three levels of thresholds have different degrees of sensitivity to the logic error rate of the error correction circuit, and we will select the appropriate class of threshold as constraint according to the expression of fidelity.

Next, we will show the correlation between different quantum superposition initial states, error probability and fidelity for single qubit. And then theoretically deduce and calculate the qubit fidelity and quantum operation fidelity of the above two error-generating mechanisms, and find the corresponding theoretical limit under the error probability threshold.

3 ERROR PROBABILITY AND FIDELITY OF SINGLE QUBIT

For any single-qubit pure state, we denote an arbitrary superposition state of $|0\rangle$ and $|1\rangle$ as $|\psi\rangle = \alpha|0\rangle + \beta|1\rangle$, where the normalization condition is $|\alpha|^2 + |\beta|^2 = 1$. In a Bloch sphere with the radius of 1, $|\psi\rangle$ is the radial vector on the sphere, taking $\alpha = \cos\frac{\theta}{2}$, $\beta = e^{i\phi}\sin\frac{\theta}{2}$, and $|\psi\rangle$ is expressed as

$$|\psi\rangle = \alpha|0\rangle + \beta|1\rangle = \cos\frac{\theta}{2}|0\rangle + e^{i\phi}\sin\frac{\theta}{2}|1\rangle, \tag{3}$$

where θ is the polar angle and ϕ is the azimuth angle. We usually use the density matrix of state $\rho = |\psi\rangle\langle\psi|$ to calculate [13].

$$\rho = \begin{pmatrix} |\alpha|^2 & \alpha\beta^* \\ \alpha^*\beta & |\beta|^2 \end{pmatrix} = \frac{1}{2}\begin{pmatrix} 1+\cos\theta & e^{-i\phi}\sin\theta \\ e^{i\phi}\sin\theta & 1-\cos\theta \end{pmatrix}. \tag{4}$$

For a error correction process, we need to perform error detection and correction for the result after each step. Without loss of generality, we assume that after each unitary operation of quantum computing, the final state $|\psi_f\rangle = \alpha|0\rangle + \beta|1\rangle$, where f means 'final'. But due to the error of quantum operation or decoherence caused by noise, the final state becomes $|\psi_e\rangle$, where e means 'errors'. Compared with $|\psi_f\rangle$, the difference generated by $|\psi_e\rangle$ may originate from one or more reasons, and we will analyze them one by one below.

3.1 The Error of Unitary Operation

The quantum gate operation in the quantum circuit is usually to apply a specific controllable external field to the qubit to control it. There are different type of external field according to the different qubit systems, such as the microwave pulse [16] in the superconducting circuit system, the laser pulse [17] in the ion trap system, and so on. Here we consider the errors that such quantum operations bring to qubits because they cannot be 100% accurate.

For example, a beam of X_π-pulse can rotate the qubit by an angle of π around the x-axis, but due to the insufficient precision, the quantum state actually rotates around the x-axis by $\pi \pm \delta$. Such an error can be understood as an unexpected unitary operation, and equivalent to a rotation of an unknown angle. In fact this unexpectedly angle can be a rotation around any axis, not necessarily the same as the operation rotation. (**Figure 1B**).

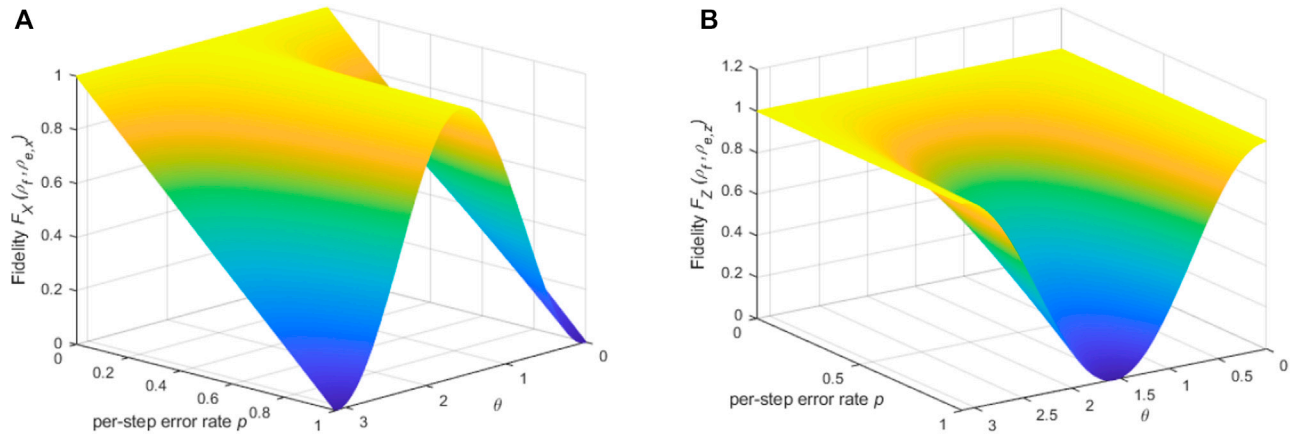

FIGURE 2 | (A) For U_x errors, the qubit fidelity $F_x(\rho_f,\rho_{e,x})$ is a function of the error probability p and the polar angle θ (ϕ is set to be 0); **(B)** For U_z errors, the qubit fidelity $F_z(\rho_f,\rho_{e,z})$ is a function of the error probability p and the polar angle θ.

According to the above operations, the single-qubit state can be written as the following process:

1. The initial state undergoes an error-free unitary operation, $|\psi_f\rangle = U|\psi_0\rangle$;
2. The initial state undergoes an unitary operation with errors, $|\psi_e\rangle = U'|\psi_0\rangle = U_eU|\psi_0\rangle = U_e|\psi_f\rangle$.

The qubit undergoes the quantum operation U' with errors, which is equivalent to the qubit first undergoes the precise operation U, and then undergoes an error operation U_e, and finally becomes the quantum state with error $|\psi_e\rangle$. U_e is also essentially a rotation operation on the Bloch sphere, so it can be decomposed into rotation around x-axis and z-axis, corresponding to the types of X and Z errors that occur in qubits respectively. Besides, the error probability is described by the rotation angle ε.

3.1.1 X Errors

$U_x = e^{i\varepsilon\cdot\sigma_x} = \cos\varepsilon\cdot I + i\sin\varepsilon\cdot\sigma_x$, the probability of error $p_{U_x} = \sin^2\varepsilon$.

After the state $|\psi_f\rangle$ is affected by U_x,

$$\begin{aligned}|\psi_e\rangle_x = U_x|\psi_f\rangle &= (\cos\varepsilon\cdot I + i\sin\varepsilon\cdot\sigma_x)(\alpha|0\rangle+\beta|1\rangle)\\ &= (\alpha\cos\varepsilon + i\beta\sin\varepsilon)|0\rangle + (\beta\cos\varepsilon + i\alpha\sin\varepsilon)|1\rangle,\end{aligned} \tag{5}$$

Since $|\psi_f\rangle$ and $|\psi_e\rangle_x$ are pure states, their density matrices are $\rho_f = |\psi_f\rangle\langle\psi_f|$, $\rho_{e,x} = |\psi_e\rangle_x\langle\psi_e|$ respectively. And the fidelity F_x under the X error of probability p is

$$F_x(\rho_f,\rho_{e,x}) = \mathrm{Tr}^2\left(\sqrt{\sqrt{\rho_{e,x}}\rho_f\sqrt{\rho_{e,x}}}\right) = |{}_x\langle\psi_e\,|\,\psi_f\rangle|^2. \tag{6}$$

Bringing in the $|\psi_f\rangle$ and $|\psi_e\rangle$, we can get

$$\begin{aligned}F_x(\rho_f,\rho_{e,x}) &= \left(|\alpha|^2+|\beta|^2\right)^2\cos^2\varepsilon + \left(\alpha\beta^* + \alpha^*\beta\right)^2\sin^2\varepsilon\\ &= \cos^2\varepsilon + \sin^2\theta\cdot\cos^2\phi\cdot\sin^2\varepsilon.\end{aligned} \tag{7}$$

We can see that the fidelity $F_x(\rho_f,\rho_{e,x})$ is not only related to the error rotation angle ε, but also to the θ and ϕ angles of the quantum state $|\psi_f\rangle$. This means that even the same error will have different effects on different quantum states. **Figure 2A** plots the relationship between $F_x(\rho_f,\rho_{e,x})$ and ε, θ (For the convenience of drawing, we take $\phi = 0$.)

3.1.2 Z Errors

$U_z = e^{i\varepsilon\cdot\sigma_z} = \cos\varepsilon\cdot I + i\sin\varepsilon\cdot\sigma_z$, the probability of error $p_{U_z} = \sin^2\varepsilon$.

The same process as X errors,

$$\begin{aligned}|\psi_e\rangle_z = U_z|\psi_f\rangle &= (\cos\varepsilon\cdot I + i\sin\varepsilon\cdot\sigma_z)(\alpha|0\rangle+\beta|1\rangle)\\ &= (\cos\varepsilon + i\sin\varepsilon)\alpha|0\rangle + (\cos\varepsilon - i\sin\varepsilon)\beta|1\rangle.\end{aligned} \tag{8}$$

After the Z error for probability p, the density matrix becomes $\rho_{e,z} = |\psi_e\rangle_z\langle\psi_e|$, and the fidelity

$$F_z(\rho_f,\rho_{e,z}) = |{}_z\langle\psi_e\,|\,\psi_f\rangle|^2 = \frac{1}{2}\left(1+\cos^2\theta+\sin^2\theta\cdot\cos 2\varepsilon\right). \tag{9}$$

It can be found that for Z errors, the fidelity $\rho_{e,z} = |\psi_e\rangle_z\langle\psi_e|$ is not affected by the phase angle ϕ, but is still affected by the polar angle θ, see **Figure 2B**.

3.2 Natural Decoherence

We analyzed the case where the error is a unitary operator above, which ensures that the qubit is still pure. And because of the unitarity of the operator, unitary errors are in principle completely reversible. But if the error causes the qubit to evolve from a pure state to a mixed state, its information will be irreversibly lost, usually described as decoherence caused by the environment.

Under the conditions of Born approximation (weak coupling between quantum system and environment) and Markovian approximation (each noise is temporally uncorrelated), the decoherence problem of quantum system is usually described

by the master equation of density matrix (quantum Liouville equation) [18].

$$\partial_t \rho = -\frac{i}{\hbar}[H, \rho] + \sum_k \Gamma_k \mathcal{L}_k[\rho], \tag{10}$$

where H represents the coherent dynamic evolution Hamiltonian, and $\mathcal{L}_k[\rho] = ([\mathcal{L}_k, \rho\mathcal{L}_k^\dagger] + [\mathcal{L}_k\rho, \mathcal{L}_k^\dagger])/2$ represents the incoherent evolution. $\mathcal{L}_k$ is the Lindblad quantum transition operator, which is used to describe the effect of different decoherence effects on the quantum state ρ, and Γ_k represents the rate (influence degree) of the corresponding $\mathcal{L}_k$.

The research on the master equation and multi-body quantum system is complicated, and we can refer to [19,20] for details. In universal quantum computing, any quantum operation can be decomposed into a combination of single-qubit gates and two-qubit gates. So theoretically only the decoherence of at most two bodies need to be considered in quantum computing. In this subsection, we first consider the single-qubit decoherence problem.

In theory, decoherence occurs in the entire process of quantum computing, that is, the entire process from initialization, quantum gate operation, to measurement and memory. In the stage without quantum operations, we can set the Hamiltonian H of the coherent evolution part to 0. It means that in such stage the qubit will undergo natural decoherent decay. Although such model is relatively naive, it can also correspond to the process of qubit storage and preparation, which is of great significance to quantum computing.

For the natural decoherence model of single qubit, we also categorize the types of errors [15]:

Amplitude damping. The conversion between $|0\rangle \rightleftharpoons |1\rangle$ is called amplitude damping. This includes the transition of $|0\rangle \rightarrow |1\rangle$ and the decay of $|1\rangle \rightarrow |0\rangle$. However, the probability of a spontaneous transition in a quantum system in equilibrium is negligible compared to the probability of decay [21]. During longitudinal relaxation, single qubit exchange energy with the environment, resulting in irreversible information leakage.

Dephasing. The decay of the phase angle ϕ is called pure dephasing. Pure dephasing does not exchange energy with the environment, so it is in principle reversible. In theory, the dynamic decoupling method can completely eliminate the pure dephase decay [22], and in practice scientists are trying to achieve it.

For the master equation solution of the above decoherence model, it can be described by a simplified form of the Bloch-Redfield density matrix [15,23,24],

$$\rho_{\mathrm{BR}} = \begin{pmatrix} 1 + (|\alpha|^2 - 1)e^{-\Gamma_1 t} & \alpha\beta^* e^{-\Gamma_2 t} \\ \alpha^*\beta e^{-\Gamma_2 t} & |\beta|^2 e^{-\Gamma_1 t} \end{pmatrix}, \tag{11}$$

The operator interaction strength Γ_k represents the decay rate, the amplitude damping rate is Γ_1, and the transverse decoherence rate is $\Gamma_2 = \Gamma_1/2 + \Gamma_\phi$, which includes both amplitude damping and pure dephasing effects. The probability amplitude of $|1\rangle$ is attenuated from $|\beta|^2$ to $|\beta|^2 e^{-\Gamma_1 t}$, and the probability amplitude of $|0\rangle$ is $1 + (|\alpha|^2 - 1)e^{-\Gamma_1 t}$; the decay rate of the off-diagonal term is $e^{-\Gamma_2 t}$.

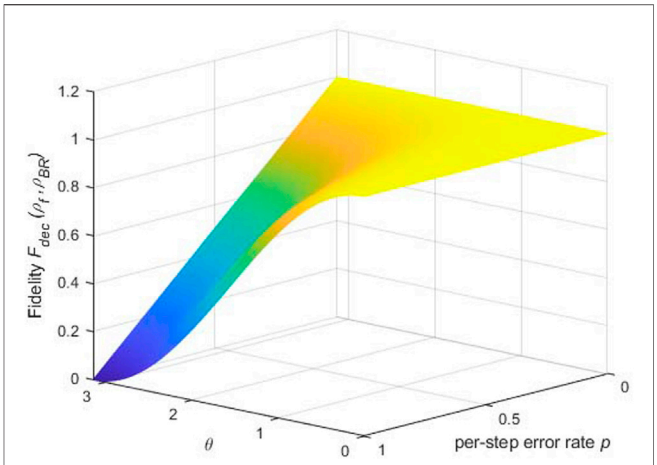

FIGURE 3 | For natural decoherence, the quantum state fidelity $F_{\mathrm{dec}}(\rho_f, \rho_{\mathrm{BR}})$ as a function of decay probability p and the polar angle θ.

In the standard Bloch-Redfield model, the off-diagonal term also has a frequency detuning attenuation term $e^{-i\delta\omega t}$, which represents the attenuation caused by the frequency detuning between the qubit and the control system. The Hamiltonian H is set to 0, so the detuning term doesn't need to be considered.

In addition, the standard Bloch-Redfield model cannot still accurately describe the decoherence of superconducting qubits. The off-diagonal term in the density matrix should also normally contain the non-exponential decay term $e^{-\chi_N(t)}$, which can describe $1/f$-type noise. For the sake of simplicity, we do not consider the non-exponential decay term here.

With the decoherent density matrix, we compute the fidelity $F_{\mathrm{dec}}(\rho_f, \rho_{\mathrm{BR}})$

$$\begin{aligned} F_{\mathrm{dec}}(\rho_f, \rho_{\mathrm{BR}}) &= \mathrm{Tr}^2\left(\sqrt{\sqrt{\rho_{\mathrm{BR}}}\,\rho_f\,\sqrt{\rho_{\mathrm{BR}}}}\right) \\ &= \left(\sqrt{|\alpha|^2\left[e^{-\Gamma_1 t}(|\alpha|^2 - 1) + 1\right]} + |\beta|^2\sqrt{e^{-\Gamma_1 t}}\right)^2, \end{aligned} \tag{12}$$

Bring $\alpha = \cos\frac{\theta}{2}$ and $\beta = e^{i\phi}\sin\frac{\theta}{2}$ in, we can get

$$\begin{aligned} F_{\mathrm{dec}}(\rho_f, \rho_{\mathrm{BR}}) &= \cos^2\frac{\theta}{2} - \sin^2\frac{\theta}{2}\cdot\cos\theta\cdot e^{-\Gamma_1 t} \\ &\quad + 2\sin^2\frac{\theta}{2}\cdot\left|\cos\frac{\theta}{2}\right|\cdot\sqrt{e^{-\Gamma_1 t} - \sin^2\frac{\theta}{2}\cdot e^{-2\Gamma_1 t}}. \end{aligned} \tag{13}$$

It can be found that there is no related term of $e^{-\Gamma_2 t}$ in the fidelity $F_{\mathrm{dec}}(\rho_f, \rho_{\mathrm{BR}})$. Since $\Gamma_2 = \Gamma_1/2 + \Gamma_\phi$, it means that $F_{\mathrm{dec}}(\rho_f, \rho_{\mathrm{BR}})$ is not affected by pure dephasing, which also reflects the reversibility of pure dephasing in the decoherence process. The relationship between $F_{\mathrm{dec}}(\rho_f, \rho_{\mathrm{BR}})$ and the polar angle θ, the amplitude damping probability $1 - e^{-\Gamma_1 t}$ is shown in **Figure 3**.

For different quantum states ρ_f, the effect of natural decoherence on fidelity is also different. The larger the polar angle θ, the greater the effect of amplitude damping decoherence on fidelity, and vice versa.

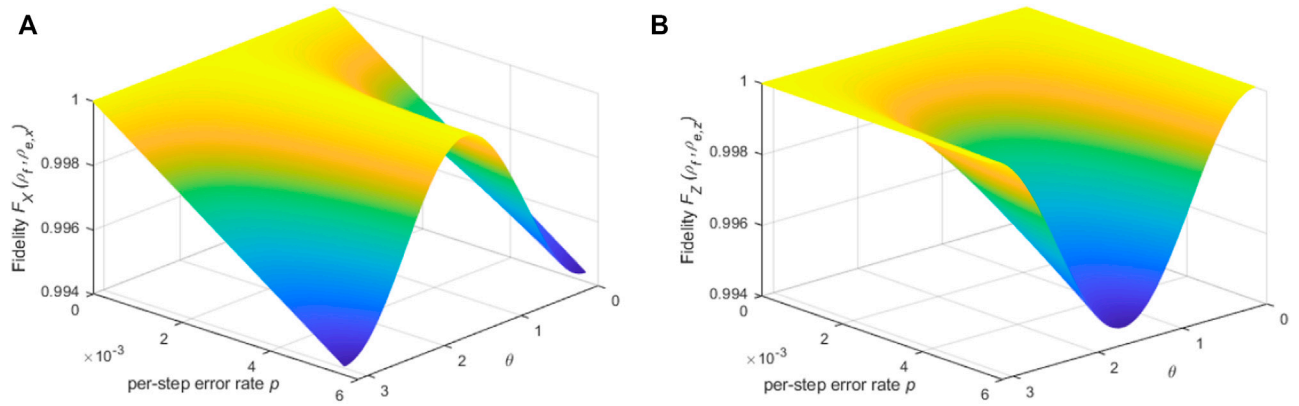

FIGURE 4 | (A) The value range of fidelity $F_x(\rho_f,\rho_{e,x})$ after limiting the error probability p to the surface code error threshold range; **(B)** Under the same error probability value range, the value range and the gradient trend of $F_z(\rho_f,\rho_{e,z})$.

4 SURFACE CODE ERROR PROBABILITY THRESHOLD AND THE MINIMUM FIDELITY

Surface codes have become widely used error correction schemes in various experimental platforms due to their neighbor interactions and the lattice structure that is easy to expand. In the field of error correction, the threshold theorem is the basic principle that guarantees the effectiveness of error correction schemes. Error corrections need additional auxiliary qubits and gates, which will introduce new errors. If there are too many additional errors introduced by the error correction circuits, the errors will continue to accumulate during the error correction cycle. Therefore, we need to require the error probability of the qubits and operations to be lower than a certain threshold p_{th}, so that the error probability of the final result of the circuit can be reduced by continuously implementing the error correction cycle [13].

For the X error correction circuit of the surface code (see **Figure 1A**), there are a total of 8 basic steps, including single-qubit gates, two-qubit gates, measurement and other operations. Considering these 8 steps comprehensively, error probability threshold is $p_{\text{th}} = 0.0057$ for each step [9].

The author also divided the errors into three classes, and studied the sensitivity of each type of errors to the threshold: Class0 represents the single-qubit error of the data qubit, $p_{\text{th},0} \cong 0.043$; Class1 represents the initialization of the auxiliary qubit, H gate and measurement errors, $p_{\text{th},1} \cong 0.12$; Class3 represents two-qubit gate errors, $p_{\text{th},2} \cong 0.0125$. However, since these types of error threshold are larger than the overall threshold p_{th} when considered separately, we take $p_{\text{th}} = 0.0057$ for calculation.

4.1 Unitary Errors

4.1.1 X Errors

Assuming that only X errors occur, the error probability threshold $p_{\text{th}} = \sin^2\varepsilon$, $\varepsilon = \arcsin\sqrt{p_{\text{th}}} \cong 0.0756$. According to **Eq. 8**, we can get the fidelity when the error probability p is between $0 \sim 0.0057$,

$$F_x(\rho_f,\rho_{e,x}) = 1 - (1 - \sin^2\theta \cdot \cos\phi)p. \tag{14}$$

Still taking $\phi = 0$, the function curve is shown in **Figure 4A**.

It is easy to know that the minimum value of $F_x(\rho_f,\rho_{e,x})$ is obtained at $\theta = 0, \pi$. At this time, the quantum state is at the two poles of the Bloch sphere, and the X error will completely flip the qubit. If $p = p_{\text{th}}$, then for $|\psi_f\rangle = |0\rangle$ or $|\psi_f\rangle = |1\rangle$, the minimum fidelity $F_x(\rho_f,\rho_{e,x})_{\min} = 1 - p_{\text{th}} = 0.9943$. That is, the minimum fidelity of unitary operation under X error is 99.43%.

4.1.2 Z Errors

On the other hand, assuming that only Z errors occur, we bring in $\varepsilon = \arcsin\sqrt{p}$,

$$\begin{aligned} F_z(\rho_f,\rho_{e,z}) &= \frac{1}{2}(1 + \cos^2\theta + \sin^2\theta \cdot \cos 2\varepsilon) \\ &= 1 - \sin^2\theta \cdot p, \end{aligned} \tag{15}$$

We can also get the function curve of $(\rho_f,\rho_{e,z})$ when $0 < p \leq 0.0057$, as shown in **Figure 4B**.

From **Eq. 15**, if $\theta = 0$ or π, we have $\sin\theta = 0$, $F_z(\rho_f,\rho_{e,z})$ is independent of p, and Z error will not affect the fidelity. In fact, $\theta = 0, \pi$ corresponds to $|0\rangle$ and $|1\rangle$, and the Z error is to rotate the quantum state around the z axis, which naturally does not change these two quantum states. If $0 < \theta < \pi$, the minimum fidelity value when $\theta = \pi/2$ is $F_z(\rho_f,\rho_{e,z})_{\min} = 1 - p_{\text{th}}$, which is also 99.43%.

4.1.3 Rotation Errors Around an Arbitrary Axis *m* by an Angle of ε

Through the discussion of X and Z errors, we find that the minimum values of their fidelity are the same, although the quantum states when taking the minimum value are different. In fact, we can show that the minimum value of fidelity is $1 - p$ (or $1 - \sin^2\varepsilon$) for the error when the state is unexpectedly rotated by ε around any axis m.

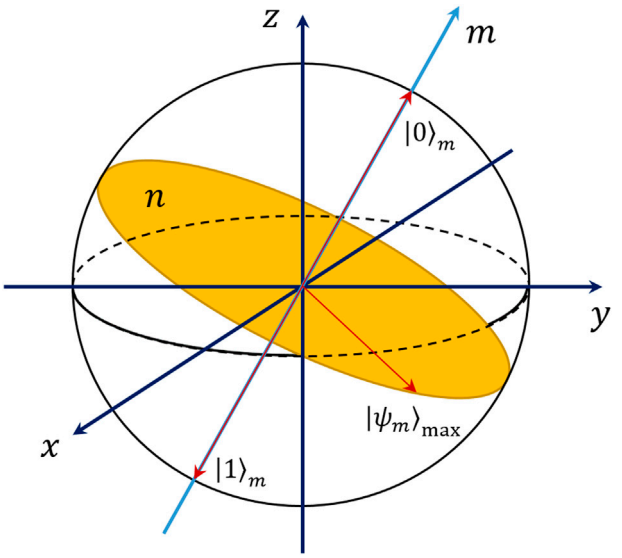

FIGURE 5 | For the rotation operation of any axis m, its error operator is U_m. The maximum of fidelity $F(|\psi_f\rangle, |\psi_m\rangle)$ is obtained when the quantum state vector coincides with the m-axis, and we mark the states as $|0_m\rangle$ and $|1_m\rangle$; And the minimum of $F(|\psi_f\rangle, |\psi_m\rangle)$ is obtained when the state falls on the normal plane n of the m-axis, we mark it as $|\psi_m\rangle_{max}$.

Proof: From **Section 3.1**, it can be seen that the final state with error $|\psi_m\rangle = U_m|\psi_f\rangle$, then let $U_m = e^{i\varepsilon\cdot\sigma_m}$, U_m represents the rotation of ε around the m-axis operation, σ_m is the operation of rotating π around the m-axis. ${\sigma_m}^2$ means 2π rotation around the m-axis, so there is ${\sigma_m}^2 = I$. Then the fidelity

$$\begin{aligned} F\left(|\psi_f\rangle, |\psi_m\rangle\right) &= \left|\langle\psi_f|U_e|\psi_f\rangle\right|^2 \\ &= \left|\langle\psi_f|(\cos\varepsilon\cdot I + i\sin\varepsilon\cdot\sigma_m)|\psi_f\rangle\right|^2 \\ &= \cos^2\varepsilon + \sin^2\varepsilon\left|\langle\psi_f|\sigma_m|\psi_f\rangle\right|^2 \\ &= 1 - p + p\left|\langle\psi_f|\sigma_m|\psi_f\rangle\right|^2. \end{aligned} \tag{16}$$

When $\langle\psi_f|\sigma_m|\psi_f\rangle = 0$, we have $F(|\psi_f\rangle, |\psi_m\rangle)_{min} = 1 - p$; and when $\langle\psi_f|\sigma_m|\psi_f\rangle = 1$, $F(|\psi_f\rangle, |\psi_m\rangle)_{max} = 1$. From the perspective of the Bloch sphere, when the fidelity gets the maximum, the qubit state vectors just falls on the m-axis and we marked them as $|0\rangle_m$ and $|1\rangle_m$. At this point, the operation of rotating around the m-axis cannot change the quantum state. When the fidelity gets the minimum, the state vector falls on the normal plane n of the m-axis, and we marked them as $|\psi_m\rangle_{max}$, see **Figure 5**.

The m-axis is also easy to determine if we know $|\psi_f\rangle$ and $|\psi_m\rangle$. Take the two points which are the intersection of $|\psi_f\rangle$ and $|\psi_m\rangle$ with the Bloch sphere respectively and connect them. The midpoint of the above line segment and the center of the sphere, these two points can determine the m-axis, which is perpendicular to the above line segment.

Moreover, U_m can be decomposed into rotating ε_1 around the x-axis first, and then rotating ε_2 around the z-axis, that is $e^{i\varepsilon\cdot\sigma_m} = e^{i\varepsilon_2\cdot\sigma_z}\cdot e^{i\varepsilon_1\cdot\sigma_x}$. If $|\psi_f\rangle = \cos\frac{\theta_1}{2}|0\rangle + e^{i\phi_1}\sin\frac{\theta_1}{2}|1\rangle$, and $|\psi_m\rangle = \cos\frac{\theta_2}{2}|0\rangle + e^{i\phi_2}\sin\frac{\theta_2}{2}|1\rangle$, we can have

$$\begin{aligned} |\psi_m\rangle = e^{i\varepsilon\cdot\sigma_m}|\psi_f\rangle &= e^{i\varepsilon_2\cdot\sigma_z}\cdot e^{i\varepsilon_1\cdot\sigma_x}|\psi_f\rangle \\ &= e^{i\left(\phi_2-\phi_1\right)\cdot\sigma_z}\cdot e^{i\left(\theta_2-\theta_1\right)\cdot\sigma_x}|\psi_f\rangle. \end{aligned} \tag{17}$$

4.2 Natural Decoherence

For the natural decoherent state ρ_{BR}, the amplitude damping probability $p_{dec} = 1 - e^{-\Gamma_1 t}$. If the characteristic time T_1 is fixed, according to the error probability threshold pth, we can obtain the longest lifetime $\tau = -T_1 \ln p$th that the qubit can be used for quantum computing.

According to the work of Krantz et al. [15], taking $T_1 = 85\ \mu$s, we can get $\tau = 0.489\ \mu$s. This means that a superconducting qubit with a amplitude damping lifetime of 85 μs has 489 ns available for quantum operations before decoherence. This time seems very short, but it is undoubtedly sufficient for a superconducting system with a single operation time of 10 ~ 100 ns.

Similarly, we take the threshold $p_{th} = 0.0057$ of the surface code scheme, then there is $0.9943 < e^{-\Gamma_1 t} < 1$, and the relationship between $F_{dec}(\rho_f, \rho_{BR})$ and the polar angle θ and time t is shown in **Figure 6**.

It can be found that the fidelity is minimized when $\theta = \pi$, $F_{dec}(\rho_f, \rho_{BR})_{min} = e^{-\Gamma_1 t} = 0.9943$.

5 DISCUSSION

From the analysis above, we studied the fidelity of quantum unitary operations and natural decoherence under surface code threshold requirements. But in each case, we assumed that only this type of error occurs, and in practice the operation errors and decoherence would occur at the same time. Therefore, the actual error probability $p = 1 - (1 - p_U)(1 - p_{dec}) = p_U + p_{dec} - p_U \cdot p_{dec}$, since $0 < p_U$, $p_{dec} < 1$, so $p > p_U$ and also $p > p_{dec}$. Given all this, the actual quantum operation fidelity should be larger than the above calculated value of 99.43%, and the actual available decoherence time should be shorter than 489 ns.

At the same time, the threshold theorem guarantees that the circuit can correct errors by continuously increasing the number of cycles when the error probability is lower than the threshold. However, the closer the error probability is to the threshold, the more cycles are required. Due to the limited quantum resources (number of qubits, number of quantum gates), it is impossible for us to require that the actual error probability only just reaches the threshold, which will cause enormous amount of qubits. Therefore, there is a recognized fidelity standard of 99.9% (the error probability per step is 10^{-3}), which is assumed in some articles [9,11]. So that for the surface code, the number of physical qubits can be controlled between 10^3 ~ 10^4 to encode a logical qubit.

For different quantum error correction codes, their error probability thresholds are different. Therefore the quantum gate fidelity and coherence time required for error correction will also be different. This will further affect the number of cycles of the error correction code, which is reflected in the required quantum resources (the corresponding amount of qubits and quantum operations). Based on our above processing method, the minimum required gate fidelity and qubit coherence time can be

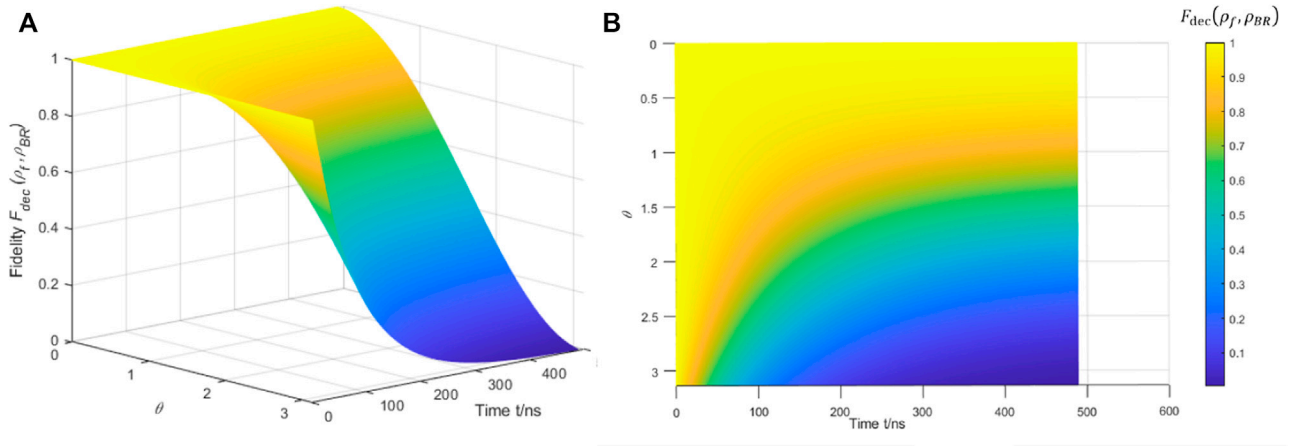

FIGURE 6 | (A) The amplitude damping probability p_{dec} is limited in the surface code error threshold range. This figure shows the value range and gradient trend of the quantum state fidelity $F_{\mathrm{dec}}(\rho_f,\rho_{\mathrm{BR}})$; **(B)** The two-dimensional drawing of **(A)**.

calculated by just obtaining the error probability threshold of the error correction code. Then according to the minimum standard, we can seek the balance between the number of quantum resources and their fidelity, which provides theoretical standards for experiments.

Two-qubit gate errors. In the previous sections, we only discussed the fidelity of single-qubit operations, but the set of general quantum gates also includes two-qubit gates, such as C-NOT gates. For a two-qubit gate, both qubit 1 and qubit 2 will have unitary errors with probability p respectively, resulting in a lower fidelity than single-qubit gate. We can regard the error of two qubits as two independent and unaffected operators' direct product $U_{\mathrm{qubit},\,1} \otimes U_{\mathrm{qubit},\,2}$, and the research on the fidelity of two-qubit gate is also worthy of our further study focus on.

Decoherence with driven field. In the decoherence part, we only perform the correlation calculation of natural decoherence (let the Hamiltonian $H = 0$). But decoherence occurs throughout the computing process, including when quantum operations are excuted. When an external field drives the quantum state evolution, decoherence occurs. And this process can be described by the master equation of the density matrix with a time-independent Hamiltonian H.

In quantum computing, single-qubit gate and two-qubit gate are usually fixed rotations rather than time-dependent continuous transformations. So for the master equation, in the part of the Heisenberg evolution $\partial_t \rho = -i/\hbar[H,\rho]$, the Hamiltonian H is time-independent, only ρ evolves with time. The incoherent evolution led by Lindblad operator $\mathcal{L}_k$ also affects the evolution of ρ in the master equation, so the qubit decoherence problem with driving field is relatively complicated, but it is also more suitable for studying the decoherence phenomenon during executing quantum operations.

6 CONCLUSION

In this work, we present a classification discussion about the sources of quantum errors according to the unitarity of the reduced evolutionary operators. For an unitary error, we can understand it as the precision error of the quantum operation. The effect of it is equivalent to the effect of an extra unitary rotation operation, and the quantum operation fidelity can be calculated according to the error probability threshold of the surface code. The non-unitary error can be understood as the decoherence process of qubits. We focus on the situation of natural decoherence, and calculate the qubit coherence duration that can be used for quantum error correction according to the evolution properties of decoherence.

Decoherence time and quantum gate operation fidelity are important parameters in the preparation of qubits and quantum control experimentally. Our work clarifies the mechanism of quantum error sources and provides theoretical support for laboratory technical.

DATA AVAILABILITY STATEMENT

The original contributions presented in the study are included in the article/Supplementary Material, further inquiries can be directed to the corresponding author.

AUTHOR CONTRIBUTIONS

KL independently did the calculations and wrote the manuscript.

FUNDING

This work was supported by National Natural Science Foundation of China under Grant No. 11725524.

ACKNOWLEDGMENTS

We thank Yitian Wang for fruitful discussions, and Professor Qingyu Cai's great supports.

REFERENCES

1. Shor PW. Algorithms for Quantum Computation: Discrete Logarithms and Factoring. In: Proceedings 35th annual symposium on foundations of computer science. Santa Fe, NM, USA: IEEE (1994). p. 124–34.
2. Shor PW. Polynomial-time Algorithms for Prime Factorization and Discrete Logarithms on a Quantum Computer. *SIAM Rev* (1999) 41:303–32. doi:10.1137/s0036144598347011
3. Grover LK. A Fast Quantum Mechanical Algorithm for Database Search. In: Proceedings of the twenty-eighth annual ACM symposium on Theory of computing (1996). p. 212–9. doi:10.1145/237814.237866
4. Grover LK. Quantum Mechanics Helps in Searching for a Needle in a Haystack. *Phys Rev Lett* (1997) 79:325–8. doi:10.1103/physrevlett.79.325
5. Bruzewicz CD, Chiaverini J, McConnell R, Sage JM. Trapped-ion Quantum Computing: Progress and Challenges. *Appl Phys Rev* (2019) 6:021314. doi:10.1063/1.5088164
6. Martinis JM, Cooper KB, McDermott R, Steffen M, Ansmann M, Osborn KD, et al. Decoherence in Josephson Qubits from Dielectric Loss. *Phys Rev Lett* (2005) 95:210503. doi:10.1103/physrevlett.95.210503
7. Arute F, Arya K, Babbush R, Bacon D, Bardin JC, Barends R, et al. Quantum Supremacy Using a Programmable Superconducting Processor. *Nature* (2019) 574:505–10. doi:10.1038/s41586-019-1666-5
8. Wu Y, Bao W-S, Cao S, Chen F, Chen M-C, Chen X, et al. Strong Quantum Computational Advantage Using a Superconducting Quantum Processor. *Phys Rev Lett* (2021) 127:180501. doi:10.1103/physrevlett.127.180501
9. Fowler AG, Mariantoni M, Martinis JM, Cleland AN. Surface Codes: Towards Practical Large-Scale Quantum Computation. *Phys Rev A* (2012) 86:032324. doi:10.1103/physreva.86.032324
10. Chen Z, Satzinger KJ, Atalaya J. Exponential Suppression of Bit or Phase Errors with Cyclic Error Correction. *Nature* (2021) 595:383.
11. Gidney C, Ekerå M. How to Factor 2048 Bit RSA Integers in 8 hours Using 20 Million Noisy Qubits. *Quantum* (2021) 5:433. doi:10.22331/q-2021-04-15-433
12. Gouzien É, Sangouard N. Factoring 2048-bit RSA Integers in 177 Days with 13 436 Qubits and a Multimode Memory. *Phys Rev Lett* (2021) 127:140503. doi:10.1103/physrevlett.127.140503
13. [Dataset] Nielsen MA, Chuang I. *Quantum Computation and Quantum Information* (2002).
14. Ithier G, Collin E, Joyez P, Meeson PJ, Vion D, Esteve D, et al. Decoherence in a Superconducting Quantum Bit Circuit. *Phys Rev B* (2005) 72:134519. doi:10.1103/physrevb.72.134519
15. Krantz P, Kjaergaard M, Yan F, Orlando TP, Gustavsson S, Oliver WD. A Quantum Engineer's Guide to Superconducting Qubits. *Appl Phys Rev* (2019) 6:021318. doi:10.1063/1.5089550
16. Ithier G. *Manipulation, Readout and Analysis of the Decoherence of a Superconducting Quantum Bit*. Ph.D. thesis. Paris, France: Université Pierre et Marie Curie-Paris VI (2005).
17. Olmschenk S, Younge KC, Moehring DL, Matsukevich DN, Maunz P, Monroe C. Manipulation and Detection of a Trapped Yb^+ Hyperfine Qubit. *Phys Rev A* (2007) 76:052314. doi:10.1103/physreva.76.052314
18. Devitt SJ, Munro WJ, Nemoto K. Quantum Error Correction for Beginners. *Rep Prog Phys* (2013) 76:076001. doi:10.1088/0034-4885/76/7/076001
19. Burkard G, Koch RH, DiVincenzo DP. Multilevel Quantum Description of Decoherence in Superconducting Qubits. *Phys Rev B* (2004) 69:064503. doi:10.1103/physrevb.69.064503
20. Clerk AA, Devoret MH, Girvin SM, Marquardt F, Schoelkopf RJ. Introduction to Quantum Noise, Measurement, and Amplification. *Rev Mod Phys* (2010) 82:1155–208. doi:10.1103/revmodphys.82.1155
21. Berns DM, Oliver WD, Valenzuela SO, Shytov AV, Berggren KK, Levitov LS, et al. Coherent Quasiclassical Dynamics of a Persistent Current Qubit. *Phys Rev Lett* (2006) 97:150502. doi:10.1103/physrevlett.97.150502
22. Bylander J, Gustavsson S, Yan F, Yoshihara F, Harrabi K, Fitch G, et al. Noise Spectroscopy through Dynamical Decoupling with a Superconducting Flux Qubit. *Nat Phys* (2011) 7:565–70. doi:10.1038/nphys1994
23. Redfield AG. On the Theory of Relaxation Processes. *IBM J Res Dev* (1957) 1:19–31. doi:10.1147/rd.11.0019
24. Bloch F. Generalized Theory of Relaxation. *Phys Rev* (1957) 105:1206–22. doi:10.1103/physrev.105.1206

Conflict of Interest: The author declares that the research was conducted in the absence of any commercial or financial relationships that could be construed as a potential conflict of interest.

Publisher's Note: All claims expressed in this article are solely those of the authors and do not necessarily represent those of their affiliated organizations, or those of the publisher, the editors and the reviewers. Any product that may be evaluated in this article, or claim that may be made by its manufacturer, is not guaranteed or endorsed by the publisher.

frontiers | Frontiers in Physics

ORIGINAL RESEARCH
published: 04 July 2022
doi: 10.3389/fphy.2022.875673

Rydberg Wire Gates for Universal Quantum Computation

Seokho Jeong[1], *Xiao-Feng Shi*[2], *Minhyuk Kim*[1] *and Jaewook Ahn*[1]*

[1]Department of Physics, KAIST, Daejeon, South Korea, [2]School of Physics, Xidian University, Xi'an, China

Rydberg atom arrays offer flexible geometries of strongly interacting neutral atoms, which are useful for many quantum applications such as quantum simulation and quantum computation. Here, we consider an all-optical gate-based quantum computing scheme for the Rydberg atom arrays, in which auxiliary atoms (wire atoms) are used as a mean of quantum-mechanical remote-couplings among data-qubit atoms, and optical individual-atom addressing of the data and wire atoms is used to construct universal quantum gates of the data atoms. The working principle of our gates is to use the wire atoms for coupling mediation only, while leaving them in noncoupling ground states before and after each gate operation, which allows the double-excited states of data qubits to be accessible by a sequence of π or $\pi/2$ pulses addressing the data and wire atoms. Optical pulse sequences are constructed for standard one-, two-, and multi-qubit gates, and the arbitrary two-qubit state preparation is considered for universal computation prospects. We further provide a detailed resource estimate for an experimental implementation of this scheme in a Rydberg quantum simulator.

Keywords: quantum gates, Rydberg atom, CNOT, Toffoli, quantum computation

OPEN ACCESS

Edited by:
Aixi Chen,
Zhejiang Sci-Tech University, China

Reviewed by:
Guin-Dar Lin,
National Taiwan University, Taiwan
Qing Ai,
Beijing Normal University, China

***Correspondence:**
Jaewook Ahn
jwahn@kaist.ac.kr

Specialty section:
This article was submitted to Quantum Engineering and Technology, a section of the journal Frontiers in Physics

Received: *14 February 2022*
Accepted: *23 May 2022*
Published: *04 July 2022*

Citation:
Jeong S, Shi X-F, Kim M and Ahn J (2022) Rydberg Wire Gates for Universal Quantum Computation. Front. Phys. 10:875673. doi: 10.3389/fphy.2022.875673

1 INTRODUCTION

Quantum computing is being actively studied as a mean to revolutionize humankind's computational capability beyond the limits of digital computers [1, 2]. Quantum computing hardware are two-level physical systems, which we refer to as qubits hereafter, and quantum computation performs operations of universal quantum gates on them. Gate-based quantum computations have been demonstrated in many physical systems, including linear optics [3, 4], circuit quantum electrodynamics of superconductor [5–7], trapped ions [8–10], defects in solid-state materials [11, 12], and neutral atoms [13, 14].

Neutral atoms have been considered for gate-based quantum computations using interactions between the Rydberg atoms [15, 16]. The advantages of using Rydberg atoms are strong dipole–dipole interactions that can be switched on and off by fast laser excitation, large-scale atom arrays that can be prepared with almost any desired geometries and topologies [17–19], and stable ground hyperfine states that can be used for long-term quantum information. Quantum gates using Rydberg atoms can utilize the distance-dependent interactions [20] or the Rydberg blockade effect which prohibits adjacent atoms from being excited to a Rydberg state [21, 22]. There are many Rydberg atom schemes for quantum gates and entanglements [23–26] and experimental demonstrations [27–31, 33, 34]. The single-qubit gate fidelity of the recent demonstrations was recorded 0.97 in the alkali atom system [29] and 0.99 in the alkaline-earth atomic system [31]. Many of these previous studies are based on coding quantum information in the stable states, which are the hyperfine-Zeeman substates, requiring a hybrid microwave or Raman excitation scheme in addition to Rydberg atom excitation.

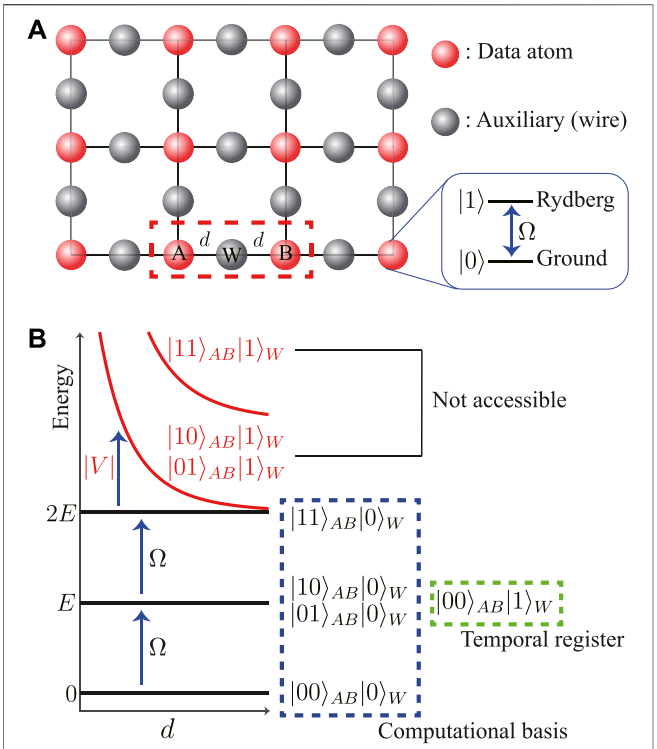

FIGURE 1 | The Rydberg wire gate scheme: **(A)** A 2D atomic array consists of data atoms (red spheres) and auxiliary (wire) atoms (gray spheres). Atomic ground state $|0\rangle$ and Rydberg state $|1\rangle$ are used for the two-level system of each atom. Wire atoms, e.g., *W*, mediate the couplings between two adjacent data atoms, e.g., *A* and *B* which are separated from *W* by a distance *d*. **(B)** The energy level diagram of the three atoms, *A*, *W*, and *B*. We use four computational basis states, $|00\rangle_{AB}|0\rangle_W$, $|01\rangle_{AB}|0\rangle_W$, $|10\rangle_{AB}|0\rangle_W$, and $|11\rangle_{AB}|0\rangle_W$ (in the blue dashed rectangle), out of five accessible states including $|00\rangle_{AB}|1\rangle_W$, which is considered as a temporal register (in the light green dashed rectangle). The other states, $|10\rangle_{AB}|1\rangle_W$, $|01\rangle_{AB}|1\rangle_W$, and $|11\rangle_{AB}|1\rangle_W$ are not accessible due to the Rydberg blockade.

In this article, we consider an all-optical quantum gate scheme in a Rydberg atom array, which does not resort to the ground sublevels and, instead, utilizes auxiliary atoms (wire atoms) to mediate coupling among qubit atoms (data atoms), and single-atom addressing operations. When we use a Rydberg state and ground state to be the two qubit states for a data qubit and use a cluster of data and wire qubits in a Rydberg atom array, in which the wire atoms between the data qubits mediate interactions between the data atoms, by a sequence of single-atom addressing operations. The advantage of this setup comes in twofold. First, the gates are all realized with fast laser excitation of the ground-Rydberg transitions, so that the quantum circuit for a certain computational task (including digital quantum simulation) can be carried out fast. Second, the distance between the data atoms can be large, for which analyses shown later with practical and currently available resources estimates that, for example, a **CZ** gate between two atoms separated about 19 μm could be created with a high fidelity over 98% within a duration $2\pi/\Omega$, where Ω is the Rydberg Rabi frequency.

In the rest of the article, we first outline the main idea of the quantum wire gates based on the Rydberg interaction and single-atom addressing in **Section 2**, and then construct single- and two-qubit gates in **Sections 3**, **4**. We then discuss the general two-qubit state generation and multi-qubit gates in **Sections 5**, **6**. Experimental implementations, gate performances, and alternative schemes are discussed in **Section 7**.

2 SINGLE-ATOM ADDRESSING IN A RYDBERG-ATOM SYSTEM

We aim to construct quantum gates with a sequence of individual-atom addressing in an array of atoms. We consider a two-dimensional (2D) array of atoms as shown in **Figure 1A**. In the Rydberg blockade regime, adjacent two atoms are inhibited from being excited to an antiblockade state, $|11\rangle$, so the computational space of the two atoms is limited to $\{|00\rangle, |01\rangle, |10\rangle\}$ excluding $|11\rangle$ (the antiblockade two-atom state), when the two-level system, $\{|0\rangle, |1\rangle\}$, is defined with the ground and Rydberg states of each atom. However, because $|11\rangle$ is necessary for general quantum computation, we use the auxiliary atoms (which we refer to as wire atoms, hereafter) to mediate couplings among the data atoms. In **Figure 1A**, data atoms are illustrated with red spheres and wire atoms are with gray spheres.

In the three-atom system, *AWB* in **Figure 1A**, *A* and *B* are the data atoms and *W* is the wire atom to couple *A* and *B*. When the wire atom is excited to $|1\rangle$, only for data processing of $|AB\rangle$ and otherwise left to be $|0\rangle_W$, there are five computational base states $|00\rangle_{AB}|0\rangle_W$, $|01\rangle_{AB}|0\rangle_W$, $|10\rangle_{AB}|0\rangle_W$, $|11\rangle_{AB}|0\rangle_W$, and $|00\rangle_{AB}|1\rangle_W$. Here, the first four base states are the computational basis for the two-data (AB) system and the last $|00\rangle_{AB}|1\rangle_W$ can be considered as a temporal register, as in **Figure 1B**. There are three available atom addressings:

$$\tilde{W}(\Theta,\phi) = e^{-\frac{i}{\hbar}\int H_W dt}, \tag{1a}$$

$$\tilde{A}(\Theta,\phi) = e^{-\frac{i}{\hbar}\int \left(\frac{\hbar\Omega}{2}\hat{n}_\phi\cdot\vec{\sigma}^A + Vn_W n_A\right)dt}, \tag{1b}$$

$$\tilde{B}(\Theta,\phi) = e^{-\frac{i}{\hbar}\int \left(\frac{\hbar\Omega}{2}\hat{n}_\phi\cdot\vec{\sigma}^B + Vn_W n_B\right)dt}, \tag{1c}$$

where Θ and ϕ are the Rabi rotation angle and axis, respectively. H_W is the Hamiltonian of single-addressing of W given by

$$H_W = \frac{\hbar\Omega}{2}\hat{n}_\phi\cdot\vec{\sigma}^W + Vn_W(n_A + n_B) \tag{2}$$

in the Rydberg blockade regime of adjacent atoms, i.e., $d < d_B < \sqrt{2}d$, where d and d_B are the interatom and blockade distances, respectively. Ω is the Rabi frequency, $\hat{n}_\phi$ is the rotational axis defined by a laser phase ϕ, $V = C_6/d^6$ is the van der Waals interaction with coefficient C_6, and $\vec{\sigma} = (\sigma_x, \sigma_y, \sigma_z)$ is the Pauli vector and $n = (1 - \sigma_z)/2$ is the excitation number.

It is noted that the atom-addressing operations in **Eqs 1a–c** are three-qubit gates. We intend to use them for general quantum

computations of the data AB atoms. $\tilde{W}$ changes $|00\rangle_{AB}|0\rangle_W$ to $|00\rangle_{AB}|1\rangle_W$ and preserves all the other states and their superpositions. Thus, the $\tilde{W}$ operation is the inverted controlled rotation gate, where AB are the control qubits and W is the target qubit. The other three operators are reduced to single- and two-atom rotations in the data-qubit (AB) basis as

$$\mathbf{R}_A \otimes \mathbf{I}_B = \langle 0|_W \tilde{A}|0\rangle_W, \tag{3a}$$

$$\mathbf{I}_A \otimes \mathbf{R}_B = \langle 0|_W \tilde{B}|0\rangle_W, \tag{3b}$$

$$\mathbf{R}_A \otimes \mathbf{R}_B = \langle 0|_W \tilde{A}\tilde{B}|0\rangle_W, \tag{3c}$$

where $\mathbf{R}$ is the single-qubit rotation and $\mathbf{I}$ is the identity.

3 STANDARD ONE-QUBIT GATES

With the atom-addressing operations, $\tilde{W}$, $\tilde{A}$, and $\tilde{B}$, in **Eqs 1a–c**, we construct standard one-qubit gates which include Pauli gates, **X**, **Y**, and **Z**, general rotation $\mathbf{R}(\Theta, \phi)$, Hadamard gate **H**, and phase gate, **P**.

Pauli gates rotate the quantum state of one atom, while leaving the other atoms unchanged. For the data atoms, A and B, Pauli **X**-gates are given by

$$\mathbf{X}_A \otimes \mathbf{I}_B = e^{i\alpha}\langle 0|_W \tilde{X}_A|0\rangle_W, \tag{4a}$$

$$\mathbf{I}_A \otimes \mathbf{X}_B = e^{i\alpha}\langle 0|_W \tilde{X}_B|0\rangle_W, \tag{4b}$$

where $\tilde{X}_A = \tilde{A}(\pi, 0)$, $\tilde{X}_B = \tilde{B}(\pi, 0)$, and $\alpha = \pi/2$ is the global phase. Likewise, Pauli **Y** and **Z** gates are given by

$$\mathbf{Y}_A \otimes \mathbf{I}_B = e^{i\alpha}\langle 0|_W \tilde{Y}_A|0\rangle_W, \tag{5a}$$

$$\mathbf{I}_A \otimes \mathbf{Y}_B = e^{i\alpha}\langle 0|_W \tilde{Y}_B|0\rangle_W, \tag{5b}$$

$$\mathbf{Z}_A \otimes \mathbf{I}_B = e^{i\alpha}\langle 0|_W \tilde{X}_A\tilde{Y}_A|0\rangle_W, \tag{5c}$$

$$\mathbf{I}_A \otimes \mathbf{Z}_B = e^{i\alpha}\langle 0|_W \tilde{X}_B\tilde{Y}_B|0\rangle_W, \tag{5d}$$

where $\tilde{Y}_A = \tilde{A}(\pi, \pi/2)$ and $\tilde{Y}_B = \tilde{B}(\pi, \pi/2)$. The general rotations are given by

$$\mathbf{R}_A(\Theta, \phi) \otimes \mathbf{I}_B = \langle 0|_W \tilde{A}(\Theta, \phi)|0\rangle_W, \tag{6a}$$

$$\mathbf{I}_A \otimes \mathbf{R}_B(\Theta, \phi) = \langle 0|_W \tilde{B}(\Theta, \phi)|0\rangle_W. \tag{6b}$$

The Hadamard gate, **H**, converts the quantum states, $|0\rangle$ and $|1\rangle$, to the superposition states, $|+\rangle = (|0\rangle + |1\rangle)/\sqrt{2}$ or $|-\rangle = (|0\rangle - |1\rangle)/\sqrt{2}$, respectively. The Hadamard gate is identical to $e^{i\pi/4}\mathbf{X}\sqrt{\mathbf{Y}}$, given by

$$\mathbf{H}_A \otimes \mathbf{I}_B = e^{i\alpha}\langle 0|_W \tilde{X}_A\sqrt{\tilde{Y}_A}|0\rangle_W, \tag{7a}$$

$$\mathbf{I}_A \otimes \mathbf{H}_B = e^{i\alpha}\langle 0|_W \tilde{X}_B\sqrt{\tilde{Y}_B}|0\rangle_W, \tag{7b}$$

where $\sqrt{\tilde{Y}_A} = \tilde{A}(\pi/2, \pi/2)$ and $\sqrt{\tilde{Y}_B} = \tilde{B}(\pi/2, \pi/2)$ are the pseudo-Hadamard gates. $\alpha = \pi/2$.

The phase gates, $\mathbf{P}_A(\phi)$ and $\mathbf{P}_B(\phi)$, are given by

$$\mathbf{P}_A(\phi) \otimes \mathbf{I}_B = e^{i\phi/2}\langle 0|_W \tilde{X}_A^\dagger \tilde{A}(\pi, \phi/2)|0\rangle_W, \tag{8a}$$

$$\mathbf{I}_A \otimes \mathbf{P}_B(\phi) = e^{i\phi/2}\langle 0|_W \tilde{X}_B^\dagger \tilde{B}(\pi, \phi/2)|0\rangle_W. \tag{8b}$$

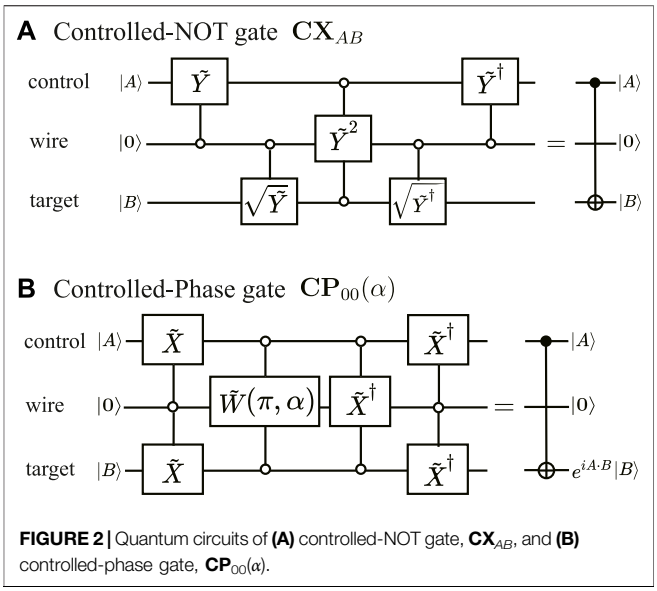

FIGURE 2 | Quantum circuits of **(A)** controlled-NOT gate, $\mathbf{CX}_{AB}$, and **(B)** controlled-phase gate, $\mathbf{CP}_{00}(\alpha)$.

S and **T** gates are obtained as $\mathbf{S}_A = \mathbf{P}_A(\pi/2)$, $\mathbf{S}_B = \mathbf{P}_B(\pi/2)$, $\mathbf{T}_A = \mathbf{P}_A(\pi/4)$, and $\mathbf{T}_B = \mathbf{P}_B(\pi/4)$.

The global phase, α, of the abovementioned gates can be eliminated with a global phase gate. One example is

$$\begin{aligned}\mathbf{Ph}(\alpha) = {} & \langle 0|_W \tilde{Y}_B\tilde{X}_W^\dagger\tilde{W}(\pi, \alpha)\tilde{Y}_{AB}^\dagger\tilde{X}_W^\dagger\tilde{W}(\pi, \alpha) \\ & \times \tilde{Y}_B^\dagger\tilde{X}_W^\dagger\tilde{W}(\pi, \alpha)\tilde{Y}_{AB}\tilde{X}_W^\dagger\tilde{W}(\pi, \alpha)|0\rangle_W,\end{aligned} \tag{9}$$

which is a combination of four two-qubit phase rotations, $|00\rangle \rightarrow e^{i\alpha}|00\rangle$ which is performed by $\tilde{X}_W^\dagger\tilde{W}(\pi, \alpha)$, $|01\rangle \rightarrow e^{i\alpha}|01\rangle$ by $\tilde{Y}_B\tilde{X}_W^\dagger\tilde{W}(\pi, \alpha)\tilde{Y}_B^\dagger$, $|10\rangle \rightarrow e^{i\alpha}|10\rangle$ by $\tilde{Y}_A^\dagger\tilde{X}_W^\dagger\tilde{W}(\pi, \alpha)\tilde{Y}_A$, and $|11\rangle \rightarrow e^{i\alpha}|11\rangle$ by $\tilde{Y}_{AB}^\dagger\tilde{X}_W^\dagger\tilde{X}_W(\pi, \alpha)\tilde{Y}_{AB}$, where $\tilde{Y}_{AB}$ denotes $\tilde{Y}_A\tilde{Y}_B$.

4 STANDARD TWO-QUBIT GATES

Now, we consider the standard two-qubit gates including the controlled-NOT gate, **CNOT**, the swap gate, **SWAP**, and the controlled-phase gate, **CP**.

The controlled-NOT gate, **CNOT**, flips the target qubit (the second qubit) only when the control qubit (the first qubit) is in $|1\rangle$, i.e., $|AB\rangle \rightarrow |A, A \oplus B\rangle$, which is also the controlled **X**-gate, i.e., **CNOT** = **CX**. With the atom addressing, $\mathbf{CX}_{AB}$ and $\mathbf{CX}_{BA}$ are, respectively, given by

$$\mathbf{CX}_{AB} = \langle 0|_W \tilde{Y}_A^\dagger\sqrt{\tilde{Y}_B^\dagger}\tilde{Y}_W^2\sqrt{\tilde{Y}_B}\tilde{Y}_A|0\rangle_W, \tag{10a}$$

$$\mathbf{CX}_{BA} = \langle 0|_W \tilde{Y}_B^\dagger\sqrt{\tilde{Y}_A^\dagger}\tilde{Y}_W^2\sqrt{\tilde{Y}_A}\tilde{Y}_B|0\rangle_W, \tag{10b}$$

of which the sequence can be understood as follows: In $\mathbf{CX}_{AB}$, $\tilde{Y}_W^2$ at the center works as an inverted-**CZ** gate, which flips only the sign of the coefficient of $|00\rangle_{AB}|0\rangle_W$. When this is multiplied by $\tilde{Y}_{AB}$ from one side and by its Hermitian conjugate from the other side, we get the controlled-Z gate, similarly as in Ref. [32], i.e.,

$$\mathbf{CZ}_{AB} = \mathbf{CZ}_{BA} = \langle 0|_W \tilde{Y}_{AB}^\dagger\tilde{Y}_W^2\tilde{Y}_{AB}|0\rangle_W, \tag{11}$$

which is then multiplied by $\sqrt{Y_A}$ and its Hermitian conjugate, to attain $\mathbf{CX}_{AB}$. The quantum circuit of $\mathbf{CX}_{AB}$ is presented in **Figure 2A**. Likewise, the controlled-Y gates are given by

$$\mathbf{CY}_{AB} = \langle 0|_W \tilde{Y}_A^\dagger \sqrt{\tilde{X}_B^\dagger} \tilde{Y}_W^2 \sqrt{\tilde{X}_B} \tilde{Y}_A |0\rangle_W, \tag{12a}$$

$$\mathbf{CY}_{BA} = \langle 0|_W \tilde{Y}_B^\dagger \sqrt{\tilde{X}_A^\dagger} \tilde{Y}_W^2 \sqrt{\tilde{X}_A} \tilde{Y}_B |0\rangle_W. \tag{12b}$$

SWAP gate performs the state swapping of two qubits, i.e., $|AB\rangle \rightarrow |BA\rangle$, which is also the exchange of the coefficients of $|01\rangle$ and $|10\rangle$. In our atom-addressing scheme, an **X**-gate version of **SWAP** gate is given by

$$\mathbf{SWAP} = \langle 0|_W \tilde{X}_A \tilde{X}_W \tilde{X}_{AB} \tilde{X}_W \tilde{X}_{AB}^\dagger \tilde{X}_W \tilde{X}_A^\dagger |0\rangle_W, \tag{13}$$

in which the first three-pulse combination, $X_A^\dagger \tilde{X}_W \tilde{X}_A^\dagger$, exchanges the coefficients of $|10\rangle_{AB}|0\rangle_W$ and $|00\rangle_{AB}|1\rangle_W$. The coefficient of $|00\rangle_{AB}|1\rangle_W$ is then exchanged with that of $|01\rangle_{AB}|0\rangle_W$ by the second combination, $\tilde{X}_B \tilde{X}_W \tilde{X}_B^\dagger$, before the coefficient of $|00\rangle_{AB}|1\rangle_W$ is returned to $|10\rangle_{AB}|0\rangle_W$ by $\tilde{X}_A \tilde{X}_W \tilde{X}_A$.

The controlled-phase gate, $\mathbf{CP}(\alpha)$, puts the local phase of $|11\rangle$ of AB data qubits. In our atom-addressing scheme, W-atom addressing, $\tilde{W}(\pi, \alpha)$, converts $|00\rangle_{AB}|0\rangle_W$ to $-ie^{i\alpha}|00\rangle_{AB}|1\rangle_W$ and $\tilde{W}(\pi, \pi)\tilde{W}(\pi, \alpha)$ converts $|00\rangle_{AB}$ to $e^{i\alpha}|00\rangle_{AB}$, so $\mathbf{CP}_{00}(\alpha)$, which puts the local phase of $|00\rangle$, is given by

$$\mathbf{CP}_{00}(\alpha) = \langle 0|_W \tilde{X}_W^\dagger \tilde{W}(\pi, \alpha)|0\rangle_W. \tag{14}$$

The quantum circuit of $\mathbf{CP}_{00}(\alpha)$ is presented in **Figure 2B**. The standard $\mathbf{CP}(\alpha) = \mathbf{CP}_{11}(\alpha)$ is, therefore, obtained by

$$\mathbf{CP}(\phi) = \langle 0|_W \tilde{X}_{AB}^\dagger \tilde{X}_W^\dagger \tilde{W}(\pi, \phi) \tilde{X}_{AB}|0\rangle_W, \tag{15}$$

where the $\mathbf{CP}_{00}(\alpha)$ in the middle is multiplied by $\tilde{X}_{AB}$ from one side and by the conjugate of $\tilde{X}_{AB}$ from the other side, which respectively exchanges and exchanges back the coefficients of $|00\rangle$ and $|11\rangle$. As a result, we get $|11\rangle \rightarrow e^{i\alpha}|11\rangle$. Similarly, $\mathbf{CP}_{01}(\phi)$ and $\mathbf{CP}_{10}(\phi)$ are obtained as

$$\mathbf{CP}_{01}(\phi) = \langle 0|_W \tilde{X}_B^\dagger \tilde{X}_W^\dagger \tilde{W}(\pi, \phi) \tilde{X}_B|0\rangle_W, \tag{16}$$

$$\mathbf{CP}_{10}(\phi) = \langle 0|_W \tilde{X}_A^\dagger \tilde{X}_W^\dagger \tilde{W}(\pi, \phi) \tilde{X}_A|0\rangle_W. \tag{17}$$

5 ARBITRARY TWO-QUBIT STATE GENERATION

The general two-qubit state generation is to find a unitary operation which transforms the initial state $|00\rangle_{AB}$ to an arbitrary two-qubit state, i.e.,

$$U|00\rangle = a_0|00\rangle + a_1|01\rangle + a_2|10\rangle + a_3|11\rangle. \tag{18}$$

The above U can be in principle constructed with the single- and two-qubit gates. Also, it is sufficient to define the general rotations and at least one inversion operation among the two-qubit base states, $\{|00\rangle, |01\rangle, |10\rangle, |11\rangle\}$ of AB atoms.

Inversion operations are the reflection of the two-qubit state vector about a given plane. For example, **CZ** inverts the state vector about the plane orthogonal to $|11\rangle$, i.e., $\tilde{M}_{11} = \mathbf{CZ}$. Likewise, $\tilde{M}_{00} = \mathbf{CP}_{00}(\pi)$, $\tilde{M}_{01} = \mathbf{CP}_{01}(\pi)$, and $\tilde{M}_{10} = \mathbf{CP}_{10}(\pi)$.

General rotations are the base-pair rotation between a pair of two-qubit base states, i.e., $\tilde{R}_{jk}(\Theta, \phi)|j\rangle = \cos\frac{\Theta}{2}|j\rangle - ie^{i\phi}\sin\frac{\Theta}{2}|k\rangle$ for $j, k \in \{|00\rangle, |01\rangle, |10\rangle, |11\rangle\}$. $\tilde{R}_{00,01}(\Theta, \phi)$ rotates the quantum information stored in the base pair, $|00\rangle$ and $|01\rangle$, which are, for example, given by

$$\tilde{R}_{00,01}(\Theta, \phi) = \langle 0|_W \tilde{X}_W \tilde{X}_B \tilde{W}(\Theta, -\phi) \tilde{X}_B^\dagger \tilde{X}_W^\dagger |0\rangle_W, \tag{19}$$

where the first two π-pulse operations, $\tilde{X}_B^\dagger$ and $\tilde{X}_W^\dagger$, perform $|00\rangle_{AB}|0\rangle_W \rightarrow |00\rangle_{AB}|1\rangle_W$ and $|01\rangle_{AB}|0\rangle_W \rightarrow |00\rangle_{AB}|0\rangle_W$, respectively, which means that the quantum state of B atom is transferred to W atom. Then, the state vector of W atom is rotated by $\tilde{W}(\Theta, -\phi)$ and transferred back to B atom by the last two π-pulse operations. Similarly, other rotations can be obtained as follows:

$$\tilde{R}_{00,11}(\Theta, \phi) = \langle 0|_W \tilde{X}_W \tilde{X}_{AB} \tilde{W}(\Theta, -(\phi + \pi/2)) \tilde{X}_{AB}^\dagger \tilde{X}_W^\dagger |0\rangle_W, \tag{20a}$$

$$\tilde{R}_{01,10}(\Theta, \phi) = \langle 0|_W \tilde{X}_B \tilde{X}_W \tilde{X}_{AB} \tilde{W}(\Theta, -(\phi + \pi/2)) \tilde{X}_{AB}^\dagger \tilde{X}_W^\dagger \tilde{X}_B^\dagger |0\rangle_W, \tag{20b}$$

$$\tilde{R}_{01,11}(\Theta, \phi) = \langle 0|_W \tilde{X}_B \tilde{X}_W \tilde{X}_A \tilde{W}(\Theta, -\phi) \tilde{X}_A^\dagger \tilde{X}_W^\dagger \tilde{X}_B^\dagger |0\rangle_W, \tag{20c}$$

$$\tilde{R}_{10,11}(\Theta, \phi) = \langle 0|_W \tilde{X}_A \tilde{X}_W \tilde{X}_B, \tilde{W}(\Theta, -\phi) \tilde{X}_B^\dagger \tilde{X}_W^\dagger \tilde{X}_A^\dagger |0\rangle_W. \tag{20d}$$

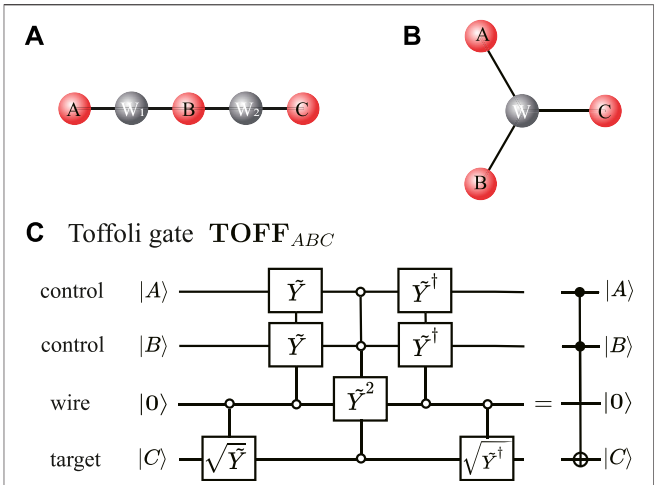

FIGURE 3 | (A) A 5-atom chain and **(B)** an Y-shape atomic array to implement the multi-qubit wire gates. **(C)** Quantum circuit of the Toffoli gate **TOFF**$_{ABC}$ for the control atoms A, B and the target atom C.

6 MULTI-QUBIT GATES

While the multi-qubit gates can be decomposed to a sequence of single- and two-qubit elementary gates, the standard three-qubit gates require many elementary gates. For example, a Toffoli gate needs 15 or 17 elementary gates. In the following, we consider the possibilities of using wire atom arrangements which can reduce the number of gates significantly for the Toffoli and **CCZ** gates.

If we use the simple linear configuration, as in **Figure 3A**, of *ABC* data atoms and two wire atoms W_1 and W_2, their pulse-sequence solutions, e.g., for the Toffoli and **CCZ** gates, are rather complicated:

$$\mathbf{CCZ} = \langle 00|_{W_{12}} \sqrt{\tilde{Y}_C} \tilde{Y}_{AB} \tilde{X}^{\dagger}_{W_2} \tilde{Y}_{W_1} \tilde{X}^{\dagger}_{BC} \sqrt{\tilde{X}_{W_2}} \tilde{X}^2_{BC}, \times \sqrt{\tilde{X}^{\dagger}_{W_2}} \tilde{X}^{\dagger}_{BC} \tilde{X}_{W_{12}} \tilde{Y}^{\dagger}_{AB} \sqrt{\tilde{Y}^{\dagger}_C} |00\rangle_{W_{12}}, \quad (21)$$

$$\mathbf{TOFF} = \langle 00|_{W_{12}} \sqrt{\tilde{Y}^{\dagger}_B \tilde{Y}_C} \tilde{Y}_{AB} \tilde{X}^{\dagger}_{W_2} \tilde{Y}_{W_1} \tilde{X}^{\dagger}_{BC} \sqrt{\tilde{X}_{W_2}} \tilde{X}^2_{BC} \times \sqrt{\tilde{X}^{\dagger}_{W_2}} \tilde{X}^{\dagger}_{BC} \tilde{X}_{W_{12}} \tilde{Y}^{\dagger}_{AB} \sqrt{\tilde{Y}^{\dagger}_C \tilde{Y}_B} |00\rangle_{W_{12}}. \quad (22)$$

Instead, if we use the *Y*-shape configuration, as shown in **Figure 3B**, which has one wire atom, *W*, which couples all the three data atoms, *ABC*, simultaneously, their solutions are simple, given as the extensions of **CX** and **CZ** in **Eqs 10a**,b, **11**. The **CCZ** utilizes the fact that $\langle 0|_W \tilde{Y}^2_W |0\rangle_W$ is the inverted-**CCZ**, to attain

$$\mathbf{CCZ} = \langle 0|_W \tilde{Y}^{\dagger}_{ABC} \tilde{Y}^2_W \tilde{Y}_{ABC} |0\rangle_W, \quad (23)$$

where $\tilde{Y}_{ABC} = \tilde{Y}_A \tilde{Y}_B \tilde{Y}_C$ and $\tilde{Y}^{\dagger}_{ABC}$ are for the bitwise flip and flip-back of the data atoms, applied before and after to change the inverted-**CCZ** to **CCZ**. The Toffoli gate of the *AB* controls and *C* target is also obtained as

$$\mathbf{TOFF}_{\mathrm{ABC}} = \langle 0|_{\mathrm{W}} \sqrt{\tilde{Y}^{\dagger}_{\mathrm{C}}} \tilde{Y}^{\dagger}_{\mathrm{AB}} \tilde{Y}^2_{\mathrm{W}} \tilde{Y}_{\mathrm{AB}} \sqrt{\tilde{Y}_{\mathrm{C}}} |0\rangle_{\mathrm{W}}, \quad (24)$$

where $\sqrt{\tilde{Y}^{\dagger}_{\mathrm{C}}}$ and $\sqrt{\tilde{Y}_{\mathrm{C}}}$ on both ends are the pseudo-Hadamard and its inverse acting on the target. The quantum circuit of $\mathbf{TOFF}_{\mathrm{ABC}}$ is presented in **Figure 3C**.

7 DISCUSSION AND CONCLUSION

Experimental implementation: Rydberg wire gates introduced previously can be implemented in optical-tweezer atomic systems, which have been previously demonstrated elsewhere [20, 29, 30]. As an example, we consider three rubidium (^{87}Rb) atoms arranged in the linear chain geometry. Once the single atoms are loaded to individual tweezers from magneto-optical trap, the atoms are prepared to one of the magnetic sublevels in hyperfine ground states as the ground state $|0\rangle$ (for example, $|0\rangle = |5S_{1/2}, F = 2, m_F = 2\rangle$). The states $|0\rangle$ and $|1\rangle$ are coupled by Rydberg state excitation lasers, and in general two-photon excitation is used to transit to $|nS\rangle$ or $|nD\rangle$ Rydberg levels *via* $|5P_{3/2}\rangle$ with 780 and 480 nm lights. For $|1\rangle = |69S_{1/2}\rangle$, the atoms undergo van der Waals interaction, and the interaction strength when the interatomic distance $d = 7\,\mu$m becomes $V = |C_6|/d^6 = (2\pi)6.2$ MHz, where $C_6 = -(2\pi)732\ \mathrm{GHz}\cdot\mu\mathrm{m}^6$. Individual-atom addressing to couple between $|0\rangle$ and $|1\rangle$ can be implemented by diffracting multiple laser beams from an acousto-optic modulator (AOM), then focusing to the individual atoms. The switching of individual beams can be done by controlling the amplitude and frequency of radio-frequency wave to AOM. The individual addressing lasers can be either ground-Rydberg resonant lasers [30] or far-detuned lasers [35], in which the latter suppress the Rydberg state excitation with the additional AC Stark shift combined with global resonant lasers.

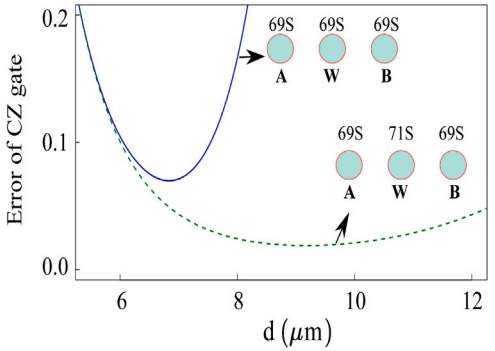

FIGURE 4 | Performance estimation of the **CZ** gate for the present van der Waals scheme (solid line) in comparison with the Förster resonance scheme (dashed line).

Gate performance: the performance of the Rydberg wire gate schemes can be estimated with numerical calculations. In **Figure 4**, we estimate the average fidelity of $\mathbf{CP}_{00}(\pi)$ gate for all the initial states $\{|00\rangle_{AB}, |01\rangle_{AB}, |10\rangle_{AB}, |11\rangle_{AB}\}$ using the time-dependent Schrödinger equations. For $|1\rangle = |69S_{1/2}, m_j = 1/2\rangle$, the results with respect to the interatomic distance are shown with the solid line in **Figure 4**. For Rabi frequency $\Omega = (2\pi)$ 2 MHz, the gate duration is 0.5 μs. It is expected that the maximum fidelity $\mathcal{F}$ can be reached to 94% when the lattice constant is around 6.8 μm.

Gate imperfection sources: The sources of finite infidelities related to the Rydberg atomic properties can be characterized. The finite lifetime of Rydberg state gives imperfection to the transition to $|1\rangle$. For the lifetime of $|1\rangle$ to be τ, this gives the average gate error $\frac{9\pi}{4\Omega\tau}$ [36]. Another source of gate infidelity is the Rydberg blockade error: as the Rydberg interaction strength is proportional to $1/d^6$, the interaction strength within the blockade distance d_B is finite, and there is nonzero residual interactions outside. For the interaction strength, *V*, between a nearest neighbor Rydberg atomic pair, the gate error is given by $\frac{\hbar^2\Omega^2}{2V^2}$ for the initial state $|10\rangle_{AB}$, $|01\rangle_{AB}$ and $\frac{\hbar^2\Omega^2}{8V^2}$ for $|11\rangle_{AB}$ [37, 38]. In addition, the phase shift $\frac{2\pi V_2}{\hbar\Omega}$ occurs for the initial state $|11\rangle_{AB}$, due to the nonzero interactions between atom *A* and *B*. Considering all these error budgets, we estimate the average fidelity error as

$$1 - \mathcal{F} = \frac{9\pi}{4\Omega\tau} + \frac{9\hbar^2\Omega^2}{32V^2} + \frac{\pi V}{128\hbar\Omega}, \quad (25)$$

where the terms denote the Rydberg state decay error, the Rydberg blockade error, and the residual interaction error, respectively. Their estimated infidelity contributions are 4×10^{-3}, 2.04×10^{-2} and 9.12×10^{-2}, respectively, at $d = 6.8\,\mu$m. While our fidelity estimation considers limitedly sub-μs pulsed gate significantly shorter than the typical coherence time of Rydberg atoms, a detailed analysis, for example, in a large-scale quantum circuit requires many-body effects and open

quantum system dynamics [39–43].Toward the higher fidelity gates, we discuss methods to improve the gate fidelity to suppress the last two errors in **Eq. 25**. One approach is to utilize the dipole–dipole interaction by Förster resonance between the nearest neighbor atomic pair. Near the principal quantum number $n = 69$ discussed previously, there exist two transition channels between the Rydberg pair states, $|69S_{1/2} + 71S_{1/2}\rangle \leftrightarrow |69P_{3/2} + 70P_{1/2}\rangle$ and $|69S_{1/2} + 71S_{1/2}\rangle \leftrightarrow |69P_{1/2} + 70P_{3/2}\rangle$ by the dipole–dipole interaction, with Förster defects of 6.6 and 19.7 MHz, respectively [44]. This induces the dipole–dipole interaction with the strength of $V' = C_3/d^3$, where $C_3 = (2\pi)$ 12.32 GHz · μm^3, with the interatomic distance less than the crossover distance 11 μm [45]. In realizing the $\mathbf{CP}_{00}(\pi)$ gate, the atom W is to be excited to $|1'\rangle = |71S_{1/2}, m_j = 1/2\rangle$ state, while the data atoms A and B are excited to $|1\rangle$. Then, the interaction strength between $A(B)$ and W is increased due to the Förster resonance, so the interatomic distance can also be increased. This further reduces the long range residual van der Waals interaction between A and B, thus the gate infidelity can be suppressed. In **Figure 4**, we illustrate the improved performance of the $\mathbf{CP}_{00}(\pi)$ gate of the dipole–dipole interaction (the dashed line). The overall fidelities $\mathcal{F}$ are increased compared to the previous example, and the maximum reached to 98% at $d = 9.17$ μm.

Weakness of the Rydberg wire gates: The weakness of the present scheme is that the Rydberg states are not stable. There is a constant decay process occurring during the quantum control process. However, for a fast quantum control process, the decay-induced error can be relatively small for the decay error and is proportional to the Rydberg superposition time. Moreover, the quantum error correction can, in principle, be executed by the gates shown in this article, so that the error during the control process can be corrected. Because both the main control process and error correction are fast. Thanks to the fast pulsed operations of quantum wire gates, the overall speed to reach a wanted computational result can still surpass the traditional method of coding information with the stable hyperfine-Zeeman substates.

In summary, the Rydberg wire gates are proposed, which utilize auxiliary atoms to couple the data atoms. By coding the information with a ground-state qubit state and a Rydberg qubit state, the universal gate set can be realized based on the strong, local interactions of the neutral Rydberg atoms. The gates are realized by the fast laser excitation of Rydberg states, so that their speed can be fast, and the well-separated data atoms can be rapidly entangled. Fast entangling operations are important basic elements in a quantum circuit for large-scale quantum computation, and long-distance entanglement can greatly simplify complex operations between distant qubits in the array. The new idea of Rydberg wire gates can bring new prospective in neutral-atom quantum science and technology.

DATA AVAILABILITY STATEMENT

The original contributions presented in the study are included in the article/Supplementary Material. Further inquiries can be directed to the corresponding author.

AUTHOR CONTRIBUTIONS

JA conceived the idea. SJ, XF-S, and MK conducted the research and analysis. All contributed to the manuscript.

FUNDING

This research was supported by the Samsung Science and Technology Foundation (Grant No. SSTF-BA1301-52), National Research Foundation of Korea (Grant No. 2017R1E1A1A0107430), and Natural Science Foundation of China (Grant No. 12074300).

REFERENCES

1. Feynman RP. Simulating Physics with Computers. *Int J Theor Phys* (1982) 21: 467–88. doi:10.1007/bf02650179
2. Nielsen MA, Chuang I. *Quantum Computation and Quantum Information*. Cambridge: Cambridge Univ. Press (2002).
3. O'brien JL. *Opt Quan Comput Sci* (2007) 318:1567.
4. Kok P, Munro WJ, Nemoto K, Ralph TC, Dowling JP, Milburn GJ. Linear Optical Quantum Computing with Photonic Qubits. *Rev Mod Phys* (2007) 79: 135–74. doi:10.1103/revmodphys.79.135
5. Arute F, Arya K, Babbush R, Bacon D, Bardin JC, Barends R, et al. Quantum Supremacy Using a Programmable Superconducting Processor. *Nature* (2019) 574:505–10. doi:10.1038/s41586-019-1666-5
6. Krantz P, Kjaergaard M, Yan F, Orlando TP, Gustavsson S, Oliver WD. A Quantum Engineer's Guide to Superconducting Qubits. *Appl Phys Rev* (2019) 6:021318. doi:10.1063/1.5089550
7. Blais A, Grimsmo AL, Girvin SM, Wallraff A. Circuit Quantum Electrodynamics. *Rev Mod Phys* (2021) 93:025005. doi:10.1103/revmodphys.93.025005
8. Kielpinski D, Monroe C, Wineland DJ. Architecture for a Large-Scale Ion-Trap Quantum Computer. *Nature* (2002) 417:709–11. doi:10.1038/nature00784
9. Schindler P, Nigg D, Monz T, Barreiro JT, Martinez E, Wang SX, et al. A Quantum Information Processor with Trapped Ions. *New J Phys* (2013) 15: 123012. doi:10.1088/1367-2630/15/12/123012
10. Pogorelov I, Feldker T, Marciniak CD, Postler L, Jacob G, Kriegelsteiner O, et al. Compact Ion-Trap Quantum Computing Demonstrator. *PRX Quan* (2021) 2:020343. doi:10.1103/prxquantum.2.020343
11. van der Sar T, Wang ZH, Blok MS, Bernien H, Taminiau TH, Toyli DM, et al. Decoherence-protected Quantum gates for a Hybrid Solid-State Spin Register. *Nature* (2012) 484:82–6. doi:10.1038/nature10900
12. Childress L, Hanson R. Diamond NV Centers for Quantum Computing and Quantum Networks. *MRS Bull* (2013) 38:134–8. doi:10.1557/mrs.2013.20
13. Weiss DS, Saffman M. Quantum Computing with Neutral Atoms. *Phys Today* (2017) 70:44–50. doi:10.1063/pt.3.3626
14. Henriet L, Beguin L, Signoles A, Lahaye T, Browaeys A, Reymond G-O, et al. Quantum Computing with Neutral Atoms. *Quantum* (2020) 4:327. doi:10.22331/q-2020-09-21-327
15. Saffman M, Walker TG, Mølmer K. Quantum Information with Rydberg Atoms. *Rev Mod Phys* (2010) 82:2313–63. doi:10.1103/revmodphys.82.2313
16. Saffman M. Quantum Computing with Atomic Qubits and Rydberg Interactions: Progress and Challenges. *J Phys B: Mol Opt Phys* (2016) 49: 202001. doi:10.1088/0953-4075/49/20/202001
17. Kim M, Song Y, Kim J, Ahn J. Quantum Ising Hamiltonian Programming in Trio, Quartet, and Sextet Qubit Systems. *PRX Quan* (2020) 1:020323. doi:10.1103/PRXQuantum.1.020323

18. Song Y, Kim M, Hwang H, Lee W, Ahn J. Quantum Simulation of Cayley-Tree Ising Hamiltonians with Three-Dimensional Rydberg Atoms. *Phys Rev Res* (2021) 3:013286. doi:10.1103/PhysRevResearch.3.013286
19. Kim M, Kim K, Hwang J, Moon E-G, Ahn J. Rydberg Quantum Wires for Maximum Independent Set Problems. *Nat Phys* (2022). doi:10.1038/s41567-022-01629-5
20. Jo H, Song Y, Kim M, Ahn J. Rydberg Atom Entanglements in the Weak Coupling Regime. *Phys Rev Lett* (2020) 124:033603. doi:10.1103/PhysRevLett.124.033603
21. Gaëtan A, Miroshnychenko Y, Wilk T, Chotia A, Viteau M, Comparat D, et al. Observation of Collective Excitation of Two Individual Atoms in the Rydberg Blockade Regime. *Nat Phys* (2009) 5:115–8. doi:10.1038/nphys1183
22. Urban E, Johnson TA, Henage T, Isenhower L, Yavuz DD, Walker TG, et al. Observation of Rydberg Blockade between Two Atoms. *Nat Phys* (2009) 5:110–4. doi:10.1038/nphys1178
23. Jaksch D, Cirac JI, Zoller P, Rolston SL, Côté R, Lukin MD. Fast Quantum Gates for Neutral Atoms. *Phys Rev Lett* (2000) 85:2208–11. doi:10.1103/physrevlett.85.2208
24. Shi X-F. Deutsch, Toffoli, and CNOT Gates via Rydberg Blockade of Neutral Atoms. *Phys Rev Appl* (2018) 9:051001. doi:10.1103/physrevapplied.9.051001
25. Shi X-F. Transition Slow-Down by Rydberg Interaction of Neutral Atoms and a Fast Controlled-Not Quantum Gate. *Phys Rev Appl* (2020) 14:054058. doi:10.1103/physrevapplied.14.054058
26. Saffman M, Beterov II, Dalal A, Páez EJ, Sanders BC. Symmetric Rydberg Controlled-*Z* gates with Adiabatic Pulses. *Phys Rev A* (2020) 101:062309. doi:10.1103/physreva.101.062309
27. Isenhower L, Urban E, Zhang XL, Gill AT, Henage T, Johnson TA, et al. Demonstration of a Neutral Atom Controlled-Not Quantum Gate. *Phys Rev Lett* (2010) 104:010503. doi:10.1103/PhysRevLett.104.010503
28. Levine H, Keesling A, Omran A, Bernien H, Schwartz S, Zibrov AS, et al. High-Fidelity Control and Entanglement of Rydberg-Atom Qubits. *Phys Rev Lett* (2018) 121:123603. doi:10.1103/physrevlett.121.123603
29. Levine H, Keesling A, Semeghini G, Omran A, Wang TT, Ebadi S, et al. Parallel Implementation of High-Fidelity Multiqubit Gates with Neutral Atoms. *Phys Rev Lett* (2019) 123:170503. doi:10.1103/physrevlett.123.170503
30. Graham TM, Kwon M, Grinkemeyer B, Marra Z, Jiang X, Lichtman MT, et al. Rydberg-Mediated Entanglement in a Two-Dimensional Neutral Atom Qubit Array. *Phys Rev Lett* (2019) 123:230501. doi:10.1103/physrevlett.123.230501
31. Madjarov IS, Covey JP, Shaw AL, Choi J, Kale A, Cooper A, et al. High-fidelity Entanglement and Detection of Alkaline-Earth Rydberg Atoms. *Nat Phys* (2020) 16:857–61. doi:10.1038/s41567-020-0903-z
32. Maller KM, Lichtman MT, Xia T, Sun Y, Piotrowicz MJ, Carr AW, et al. Rydberg-blockade Controlled-Not Gate and Entanglement in a Two-Dimensional Array of Neutral-Atom Qubits. *Phys Rev A* (2015) 92:022336. doi:10.1103/physreva.92.022336
33. Graham TM, Song Y, Scott J, Poole C, Phuttitarn L, Jooya K, et al. Demonstration of Multi-Qubit Entanglement and Algorithms on a Programmable Neutral Atom Quantum Computer (2021). arXiv:2112.14589.
34. Schine N, Young AW, Eckner WJ, Martin MJ, Kaufman AM. Long-lived Bell States in an Array of Optical Clock Qubits (2021). arXiv:2111.14653.
35. Omran A, Levine H, Keesling A, Semeghini G, Wang TT, Ebadi S, et al. Generation and Manipulation of Schrödinger Cat States in Rydberg Atom Arrays. *Science* (2019) 365(6453):570–4. doi:10.1126/science.aax9743
36. Shi X-F. Rydberg Quantum gates Free from Blockade Error. *Phys Rev Appl* (2017) 7:064017. doi:10.1103/physrevapplied.7.064017
37. Saffman M, Walker TG. Analysis of a Quantum Logic Device Based on Dipole-Dipole Interactions of Optically Trapped Rydberg Atoms. *Phys Rev A* (2005) 72:022347. doi:10.1103/physreva.72.022347
38. Shi X-F. Quantum Logic and Entanglement by Neutral Rydberg Atoms: Methods and Fidelity. *Quan Sci. Technol.* (2022) 7:023002. doi:10.1088/2058-9565/ac18b8
39. Chen X-Y, Zhang N-N, He W-T, Kong X-Y, Tao M-J, Deng F-G, et al. Global Correlation and Local Information Flows in Controllable Non-markovian Open Quantum Dynamics. *Npj Quan Inf* (2022) 8:22. doi:10.1038/s41534-022-00537-z
40. Tao M-J, Zhang N-N, Wen P-Y, Deng F-G, Ai Q, Long G-L. Coherent and Incoherent Theories for Photosynthetic Energy Transfer. *Sci Bull* (2020) 65:318–28. doi:10.1016/j.scib.2019.12.009
41. Ishizaki A, Fleming GR. Theoretical Examination of Quantum Coherence in a Photosynthetic System at Physiological Temperature. *Proc Natl Acad Sci U.S.A* (2009) 106:17255–60. doi:10.1073/pnas.0908989106
42. Wang B-X, Tao MJ, Ai Q, Xin T, Lambert N, Ruan1 D, et al. Efficient Quantum Simulation of Photosynthetic Light Harvesting. *Npj Quan Inf* (2018) 4:5625. doi:10.1038/s41534-018-0102-2
43. Zhang N-N, Tao M-J, He W-T, Chen X-Y, Kong X-Y, Deng F-G, et al. Efficient Quantum Simulation of Open Quantum Dynamics at Various Hamiltonians and Spectral Densities. *Front Phys* (2021) 16:51501. doi:10.1007/s11467-021-1064-y
44. Weber S, Tresp C, Menke H, Urvoy A, Firstenberg O, Büchler HP, et al. Calculation of Rydberg Interaction Potentials. *J Phys B: Mol Opt Phys* (2017) 50:133001. doi:10.1088/1361-6455/aa743a
45. Walker TG, Saffman M. Consequences of Zeeman degeneracy for the van der Waals blockade between Rydberg atoms. *Phys Rev A* (2008) 77:032723. doi:10.1103/physreva.77.032723

Conflict of Interest: The authors declare that the research was conducted in the absence of any commercial or financial relationships that could be construed as a potential conflict of interest.

Publisher's Note: All claims expressed in this article are solely those of the authors and do not necessarily represent those of their affiliated organizations, or those of the publisher, the editors, and the reviewers. Any product that may be evaluated in this article, or claim that may be made by its manufacturer, is not guaranteed or endorsed by the publisher.

frontiers | Frontiers in Physics

ORIGINAL RESEARCH
published: 04 July 2022
doi: 10.3389/fphy.2022.907284

Topological Charge Measurement of the Mid-Infrared Vortex Beam *via* Spatially Dependent Four-Wave Mixing in an Asymmetric Semiconductor Double Quantum Well

Yi Song, Ling Li, Tao Shui*, Die Hu and Wen-Xing Yang**

School of Physics and Optoelectronic Engineering, Yangtze University, Jingzhou, China

We theoretically propose a scheme to measure the topological charge (TC) of a mid-infrared vortex beam *via* observing the intensity distribution of the four-wave mixing (FWM) field in an asymmetric semiconductor double quantum well. Due to the existence of Fano-type interferences, the special inherent interference takes place, and thus generates the interference-type phase and intensity patterns for the FWM field. Furthermore, it is demonstrated that the intensity and visibility of the interference-type intensity pattern can be drastically manipulated by adjusting the intensity and detuning the control field. Subsequently, we perform the TC measurement of the vortex driving field *via* directly monitoring the number of light spots of the FWM field. By choosing the suitable control parameters, the detectable value of the TC can reach to 120 with the visibility exceeding 0.97. Our scheme may provide the possibility for the realization of a mid-infrared OAM detector in a compact solid-state system.

Keywords: topological charge, optical vortex, semiconductor quantum well, Fano-type interference, four-wave mixing

OPEN ACCESS

Edited by:
Guangling Cheng,
East China Jiaotong University, China

Reviewed by:
Yuxuan Ren,
Fudan University, China
Jietai Jing,
East China Normal University, China

****Correspondence:***
Ling Li
lilingling504@126.com
Tao Shui
ahushuitao@126.com
Wen-Xing Yang
wenxingyang2@126.com

Specialty section:
This article was submitted to Quantum Engineering and Technology, a section of the journal Frontiers in Physics

Received: *29 March 2022*
Accepted: *17 May 2022*
Published: *04 July 2022*

Citation:
Song Y, Li L, Shui T, Hu D and Yang W-X (2022) Topological Charge Measurement of the Mid-Infrared Vortex Beam via Spatially Dependent Four-Wave Mixing in an Asymmetric Semiconductor Double Quantum Well. Front. Phys. 10:907284. doi: 10.3389/fphy.2022.907284

1 INTRODUCTION

In the past several decades, the study of optical vortices carrying an orbital angular momentum (OAM) of $l\hbar$ per photon has been an active area in the field of optics since it was first proposed and experimentally observed by Allen et al. in 1992 [1]. As a structured light beam, the vortex beam contains a helical phase term $e^{il\phi}$, where l is the topological charge (TC) [2]. The exchange and manipulation of optical vortices have been extensively investigated in a variety of structures and materials, such as liquid crystal films [3], metamaterials [4, 5], Dammann vortex grating [6], cold atomic ensembles [7–11], quantum dots [12, 13], molecular magnets [14], and graphene [15]. Meanwhile, optical vortices have been widely used in optical tweezers [16, 17], optical communication [18, 19], microscopic imaging [20, 21], quantum entanglement [22, 23], quantum teleportation [24, 25], and quantum information processing [26]. For most of these applications, it is of great importance to accurately measure the TCs of optical vortices. Until now, numerous approaches have been proposed to realize the TC measurement, such as using the torque measurement [27, 28], rotational Doppler effect [29], the diffractive optical elements including apertures [30, 31] and gratings [32, 33], the interference mechanisms of oblique plane waves [34], spherical waves [35, 36], Young's double-slit [37, 38] and Mach–Zehnder [39, 40]. However, these

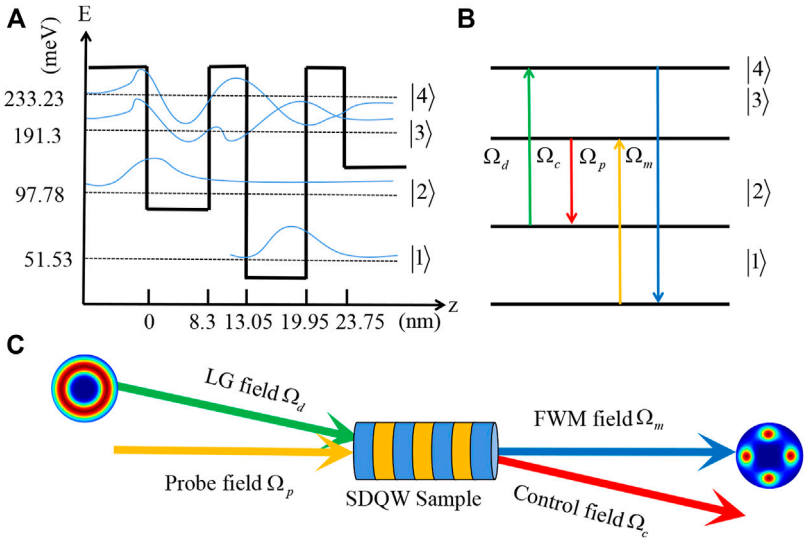

FIGURE 1 | (A) Schematic energy-band diagram of a single period of the asymmetric SDQW. **(B)** The corresponding energy-level arrangement. **(C)** Geometry of the four applied fields. In the FWM process, control field Ω_c, vortex driving field Ω_d, and probe field Ω_p interact with the SDQW and generate FWM field Ω_m under the phase-matching condition $\vec{k}_p + \vec{k}_d = \vec{k}_m + \vec{k}_c$.

approaches mostly require some specialized optical components or a good number of optical elements with fine alignment. Therefore, realizing the TC measurement of a vortex beam in a simple and efficient optical system still remains to be explored.

On the other hand, as a solid-state material working in the mid-infrared band, semiconductor quantum wells (SQWs) provide a promising platform for the coherent control of mid-infrared light transmission due to their advantages of high nonlinear optical coefficients, large electric dipole moments, and a flexible structure design. Until now, a host of breakthroughs have been made such as electromagnetically induced transparency (EIT) [41, 42], electromagnetically induced grating [43, 44], all-optical switching [45], optical solutions [46, 47], Goos–Hänchen shift [48, 49], and four-wave mixing (FWM) [50–52]. Recently, the transfer and modulation of mid-infrared optical vortices have been realized *via* the high-efficient FWM process in SQWs [53–55]. Thus, it reminds us of one question: Can we realize the TC measurement of a mid-infrared vortex beam in a SQW system?

To answer this question, a scheme is proposed in this article for measuring the TC of a mid-infrared vortex beam *via* observing the intensity distribution of the generated FWM field in an asymmetric semiconductor double quantum well (SDQW). In this SDQW, Fano-type interference exists, which arises from the absorption paths of two states coupled to an electronic continuum [52, 56, 57]. Different from previous studies, the distinguishing features of this scheme are given as follows: First and foremost, with the help of the Fano-type interference, the special inherent interference leads to the interference-type phase and intensity patterns for the generated FWM field. This is a significant advantage of our proposed scheme compared with Refs. [53, 54]. Second, by adjusting the intensity and detuning of the control field, the interference-type intensity pattern of the FWM field can be drastically manipulated. In particular, by an appropriate choice of the intensity Ω_c and detuning Δ_c, a high-visibility interference-type pattern accompanied by an appropriate intensity can be achieved. Third, by monitoring the number of light spots of the FWM field, the measurable TC value can reach up to 120 in our scheme, which is a great improvement compared with previous schemes [38, 58].

2 MODELS AND EQUATIONS

As shown in **Figure 1A**, we consider an asymmetric SDQW with four-subband configurations, which can be grown by molecular-beam epitaxy [56]. In this designed SDQW, an 8.3-nm thick $Al_{0.07}Ga_{0.93}As$ layer and a 6.9-nm GaAs layer are separated by an $Al_{0.32}Ga_{0.68}As$ potential barrier with the thickness of 4.75 nm. On the right side of the right well is a thin barrier with a thickness of 3.8 nm, which is followed by a thick $Al_{0.16}Ga_{0.84}As$ layer [52, 59, 60]. The eigenenergies and wave functions for the four conduction subbands can be obtained by solving the effective mass Schrödinger equation [61]. In the proposed SDQW, the eigenenergies of the four subbands $|1\rangle$, $|2\rangle$, $|3\rangle$, and $|4\rangle$ are ω_1 = 51.53 meV, ω_2 = 97.78 meV, ω_3 = 191.3 meV, and ω_4 = 233.23 meV, respectively [52]. Owing to the existence of resonant tunneling, the two closely spaced delocalized subbands $|3\rangle$ and $|4\rangle$ can be represented by a coherent superposition of the first excited subband in the shallow well $|se\rangle$ and deep well $|de\rangle$, that is, $|3\rangle = (|se\rangle - |de\rangle)/\sqrt{2}$ and $|4\rangle = (|se\rangle + |de\rangle)/\sqrt{2}$. A pulse probe field $\Omega_p = \Omega_{p0} \exp(-t^2/\tau^2)$ (Ω_{p0} and τ are the initial Rabi frequency and pulse width) is applied to the transition $|3\rangle \leftrightarrow |1\rangle$, while the transitions $|3\rangle \leftrightarrow |2\rangle$ and $|4\rangle \leftrightarrow |2\rangle$ are driven by a continuous-wave (cw) control field

Ω_c and a vortex driving field Ω_d. Subsequently, a pulse FWM field Ω_m can be efficiently generated *via* the FWM process $|1\rangle \rightarrow |3\rangle \rightarrow |2\rangle \rightarrow |4\rangle \rightarrow |1\rangle$ (**Figures 1B,C**). In our scheme, the vortex driving field Ω_d is a Laguerre–Gaussian (LG) mode with the form [12]

$$\Omega_d(r,\phi) = \Omega_{d0}\frac{1}{\sqrt{|l|!}}\left(\frac{\sqrt{2}\,r}{w_0}\right)^{|l|} L_p^{|l|}\left(2r^2/w_0^2\right)e^{-r^2/w_0^2}e^{il\phi}, \quad (1)$$

where r and ϕ are the radial radius and azimuthal angle, respectively. Ω_{d0} and w_0 represent the initial Rabi frequency and beam waist, respectively. The radial index and TC are labeled by p and l, respectively. Here, $L_p^{|l|}$ is the Laguerre polynomial.

$$L_p^{|l|}(x) = \frac{e^x x^{-|l|}}{p!}\frac{d^p}{dx^p}\left[x^{|l|+p}e^{-x}\right]. \quad (2)$$

It can be seen from **Eqs 1**, **2** that the Laguerre polynomial $L_p^{|l|}$ determines the radial distribution of the intensity of the LG mode. For simplicity, it is assumed that all the four subbands have the same effective mass. Furthermore, this SDQW is designed to have a low electron sheet density so that the electron–electron interactions can be reasonably neglected [62]. Under the rotating-wave and electric-dipole approximations, the interaction Hamiltonian for this system in the interaction picture can be written as ($\hbar = 1$).

$$H_{\rm int}^I = \left(\Delta_p - \Delta_c\right)|2\rangle\langle 2| + \Delta_p|3\rangle\langle 3| + \left(\Delta_p - \Delta_c + \Delta_d\right)|4\rangle\langle 4| - \left(\Omega_p e^{i\vec{k}_p\cdot\vec{r}}|3\rangle\langle 1| + \Omega_c e^{i\vec{k}_c\cdot\vec{r}}|3\rangle\langle 2| + \Omega_d e^{i\vec{k}_d\cdot\vec{r}}|4\rangle\langle 2| + \Omega_m e^{i\vec{k}_m\cdot\vec{r}}|4\rangle\langle 1| + H.c.\right), \quad (3)$$

where $\Delta_p = (\omega_3 - \omega_1) - \omega_p$, $\Delta_c = (\omega_3 - \omega_2) - \omega_c$, and $\Delta_d = (\omega_4 - \omega_2) - \omega_d$ are the probe field, control field, and vortex field detunings, respectively. $\vec{k_j}$ ($j = p, c, d,$ and m) is the wave vector of the corresponding applied field. The Rabi frequencies of the corresponding applied fields are $\Omega_p = \mu_{31}E_p/2\hbar$, $\Omega_c = \mu_{32}E_c/2\hbar$, $\Omega_d = \mu_{24}E_d(r,\phi)/2\hbar$ and $\Omega_m = \mu_{41}E_m(r,\phi)/2\hbar$ with μ_{ij} ($i, j = 1$–4; $i \neq j$) being the transition dipole moment between subbands $|i\rangle \leftrightarrow |j\rangle$ and $E_{p,c,d,m}$ being the slowly varying electric field amplitude of the applied field. According to Ref. [63], the light intensity I_i ($j = p, c, d,$ and m) of the applied field is proportional to the square of the electric field amplitude E_i, that is, $I_i \propto |E_i|^2$. In other words, $I_i \propto |\Omega_i|^2$, which means that the Rabi frequency of an applied field can be used to represent its light intensity. Meanwhile, the electron wave function can be written as

$$|\Psi\rangle = A_1|1\rangle + A_2e^{i\left(\vec{k}_p-\vec{k}_c\right)\cdot\vec{r}}|2\rangle + A_3e^{i\overrightarrow{k_p}\cdot\vec{r}}|3\rangle + A_4e^{i\left(\overrightarrow{k_p}-\vec{k}_c+\vec{k}_d\right)\cdot\vec{r}}|4\rangle, \quad (4)$$

where A_j ($j = 1, 2, 3, 4$) stands for the time-dependent probability amplitude for finding particles in the corresponding subband. Substituting **Eqs 3**, **4** into the Schrödinger equation $i\partial\Psi/\partial t = H_{\rm int}^I\Psi$, the equations of motion for the probability amplitudes can be obtained as [52].

$$i\frac{\partial A_1}{\partial t} = -\Omega_p^*A_3 - \Omega_m^*e^{i\delta\vec{k}\cdot\vec{r}}A_4, \quad (5)$$

$$i\frac{\partial A_2}{\partial t} = \left(\Delta_p - \Delta_c\right)A_2 - i\gamma_2A_2 - \Omega_c^*A_3 - \Omega_d^*A_4, \quad (6)$$

$$i\frac{\partial A_3}{\partial t} = \Delta_pA_3 - i\gamma_3A_3 - \Omega_pA_1 - \Omega_cA_2 + i\zeta A_4, \quad (7)$$

$$i\frac{\partial A_4}{\partial t} = \left(\Delta_d - \Delta_c + \Delta_p\right)A_4 - i\gamma_4A_4 - \Omega_dA_2 - \Omega_me^{-i\delta\vec{k}\cdot\vec{r}}A_1 + i\zeta A_3, \quad (8)$$

in which $\delta\vec{k} = \vec{k}_p - \vec{k}_c + \vec{k}_d - \vec{k}_m$ denotes a phase mismatching factor. In **Eqs 6**–**8**, the decay rate γ_j ($j = 2, 3, 4$) is introduced phenomenologically. The total decay rate γ_j ($j = 2$–4) $= \gamma_{jl} + \gamma_{jd}$ includes the population decay rate γ_{jl} and the pure dipole dephasing rate γ_{jd}. The population decay rate γ_{jl} is induced by the longitudinal optical phonon emission events at low temperatures, which can be calculated in [56]. The pure dipole dephasing rate γ_{jd} is due to a combination of quasi-elastic interface roughness scattering and acoustic phonon scattering. In the presence of the electronic continuum, the population decay rates γ_{3l} and γ_{4l} represent the decay rates from the subbands $|3\rangle$ and $|4\rangle$ to the continuum by tunneling with $\gamma_{3l} = 1.58$ meV and $\gamma_{4l} = 1.5$ meV. In the absence of the electronic continuum, γ_{3l} and γ_{4l} stand for the decay rates from the subbands $|3\rangle$ and $|4\rangle$ to the ground subband with $\gamma_{3l} \approx \gamma_{4l} = 1$ meV. For temperatures up to 10 K, the electron density can be kept to $10^{24}\mathrm{m}^{-3}$ [64]. In this sense, the dephasing rates can be estimated as $\gamma_{3d} = 0.32$ meV and $\gamma_{4d} = 0.3$ meV. It is worth noting that a cross coupling term between the two excited states $|3\rangle$ and $|4\rangle$ is introduced as $\zeta = \sqrt{\gamma_{3l}\cdot\gamma_{4l}}$ when the electronic continuum exists [56, 57, 64]. In this case, the strength of the Fano-type interference can be denoted by $P = \zeta/\sqrt{\gamma_3\cdot\gamma_4}$, where $p = 0$ and $p = 1$ correspond to no interference and perfect interference, respectively. In the limit of slowly varying amplitude approximation, both the input probe field Ω_p and the generated FWM field Ω_m, which propagate in the z-direction, obey one-dimensional Maxwell wave equations.

$$\frac{\partial\Omega_p}{\partial z} + \frac{1}{c}\frac{\partial\Omega_p}{\partial t} = \frac{ic}{2\omega_p}\nabla_\perp^2\Omega_p + i\kappa_pA_3A_1^*, \quad (9)$$

$$\frac{\partial\Omega_m}{\partial z} + \frac{1}{c}\frac{\partial\Omega_m}{\partial t} = \frac{ic}{2\omega_m}\nabla_\perp^2\Omega_m + i\kappa_mA_4A_1^*, \quad (10)$$

where $\kappa_p = 2\pi N\omega_p|\mu_{31}|^2/\hbar c$ and $\kappa_m = 2\pi N\omega_m|\mu_{41}|^2/\hbar c$ are the propagation constants with N being the electron density. The first terms on the right-hand sides of **Eqs 9**, **10** account for light diffraction. When the propagation distance L is much smaller than the Rayleigh length (i.e., $L \ll \pi w_0^2/\lambda$), the diffraction term can be ignored. In our scheme, $L = 1\mu$m, $w_0 \approx 500\,\mu$m, and $\lambda_m \approx 6.8\,\mu$m are selected so that $\pi w_0^2/\lambda_m \approx 1.154 \times 10^5\ \mu\mathrm{m} \gg 1\,\mu$m, Therefore, we can neglect the diffraction terms in **Eqs 9**, **10**. In the following, we perform a time-dependent analysis for FWM in the asymmetric SDQW, which requires both the input probe field and the generated FWM field as laser pulses, not cw lasers [65]. Then, we can perform the Fourier transformation for **Eqs 5**–**10** by defining

$$A_j(t) = \frac{1}{\sqrt{2\pi}} \int_{-\infty}^{\infty} a_j(\omega)\exp(-i\omega t)d\omega, \ (j = 2, 3, 4), \tag{11}$$

$$\Omega_n(t) = \frac{1}{\sqrt{2\pi}} \int_{-\infty}^{\infty} \Lambda_n(\omega)\exp(-i\omega t)d\omega, \ (n = p, m), \tag{12}$$

where ω is the Fourier transform variable.

In the limit of weak probe and FWM fields, most electrons remain in the ground subband $|1\rangle$, that is, $|A_1|^2 \approx 1$. Therefore, we can obtain

$$\left(\omega + \Delta_c - \Delta_p + i\gamma_2\right)a_2 + \Omega_c^* a_3 + \Omega_d^* a_4 = 0, \tag{13}$$

$$\left(\omega - \Delta_p + i\gamma_3\right)a_3 + \Omega_c a_2 - i\zeta a_4 = -\Lambda_p, \tag{14}$$

$$\left(\omega - \Delta_d + \Delta_c - \Delta_p + i\gamma_4\right)a_3 + \Omega_d a_2 - i\zeta a_3 = -\Lambda_m, \tag{15}$$

$$\frac{\partial \Lambda_p}{\partial z} - i\frac{\omega}{c}\Lambda_p = i\kappa_p a_3 a_1^*, \tag{16}$$

$$\frac{\partial \Lambda_m}{\partial z} - i\frac{\omega}{c}\Lambda_m = i\kappa_m a_4 a_1^*. \tag{17}$$

By analytically solving **Eqs 13–15**, one can obtain a_j (j = 2, 3, and 4) as

$$a_2 = \frac{i\zeta\Omega_c^*\Lambda_m + \left(\omega - \Delta_d + \Delta_c - \Delta_p + i\gamma_4\right)\Omega_c^* + i\zeta\Omega_d^*\Lambda_p + \left(\omega - \Delta_p + i\gamma_3\right)\Omega_d^*\Lambda_m}{D(\omega)}, \tag{18}$$

$$a_3 = \frac{-D_p(\omega)}{D(\omega)}\Lambda_p + \frac{D_1(\omega)}{D(\omega)}\Lambda_m, \tag{19}$$

$$a_4 = \frac{-D_m(\omega)}{D(\omega)}\Lambda_m + \frac{D_2(\omega)}{D(\omega)}\Lambda_p, \tag{20}$$

where
$D_1(\omega) = i\zeta(\omega + \Delta_c - \Delta_p + i\gamma_2) + \Omega_c\Omega_d^*$,
$D_2(\omega) = i\zeta(\omega + \Delta_c - \Delta_p + i\gamma_2) + \Omega_d\Omega_c^*$,
$D_p(\omega) = |\Omega_d|^2 - (\omega + \Delta_c - \Delta_p + i\gamma_2)(\omega - \Delta_d + \Delta_c - \Delta_p + i\gamma_4)$,
$D_m(\omega) = |\Omega_c|^2 - (\omega + \Delta_c - \Delta_p + i\gamma_2)(\omega - \Delta_p + i\gamma_3)$ and $D(\omega) = -\zeta^2(\omega + \Delta_c - \Delta_p + i\gamma_2) - (\omega + \Delta_c - \Delta_p + i\gamma_2)(\omega - \Delta_p + i\gamma_3)(\omega - \Delta_d + \Delta_c - \Delta_p + i\gamma_4) + i\zeta\Omega_d\Omega_c^* + (\omega - \Delta_d + \Delta_c - \Delta_p + i\gamma_4)|\Omega_c|^2 + i\zeta\Omega_c\Omega_d^* + (\omega - \Delta_p + i\gamma_3)|\Omega_d|^2$.

Considering the initial conditions for the pulse probe and FWM fields, that is, $\Lambda_p(0, \omega) \neq 0$, and $\Lambda_m(0, \omega) = 0$, we obtain the analytical solution of the FWM field as follows:

$$\Lambda_m(z, \omega) = \Lambda_p(0, \omega)S(\omega)\left[e^{izK_+(\omega)} - e^{izK_-(\omega)}\right], \tag{21}$$

where

$$K_\pm(\omega) = \frac{\omega}{c} - \frac{D_m(\omega)\kappa_m + D_p(\omega)\kappa_p \pm \sqrt{G(\omega)}}{2D(\omega)} = K_\pm(0) + K_\pm^1(\omega) + O(\omega^2), \tag{22}$$

$$S(\omega) = \frac{\kappa_m D_2(\omega)}{\sqrt{G(\omega)}} = S(0) + O(\omega), \tag{23}$$

with $G(\omega) = [D_p(\omega)\kappa_p - D_m(\omega)\kappa_m]^2 + 4D_1(\omega)D_2(\omega)\kappa_m\kappa_p$, by seeking the approximated inverse Fourier transform with the approximation of neglecting the $O(\omega)$ term in $S(\omega)$ and the $O(\omega^2)$ term in $K_\pm(\omega)$ [52]. Then it is straightforward to obtain

$$\Omega_m(z, t) = S(0)\left[\Omega_p\left(0, t - z/V_{g-}\right)e^{izK_-(0)} - \Omega_p\left(0, t - z/V_{g+}\right)e^{izK_+(0)}\right], \tag{24}$$

where the group velocities $V_{g\pm}$ are determined by $1/V_{g\pm} = \mathrm{Re}[K_\pm^1(0)]$. Note that there exist two modes described by the dispersion relations $K_+(0)$ and $K_-(0)$. Re $[K_\pm(0)]$ and Im $[K_\pm(0)]$ represent the phase shifts per unit length and absorption coefficients at the center frequency $\omega = 0$, respectively. A previous study [52] has demonstrated that the absorption of the $K_+(0)$ mode is much greater than that of the $K_-(0)$ mode. Therefore, the rapid decay $K_+(0)$ mode can be reasonably ignored after a short propagation distance L. Therefore, **Eq. 24** can be simplified to

$$\Omega_m(L, t) = \Omega_p\left(0, t - L/V_g\right)S(0)e^{iKL}, \tag{25}$$

where $V_g = V_{g-}$ and $K = K_-(0)$. By using $S(0) = \kappa_m[-\zeta(i\Delta_p - i\Delta_c + \gamma_2) + \Omega_d\Omega_c^*]/\sqrt{G(0)}$ and $K = \mathrm{Re}(K) + i\mathrm{Im}(K)$, **Eq. 25** can be rewritten as

$$\Omega_m(L, t) = \frac{\kappa_m\Omega_p\left(0, t - L/V_g\right)\left[-\zeta\left(i\Delta_p - i\Delta_c + \gamma_2\right) + \Omega_d\Omega_c^*\right]}{\sqrt{G(0)}}e^{-\mathrm{Im(K)L + iRe(K)L}}, \tag{26}$$

where the intensity of the FWM field is $\propto |\kappa_m\Omega_p(0, t - z/V_g)[-\zeta(i\Delta_p - i\Delta_c + \gamma_2) + \Omega_d\Omega_c^*]e^{-\mathrm{Im}(K)L}/\sqrt{G(0)}|^2$. The factor $e^{i\,\mathrm{Re}(K)L}$ reflects the phase distribution of the FWM field. Obviously, both the phase and intensity distribution of the FWM field are modulated by dispersion relation K.

3 RESULTS AND DISCUSSIONS

We first explore the influence of the Fano-type interference on the phase and intensity distribution of the generated FWM field in **Figure 2**. Here, the mode of the vortex driving field Ω_d is $LG_{p=0}^{l=4}$. In the absence of the electronic continuum, the Fano-type interference does not exist (i.e., p = 0). In this situation, the system is simplified as a common double-Λ SDQW [55]. One can find from **Figures 2A,C** that the phase wavefront twists in the anticlockwise direction and the intensity distribution exhibits a single-ring pattern at the radial position r = 0.71 mm. A phase singularity exists at the center of zero intensity, around which the helical phase changes from 0 to 8π. As explained, the OAM of the vortex driving field can be transferred to the generated FWM field *via* the FWM process [55]. In the presence of the electronic continuum, the Fano-type interference exists (i.e., p = 0.83) [52]. Different from **Figures 2A,C**, the FWM field displays four phase singularities on the inner side of the twisted phase wavefront in the phase profiles and the helical phase changes from 0 to 2π around every phase singularity (**Figure 2B**). Meanwhile, a petal-like intensity pattern with four light spots on the circle with radius r = 0.71 mm can be observed (**Figure 2D**). As a matter of fact, the cross coupling term ζ in **Eq. 26** acts as a plane wave and then makes inherent interference with the vortex driving field. Therefore, we can observe an interference-type intensity pattern with four light spots and an interference-type phase pattern with four phase singularities, which satisfies the conservation of OAM [66, 67].

In order to have a deeper understanding for the effect of the Fano-type interference, we plot the spatial distribution of the real and imaginary parts of the dispersion relation K in **Figure 3**. Note

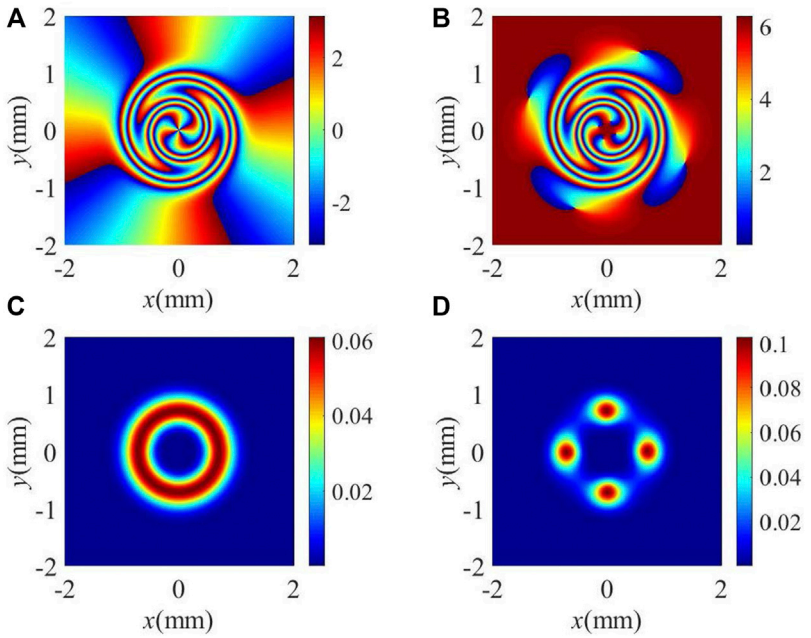

FIGURE 2 | (A,B) Phase and **(C,D)** intensity patterns of the FWM field without and with including electronic continuum, **(A,C)** without including electronic continuum: $\gamma_{3l} = \gamma_{4l} = 1$ meV and $p = 0$, **(B,D)** with including electronic continuum: $\gamma_{3l} = 1.58$ meV and $\gamma_{4l} = 1.50$ meV and $p = 0.83$. Other parameters used are $\gamma_2 = 2.36 \times 10^{-6}$ μeV, $\gamma_{3d} = 0.32$ meV, $\gamma_{4d} = 0.30$ meV, $|\Omega_c| = 25$ meV, $|\Omega_{d0}| = 30$ meV, $\Delta_c = 5$ meV, $\Delta_p = \Delta_d = 0$, and $\kappa_m = \kappa_p = 9.6 \times 10^3 \mu m^{-1}$meV, $l = 4$, $p = 0$, $w_0 = 500$ μm, and $L = 1$ μm.

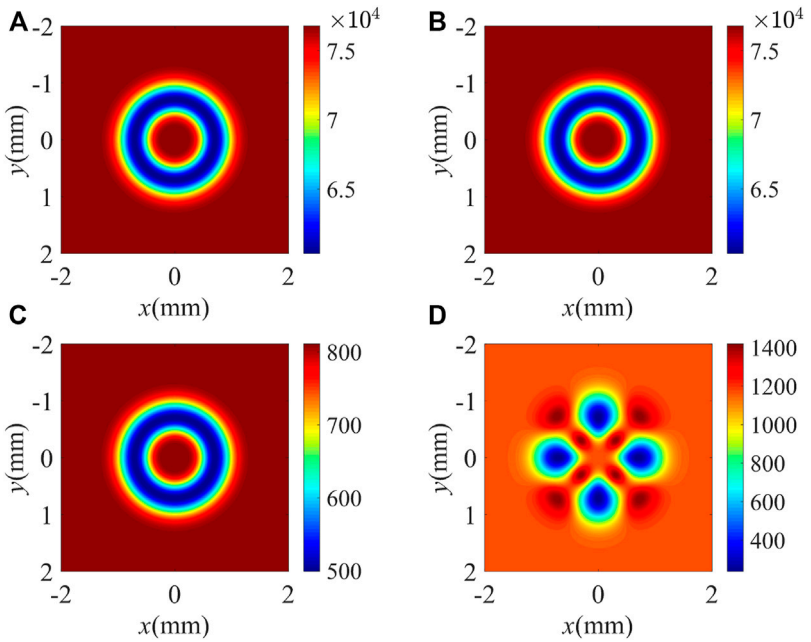

FIGURE 3 | (A,B) Real and **(C,D)** imaginary parts of the dispersion relation K. **(A,C)** without including electronic continuum: $\gamma_{3l} = \gamma_{4l} = 1$ meV and $p = 0$; **(B,D)** with including electronic continuum: $\gamma_{3l} = 1.58$ meV and $\gamma_{4l} = 1.50$ meV and $p = 0.83$. Other parameters are the same as in **Figure 2**.

that the phase shift Re(K) per unit length determines the phase wavefront distribution of the FWM field, while the absorption coefficient Im(K) determines the distribution of the intensity [55]. Without the Fano-type interference, the phase shift Re(K) per unit length displays an inverted crater-like pattern with a radius $r = 0.71$ mm and leads to the helical phase twisting in the

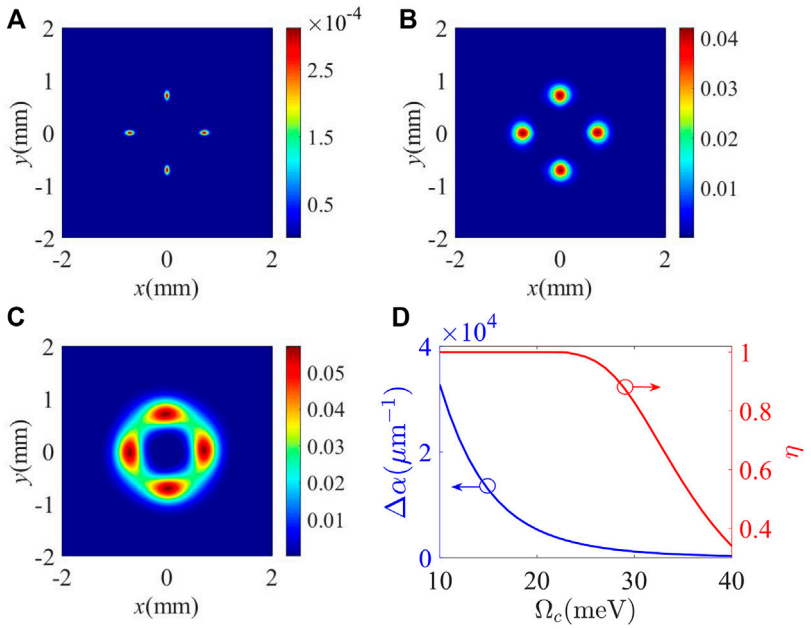

FIGURE 4 | (A–C) Intensity patterns of the FWM field for different intensities of the control field. **(A)** Ω_c = 10 meV, **(B)** Ω_c = 25 meV, and **(C)** Ω_c = 40 meV. **(D)** Absorption coefficient difference $\Delta\alpha$ and interference visibility η as a function of intensity Ω_c of the control field. Other parameters are the same as in **Figure 2B** except for Δ_c = 8 meV.

anticlockwise direction (**Figure 3A**). Meanwhile, the absorption coefficient Im(K) also exhibits an inverted crater-like pattern at r = 0.71mm, where the low absorption ring results in the appearance of an intensity ring (**Figure 3C**). With the Fano-type interference, the inverted crater-like pattern of Re(K) also makes the phase twist in the anticlockwise direction (**Figure 3B**), while the existence of four independent low-absorption regions along the angular direction leads to a discrete intensity distribution with four light spots (**Figure 3D**).

A previous study [36] has demonstrated that the number of light spots in the interference spectrum is determined by the TC of the involved optical vortex. Therefore, the inherent interference mechanism in the proposed SDQW allows us to measure the TC of the vortex driving field *via* directly monitoring the number of light spots of the FWM field. It is worth noting that the precision of the TC measurement would be limited by the intensity and visibility of the inherent interference. To achieve a high-quality interference-type pattern, we explore the influence of the intensity and detuning of the control field based on **Eq. 26**. **Figures 4A–C** show the intensity patterns of the FWM field for different values of the control intensity Ω_c. When Ω_c = 10 meV, the FWM field shows a clear four petal-like intensity pattern, but the intensities of the four light spots are very small (**Figure 4A**). As we adjust Ω_c to 25 meV and then to 40meV, as shown in **Figures 4B,C**, the intensity of the FWM field becomes more and more stronger, while the visibility of the light spots becomes more and more worse. In order to evaluate the quality of the interference-type intensity pattern, we defined interference visibility η as [63].

$$\eta = \frac{I_{\max} - I_{\min}}{I_{\max} + I_{\min}}, \tag{27}$$

where $I_{\max}$ and $I_{\min}$ represent the maximal and minimal light intensities along the angular direction in the interference-type intensity pattern of the FWM field, respectively. We can set $I_{\max} = I_0 e^{-2\alpha_{\min} L}$ and $I_{\min} = I_0 e^{-2\alpha_{\max} L}$ with $\alpha_{\min}$ and $\alpha_{\max}$ being the corresponding minimal and maximal absorption coefficients, respectively, of the FWM field along the angular direction. Then, **Eq. 27** can be rewritten as

$$\eta = \frac{e^{-2\alpha_{\min} L} - e^{-2\alpha_{\max} L}}{e^{-2\alpha_{\min} L} + e^{-2\alpha_{\max} L}} = 1 - \frac{2}{e^{2\Delta\alpha L} + 1}, \tag{28}$$

where $\Delta\alpha = \alpha_{\max} - \alpha_{\min}$ stands for the difference between the maximal and minimal absorption coefficients. It can be seen that $\Delta\alpha$ determines the interference visibility of the output FWM field. Saying concretely, the increase (decrease) of $\Delta\alpha$ would lead to the increase (decrease) of interference visibility η. Here, the absorption coefficient difference $\Delta\alpha$ and interference visibility η *versus* the azimuthal angle ϕ at radius r = 0.71 mm are plotted in **Figure 4D**. It is found that $\Delta\alpha$ decreases from 32,720.0 μm^{-1} to 350.6 μm^{-1} when Ω_c increases from 10 to 40 meV. Thus, interference visibility η shows a decreasing trend. It is worth noting that η is almost kept to 1 for 10 meV $\leq \Omega_c \leq$ 20meV because $\Delta\alpha$ has an extremely high value in this region so that term $e^{2\Delta\alpha L}$ in **Eq. 28** is close to infinity.

We also investigate the influence of control detuning Δ_c on the intensity pattern of the FWM field in **Figures 5A–C**. It can be seen that the intensity of the FWM field decreases monotonically as Δ_c increases from 2 to 14 meV (**Figures 5A–C**). Different from

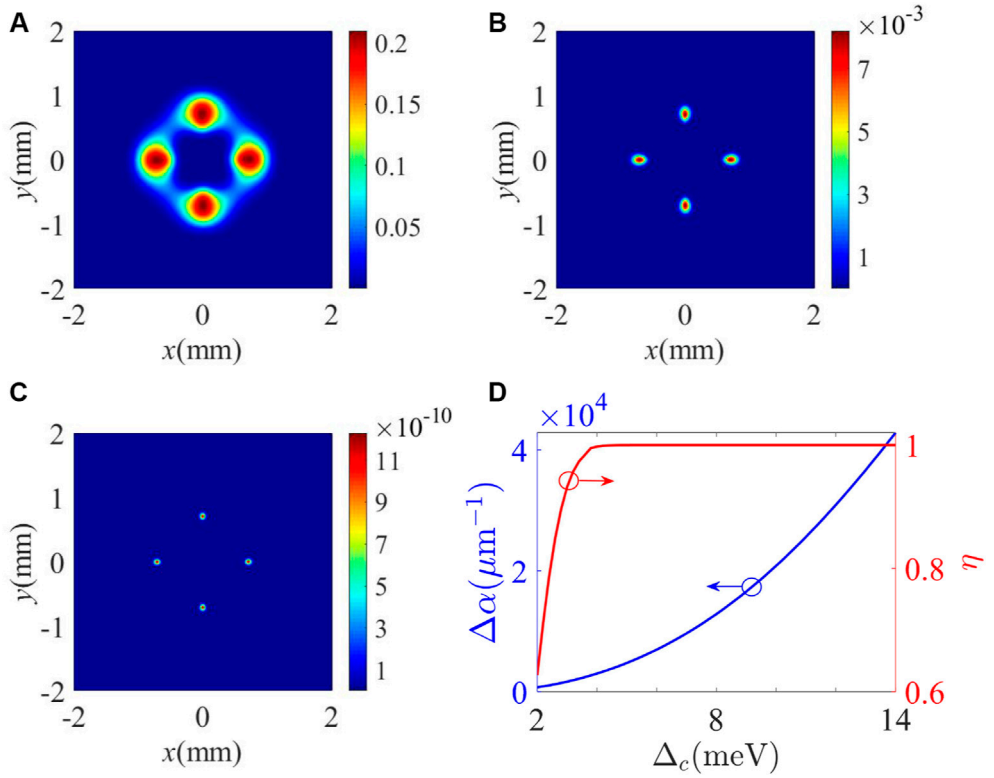

FIGURE 5 | (A–C) Intensity patterns of the FWM field for different detunings of the control field. **(A)** Δ_c = 2 meV, **(B)** Δ_c = 8 meV, **(C)** and Δ_c = 14 meV. **(D)** Absorption coefficient difference $\Delta\alpha$ and interference visibility η as a function of detuning Δ_c of the control field. Other parameters are the same as in **Figure 2B** except for Ω_c = 15 meV.

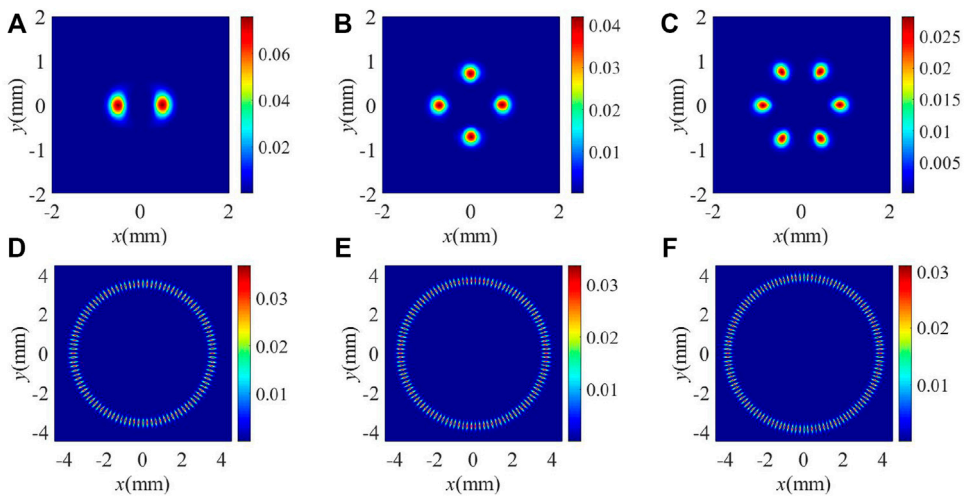

FIGURE 6 | (A–F) Intensity patterns of the FWM field for different TCs of the vortex driving field. **(A)** / = 2, **(B)** / = 4, **(C)** / = 6, **(D)** / = 100, **(E)** / = 110, and **(F)** / = 120. Ω_c = 25 meV and Δ_c = 8 meV for **(A–C)** and Ω_c = 13 meV and Δ_c = 2 meV for **(D–F)**. Other parameters are the same as in **Figure 2B**.

the results shown in **Figure 4**, $\Delta\alpha$ increases from 735.8 μm^{-1} to 42,871 μ m^{-1} as Δ_c increases from 2 to 14 meV (**Figure 5D**). In this sense, interference visibility η increases from 0.63 to 1. As Δ_c exceeds 5.2 meV, the value of $\Delta\alpha$ is extremely high so that interference visibility $\eta \approx 1$. According to the aforementioned discussions, one can conclude that the intensity and detuning of the control field play different roles in modifying the intensity and visibility of the interference-type pattern. Therefore, a high-

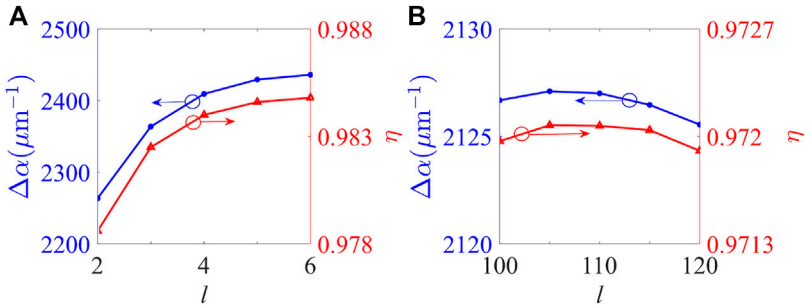

FIGURE 7 | Absorption coefficient difference $\Delta\alpha$ and interference visibility η corresponding to **(A)** the low-order TCs and **(B)** high-order TCs. Other parameters are the same as in **Figure 6**.

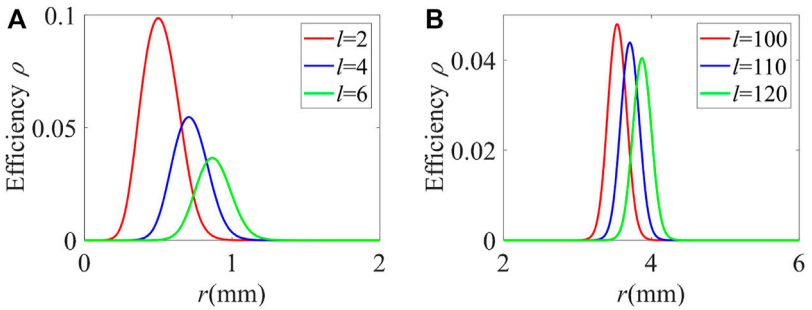

FIGURE 8 | FWM efficiency ρ *versus* radius r for different values of the TCs. **(A)** and **(B)** correspond to the cases of low-order TCs and high-order TCs, respectively. Other parameters are the same as in **Figure 6**.

visibility interference-type pattern accompanied by an appropriate intensity can be achieved *via* choosing the suitable values of the intensity and detuning of the control field.

Based on the aforementioned discussions, we perform the TC measurement of the vortex driving field *via* monitoring the number of light spots in the intensity pattern of the generated FWM field. The intensity patterns of the FWM field for different TCs of the vortex driving field are displayed in **Figure 6**, and the corresponding curves for absorption coefficient difference $\Delta\alpha$ and interference visibility η are shown in **Figure 7**. It is worth noting that the waist radius of the vortex driving field is always kept to 500 μm for the selected TCs. In the measurement of the low-order TC (i.e., $l \leq 10$), $\Omega_c = 25$ meV and $\Delta_c = 8$ meV are selected. We can clearly observe two, four, and six light spots in the intensity patterns of the FWM field when $l = 2$, 4, and 6 (**Figures 6A–C**). As shown in **Figure 7A**, $\Delta\alpha$ increases from 2,263.6 μm^{-1} to 2,436.1 μm^{-1} as l increases from 2 to 6. Therefore, interference visibility η would increase from 0.9786 to 0.9848 for the low-order TC case. Although the overall output intensity decreases in some degree due to the dependence of the Laguerre polynomial on the TC, the visibility of the interference-type pattern always exceeds 0.97. That is to say, we can realize a high-precision measurement for the low-order TC of a mid-infrared optical vortex. In the measurement of the high-order TC, $\Omega_c = 13$ meV and $\Delta_c = 2$ meV are chosen. When $l = 100$, 110, and 120, the same number of light spots can be observed in the interference-type pattern of the FWM field (**Figures 6D–F**). The overall output intensity of the FWM field only decreases slightly with the increase of l from 100 to 120. $\Delta\alpha$ first slightly increases from 2,126.7 μm^{-1} to 2,127.1 μm^{-1} as l increases from 100 to 105 and then decreases to 2,125.6 μm^{-1} as l increases to 120 (see the blue line in **Figure 7B**). Therefore, interference visibility η would slightly increase from 0.97197 to 0.97207 and then decrease to 0.97191 with the increase of l from 100 to 120 (see the red line in **Figure 7B**). The change of $\Delta\alpha$ is so small that interference visibility η is kept at the level of 0.9719. Therefore, our scheme is suitable for measuring both the low-order and high-order TC. More importantly, the measurable TC value is greatly improved compared with previous schemes [38, 58].

Before concluding, we explore the influence of the TC of the vortex driving field on the conversion efficiency of FWM. FWM efficiency ρ is defined as $\rho = |E_m^{(out)}/E_p^{(in)}|^2$ [65], where $E_p^{(out)}$ is the is the electric field amplitude E_m ($|E_m|^2 = 4\hbar^2|\Omega_m|^2/|\mu_{31}|^2$) of the generated FWM field at the exit $z = L$ and $E_p^{(in)}$ is the electric field amplitude E_p ($|E_p|^2 = 4\hbar^2|\Omega_p|^2/|\mu_{41}|^2$) of the probe field at entrance $z = 0$. Combined with **Eq. 26**, the FWM efficiency can be rewritten as

$$\rho = \frac{|\mu_{31}|^2}{|\mu_{41}|^2}\frac{|\Omega_m|^2}{|\Omega_p|^2} = \frac{|\mu_{31}|^2}{|\mu_{41}|^2}\left|\frac{\kappa_m\left[-\zeta\left(i\Delta_p - i\Delta_c + \gamma_2\right) + \Omega_d(r,\phi)\Omega_c^*\right]e^{-\mathrm{Im}(K)L}}{\sqrt{G(0)}}\right|^2, \quad (29)$$

where $\mu_{31}^2/\mu_{41}^2 = \kappa_p\omega_m/\kappa_m\omega_p$. It can be seen from **Eq. 29** that the spatial distribution of the FWM efficiency depends on the spatially dependent vortex driving field. In **Figure 8**, we plot FWM efficiency ρ *versus* radius r for different values of the TC by setting $\phi = 0$. In this situation, these curves can reflect the radial distribution of the FWM efficiency cross the center of the light spot. As shown in **Figure 8**, the FWM efficiency is spatially dependent for a certain vortex driving field. In the low-order TC case, the peak value of the FWM efficiency decreases from 9.86 to 3.66% as l increases from 2 to 6 (**Figure 8A**). In the high-order TC case, the optimal FWM efficiency decreases from 4.79 to 4.04% with the increase of l from 100 to 120 (**Figure 8B**). In the two cases, the peak of the FWM efficiency moves toward the larger radius with the increase of TC owing to the change of the ring radius of the vortex driving field. Thus, one can conclude that the FWM efficiency would decrease when the ring radius of the vortex driving field increases with the TC.

4 CONCLUSION

In conclusion, we have theoretically suggested a scheme to measure the TC of a mid-infrared vortex beam *via* observing the intensity distribution of the FWM field in an asymmetric SDQW with a four-subband configuration. In this SDQW, the effect of the Fano-type interference exists because the absorption paths of two states are coupled to an electronic continuum [56, 57]. With the help of the Fano-type interference, the cross coupling term acting as a plane wave makes inherent interference with the vortex beam and generates the interference-type patterns for the phase and intensity of the FWM field. It is demonstrated that a high-contrast interference-type pattern accompanied by appropriate intensity can be achieved *via* adjusting the intensity and detuning the control field. Furthermore, the TC measurement of the vortex beam is performed by monitoring the number of light spots of the FWM field. By properly choosing the parameters of the system, the detectable TC value can reach to 120, which is greatly improved compared with previous schemes [38, 58].

Mid-infrared optical vortices can open up new avenues toward super-resolution microscopy of arbitrarily oriented single molecules [68], fabrication of three-dimensional chiral microstructures [69], and OAM-multiplexing-based free-space optical communication [70]. Our scheme may provide the possibility for the realization of mid-infrared OAM detectors in a compact solid-state system.

DATA AVAILABILITY STATEMENT

The original contributions presented in the study are included in the article/Supplementary Material; further inquiries can be directed to the corresponding authors.

AUTHOR CONTRIBUTIONS

The idea was first conceived by W-XY. YS was responsible for the physical model, numerical calculations, and writing most of the manuscript. DH derived and discussed the efficiency of FWM. LL and TS contributed to writing the manuscript and verified the calculated results.

FUNDING

This study was funded by the National Natural Science Foundation of China (11774054, 12075036, and 12104067), the Science and Technology Research Project of Education Department of Hubei Province (Q20211314), and College Students' Innovation and Entrepreneurship Training Project of Yangtze University (Yz2020314).

ACKNOWLEDGMENTS

YS thanks Chun Meng, Xu Deng, and Tong Zhang for helpful discussions.

REFERENCES

1. Allen L, Beijersbergen MW, Spreeuw RJC, Woerdman JP. Orbital Angular Momentum of Light and the Transformation of Laguerre-Gaussian Laser Modes. *Phys Rev A* (1992) 45(11):8185–9. doi:10.1103/physreva.45.8185
2. Padgett M, Courtial J, Allen L. Light's Orbital Angular Momentum. *Phys Today* (2004) 57(5):35–40. doi:10.1063/1.1768672
3. Brasselet E. Tunable High-Resolution Macroscopic Self-Engineered Geometric Phase Optical Elements. *Phys Rev Lett* (2018) 121(3):033901. doi:10.1103/PhysRevLett.121.033901
4. Chen S, Cai Y, Li G, Zhang S, Cheah KW. Geometric Metasurface fork Gratings for Vortex-Beam Generation and Manipulation. *Laser Photon Rev* (2016) 10(2):322–6. doi:10.1002/lpor.201500259
5. Zhang Y, Gao J, Yang X. Topological Charge Inversion of Optical Vortex with Geometric Metasurfaces. *Adv Opt Mater* (2019) 7(8):1801486. doi:10.1002/adom.201801486
6. Chen P, Ge S, Ma L, Hu W, Chigrinov V, Lu Y. Generation of Equal-Energy Orbital Angular Momentum Beams via Photopatterned Liquid Crystals. *Phys Rev A* (2016) 5(4):044009. doi:10.1103/physrevapplied.5.044009
7. Hong Y, Wang Z, Ding D, Yu B. Ultraslow Vortex Four-Wave Mixing via Multiphoton Quantum Interference. *Opt Express* (2019) 27(21):29863–74. doi:10.1364/oe.27.029863
8. Qiu J, Wang Z, Ding D, Huang Z, Yu B. Control of Space-dependent Four-Wave Mixing in a Four-Level Atomic System. *Phys Rev A* (2020) 102(3):033516. doi:10.1103/physreva.102.033516
9. Hamedi HR, Kudriašov V, Ruseckas J, Juzeliūnas G. Azimuthal Modulation of Electromagnetically Induced Transparency Using Structured Light. *Opt Express* (2018) 26(22):28249–62. doi:10.1364/oe.26.028249
10. Hamedi HR, Ruseckas J, Paspalakis E, Juzeliunas G. Transfer of Optical Vortices in Coherently Prepared media. *Phys Rev A* (2019) 99(3):033812. doi:10.1103/physreva.99.033812
11. Asadpour SH, Ziauddin, Abbas M, Hamedi HR. Exchange of Orbital Angular Momentum of Light via Noise-Induced Coherence. *Phys Rev A* (2022) 105:033709. doi:10.1103/PhysRevA.105.033709

12. Mahdavi M, Sabegh ZA, Mohammadi M, Hamedi HR, Mahmoudi. M. Manipulation and Exchange of Light with Orbital Angular Momentum in Quantum Dot Molecules. *Phys Rev A* (2020) 101(6):063811. doi:10.1103/physreva.101.063811
13. Rahmatullah M, Abbas Z, Qamar S. Spatially Structured Transparency and Transfer of Optical Vortices via Four-Wave Mixing in a Quantum-Dot Nanostructure. *Phys Rev A* (2020) 101(2):023821. doi:10.1103/physreva.101.023821
14. Mahdavi M, Sabegh ZA, Hamedi HR, Mahmoudi M. Orbital Angular Momentum Transfer in Molecular Magnets. *Phys Rev B* (2021) 104:094432. doi:10.1103/PhysRevB.104.094432
15. Ding C, Li J, Dai X, Jin R-B, Hao X. Azimuthal and Radial Modulation of Double-Four-Wave Mixing in a Coherently Driven Graphene Ensemble. *Opt Express* (2021) 29(22):36840–56. doi:10.1364/oe.440690
16. Padgett M, Bowman R. Tweezers with a Twist. *Nat Photon* (2011) 5(6):343–8. doi:10.1038/nphoton.2011.81
17. Gecevičius M, Drevinskas R, Beresna M, Kazansky PG. Single Beam Optical Vortex Tweezers with Tunable Orbital Angular Momentum. *Appl Phys Lett* (2014) 104(23):231110.
18. Wang J, Yang JY, Fazal IM, Ahmed N, Yan Y, Huang H, et al. Terabit Free-Space Data Transmission Employing Orbital Angular Momentum Multiplexing. *Nat Photon* (2012) 6(7):488–96. doi:10.1038/nphoton.2012.138
19. Bozinovic N, Yue Y, Ren Y, Tur M, Kristensen P, Huang H, et al. Terabit-scale Orbital Angular Momentum Mode Division Multiplexing in Fibers. *Science* (2013) 340(6140):1545–8. doi:10.1126/science.1237861
20. Wang J, Liu K, Cheng Y, Wang H. Three-dimensional Target Imaging Based on Vortex Stripmap Sar. *IEEE Sens J* (2019) 19(4):1338–45. doi:10.1109/jsen.2018.2879814
21. Yuan T, Wang H, Cheng Y, Qin Y. Electromagnetic Vortex-Based Radar Imaging Using a Single Receiving Antenna: Theory and Experimental Results. *Sensors* (2017) 17(3):630. doi:10.3390/s17030630
22. Pan X, Yu S, Zhou Y, Zhang K, Zhang K, Lv S, et al. Orbital-angular-momentum Multiplexed Continuous-Variable Entanglement from Four-Wave Mixing in Hot Atomic Vapor. *Phys Rev Lett* (2019) 123(7):070506. doi:10.1103/PhysRevLett.123.070506
23. Li S, Pan X, Ren Y, Liu H, Yu S, Jing J. Deterministic Generation of Orbital-Angular-Momentum Multiplexed Tripartite Entanglement. *Phys Rev Lett* (2020) 124(8):083605. doi:10.1103/PhysRevLett.124.083605
24. Liu S, Lou Y, Jing J. Orbital Angular Momentum Multiplexed Deterministic All-Optical Quantum Teleportation. *Nat Commun* (2020) 11(1):3875. doi:10.1038/s41467-020-17616-4
25. Chen Y, Liu S, Lou Y, Jing J. Orbital Angular Momentum Multiplexed Quantum Dense Coding. *Phys Rev Lett* (2021) 127(9):093601. doi:10.1103/PhysRevLett.127.093601
26. Franke Arnold S, Allen L, Padgett M. Advances in Optical Angular Momentum. *Laser Photon Rev* (2008) 2(4):299–313. doi:10.1002/lpor.200810007
27. Beijersbergen MW, Woerdman JP. Measuring Orbital Angular Momentum of Light with a Torsion Pendulum. *Proc SPIE* (2005) 5736:111–25. doi:10.1117/12.584515
28. Volke-Sepúlveda K, Santillán AO, Boullosa RR. Transfer of Angular Momentum to Matter from Acoustical Vortices in Free Space. *Phys Rev Lett* (2008) 100(2):24302.
29. Vasnetsov MV, Torres JP, Petrov DV, Torner L. Observation of the Orbital Angular Momentum Spectrum of a Light Beam. *Opt Lett* (2003) 28(23):2285–7. doi:10.1364/ol.28.002285
30. Hickmann JM, S Fonseca EJ, Soares WC, Chávez-Cerda S. Unveiling a Truncated Optical Lattice Associated with a Triangular Aperture Using Light's Orbital Angular Momentum. *Phys Rev Lett* (2010) 105(5):053904. doi:10.1103/PhysRevLett.105.053904
31. Silva JG, Jesus-Silva AJ, Alencar MARC, Hickmann JM, Fonseca EJS. Unveiling Square and Triangular Optical Lattices: a Comparative Study. *Opt Lett* (2014) 39(4):949–52. doi:10.1364/ol.39.000949
32. Moreno I, Davis JA, Pascoguin BML, Mitry MJ, Cottrell DM. Vortex Sensing Diffraction Gratings. *Opt Lett* (2009) 34(19):2927–9. doi:10.1364/ol.34.002927
33. Dai K, Gao C, Zhong L, Na Q, Wang Q. Measuring Oam States of Light Beams with Gradually-Changing-Period Gratings. *Opt Lett* (2015) 40(4):562–5. doi:10.1364/ol.40.000562
34. Heckenberg NR, McDuff R, Smith CP, White AG. Generation of Optical Phase Singularities by Computer-Generated Holograms. *Opt Lett* (1992) 17(3):221–3. doi:10.1364/ol.17.000221
35. Vickers J, Burch M, Vyas R, Singh S. Phase and Interference Properties of Optical Vortex Beams. *J Opt Soc Am A* (2008) 25(3):823–7. doi:10.1364/josaa.25.000823
36. Huang H, Ren Y, Yan Y, Ahmed N, Yue Y, Bozovich A, et al. Phase-shift Interference-Based Wavefront Characterization for Orbital Angular Momentum Modes. *Opt Lett* (2013) 38(13):2348–50. doi:10.1364/ol.38.002348
37. Sztul HI, Alfano RR. Double-slit Interference with Laguerre-Gaussian Beams. *Opt Lett* (2006) 31(7):999–1001. doi:10.1364/ol.31.000999
38. Emile O, Emile J. Young's Double-Slit Interference Pattern from a Twisted Beam. *Appl Phys B* (2014) 117(1):487–91. doi:10.1007/s00340-014-5859-1
39. Leach J, Miles JP, Stephen MB, Franke-Arnold S, Courtial J. Measuring the Orbital Angular Momentum of a Single Photon. *Phys Rev Lett* (2002) 88(25):257901. doi:10.1103/physrevlett.88.257901
40. Gao C, Qi X, Liu Y, Xin J, Wang L. Sorting and Detecting Orbital Angular Momentum States by Using a Dove Prism Embedded Mach–Zehnder Interferometer and Amplitude Gratings. *Opt Commun* (2011) 284(1):48–51. doi:10.1016/j.optcom.2010.08.083
41. Phillips M, Wang H. Spin Coherence and Electromagnetically Induced Transparency via Exciton Correlations. *Phys Rev Lett* (2002) 89(18):186401. doi:10.1103/physrevlett.89.186401
42. Ku P-C, Sedgwick F, Chang-Hasnain CJ, Palinginis P, Li T, Wang H, et al. Slow Light in Semiconductor Quantum wells. *Opt Lett* (2004) 29(19):2291–3. doi:10.1364/ol.29.002291
43. Zhou F, Qi Y, Sun H, Chen D, Yang J, Niu Y, et al. Electromagnetically Induced Grating in Asymmetric Quantum wells via Fano Interference. *Opt Express* (2013) 21(10):12249–59. doi:10.1364/oe.21.012249
44. Tian SC, Wan RG, Wang LJ, Shu SL, Lu HY, Zhang X, et al. Asymmetric Light Diffraction of Two-Dimensional Electromagnetically Induced Grating with PT Symmetry in Asymmetric Double Quantum wells. *Opt Express* (2018) 26(25):32918–30. doi:10.1364/oe.26.032918
45. Wu JH, Gao JY, Xu JH, Silvestri L, Artoni M, Rocca GCL, et al. Ultrafast All Optical Switching via Tunable Fano Interference. *Phys Rev Lett* (2005) 95(5):057401. doi:10.1103/PhysRevLett.95.057401
46. Yang WX, Hou JM, Lee RK. Ultraslow Bright and Dark Solitons in Semiconductor Quantum wells. *Phys Rev A* (2008) 77(3):033838. doi:10.1103/physreva.77.033838
47. Zhu C, Huang G. Slow-light Solitons in Coupled Asymmetric Quantum wells via Interband Transitions. *Phys Rev B* (2009) 80(23):235408. doi:10.1103/physrevb.80.235408
48. Yang WX, Liu S, Zhu Z, Ziauddin, Lee RK. Tunneling-induced Giant Goos-Hänchen Shift in Quantum wells. *Opt Lett* (2015) 40(13):3133–6. doi:10.1364/ol.40.003133
49. Asadpour SH, Nasehi R, Soleimani HR, Mahmoudi M. Phase Control of Goos–Hänchen Shift via Biexciton Coherence in a Multiple Quantum Well. *Superlattices and Microstructures* (2015) 85:112–23. doi:10.1016/j.spmi.2015.05.019
50. Sun H, Fan S, Zhang H, Gong S. Tunneling-induced High-Efficiency Four-Wave Mixing in Asymmetric Quantum wells. *Phys Rev B* (2013) 87(23):235310. doi:10.1103/physrevb.87.235310
51. Meng L-C, Zhang W-J, Liu J, Xie X-T. A Dimer *PT* -symmetric Model Simulated in *GaAs/AlGaAs* Quantum wells. *Epl* (2016) 114(3):34001. doi:10.1209/0295-5075/114/34001
52. Liu S, Yang W-X, Chuang Y-L, Chen A-X, Liu A, Huang Y, et al. Enhanced Four-Wave Mixing Efficiency in Four-Subband Semiconductor Quantum wells via Fano-type Interference. *Opt Express* (2014) 22(23):29179–90. doi:10.1364/oe.22.029179
53. Zhang Y, Wang Z, Qiu J, Hong Y, Yu B. Spatially Dependent Four-Wave Mixing in Semiconductor Quantum wells. *Appl Phys Lett* (2019) 115(17):171905. doi:10.1063/1.5121275
54. Qiu J, Wang Z, Ding D, Li W, Yu B. Highly Efficient Vortex Four-Wave Mixing in Asymmetric Semiconductor Quantum wells. *Opt Express* (2020) 28(3):2975–86. doi:10.1364/oe.379245
55. Wang Z, Zhang Y, Paspalakis E, Yu B. Efficient Spatiotemporal-Vortex Four-Wave Mixing in a Semiconductor Nanostructure. *Phys Rev A* (2020) 102(6):063509. doi:10.1103/physreva.102.063509

56. Schmidt H, Campman KL, Gossard AC, Imamolu A. Tunneling Induced Transparency: Fano Interference in Intersubband Transitions. *Appl Phys Lett* (1997) 70(25):3455. doi:10.1063/1.119199
57. Faist J, Capasso F, Sirtori C, Pfeiffer L. Controlling the Sign of Quantum Interference by Tunnelling from Quantum wells. *Nature* (1997) 390(6660): 589–91. doi:10.1038/37562
58. Peng JX, Chen Z, Yuan QZ, Feng XL. Optomechanically Induced Transparency in a Laguerre-Gaussian Rotational-Cavity System and its Application to the Detection of Orbital Angular Momentum of Light fields. *Phys Rev A* (2019) 99(4):043817. doi:10.1103/physreva.99.043817
59. Qi Y, Niu Y, Xiang Y, Wang H, Gong S. Phase Dependence of Cross-phase Modulation in Asymmetric Quantum wells. *Opt Commun* (2011) 284(1): 276–81. doi:10.1016/j.optcom.2010.09.016
60. Faist J, Sirtori C, Capasso F, Chu S-NG, Pfeiffer LN, West KW. Tunable Fano Interference in Intersubband Absorption. *Opt Lett* (1996) 21(13):985–7. doi:10.1364/ol.21.000985
61. Carlo S, Federico C, Sivco DL, Cho AY. Giant, Triply Resonant, Third-Order Nonlinear Susceptibility $\chi^{(3)}_{3\omega}$ in Coupled Quantum wells. *Phys Rev.Lett* (1992) 68(7):1010. doi:10.1103/PhysRevLett.68.1010
62. Shih T, Reimann K, Woerner M, Elsaesser T, Waldmüller I, Knorr A, et al. Nonlinear Response of Radiatively Coupled Intersubband Transitions of Quasi-Two-Dimensional Electrons. *Phys Rev B* (2005) 72(19):195338. doi:10.1103/physrevb.72.195338
63. Born M, Wolf E. *Principles of Optics*. 7th ed. Oxford, UK: Pergamon Press (1999).
64. Liu H, Capasso F. *Intersubband Transitions in Quantum wells: Physics and Device Applications*. Amsterdam, Netherlands: Elsevier (1999).
65. Wu Y, Yang X. Highly Efficient Four-Wave Mixing in Double-Λ System in Ultraslow Propagation Regime. *Phys Rev A* (2004) 70(5):053818. doi:10.1103/physreva.70.053818
66. Li L, Chang C, Yuan X, Yuan C, Feng S, Nie S, et al. Generation of Optical Vortex Array along Arbitrary Curvilinear Arrangement. *Opt Express* (2018) 26(8):9798–812. doi:10.1364/oe.26.009798
67. Ma H, Li X, Tai Y, Li H, Wang J, Tang M, et al. Generation of Circular Optical Vortex Array. *Annalen der Physik* (2017) 529(12):1700285. doi:10.1002/andp.201700285
68. Boichenko S. Toward Super-resolution Fluorescent Microscopy of Arbitrarily Oriented Single Molecules. *Phys Rev A* (2020) 101(4):043823. doi:10.1103/physreva.101.043823
69. Ni J, Wang C, Zhang C, Hu Y, Yang L, Lao Z, et al. Three-dimensional Chiral Microstructures Fabricated by Structured Optical Vortices in Isotropic Material. *Light Sci Appl* (2017) 6(7):e17011. doi:10.1038/lsa.2017.11
70. Shen Y, Wang X, Xie Z, Min C, Fu X, Liu Q, et al. Optical Vortices 30 Years on: Oam Manipulation from Topological Charge to Multiple Singularities. *Light Sci Appl* (2019) 8(1):90. doi:10.1038/s41377-019-0194-2

Conflict of Interest: The authors declare that the research was conducted in the absence of any commercial or financial relationships that could be construed as a potential conflict of interest.

frontiers | Frontiers in Physics

ORIGINAL RESEARCH
published: 18 July 2022
doi: 10.3389/fphy.2022.933285

Ultraprecise Off-Axis Atom Localization With Hybrid Fields

Ning Jia[1], *Xing-Dong Zhao*[2], *Wen-Rong Qi*[2] *and Jing Qian*[3]*

[1]Public Experiment Center, University of Shanghai for Science and Technology, Shanghai, China, [2]School of Physics, Henan Normal University, Xinxiang, China, [3]State Key Laboratory of Precision Spectroscopy, Department of Physics, Quantum Institute for Light and Atoms, School of Physics and Electronic Science, East China Normal University, Shanghai, China

Atom localization enables a high-precision imaging of the atomic position, which has provided vast applications in fundamental and applied science. In the present work, we propose a scheme for realizing two-dimensional off-axis atom localization in a three-level Λ system. Benefiting from the use of a hybrid coupling field, which consists of one Gaussian beam and one Laguerre–Gaussian beam, our scheme shows that the atoms can be localized at arbitrary position with high spatial resolution. Considering realistic experimental parameters, our numerical simulation predicts that the atoms can be precisely localized with a spatial resolution of ~ 200 nm in the range of a radial distance of a few micrometers to the beam core. Our results provide a more flexible way to localize atoms in a two-dimensional system, possibly paving one-step closer to the nanometer scale atom lithography and ultraprecise microscopy.

Keywords: off-axis localization, Laguerre–Gaussian beam, ultraprecise, quantum interference, three-level atom

OPEN ACCESS

Edited by:
Weibin Li,
University of Nottingham,
United Kingdom

Reviewed by:
Bernhard Johan Hoenders,
University of Groningen, Netherlands
Zhaoyang Zhang,
Xi'an Jiaotong University, China

***Correspondence:**
Jing Qian
jqian1982@gmail.com

Specialty section:
This article was submitted to Quantum Engineering and Technology, a section of the journal Frontiers in Physics

Received: *30 April 2022*
Accepted: *20 June 2022*
Published: *18 July 2022*

Citation:
Jia N, Zhao X-D, Qi W-R and Qian J (2022) Ultraprecise Off-Axis Atom Localization With Hybrid Fields. Front. Phys. 10:933285. doi: 10.3389/fphy.2022.933285

1 INTRODUCTION

Nowadays, the Laguerre–Gaussian (LG) beam [1] has engendered tremendous advanced applications [2–7]. For example, it is widely used in the superresolution fluorescence microscopy such as the stimulated emission depletion [8, 9] and minimal photon fluxes [10, 11] in order to overcome the diffraction limit. Another approach to this target is utilizing the spatially dependent coherent light–matter interaction in atom-light coupling systems [12–14], which essentially depends on a spatially modulated atom-light coupling. By the detection of spontaneously emitted photons [15–18], level population [19–25], absorption [26–28], and gain [29, 30], subwavelength-scale atom localization can be obtained.

As far as we know, atom localization with LG beams can exhibit a large number of advantages [31, 32]. For example, the LG beam has a donut intensity spot naturally, which may avoid the need of two orthogonal standing wave (SW) fields for generating spatially modulated atom-light coupling in a two-dimensional (2D) atom localization system. That fact largely reduces the complexity of experimental implementation. Moreover, it is easier to create a single excitation spot in its core by a LG beam. In traditional SW-based localization schemes, due to the periodicity of the SW field intensity there may exist more than one localization spots within single optical wavelength. Therefore after one-time measurement, the probability of finding atoms at a certain position can be deeply reduced. So far, some approaches have been proposed to break this periodicity of SW fields, *via* utilizing the sensitivity of light–matter interactions to the light phase in a closed-loop atomic system [33, 34] and the interference of multiple SW fields with different wavelengths and phases [35, 36]. These methods, however, will increase the complexity of experimental setup. Although the LG beam has the aforementioned advantages in localization, it can only localize atoms in the vicinity of its beam core where the laser intensity is close to zero. Off-axis atom localization must be accompanied by the movement of the LG beam itself, which undoubtedly adds to extra complexity.

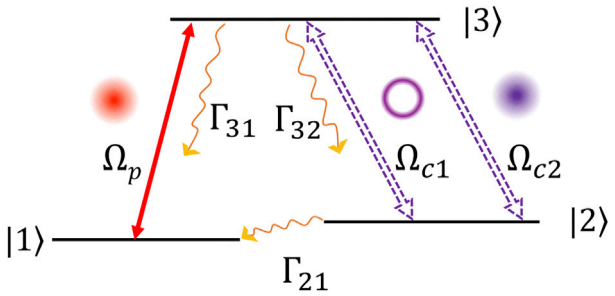

FIGURE 1 | Schematic of a Λ-type three-level system where the probe field Ω_p for the transition of states $|1\rangle$ and $|3\rangle$ is a Gaussian beam. The coupling field between $|3\rangle$ and $|2\rangle$ is composed by one LG beam Ω_{c1} and one Gaussian beam Ω_{c2}. Γ_{nm} denotes the spontaneous decay rates from $|n\rangle$ to $|m\rangle$.

In traditional SW localization schemes, the superposition of multiple SW lasers with different wavelengths and phases is commonly adopted for reaching a single excitation point [35, 36]. In addition this effect between two LG beams can show interesting patterns such as optical Ferris wheels where the light intensity can be modulated to be zero in certain positions [37]. Inspired by these contributions, in the present work, we study a 2D off-axis atom localization in a three-level Λ system, in which a Gaussian beam serves as the probe field and a LG beam together with a Gaussian beam as the hybrid coupling field. The quantum interference effect between these two beams (LG and Gaussian) can achieve a unique zero-intensity spot at arbitrary position. We show that by appropriately tuning the ratio of peak amplitudes between the LG and any Gaussian beams, atoms can be localized at arbitrary position, with a certain distance to the beam core. Both the spatial resolution and radial distance of localization can be flexibly manipulated *via* tuning laser Rabi frequencies. Depending on the numerical simulation with experimental parameters our scheme enables the realization of an efficient off-axis 2D atom localization, accompanied by a best spatial resolution ~ 200 nm and a radial distance of a few micrometers. Our scheme provides a more convenient route to the target of ultraprecise off-axis 2D atom localization.

2 THEORETICAL STRATEGY

To describe the scheme mechanism we consider a simple three-level Λ system as displayed in **Figure 1**, where states $|1\rangle$ and $|3\rangle$ are resonantly coupled by a weak probe field Ω_p and states $|3\rangle$ and $|2\rangle$ are connected by another coupling field Ω_{c2}, with zero detuning. In order to realize an off-axis atom excitation, we have assumed that the probe and coupling beams as Gaussian beams, which are

$$\Omega_i(r) = \Omega_{i0} e^{-\frac{r^2}{W_i^2}}, \tag{1}$$

where $i = p, c2$ and Ω_{i0} represent the peak amplitude and W_i the Gaussian spot size. Remarkably, states $|3\rangle$ and $|2\rangle$ are also coupled by a second LG field Ω_{c1} at the same time, as [38].

$$\Omega_{c1}(r,\theta) = \Omega_{c10}\left(\frac{r}{W_{c1}}\right)^{|l|} e^{-\frac{r^2}{W_{c1}^2}} e^{il(\theta+\theta_{c1})}, \tag{2}$$

where Ω_{c10}, W_{c1}, θ_{c1}, and l are the peak amplitude, the beam waist, the initial phase, and the winding number, respectively. r and θ are the cylindrical radius and the azimuthal angle, respectively. Here, we take the winding number $l = 1$, which enables a single-spot excitation. Other higher-order modes with $l > 1$ would lower the localization precision by redistributing the atomic population among multiple azimuthal nodes. To our knowledge, this three-level model can be experimentally realized by the D1 line of ultracold ^{87}Rb atoms with energy levels $|1\rangle = |5S_{1/2}, F = 1\rangle$, $|2\rangle = |5S_{1/2}, F = 2\rangle$, and $|3\rangle = |5P_{1/2}, F = 2\rangle$. Based on Ref. [14], we assume the decay rates from $|3\rangle \rightarrow |1\rangle$ and $|3\rangle \rightarrow |2\rangle$ are equal, typically calculated by $\Gamma_{31} = \Gamma_{32} = 2\pi \times 5.75$ MHz. The decay rate between two hyperfine ground states $|1\rangle$ and $|2\rangle$ is $\Gamma_{21} = 5$ kHz, satisfying $\Gamma_{21} \ll \Gamma_{31}, \Gamma_{32}$ [39] so the lifetime of $|2\rangle$ is about 200μs. The beam width is $W_i = W_{c1} = W$ estimated to be same for simplicity. Under the frozen-gas limit where the atomic center of mass is unvaried we can take a measurement for the population on state $|2\rangle$ by collecting its fluorescence signals with a CCD camera and a well-localized position distribution of atoms could facilitate this measurement [14].

Considering a frozen atomic gas the time evolution of the systematic density-matrix elements can be described by ($\hbar = 1$) [40].

$$\begin{aligned}
\dot{\rho}_{11} &= \Gamma_{31}\rho_{33} + \Gamma_{21}\rho_{22} - i\Omega_p(\rho_{31} - \rho_{13}),\\
\dot{\rho}_{33} &= -(\Gamma_{31} + \Gamma_{32})\rho_{33} - i\Omega_p(\rho_{13} - \rho_{31}) - i\Omega_c(\rho_{23} - \rho_{32}),\\
\dot{\rho}_{12} &= -\gamma_{12}\rho_{12} - i\Omega_p\rho_{32} + i\Omega_c\rho_{13},\\
\dot{\rho}_{13} &= -\gamma_{13}\rho_{13} - i\Omega_p(\rho_{33} - \rho_{11}) + i\Omega_c\rho_{12},\\
\dot{\rho}_{23} &= -\gamma_{23}\rho_{23} + i\Omega_p\rho_{21} - i\Omega_c(\rho_{33} - \rho_{22}),
\end{aligned} \tag{3}$$

where $\rho_{nm} = \rho_{mn}^{\star}$ and $\sum_{n=1}^{3}\rho_{nn} = 1$ mean the conservation. The population on state $|2\rangle$ is solved by $\rho_{22} = 1 - \rho_{11} - \rho_{33}$. In deriving **Eq. 3** we have defined

$$\Omega_c = \Omega_{c1} + \Omega_{c2}, \tag{4}$$

representing the superposition of two coupling fields. Γ_{nm} denotes the spontaneous decay from $|n\rangle$ to $|m\rangle$ and γ_{nm} is defined as

$$\gamma_{12} = \Gamma_{21}/2, \gamma_{13} = (\Gamma_{31} + \Gamma_{32})/2, \gamma_{23} = (\Gamma_{32} + \Gamma_{31} + \Gamma_{21})/2. \tag{5}$$

The steady solutions of **Eq. 3** can be obtained by assuming $\dot{\rho}_{nm} = \dot{\rho}_{nn} = 0$. Due to the presence of decay Γ_{21}, it is intuitive that ρ_{22} decreases with Γ_{21}. Luckily, accounting for the condition of $\Gamma_{21} \ll \Gamma_{31(32)}$ that makes the effect of Γ_{21} negligible [23, 39], then ρ_{22} takes a simple form of

$$\rho_{22}(r,\theta) = \frac{1}{1 + I_c(r,\theta)/I_p(r)}, \tag{6}$$

where $\Gamma_{31} = \Gamma_{32}$, $\Gamma_{21} = 0$ are used. $I_c = |\Omega_{c1} + \Omega_{c2}|^2$ and $I_p = |\Omega_p|^2$ stand for the laser intensities. Note that $\rho_{22}(r, \theta)$ reveals a position-dependent feature due to the use of several structured fields. From **Eq. 6**, it is apparent that the condition $I_c(r_{loc}, \theta) \ll I_p(r_{loc})$ will cause $\rho_{22} \rightarrow 1$, which means a perfect atomic confinement can be achieved at arbitrary position r_{loc} in our scheme.

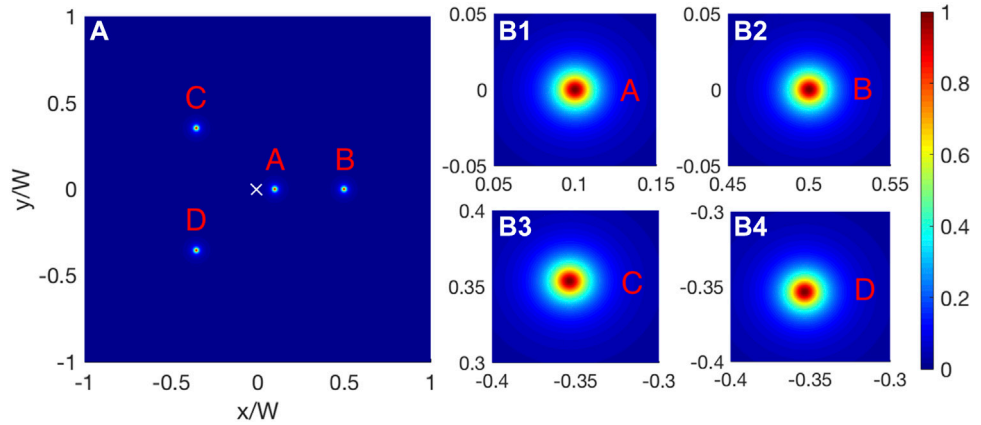

FIGURE 2 | Off-axis atom localization. **(A)** Off-axis localized positions A, B, C, and D with respect to $(\kappa_c, \theta_{c1}) = (0.1, \pi), (0.5, \pi), (0.5, \pi/4), (0.5, -\pi/4)$. The white cross denotes the center of light beams. **(B1–B4)** show the amplified images for the localized atomic positions, which have an off-axis feature. Here, $\Omega_{p0}/\Omega_{c10} = 0.01$.

3 OFF-AXIS LOCALIZATION

According to **Eq. 4** together with the definitions in **Eqs 1**, **2**, the intensity of the hybrid coupling field can be written as

$$I_c(r,\theta) = |\Omega_{c1} + \Omega_{c2}|^2 = \frac{\Omega_{c10}}{W^2} e^{-\frac{2r^2}{W^2}} \left| r + \kappa_c W e^{-i(\theta+\theta_{c1})} \right|^2, \quad (7)$$

where the peak ratio is $\kappa_c = \Omega_{c20}/\Omega_{c10}$, which can be tuned by Ω_{c20} if Ω_{c10} is fixed. Note that this hybrid coupling field is composed by one LG beam and one Gaussian beam, which resonantly couple states $|2\rangle$ and $|3\rangle$ at the same time. Finally we can arrive at an analytical solution to the equation $I_c(r, \theta) = 0$, that is, the perfect condition of localization can be reached at

$$(r_{loc}, \theta_{loc}) = (\kappa_c W, \pi - \theta_{c1}), \quad (8)$$

where the population ρ_{22} attains 1.0 in principle. That means atoms can be precisely placed at any desired position (r_{loc}, θ_{loc}) with a very high probability. While in fact, owing to the influence from intrinsic noises in the experimental setup, the observed localization resolution is quite limited. In **Section 5** we will discuss the fluctuation of laser intensities, the steady time as well as the noise from atomic thermal motion, in order to present a practical estimation for the experimental observation. Moreover, we have to point out that benefiting from the interference between two hybrid coupling fields Ω_{c1} and Ω_{c2} [41], the localization position (r_{loc}, θ_{loc}) can be widely adjusted by the beam parameters, which is not restricted merely at the beam core as in most previous works [31, 32].

As illustrated in **Figure 2A**, we show that atoms denoted as the steady population ρ_{22} on state $|2\rangle$, can be confined in any spatial position (r_{loc}, θ_{loc}) by changing the parameters (κ_c, θ_{c1}). For example when $(\kappa_c, \theta_{c1}) = (0.1, \pi), (0.5, \pi), (0.5, \pi/4), (0.5, -\pi/4)$, **Figure 2A** explicitly shows the off-axis atom localization at different positions as labeled by A ~D. **Figures 2B1–B4** amplify the distribution of atoms at different localized places. It is apparent that the spatial resolution of atom localization

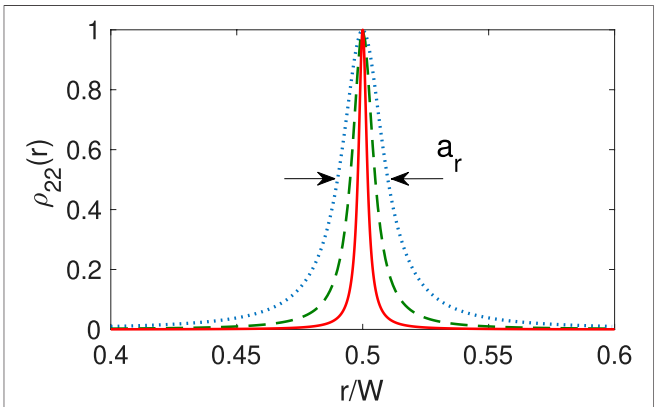

FIGURE 3 | Steady population distribution $\rho_{22}(r)$ along the radial direction r for $\kappa_p = \Omega_{p0}/\Omega_{c10} = 0.01$ (blue-dotted), 0.005 (green-dashed), and 0.002 (red-solid). a_r is the FWHM, which characterizes the spatial resolution of localization. Here, we use $\kappa_c = 0.5$.

remains unchanged for different κ_c and θ_{c1}. Therefore, thanks to the zero-intensity point $(I_c(r, \theta) = 0)$ created by the interference between two light beams Ω_{c10} and Ω_{c20}, our scheme can realize an effective off-axis localization at arbitrary position in a 2D space.

4 ULTRAPRECISE LOCALIZATION

The quality of localization also depends on a high spatial resolution, which is characterized by the full width at half maximum (FWHM) of the steady distribution ρ_{22} (r, θ). A narrower linewidth indicates that the position of atoms can be well-resolved within a smaller range. By replacing the profiles of light fields (**Eqs 1**, **2**) the expression of $\rho_{22}(r)$ takes an explicitly Lorentz form

$$\rho_{22}(r) = \frac{1}{1 + \frac{(r-\kappa_c W)^2}{\kappa_p^2 W^2}}, \tag{9}$$

where we have omitted the azimuth angle by letting $\theta = \pi - \theta_{c1}$ and paid attention to the variation of $\rho_{22}(r)$ along the radial direction. We treat the FWHM of function $\rho_{22}(r)$ as a measurement to localization, which can also be analytically solved,

$$a_r = 2\kappa_p W. \tag{10}$$

In **Figure 3**, we plot the steady distribution $\rho_{22}(r)$ vs. r for different peak ratios κ_p. Clearly a weaker probe field leads to the atomic population more confined in the vicinity of the localization point $r = r_{loc} = 0.5W$, promising for a higher resolution localization. For example, we find that $a_r = 0.02W$ when $\kappa_p = 0.01$, but this value is decreased by one order of magnitude, which is $a_r = 0.004W$ as κ_p reduces to 0.002. From **Eq. 10**, it is intuitive that $a_r \to 0$ if $\kappa_p \ll 1$, enabling an ultraprecise localization under a sufficiently weak probe field. However in a realistic system, the fact that the time for a steady state becomes much longer in the weak probe limit, results in the atomic motion non-negligible. We will discuss this point in **Section 5.2**.

5 FEASIBILITY DISCUSSION

The numbers presented in this work are considered from ^{87}Rb where the lifetime of state $|3\rangle(= |5P_{1/2}, F = 2\rangle)$ is 27.7 ns [42], leading to the decay rates $\Gamma_{31} = \Gamma_{32} = 2\pi \times 5.75$ MHz, and the lifetime of $|2\rangle(= |5S_{1/2}, F = 2\rangle)$ is 200 μs, leading to $\Gamma_{21} = 5$ kHz. We assume that the co-propagating probe and coupling lasers are overlapping in space and have a same beam width $W = 5\ \mu m$. As explicitly presented in **section 3** and **section 4**, our scheme can achieve an ultraprecise off-axis atom localization due to the flexible manipulation of peak ratios κ_c and κ_p, together with the azimuth angle θ_{c1}. Due to the rotational invariance we ignore θ_{c1} by focusing on the radial distance r. However, as for an experimental implementation these parameters are also restrained. In this section, we numerically solve the spatial resolution a_r and the peak value of $\rho_{22}(r)$ by evolving the motional **Eq. 3** under more realistic conditions coming from measurement.

5.1 Laser Intensity Noise

To obtain realistic results evaluating experimental conditions, we introduce a perturbed laser intensity by adding a random intensity noise $\delta\Omega_i$ ($i = p, c1, c2$) to the peak value Ω_{i0} [43, 44]. The resulting fluctuated Rabi frequencies Ω'_{i0} can be written as

$$\Omega'_{i0} = \Omega_{i0} + \delta\Omega_i. \tag{11}$$

In the calculation, we assume $\delta\Omega_i/\Omega_{i0} \in [-\xi, \xi]$ and pay attention to the radial population distribution $\rho_{22}(r)$. During each measurement, the perturbation term $\delta\Omega_i$ can be a random number obtained from the range of $[-\xi, \xi]\Omega_{i0}$. By taking account of sufficient measurements, the average result can show the realistic observation in the experimental setup. Note that a larger Rabi frequency leads to stronger laser noise since $\delta\Omega_i \propto \Omega_{i0}$.

Figure 4 illustrates the distribution of steady population $\rho_{22}(r)$ under the influence of laser intensity noise, which is characterized by the factor ξ. By comparing **Figures 4A–D** it is apparent that a bigger ξ will give rise to a broadened population distribution with smaller peak values, which lowers the precision of localization. Furthermore, as for atoms localized closer to the beam core ($r = 0$) the intensity noise $\delta\Omega_{c2}$ [$\propto\Omega_{c20}$] is smaller due to $r_{loc} = \kappa_c W$. Therefore by positioning atoms far from the beam core the observation will suffer from a stronger laser intensity noise, in turn yielding a lower-quality localization, see **Figures 4A–D**. This fact gives a limitation to our protocol that the atoms cannot be placed very far from the beam core. A rough estimation (not shown) shows that the average peak value of $\rho_{22}(r)$ will be smaller than 0.2 if the radial localization distance r_{loc} is larger than 10 μm. In the experiment, a better control for the laser intensity noise can improve the scheme performance.

5.2 Time Needed for a Steady State

From **section 4**, we have known that ultraprecise localization with $a_r \to 0$ in principle relies on a sufficiently small κ_p, that is, $\Omega_{p0} \ll \Omega_{c10}$. This condition leads to the time T_s for reaching steady localization much longer. Because T_s is inversely proportional to the exact laser Rabi frequencies. For a longer T_s, the atomic thermal motion does play roles and the frozen-gas approximation fails. A discussion for the effect of atomic thermal motion can be seen in **section 5.3**. An efficient localization reports that T_s is so short to make the atomic movement during the steady time negligible. In the calculation, we consider atoms under the temperature $T = 1\ \mu K$ [14], with a most probable velocity $v_p = \sqrt{2k_B T/M} \approx 1.4$ cm/s, where k_B is the Boltzmann constant and M is the atomic mass. We introduce a new constraint to the resolution factor a_r

$$v_p T_s^{max} \le a_r \big/ 10, \tag{12}$$

where the real time T_s for a steady state should be smaller than $T_s^{\max}$ so as to make the atomic motion negligible during the measurement.

Figure 5 exhibits the steady time T_s as a function of the localization distance r_{loc} for different peak probe Rabi frequencies Ω_{p0}. Here, T_s is obtained by numerically evolving the master **Eq. 3**, considering all spontaneous decays. From **Figures 5A–D**, as decreasing Ω_{p0} we find that the steady time T_s (blue-solid) increases significantly; although the position of atoms can be well-resolved with a better spatial resolution (a_r becomes smaller) at the same time. According to the constraint (12), the maximal steady time $T_s^{\max}$ permitted for localization is labeled by the red-dashed line in the figure. When $T_s < T_s^{\max}$ atoms can obtain a robust localization. Obviously, in **Figures 5A,B** where the spatial resolution a_r is relatively large, atoms can be well localized within a wider radial range $r_{loc} < 5.3\ \mu m$ and $r_{loc} < 3.7\ \mu m$. Insets explicitly show the area of off-axis localization, which is denoted as a gray

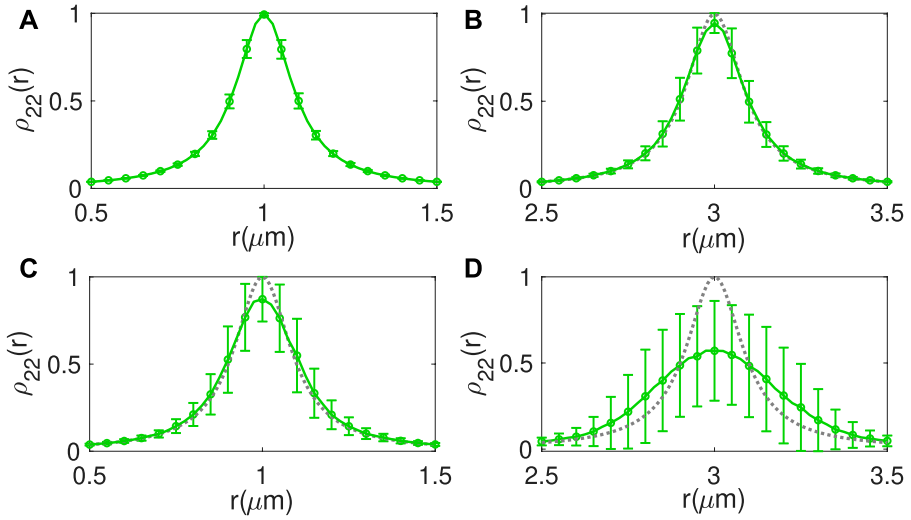

FIGURE 4 | Radial population distribution $\rho_{22}(r)$ under different intensity noises, which are given by **(A,B)** $\xi = 1.0\%$ and **(C,D)** $\xi = 5.0\%$ at different positions. We take 500 measurements for each point denoted by the error bar and the average result is shown by the green solid line. For comparison the black-dotted line indicates the result without any intensity noise, that is, $\xi = 0$. Here, $\Omega_{c20}/2\pi$ = (30, 90) MHz, respectively for **(A,C)** and **(B,D)**, corresponding to the localization positions r_{loc} = (1.0, 3.0) μm. Other parameters are $\Omega_{p0}/2\pi$ = 3 MHz, $\Omega_{c10}/2\pi$ = 150 MHz, and W = 5 μm.

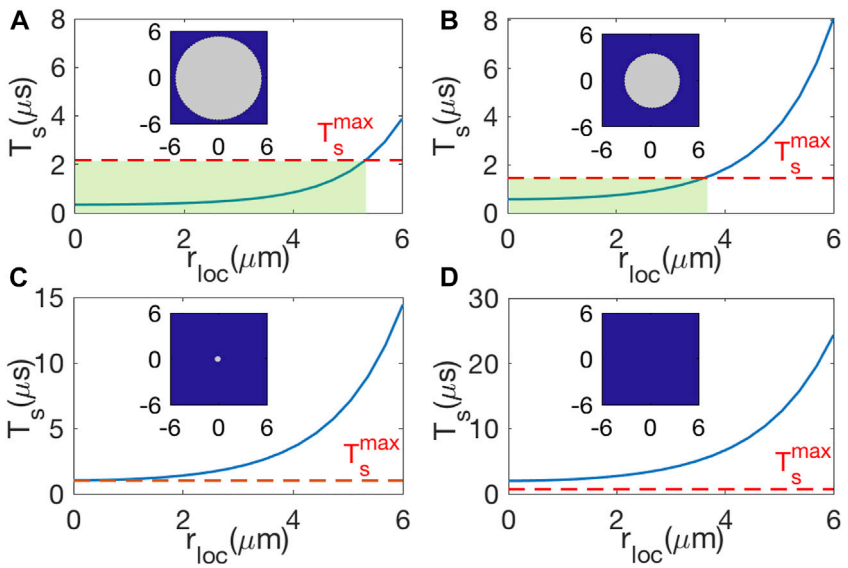

FIGURE 5 | Steady time T_s vs. the radius distance r_{loc} under **(A)** $\Omega_{p0}/2\pi = 4.5$ MHz and $a_r = 300$ nm, **(B)** $\Omega_{p0}/2\pi = 3.0$ MHz and $a_r = 200$ nm, **(C)** $\Omega_{p0}/2\pi = 2.1$ MHz and a_r = 141 nm, and **(D)** $\Omega_{p0}/2\pi$ = 1.5 MHz and a_r = 100 nm. The red-dashed line denotes the maximal T_s permitted for an efficient localization. The shaded-green region stands for the radial range where atoms can be localized. Insets: effective off-axis localization is enabled within the gray disk. Here, $\Omega_{c10}/2\pi = 150$ MHz, $W = 5$ μm, $\Omega_{c20} = r_{loc}\Omega_{c10}/W$, T = 1 μK, and Γ_{21} = 5 kHz.

disk. In fact *via* an appropriate adjustment of κ_c and θ_{c1}, atoms can be confined at arbitrary position inside the gray disk.

Whereas, when Ω_{p0} is reduced to $2\pi \times 2.1$ MHz (**Figure 5C**), the reduction of a_r causes $T_s^{\max} \leq T_s$ persistently. In this case only atom positioned at the beam core can be accurately confined so the protocol of off-axis localization fails. Furthermore, if $a_r <$ 141 nm, for example, a_r = 100 nm as in **Figure 5D**, the steady time T_s is maintained larger than the required $T_s^{\max}$, calculated by **Eq. 12** so no atoms could be localized. Because during such a longer steady time T_s most atoms have been moved away from the localization spot caused by their thermal motions, leading to a poor resolution (also see the discussion in **section 5.3**). Therefore, based on our analysis, we treat a_r = 141 nm as the best spatial resolution yet atoms can only be localized at the beam core. Effective off-axis localization needs to be at the expense of the spatial resolution. For example, a resolution of a_r = 200 nm

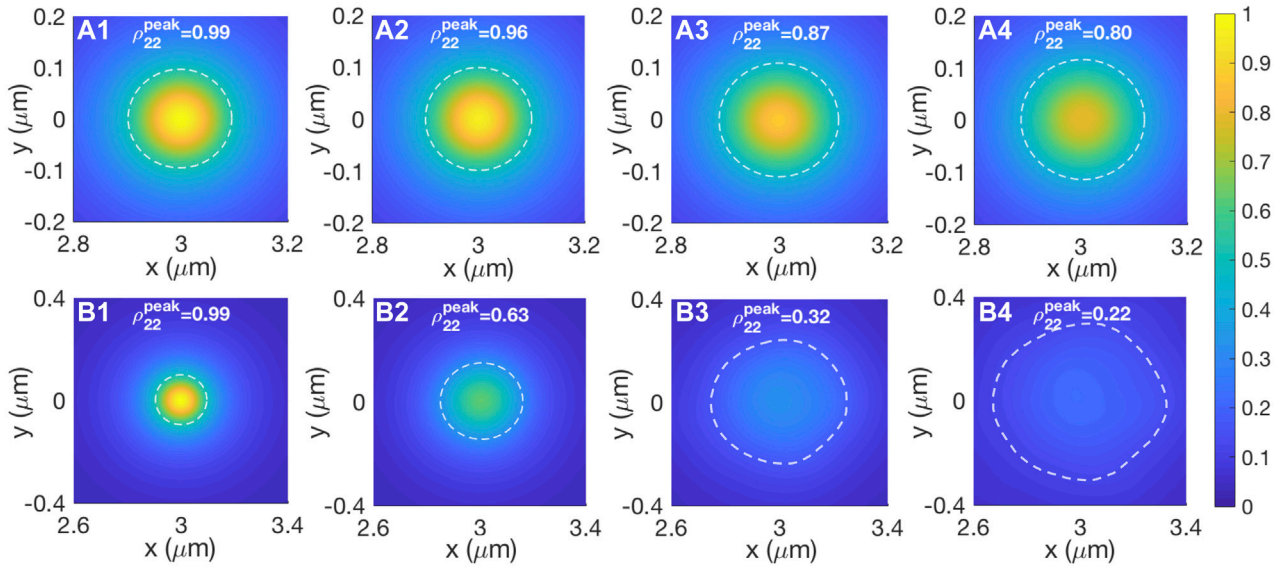

FIGURE 6 | (A1–A4) 2D population distribution of $\rho_{22}(r)$ under different temperatures T = (0, 1, 5, 10)μK. The peak value of $\rho_{22}(r)$ is given in the picture and the diameter of white-dashed rings stands for the spatial resolution a_r, which is a_r = (200, 206, 222, 247) nm, respectively. Here, we assume the measurement time is T_{meas} = 1 μs. Analogous to **(A1–A4)**, **(B1–B4)** show the case of T_{meas} = 5 μs and the calculated resolution is a_r = (200, 308, 530, 687) nm. Every point is obtained by averaging over 500 measurements.

(300 nm) can be obtained within a localized radius of $r_{loc} < 3.7$ μm (5.3 μm), see the insets of **Figures 5A,B** for a more visible representation. In addition, since the steady time is inversely proportional to the exact Rabi frequencies the limitation for a best off-axis localization can further be overcome by a stronger coupling laser. For example, when $\Omega_{c10}/2\pi$ = 300 MHz and $\Omega_{p0}/2\pi$ = 2.7 MHz the best spatial resolution of our protocol can be reduced to 91 nm if atoms are localized in the beam core (not shown).

5.3 Noise From Atomic Thermal Motion

In a real experimental setup due to atomic thermal motion, the laser intensity 'seen' by atoms would have a strong perturbation, which intuitively brings a noise on detecting the steady atomic population. Here, we consider atoms move randomly in space whose velocities satisfy a two-dimensional Maxwell–Boltzmann distribution [45].

$$f(v_x, v_y) = \frac{1}{\pi v_p^2} e^{-\left(v_x^2+v_y^2\right)/v_p^2}. \tag{13}$$

Here, v_p is the most probable velocity defined by $v_p = \sqrt{2k_BT/M}$. Other interatomic collisions are ignored. During the jth measurement we assume a simple uniform motion of atoms by letting

$$(x_j, y_j) \rightarrow (x_j + v_x T_{meas}, y_j + v_y T_{meas}), \tag{14}$$

where (v_x, v_y) are obtained stochastically from the velocity function f (v_x, v_y) and T_{meas} is the time for single measurement. By inserting **Eq. 14** into **Eqs 1**, **2** atoms can feel a fluctuated Rabi frequency $\Omega_i(t)$ (i = p, $c1$, $c2$) for each measurement. The final results are based on an average of 500 times random samplings of the velocity (v_x, v_y).

In **Figure 6**, we show the calculated population distribution $\rho_{22}(r)$ under sufficient measurements in the x–y frame. Clearly, from **Figures 6A1–A4** due to a larger probable velocity of atoms caused by the growing temperature, the peak value ρ_{22}^{peak} has an explicit decrease together with a lower spatial resolution a_r. For example, when T = 1 μK, a_r = 206 nm which is close to the value at T = 0. Because the average distance of atoms during each measurement (T_{meas} = 1 μs) is only $v_pT_{meas} \approx$ 14 nm, which is much smaller than a_r. However, as for a higher temperature the movement of atoms during each measurement can cause a bigger effect making the precision of atom localization worse. See the case of T = 10 μK in **Figure 6A4**, we observe that ρ_{22}^{peak} = 0.8 and a_r = 247 nm. For comparison in **Figures 6B1–B4** we also study the case of a longer measurement time (T_{meas} = 5 μs) where atoms can move farther, leading to a very poor spatial resolution at a finite temperature. We numerically show that at T = 10 μK the distribution of atomic population $\rho_{22}(r)$ has become slightly deformed with its peak value (spatial resolution) as low as ρ_{22}^{peak} = 0.22(a_r = 687 nm). That fact means such a long-time measurement has made most atoms away from the localization spot *via* their thermal movements. Therefore a faster measurement accompanied by a lower environment temperature can facilitate high-quality atom localization.

6 CONCLUSION

To conclude, our scheme presents a novel 2D atom localization, having both ultraprecise and off-axis features.

Differing from the previous works using a single LG field we adopt a LG beam together with a Gaussian beam as the hybrid coupling field. The previous contributions can only localize atom in the beam core where the intensity of coupling field is zero. While our protocol shows that atoms can be localized at arbitrary position due to the effect of quantum interference between these two coupling beams that leads to a zero-intensity spot in space. Our numerical simulation confirms that with an appropriate adjustment for the peak ratios of laser Rabi frequencies a wider off-axis localization range and higher quality spatial resolution can be achieved at the same time. Under experimentally feasible parameters an estimation for the implementation of realistic off-axis atom localization is predicted, promising for a resolution of ~ 200 nm and a localized radius of a few μm. In addition, we also discuss the weakness of our scheme when some intrinsic quantum noises from imperfect measurement, including laser intensity noise, limited steady time, and atomic thermal motion, are considered. Our approach may provide unique application to atomic lithography with more flexibility and better resolution [46]. An extension to the 3D off-axis atom localization is possible by implementing a spatial modulation to the probe detuning which is our next-step work [32].

DATA AVAILABILITY STATEMENT

The original contributions presented in the study are included in the article/Supplementary Material; further inquiries can be directed to the corresponding author.

AUTHOR CONTRIBUTIONS

The idea was first conceived by NJ. NJ was responsible for the physical modeling, the numerical calculations, and writing the original draft under the supervision of JQ. JQ contributed to review and editing. JQ verified results of the theoretical calculation. X-DZ contributed to editing the draft. X-DZ and W-RQ contributed to the discussion of the results.

FUNDING

This work was supported by the National Natural Science Foundation of China under Grant Nos 12104308, 12174106, 11474094, 11104076, 12104135, and 11604086; by the Science and Technology Commission of Shanghai Municipality under Grant No. 18ZR1412800.

REFERENCES

1. Babiker M, Andrews DL, Lembessis VE. Atoms in Complex Twisted Light. *J Opt* (2018) 21:013001. doi:10.1088/2040-8986/aaed14
2. Grier DG. A Revolution in Optical Manipulation. *Nature* (2003) 424:810–6. doi:10.1038/nature01935
3. Padgett M, Bowman R. Tweezers with a Twist. *Nat Photon* (2011) 5:343–8. doi:10.1038/nphoton.2011.81
4. Ran L-L, Guo Z-Y, Qu S-L. Rotational Motions of Optically Trapped Microscopic Particles by a Vortex Femtosecond Laser. *Chin Phys. B* (2012) 21:104206. doi:10.1088/1674-1056/21/10/104206
5. Dholakia K, Simpson NB, Padgett MJ, Allen L. Second-Harmonic Generation and the Orbital Angular Momentum of Light. *Phys Rev A* (1996) 54: R3742–R3745. doi:10.1103/PhysRevA.54.R3742
6. Kong F, Zhang C, Bouchard F, Li Z, Brown GG, Ko DH, et al. Controlling the Orbital Angular Momentum of High Harmonic Vortices. *Nat Commun* (2017) 8:14970. doi:10.1038/ncomms14970
7. Gauthier D, Ribič PR, Adhikary G, Camper A, Chappuis C, Cucini R, et al. Tunable Orbital Angular Momentum in High-Harmonic Generation. *Nat Commun* (2017) 8:14971. doi:10.1038/ncomms14971
8. Vicidomini G, Bianchini P, Diaspro A. Sted Super-Resolved Microscopy. *Nat Methods* (2018) 15:173–82. doi:10.1038/nmeth.4593
9. Schermelleh L, Ferrand A, Huser T, Eggeling C, Sauer M, Biehlmaier O, et al. Super-Resolution Microscopy Demystified. *Nat Cell Biol* (2019) 21:72–84. doi:10.1038/s41556-018-0251-8
10. Masullo LA, Steiner F, Zähringer J, Lopez LF, Bohlen J, Richter L, et al. Pulsed Interleaved Minflux. *Nano Lett* (2021) 21:840–6. doi:10.1021/acs.nanolett.0c04600
11. Balzarotti F, Eilers Y, Gwosch KC, Gynnå AH, Westphal V, Stefani FD, et al. Nanometer Resolution Imaging and Tracking of Fluorescent Molecules with Minimal Photon Fluxes. *Science* (2017) 355:606–12. doi:10.1126/science.aak9913
12. Proite NA, Simmons ZJ, Yavuz DD. Observation of Atomic Localization Using Electromagnetically Induced Transparency. *Phys Rev A* (2011) 83:041803. doi:10.1103/PhysRevA.83.041803
13. Miles JA, Simmons ZJ, Yavuz DD. Subwavelength Localization of Atomic Excitation Using Electromagnetically Induced Transparency. *Phys Rev X* (2013) 3:031014. doi:10.1103/PhysRevX.3.031014
14. Miles JA, Das D, Simmons ZJ, Yavuz DD. Localization of Atomic Excitation Beyond the Diffraction Limit Using Electromagnetically Induced Transparency. *Phys Rev A* (2015) 92:033838. doi:10.1103/PhysRevA.92.033838
15. Qamar S, Zhu S-Y, Zubairy MS. Precision Localization of Single Atom Using Autler-Townes Microscopy. *Opt Commun* (2000) 176:409–16. doi:10.1016/S0030-4018(00)00535-6
16. Ghafoor F, Qamar S, Zubairy MS. Atom Localization via Phase and Amplitude Control of the Driving Field. *Phys Rev A* (2002) 65:043819. doi:10.1103/PhysRevA.65.043819
17. Ghafoor F. Subwavelength Atom Localization via Quantum Coherence in a Three-Level Atomic System. *Phys Rev A* (2011) 84:063849. doi:10.1103/PhysRevA.84.063849
18. Wan R-G, Zhang T-Y. Two-Dimensional Sub-Half-Wavelength Atom Localization via Controlled Spontaneous Emission. *Opt Express* (2011) 19: 25823–32. doi:10.1364/OE.19.025823
19. Yavuz DD, Proite NA. Nanoscale Resolution Fluorescence Microscopy Using Electromagnetically Induced Transparency. *Phys Rev A* (2007) 76:041802. doi:10.1103/PhysRevA.76.041802
20. Paspalakis E, Knight PL. Localizing an Atom via Quantum Interference. *Phys Rev A* (2001) 63:065802. doi:10.1103/physreva.63.065802
21. Kapale KT, Agarwal GS. Subwavelength Atom Localization via Coherent Population Trapping. In: Frontiers in Optics (Optica Publishing Group) (2006). p. FThO5. doi:10.1364/FIO.2006.FThO5
22. Ivanov V, Rozhdestvensky Y. Two-Dimensional Atom Localization in a Four-Level Tripod System in Laser Fields. *Phys Rev A* (2010) 81:033809. doi:10.1103/PhysRevA.81.033809
23. Ivanov VS, Rozhdestvensky YV, Suominen K-A. Three-Dimensional Atom Localization by Laser Fields in a Four-Level Tripod System. *Phys Rev A* (2014) 90:063802. doi:10.1103/PhysRevA.90.063802
24. Wang Z, Yu B. High-Precision Two-Dimensional Atom Localization via Quantum Interference in a Tripod-Type System. *Laser Phys Lett* (2014) 11: 035201. doi:10.1088/1612-2011/11/3/035201
25. Zhu Z, Yang W-X, Chen A-X, Liu S, Lee R-K. Dressed-State Analysis of Efficient Three-Dimensional Atom Localization in a Ladder-Type Three-Level Atomic System. *Laser Phys* (2016) 26:075203. doi:10.1088/1054-660x/26/7/075203

26. Sahrai M, Tajalli H, Kapale KT, Zubairy MS. Subwavelength Atom Localization via Amplitude and Phase Control of the Absorption Spectrum. *Phys Rev A* (2005) 72:013820. doi:10.1103/PhysRevA.72.013820
27. Sahrai M, Mahmoudi M, Kheradmand R. Atom Localization of a Two-Level Pump-Probe System via the Absorption Spectrum. *Laser Phys* (2007) 17:40–4. doi:10.1134/S1054660X07010082
28. Zhang D, Yu R, Sun Z, Ding C, Zubairy MS. Efficient Three-Dimensional Atom Localization Using Probe Absorption in a Diamond-Configuration Atomic System. *J Phys B: Mol Opt Phys* (2019) 52:035502. doi:10.1088/1361-6455/aaf5ec
29. Qamar S, Mehmood A, Qamar S. Subwavelength Atom Localization via Coherent Manipulation of the Raman Gain Process. *Phys Rev A* (2009) 79:033848. doi:10.1103/PhysRevA.79.033848
30. Wan R-G, Zhang T-Y, Kou J. Two-Dimensional Sub-Half-Wavelength Atom Localization via Phase Control of Absorption and Gain. *Phys Rev A* (2013) 87:043816. doi:10.1103/PhysRevA.87.043816
31. Kazemi SH, Veisi M, Mahmoudi M. Atom Localization Using Laguerre-Gaussian Beams. *J Opt* (2019) 21:025401. doi:10.1088/2040-8986/aafe61
32. Jia N, Qian J, Kirova T, Juzeliūnas G, Reza Hamedi H. Ultraprecise Rydberg Atomic Localization Using Optical Vortices. *Opt Express* (2020) 28:36936–52. doi:10.1364/OE.411130
33. Ding C, Li J, Yang X, Zhang D, Xiong H. Proposal for Efficient Two-Dimensional Atom Localization Using Probe Absorption in a Microwave-Driven Four-Level Atomic System. *Phys Rev A* (2011) 84:043840. doi:10.1103/PhysRevA.84.043840
34. Hamedi HR, Juzeliūnas G. Phase-Sensitive Atom Localization for Closed-Loop Quantum Systems. *Phys Rev A* (2016) 94:013842. doi:10.1103/PhysRevA.94.013842
35. Rahmatullah U, Qamar S. Two-Dimensional Atom Localization via Probe-Absorption Spectrum. *Phys Rev A* (2013) 88:013846. doi:10.1103/PhysRevA.88.013846
36. Hong Y, Wang Z, Yu B. High-Precision Three-Dimensional Atom Localization via Kerr Nonlinearity. *J Opt Soc Am B* (2019) 36:746–51. doi:10.1364/JOSAB.36.000746
37. Franke-Arnold S, Leach J, Padgett MJ, Lembessis VE, Ellinas D, Wright AJ, et al. Optical Ferris Wheel for Ultracold Atoms. *Opt Express* (2007) 15:8619–25. doi:10.1364/OE.15.008619
38. Hamedi HR, Paspalakis E, Žlabys G, Juzeliūnas G, Ruseckas J. Complete Energy Conversion Between Light Beams Carrying Orbital Angular Momentum Using Coherent Population Trapping for a Coherently Driven Double- Λ Atom-Light-Coupling Scheme. *Phys Rev A* (2019) 100:023811. doi:10.1103/PhysRevA.100.023811
39. Wang Z, Yu B. Efficient Three-Dimensional Atom Localization via Probe Absorption. *J Opt Soc Am B* (2015) 32:1281–6. doi:10.1364/JOSAB.32.001281
40. Paspalakis E, Terzis AF, Knight PL. Quantum Interference Induced Sub-Wavelength Atomic Localization. *J Mod Opt* (2005) 52:1685–94. doi:10.1080/09500340500072489
41. Qiu J, Wang Z, Yu B. Generation of New Structured Beams via Spatially Dependent Transparency. *Quan Inf Process* (2019) 18:160. doi:10.1007/s11128-019-2278-6
42. Volz U, Schmoranzer H. Precision Lifetime Measurements on Alkali Atoms and on Helium by Beam-Gas-Laser Spectroscopy. *Phys Scr* (1996) T65:48–56. doi:10.1088/0031-8949/1996/t65/007
43. Dridi G, Guérin S, Hakobyan V, Jauslin HR, Eleuch H. Ultrafast Stimulated Raman Parallel Adiabatic Passage by Shaped Pulses. *Phys Rev A* (2009) 80:043408. doi:10.1103/PhysRevA.80.043408
44. Kang Y-H, Chen Y-H, Shi Z-C, Huang B-H, Song J, Xia Y. Nonadiabatic Holonomic Quantum Computation Using Rydberg Blockade. *Phys Rev A* (2018) 97:042336. doi:10.1103/PhysRevA.97.042336
45. Huo X, Chen JF, Qian J, Zhang W. Interaction-Enhanced Transmission Imaging with Rydberg Atoms. *Phys Rev A* (2022) 105:012817. doi:10.1103/PhysRevA.105.012817
46. Johnson KS, Thywissen JH, Dekker NH, Berggren KK, Chu AP, Younkin R, et al. Localization of Metastable Atom Beams with Optical Standing Waves: Nanolithography at the Heisenberg Limit. *Science* (1998) 280:1583–6. doi:10.1126/science.280.5369.1583

Conflict of Interest: The authors declare that the research was conducted in the absence of any commercial or financial relationships that could be construed as a potential conflict of interest.

Publisher's Note: All claims expressed in this article are solely those of the authors and do not necessarily represent those of their affiliated organizations, or those of the publisher, the editors, and the reviewers. Any product that may be evaluated in this article, or claim that may be made by its manufacturer, is not guaranteed or endorsed by the publisher.

Advantages of publishing in Frontiers

OPEN ACCESS
Articles are free to read for greatest visibility and readership

FAST PUBLICATION
Around 90 days from submission to decision

HIGH QUALITY PEER-REVIEW
Rigorous, collaborative, and constructive peer-review

TRANSPARENT PEER-REVIEW
Editors and reviewers acknowledged by name on published articles

Frontiers
Avenue du Tribunal-Fédéral 34
1005 Lausanne | Switzerland

Visit us: www.frontiersin.org
Contact us: frontiersin.org/about/contact

REPRODUCIBILITY OF RESEARCH
Support open data and methods to enhance research reproducibility

DIGITAL PUBLISHING
Articles designed for optimal readership across devices

FOLLOW US
@frontiersin

IMPACT METRICS
Advanced article metrics track visibility across digital media

EXTENSIVE PROMOTION
Marketing and promotion of impactful research

LOOP RESEARCH NETWORK
Our network increases your article's readership